UNIVERSITY OF TRENTO
Department of Physics


# Density relaxations across the glass-transition under equilibrium and non-equilibrium conditions

Supervisor:
Prof. Giulio Monaco

PhD Candidate:
Alessandro Martinelli

Doctoral Program in Physics
XXXIII cycle

# Contents

# Chapter 1

# Introduction

Amorphous systems are companions in our everyday life, few examples being car windows, glasses, mayonnaise, toothpaste or paints. Among all the materials with structural disorder, glasses play a key role in both the industrial (drugs delivery, food conservation and manufacturing, material strengthening) and scientific world. But what is a glass, exactly?
Glasses are known from the dawn of humanity and are usually defined as a liquid that is no more able to flow [1]. The cooling down of a liquid below its melting point is accompanied by an increase of the viscosity. If the crystallization is avoided (cooling the system fast enough), at a certain temperature, called the glass transition temperature $T_g$, the viscosity becomes so high that the molecules cannot explore anymore new structural configurations and the system loses its ergodicity, falling out of equilibrium. We achieve the so called glassy state. Notwithstanding that glasses have been produced for centuries, the understanding of the glass transition at the atomic length-scale still remains obscure and only recent studies have shone some light on the topic. Difficulties in investigating such amorphous systems are due to different factors. First of all, their disordered structure closely resembles the one of the liquid state, but being the dynamics frozen in time, temporal averages cannot be invoked. Furthermore, the dynamical signatures of the glass transition are expected to be present in the dynamical correlations at the medium-range length-scale, challenging to probe experimentally.
The most common family of glasses nowadays utilized are oxides of silica and boron. The relatively low $T_g$, high corrosion resistance to chemicals and almost inert behavior make these glasses the reference materials for both industrial and scientific applications. It is not surprising then that they are considered as the glassy materials par excellence.
With this Thesis we want to make a step further in the understanding of the microscopic properties of the glass transition in oxides, elucidating the dynamical aspects of such amorphous systems approaching the structural arrest. The fall-out of equilibrium of the liquid toward the glassy state will be followed, investigating the microscopic processes governing it and their spatial extent. In particular, we will measure and characterize the density fluctuations approach-

ing $T_g$ at the atomic length-scale (below the nm) and on typical rearranging times in the range of seconds.
In order to satisfy these two conditions, we will utilize here the photon-correlation technique. This scattering method was developed in the beginning with the advent of lasers under the name of *dynamic light scattering* and is based on the coherence properties of the probe radiation. In fact if the incident light is coherent it will be scattered by the density modulations in the sample, in a similar fashion to what happens in the Young's double slit experiment or with a diffraction grating. The scattered interference pattern is then related to the structural configuration of the system and, following its temporal evolution, it is possible to obtain information on the sample's dynamics. More recently, this technique has been implemented with the use of partially coherent X-rays at third generation synchrotron facilities under the name of X-Ray Photon Correlation Spectroscopy (XPCS) [2]. XPCS offers the possibility to effectively investigate inter-atomic distances and time scales as long as thousands of seconds, paving the way to the understanding of the slow dynamics in structural glasses: for this reason, XPCS has been chosen as the leading technique to pursue our study of the glass transition.
First applications of XPCS to the world of structural glasses involved the study of metallic systems [3, 4], where atomic-scale density relaxations were measured well below the glass transition temperature. These rearrangements have been recognized as stress-related phenomena, similarly to what often observed in colloidal systems [5]. In metallic glasses in fact the preparation procedure, involving a very fast quench, leads to an extremely out-of-equilibrium glass: XPCS has been demonstrated to be sensitive to stresses trapped in the system, and has given the possibility to follow their release towards near equilibrium configurations [6]. Analogously, fast relaxations were observed in oxide glasses probed with XPCS [7]. Despite the similarities with a stress-release mechanism as in metallic glasses, it was soon recognized that here the dynamics is induced by the impinging photon flux, in a pump-and-probe fashion [8]. The typical time of the relaxation process was observed to scale inversely with to the dose rate delivered to the sample and got the name of *beam-induced dynamics* [8]. Furthermore, a recent study on boron oxide has shown that the beam-induced dynamics is an effect in competition with the spontaneous structural rearrangements, effectively masking them close and below $T_g$ [9].
Despite the pioneering studies, beam-induced dynamics are still to be clarified and there are many questions demanding an answer.

1. XPCS is one of the most promising techniques to elucidate the glass transition properties. In oxide glasses, however, the beam-induced dynamics have posed difficulties in studying the spontaneous density fluctuations. Is there any chance to utilize this technique to investigate the structural relaxation in such systems?

2. Beam-induced dynamics are observed in many oxides, ranging from silicates to borates. Which is the origin of this effect? Is it universal in

all oxide glasses or are there peculiar, system dependent, differences?

3. It is well understood that dynamics in glasses are sensitive to trapped-in stresses. How do these stresses depend on the physical properties of the glasses, i.e. their structure or elasticity?

4. It was demonstrated that beam-induced dynamics are present at photon fluxes and doses where radiation damage is still negligible. What is the role of these photo-induced displacements on the structural properties of the oxide glasses?

**Structure of this Thesis**

My Thesis is composed of 7 Chapters, where the results of different experiments have been collected for their relevance on the different topics. More specifically, it has been organized starting from the experiments in systems at equilibrium and moving then to non-equilibrium conditions. In the end, I will discuss an interesting link between these two classes of experiments.

- Chapter 2 is dedicated to introduce the fundamental concepts touched in this Thesis.
  The glassy state is discussed, highlighting in particular the out-of equilibrium nature of glasses from a thermodynamical point of view. The theoretical description of the density correlations is then introduced, elucidating the experimentally accessible observables which characterize the dynamics of amorphous systems. Finally, the concepts of dynamical heterogeneities and four-point susceptibility are presented together with recent results regarding the glassy dynamics.

- Chapter 3 is devoted to discuss the details of the experimental techniques utilized here.
  An introduction to the theory behind coherent scattering experiments is reported, giving a summary of the state of the art. The coherence properties of the scattered field are then discussed and related to the density correlations introduced in the previous Chapter. Different aspects of the photon correlation spectroscopy technique are then touched, highlighting the new possibilities offered by X-ray Photon Correlation Spectroscopy (XPCS). In the end, a few fundamental aspects regarding the experiments performed at synchrotron radiation centers are reported.

- Chapter 4 discusses the equilibrium dynamics in the undercooled $LiBO_2$ liquid.
  The sample preparation of lithium borate glasses, together with further experimental details, is described. As a second point, the results of an XPCS investigation of liquid $LiBO_2$ are presented and those results are compared with models and other results available in the literature. The Chapter closes with a description of the visible photon correlation setup

here utilized and a semi-logarithmic acquisition scheme implemented to improve the performances of our setup. Finally, the glass transition temperature together with the fragility index have been measured.

- Chapter 5 is dedicated to the study of the out-of-equilibrium dynamics. The first part covers the investigation of the stress induced dynamics in a colloidal glass, which is utilized to introduce the formalism of stress-related velocity fields, compressed correlation functions and ballistic-like rearrangements. The reported dynamics are shown to proceed through anisotropic rearrangements characterized by dynamical heterogeneities involving few thousands of particles. The second part of the Chapter tackles the problem of beam-induced dynamics. We start by introducing recent advancements in the field and then discuss results obtained for a series of alkali-borates glasses. Here the beam-induced dynamics are exploited as a probe sensitive to the medium-range network topology of the glasses and are shown to be related to the stress-rigidity of the network.

- Chapter 6 exploits the potential of XPCS and, in particular, of beam-induced dynamics to probe the internal stresses of glasses which, in the end, are released by the X-ray beam exposure.
  The first part of the Chapter describes a study of the photo-induced dynamics as a function of the temperature for the $LiBO_2$ glass. The signatures of stress-related dynamics in the probed system are discussed, focusing the attention on the stretching parameter of the density correlation functions and on how the thermal annealing procedure releases partially the stresses stored in the network. The second part of the Chapter is dedicated to the X-ray dose dependent dynamics observed in two samples of lithium-borate glasses. The details of the dynamics, characterized by a stress-release process at low absorbed doses, are presented and the similarities and differences with respect to dynamics in the colloidal systems reported in Chapter 5 are highlighted. Finally, the effect of X-ray photons on glassy samples is elucidated, showing that the beam-induced dynamics effectively anneals the samples, leading to glasses with dynamical properties similar to the ones observed in undercooled liquids.

- Chapter 7 reports the main conclusions of this Thesis, summarizing the findings discussed in the previous Chapters.

# Chapter 2

# Modelling disordered systems: from liquids to glasses

This chapter is dedicated to the glass transition and its related properties: starting from a phenomenological description, we will discuss the behavior of macroscopic observables (for example the viscosity) approaching the arrested phase. We will then describe the thermodynamic aspects of the glassy state and, as a last point touched here, we will introduce the formalism of the density correlations, essential in order to discuss the dynamical properties approaching the glass transition.

## 2.1 The glassy state

*"Glass, in the popular and basically correct conception, is a liquid that has lost its ability to flow"* [1]. In a single sentence, Angell captured many facets and aspects of glasses. Actually, this coarse definition finds its roots in the usual melt-quench way of producing them. Many other approaches have been developed in the last century, few examples being physical or chemical vapor deposition [10–12]. Despite that, Angell grasps a peculiar and fundamental property of glasses: their structure is (almost) equal to the one of the corresponding liquid. The lack of long range order and ergodicity (they indeed cannot "flow" and do not sample the phase space like the liquid, as we will see later in this chapter) poses severe difficulties and limitations in modeling and simulating such systems. This is one of the main reasons why the glass transition is still nowadays somehow obscure and a hot topic of intense research both from a theoretical and experimental point of view.
We will try to understand more aspects of the glass transition starting from the ancient, well established way of production: the melt-quench technique. Consider a *good glass former* melt, that is a substance unlikely to crystallize upon cooling (for example molten oxide-based sand) and cool it down fast enough below the melting temperature: the system will enter the so called super-cooled liquid state, a liquid characterized by an increased (up to 14 orders of magnitude and more) viscosity. If the system is further cooled down and

the crystallization avoided, at a certain point the viscosity becomes so high that the liquid loses its ability to flow in an easily observable time-scale: we say that the system has entered the glassy phase. The transition between the liquid to glassy state takes place in a range of temperatures which are known as the glass transition temperatures, however usually a single temperature, $T_g$, is defined as the one where the shear viscosity, $\eta$, reaches $10^{12}$ Pa $\cdot$ s.
It is important to introduce here that, since real world glasses are intrinsically out of equilibrium (we will introduce later the concept of *ideal glass*), the glass transition temperature together with the other characteristic thermodynamic properties will depend on the thermal history of the glass itself.
In the next sections we will develop in detail all the concepts introduced here, trying to clarify the peculiar aspects of the glass transition.

### 2.1.1 The temperature dependence of viscosity

The aim of this section is to present phenomenologically the role of viscosity and its temperature dependence in undercooled liquids toward the glass transition. To start with, we should become familiar with the concept of frequency-dependent viscosity: a liquid is effectively liquid (in the sense that is able to flow) only on a given timescale. For example, if we consider water at ambient temperature and we perturb it with an external stress with frequency of few THz it will respond like a solid [13].
This *elastic* behavior is in net contrast with the more typical *viscous* one observed in everyday life. We present here an over-simplified model for visco-elastic properties of materials, following the Maxwell approach [14]. A more complete formalism can be built starting from dedicated textbooks of elasticity [15]. Let us consider a solid material subjected to a shear stress. Its stress-strain relation will be given by

$$\sigma(t) = G\epsilon(t) \tag{2.1}$$

where $\sigma(t)$ is the stress, $\epsilon(t)$ is the strain and $G$ is the shear modulus. It is clear that Eq.(2.1) is the equation governing the motion of a simple spring, with $G$ the elastic constant. We can now consider an energy dissipation mechanism. In the Maxwell model, it takes the form of a viscous liquid damper, with a strain rate proportional to the stress

$$\dot{\epsilon}(t) = \frac{\sigma(t)}{\eta} \tag{2.2}$$

where $\eta$ is the shear viscosity of the liquid. We can now combine Eq.(2.1) and Eq.(2.2) together to describe a visco-elastic medium

$$\dot{\epsilon}(t) = \frac{\dot{\sigma}(t)}{G_\infty} + \frac{\sigma(t)}{\eta} \tag{2.3}$$

with $G_\infty$ the infinite frequency shear modulus[1]. In Fourier space, Eq.(2.3) reads

[1]It is useful to define $G_\infty = \lim_{\omega\to\infty} G(\omega)$, with $\omega$ the frequency of the excitation. The choice here is justified since a liquid behaves like a solid in the limit of high frequencies.

$$\tilde{\sigma}(\omega) = \tilde{\eta}(\omega) i\omega \tilde{\epsilon}(\omega) = \frac{G_\infty}{i\omega + G_\infty/\eta} i\omega \tilde{\epsilon}(\omega) \tag{2.4}$$

The complex viscosity defined in Eq.(2.4) shows two limiting behaviors as a function of the frequency. For $\omega \ll G_\infty/\eta$ we are in the *viscous* regime, with the dynamics governed by Eq.(2.2), while for $\omega \gg G_\infty/\eta$ the material behaves like an *elastic* medium and Eq.(2.4) corresponds to Eq.(2.1). The crossover between the two regimes is given by the Maxwell frequency $\omega_M = G_\infty/\eta$. To grasp better the meaning of this frequency, the dynamical equation can be solved in the homogeneous case ($\dot{\epsilon}(t) = 0$) with the boundary condition $\sigma(0) = \sigma_0$. The solution is given by

$$\sigma(t) = \sigma_0 \exp[-\omega_M t] = \sigma_0 \exp[-t/\tau_M] \tag{2.5}$$

with the Maxwell relaxation time defined as $\tau_M = 1/\omega_M$. This relaxation time is the time needed for the system to respond to (or relax) an external perturbation (or spontaneous fluctuation), and indeed is the one which is probed with the techniques discussed in the next chapters. This relaxation time ranges from few picoseconds for liquid systems (like water at ambient temperature [13]) to hundred of seconds at the glass transition temperature $T_g$ and up to geological time-scales (for example for the windows of our houses).
It has to be noted that since $G_\infty$ is weakly temperature dependent, the relaxation time temperature dependence is very similar to the viscosity one [16]. A consequence of this property is that the empirical equations developed to describe the viscosity as a function of temperature work extremely well for the relaxation time too. Moreover, since typically $G_\infty \approx 10^9$ Pa, another definition of the glass transition temperature naturally arises: it can be defined as the temperature where the system needs $\sim 10^2$ seconds to relax towards the equilibrium. Before proceeding, we highlight that the relaxation mechanisms in glasses are in fact more complex [17–19]. A secondary process decouples from the main, structural relaxation one, at a temperature $\approx 1.2\ T_g$. The structural relaxation, also known as $\alpha-$relaxation, is the slowest process, characterized by the Maxwell relaxation time and related to the results reported hereafter. The faster process that becomes effective at low-enough temperature, known as the $\beta$-relaxation, corresponds to the rattling of a particle in the transient cage of neighbor particles. Despite being not crucial for the discussion reported in this thesis, we will briefly discuss this decoupling of relaxation processes in chapter 4.
Historically, glasses can be classified according to the temperature dependence of the viscosity. To appreciate the properties for systems with very different glass transition temperatures (for example oxide and organic glasses), the viscosity (or its logarithm) is usually reported as a function of the normalized inverse temperature $T_g/T$, in a so called *Angell-plot*. An example of this plot with few representative glass forming systems is reported in Fig.(2.1). Depending on the behavior of viscosity in the *Angell-plot*, two limiting families can be defined: "strong" and "fragile" glasses. The first one is represented by those systems

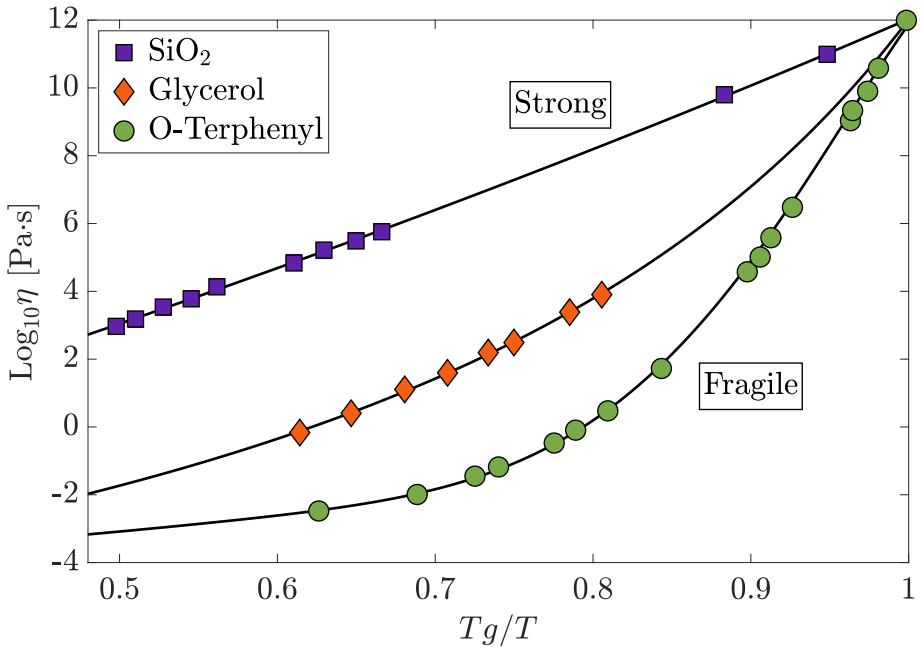


Figure 2.1: Logarithm of the viscosity as a function of the inverse temperature normalized for $T_g$. Here three typical glass formers have been reported: the strong $SiO_2$ with a kinetic fragility $m = 20$, the fragile o-terphenyl ($m = 80$) and the intermediate glycerol ($m = 50$). The black solid lines are fits to the viscosity data with an Arrhenius and a VFT equation for silica and for the two organic glasses, respectively. *Data taken from [1].*

which display an Arrhenius-like behavior [1, 20]

$$\eta = \eta_0 \exp\left(\frac{E}{k_B T}\right) \tag{2.6}$$

with $\eta_0$ the "infinite" temperature viscosity limit (almost $10^{-5}$Pa $\cdot$ s for any glass forming liquid), $E$ an activation energy and $k_B$ the Boltzmann constant. In Fig.(2.1) the prototypical strong glass former $SiO_2$ displays an Arrhenius temperature dependence, and its behavior is clearly represented by a straight line. Fragile glasses behave in a different way (see for example green circles in Fig.(2.1)), having a faster than exponential divergence of the viscosity in the proximity of $T_g$ [21–23]

$$\eta = \eta_0 \exp\left(\frac{B}{T - T_0}\right) \tag{2.7}$$

where $B$ and $T_0$ are phenomenological parameters. This equation, known as Vogel-Fulcher-Tammann (VFT) from the names of the 3 scientists who independently reported it (more details about the history of the equation can be found in [24]), reduces to Eq.(2.6) when $T_0 = 0$. From Fig.(2.1) one can observe that the classification *strong* and *fragile* glasses does not need the introduction of Eq.(2.6, 2.7). The differences can be captured by the viscosity

change rate close to $T_g$ and are classified by the so called kinetic fragility $m$[1, 20]

$$m = \lim_{T \to T_g} \frac{\partial \log_{10} \eta}{\partial \frac{T_g}{T}} \tag{2.8}$$

The fragility ranges from values of $m \sim 17$ for strong glass formers to $m \sim 150$ for very fragile ones.

### 2.1.2 The glass transition: thermodynamics

If in the previous sections we have introduced the glass transition from a phenomenological point of view, we review here the thermodynamic aspects of this intriguing *falling out of equilibrium* process.

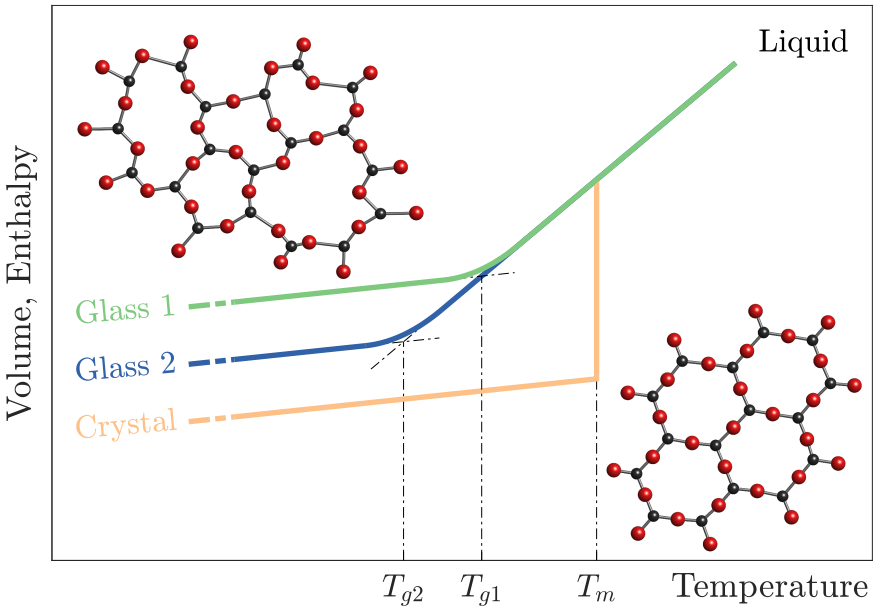


Figure 2.2: Volume (and enthalpy) as a function of temperature, showing the possible routes for a liquid upon cooling. Two glassy states are reported, which differ for the cooling rate from the liquid phase. A 2-dimensional sketch of the structural configuration for $SiO_2$ is reported: on the right side the crystalline state, an ordered-packing of tetrahedrons; in the glassy phase (top left) this configuration is distorted, leading to the loss of long range order.

Experimentally, during the glass transition an abrupt (but *continuous*) change of the thermal expansion coefficient $\alpha_p$[2] and the heat capacity $C_p$[3] is observed

[2]The isobaric thermal expansion coefficient is defined as the derivative of the volume, $V$, at constant pressure with respect to the temperature, $\alpha_p = \frac{1}{V}\left(\frac{\partial V}{\partial T}\right)_p$.

[3]The isobaric heat capacity is defined as the derivative of the enthalpy, $h$, at constant pressure with respect to the temperature, $C_p = \left(\frac{\partial h}{\partial T}\right)_p$.

[19, 25]. In Fig.(2.2) a diagram of the volume (or enthalpy) as a function of temperature is reported. As it can be seen, upon cooling down the liquid, two routes are possible: at the melting temperature $T_m$ the system can crystallize (orange solid line) undergoing a first order phase transition, or it can continue on the equilibrium line in the undercooled liquid. On further cooling, the system reaches the glass transition temperature $T_g$ and, unable to explore the phase space, deviates from the equilibrium configuration. It is important to stress here that this deviation is continuous in the first derivative (the change of slope in Fig.(2.2) is smooth), as just said. Since this change of derivative takes place over a range of temperatures, the glass transition can be located as the virtual intersection of the liquid line with the extrapolation of the glassy one (black dashed lines). Moreover, being the glassy state an out of equilibrium one, different glasses can be prepared following different thermal protocols: the green curve represents a fast-quenched glass (with a higher enthalpy, thus closer to the liquid-like configuration) while the blue curve is representative of a slow-quenched glass (closer to the equilibrium configuration). The glass transition temperature changes according to the thermal history, being lower for slow quenched glasses (this variation is relatively small, roughly 5°C after a change of cooling rate of an order of magnitude [18]).
We want now to discuss what happens microscopically during the glass transition. To start with, we recall the definition of configurational entropy of a system of $N$ particles with volume $V$

$$S_C(N, V, E) = k_B \log \Omega \tag{2.9}$$

with $E$ the energy, $k_B$ the Boltzmann's constant and $\Omega$ the number of states that the system can visit. By construction, $S$ cannot be negative ($\Omega \geq 1$). A perfect crystal at $T = 0\,\mathrm{K}$ has zero entropy by definition, since only one particles' configuration exists which satisfies the symmetry requirements (for a sketch of the long range order, see Fig.(2.2)). The melting of the crystal, being a first order phase transition, is accompanied by a discontinuity in the entropy($\Delta S_m$, sometimes called "melting entropy"). Now let us consider an undercooled liquid: its entropy must decrease upon cooling since, following Eq.(2.9), more and more configurations become prohibited. This behavior can be written in the following form [26]

$$S_C(T) = \Delta S_m - \int_T^{T_m} \Delta C_p(T')\, d\log T' \tag{2.10}$$

with $\Delta C_p(T) = C_p(T)_{liquid} - C_p(T)_{crystal}$ and $T_m$ the melting temperature. In the end, if the glass transition is avoided and the system is kept in equilibrium, a disordered structure with zero configurational entropy is reached: the *ideal glass*. The ideal glass transition would then be a phase transition, accompanied with a discontinuity in the specific heat. This state would be achieved at the so called Kauzmann temperature $T_K$ defined by the following integral equation [1, 19, 26]

$$\Delta S_m = \int_{T_K}^{T_m} \Delta C_p(T')\, d\log T' \tag{2.11}$$

The zero configurational entropy of the ideal glass imposes that it must be a *unique*, perfect ordered amorphous phase. This counter intuitive concept of glass is known as "Kauzmann paradox" [27]. Up to now, nobody has created an ideal glass neither experimentally nor in simulations. The ideal glass is indeed kinetically prohibited, since the freezing of degrees of freedom and the loss of ergodicity drive the system out of equilibrium before reaching $T_K$ [19].
Up to now, we have attacked the glass transition from two different points of view: the kinetic and the thermodynamic one. The first, as we have seen, is related to the slowing down of the dynamics as a consequence of the increased viscosity (equivalently, of the relaxation time). On the other hand, the thermodynamic aspects of the glass transition are governed by the entropy of the system. The connection between these two approaches was established a long time ago by Adam and Gibbs [28]

$$\tau(T), \eta(T) = A \exp(\frac{B}{TS_C}) \tag{2.12}$$

with $A$ and $B$ constants. It is important to notice here that $A$ depends on the chosen observed quantity, i.e. the relaxation time $\tau$ or the viscosity $\eta$.
In this view, the slowing down of the dynamics is then a consequence of the reduction of possible configurations that the undercooled liquid can sample. Moreover, Adam and Gibbs proposed that, upon cooling, the exploration of new configurations involves rearrangements of an increasing number of correlated particles, called Cooperative Rearranging Regions (CRR). A beautiful result of this theory was reported in [26], where it was shown that Eq.(2.11) leads to the empirical Vogel-Fulcher-Tammann (Eq.(2.7)) dependence of the relaxation time for fragile glass formers (for example o-terphenyl or n-propanol). Furthermore, for fragile glasses the connection between the entropy-driven and kinetic-driven glass transition is highlighted even more by some empirical observations. For example, if the Kautzmann temperature $T_K$ is extrapolated from calorimetric measurements and compared with the $T_0$ of the VFT (the temperature at which the relaxation time or viscosity diverges, with a complete freezing of the system), one finds an incredible agreement in the order of 10% [29]. Another peculiar correspondence is found comparing the kinetic fragility, discussed above, and the calorimetric one [30].
All those pieces put together show that the glass transition cannot be simply seen as a pure kinetic transition, but needs more attention from a thermodynamic and statistical point of view. This aspect will be tackled in detail in the next section.

### 2.1.3 The glass transition: energy landscape and aging

In this section we will describe and discuss the potential energy hyper-surface, namely the *potential energy landscape* (PEL) [31] that the system explores

during its route toward the glassy state. Let us start considering a system of $N$ particles (for simplicity assume here indistinguishable structure-less particles), which interact with a many-body potential $\Phi(\vec{r}_1, ..., \vec{r}_N)$. The system is then described by a $3(N-1)$ potential energy hyper-surface [1, 17, 19, 25, 32, 33]. A sketch of a PEL is reported in Fig.(2.3). As it can be seen there, the potential surface is composed of many local minima and maxima, separated by energy barriers of different height [17]. The temperature corresponds to a given energy value (plus fluctuations) and therefore selects a given class of minima. Each minimum is a point of stability of the system (*inherent structure*), and different minima for the same potential energy correspond to different configurations. The system rattles between neighbor basins due to thermal energy. At high temperatures, the system is able to sample the PEL, easily escaping even the deepest basins ("metabasins" or "craters")[17, 29, 33]. The undercooled liquid then explores the surface of the PEL in an ergodic way, moving almost freely around in a timescale small compared to the one of observation. Lowering the temperature, when $k_BT$ becomes comparable to the depth of a metabasin, the dynamics strongly slows down, entering the glassy state and losing ergodicity. If the crystal state is avoided, the system gets trapped in a metabasin, and can only sample nearby basins on a reasonable time-scale. Stillinger proposed that the structural relaxation (also known as $\alpha$-relaxation) is related to this trapping in metabasins, while faster relaxations (for example the $\beta$-relaxation) are related to jumps between shallow basins [17]. Moreover, in this picture, one can discriminate between fragile and strong glasses: the former are characterized by many metabasins, in which the system gets easily stuck during the cooling, while in the latter case just few of them are present [19, 29].
It is important to stress the fact that the ideal glass must be characterized by a singular basin, since its configurational entropy is zero (see Fig.(2.3)).
To go a step further in the understanding of the PEL, we need to know the basins' distribution. The number of minima, $\Omega(N)$, is expected to increase in an exponential fashion with the number of particles $N$ [17, 32, 34, 35]. In the end, the basins can be classified according to their depth (normalized for the total number of particles $N$), $\phi = \Phi/N$, and it is possible to write [17, 19, 25, 32]

$$\frac{d\Omega}{d\phi} \sim \exp(N\sigma(\phi)) \tag{2.13}$$

where the quantity of interest here is the basin enumeration function $\sigma(\phi)$. Taking the logarithm of Eq.(2.13), it is easy to show that $k_B\sigma(\phi)$ corresponds to the density of configurational entropy per particle (Eq.(2.9)). $\sigma(\phi)$ is then a measurement of how many basins of depth $\phi$ are present in the PEL.
The Helmholtz free energy, $A = U - TS$, with $U$ the internal energy of the system, can be written as

$$\frac{A}{N} = \bar{\phi} + E^v - Tk_B\sigma(\bar{\phi}) \tag{2.14}$$

with $\bar{\phi}$ the average energy of the basins populated and $E^v$ the vibrational energy [19, 25, 36–40]. The Helmholtz free energy is of extreme importance

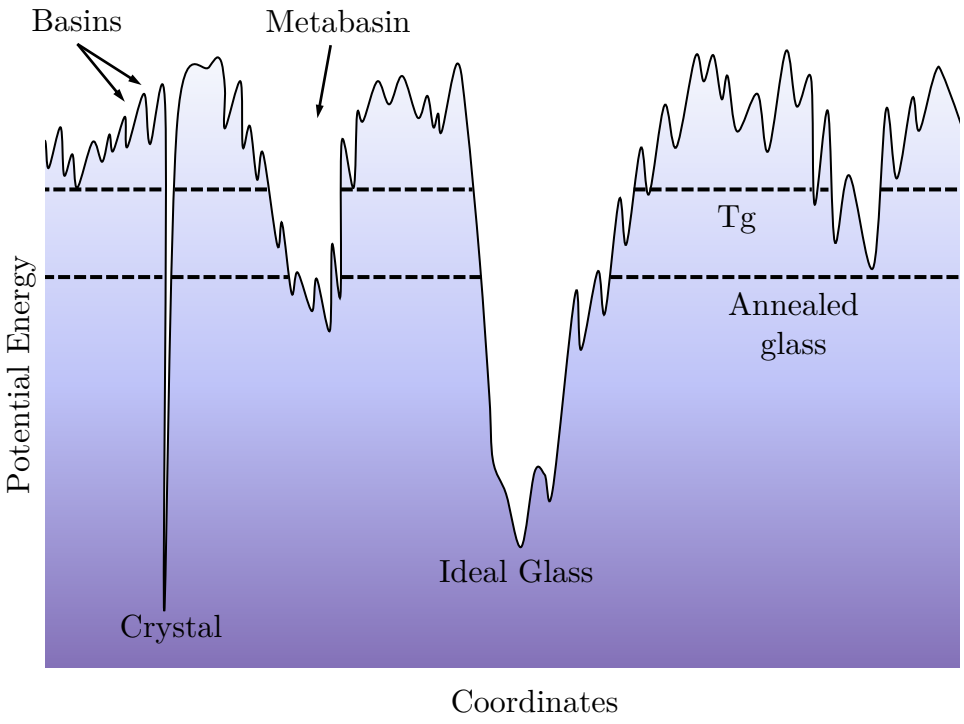


Figure 2.3: Sketch of a one-dimensional potential energy landscape (PEL). On cooling, the system explores different basins, eventually being trapped in one of the deepest close to $T_g$ (metabasins). The annealing procedure (heating the sample close to the glass transition temperature and cooling down slowly) restores partially the ergodicity, letting the system relax to lower local minima: accordingly, the glass transition temperature (and configurational entropy) for the annealed glass is lower than the pristine one.

for describing the transition between the equilibrium undercooled liquid to the out-of equilibrium glassy state.
Indeed, let us consider the system at the starting temperature $T_i$ in the supercooled liquid state. By definition, the system will be at the thermodynamic equilibrium if $\phi = \bar{\phi}$, that is the occupied basin is, within fluctuations, the one corresponding to the expected energy. Now we can couple the equilibrium system to a lower temperature thermal bath at $T_f < T_i$: this procedure is equivalent to abruptly change the temperature of the undercooled liquid. The new value of $\phi$ at equilibrium can be calculated minimizing the free energy, imposing $\partial A/\partial\phi = 0$ [40]. Two distinct contributions to the free energy must be now taken into account: the vibrational and the basin one. After the quench, the system is located in an out of equilibrium basin: the vibrational degrees of freedom, associated with the term $E^v$ in Eq.(2.14), are the first to thermalize (in a time of the order of ps) [40, 41]. At longer times, the system starts to explore new basins, trying to achieve the condition $\phi = \bar{\phi}$. The time needed for reaching equilibrium depends on the final temperature $T_f$ and its dependence is logarithmic in time [41–43]. This potential energy landscape "exploration"

is known as *aging*. Upon undercooling the liquid, one needs to wait for each temperature step $\delta T$ that aging brings the system on the equilibrium curve. However, at some point, the time needed to completely age the system becomes too long (practically infinite), and the system falls out of equilibrium. It is clear, from this thermodynamic consideration, that the glassy state has "memory" of the thermal history, since the final position in the PEL depends on how it is reached. An experimental way to erase this memory (or better, to control it) is the annealing procedure: the glass is heated close to the glass transition, restoring partially the ergodicity, and then cooled down in a slow and controlled way.

## 2.2 Density correlation functions

This section is dedicated to introduce some observables useful to describe both the structural properties of amorphous systems and the relaxation processes from a microscopic point of view. In particular, the attention will be focused on the (space-time) density correlations, quantities which can be studied both experimentally and in simulations.

### 2.2.1 Two-body correlations

Let us consider a system of $N$ particles, with time-dependent position $\mathbf{R}(t) = [\mathbf{r}_1(t), ..., \mathbf{r}_N(t)]$. A configuration of the system will be mathematically described by a sum of Dirac-deltas

$$\rho(\mathbf{r}, t) = \sum_{i=1}^{N} \delta[\mathbf{r} - \mathbf{r}_i(t)] \tag{2.15}$$

The single particle density function can then be defined [44]

$$\rho_N^{(1)}(\mathbf{r}, t) = \Big\langle \sum_{i=1}^{N} \delta[\mathbf{r} - \mathbf{r}_i(t)] \Big\rangle \tag{2.16}$$

with $\langle ... \rangle$ an ensemble average. To simplify the notation, we can for the moment forget the time $t$, that is equivalent to study a completely frozen system (or a snapshot of it). For a uniform system, it is easy to show that the single particle density corresponds to the average number density $\rho$

$$\rho_N^{(1)}(\mathbf{r}) = \Big\langle \sum_{i=1}^{N} \delta[\mathbf{r} - \mathbf{r}_i] \Big\rangle = N/V = \rho \tag{2.17}$$

with $V$ the volume. As it can be seen, the single particle density gives no information about the mutual position of particles in the system. Indeed, Eq.(2.17) returns the same value $\rho$ both for a completely random system and a crystalline one. In order to discriminate between such systems, a two particle

density function must be introduced [44]

$$\rho_N^{(2)}(\mathbf{r}_1, \mathbf{r}_2) = \Big\langle \sum_{i=1}^{N} \sum_{j \neq i}^{N} \delta[\mathbf{r}_1 - \mathbf{r}_i] \delta[\mathbf{r}_2 - \mathbf{r}_j] \Big\rangle \tag{2.18}$$

The two particle density function gives the probability to find simultaneously a particle in $\mathbf{r}_1$ and $\mathbf{r}_2$. It is clear that for a completely random arrangement of particles, the two particle density function can be written as the product of two single particle densities. However, when the structural arrangement deviates from randomness, the pair distribution function $g_N^{(2)}(\mathbf{r}_1, \mathbf{r}_2)$ must be introduced

$$g_N^{(2)}(\mathbf{r}_1, \mathbf{r}_2) = \frac{\rho_N^{(2)}(\mathbf{r}_1, \mathbf{r}_2)}{\rho_N^{(1)}(\mathbf{r}_1)\rho_N^{(1)}(\mathbf{r}_2)} = \frac{\rho_N^{(2)}(\mathbf{r}_1, \mathbf{r}_2)}{\rho^2} \tag{2.19}$$

with the last equality valid for an homogeneous system. In the following, the subscript and superscript will be dropped for convenience, referring simply to $g(\mathbf{r})$ (notice here that without losing generality we can embed the 2-vectors dependence in just one variable $\mathbf{r}$). Moreover, if the system is isotropic, the vector $\mathbf{r}$ becomes a scalar.

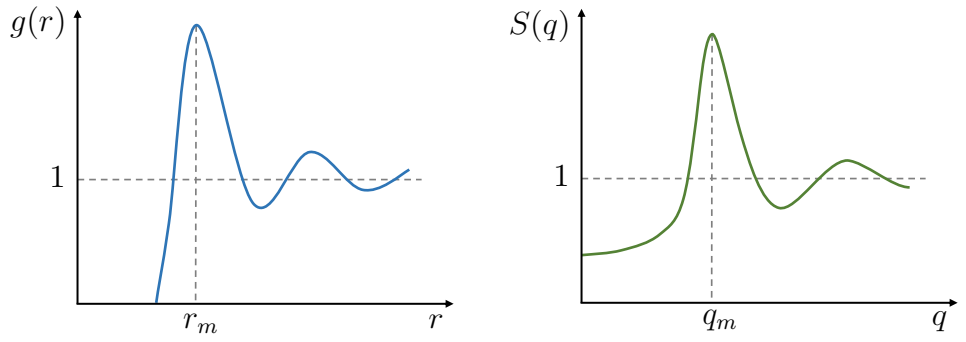


Figure 2.4: Sketch representing the pair distribution function $g(r)$ for an homogeneous isotropic system (*left*) and the relative static structure factor $S(q)$ (*right*). On the horizontal axis the positions of the first peak have been reported. *Figure adapted and redrawn from [45].*

A sketch of a pair distribution function $g(r)$ for an homogeneous isotropic system is shown in Fig.(2.4). Starting from the figure, we can make few observations. First of all, $g(r)$ must tend to 1 for $r \to \infty$, since two particles infinitely far away must be independent. Furthermore, $g(r) = 0$ for $r \to 0$ since two particles cannot stay in the same position. $g(r)$ is then an oscillating function, with peaks located at the most probable distances. The main peak describes the nearest-neighbor shell (or "cage") of particles and is located at $r_m$. The peaks are sharper the more ordered the structure, tending to Dirac-deltas for an infinite perfect (vibration free) crystal.
We are now ready to switch on again the time $t$. The probability of finding a

particle $j$ in a region around a point $\mathbf{r}$ at time $t$ given a particle $i$ at the origin at time $t = 0$ is given by the van Hove function (also known as density–density time-correlation function) [44]

$$\begin{aligned} G(\mathbf{r},t) &= \Big\langle \frac{1}{N}\sum_{i=1}^{N}\sum_{j=1}^{N}\delta[\mathbf{r}-\mathbf{r}_j(t)+\mathbf{r}_i(0)]\Big\rangle \\ &= \frac{1}{N}\Big\langle \int \sum_{i=1}^{N}\sum_{j=1}^{N}\delta[\mathbf{r}'+\mathbf{r}-\mathbf{r}_j(t)]\delta[\mathbf{r}'-\mathbf{r}_i(0)]\mathrm{d}\mathbf{r}'\Big\rangle \\ &= \frac{1}{N}\Big\langle \int \rho(\mathbf{r}'+\mathbf{r},t)\rho(\mathbf{r}',0)\mathrm{d}\mathbf{r}'\Big\rangle = \frac{1}{\rho}\langle\rho(\mathbf{r},t)\rho(\mathbf{0},0)\rangle \end{aligned} \tag{2.20}$$

The van Hove function can be naturally split in two terms, taking a cue from Eq.(2.18). We divide the term with $i = j$, calling it the *self* part, from the one with $i \neq j$, the *distinct* part

$$G(\mathbf{r},t) = G_s(\mathbf{r},t) + G_d(\mathbf{r},t) \tag{2.21}$$

thus defined as

$$G_s(\mathbf{r},t) = \frac{1}{N}\Big\langle \sum_{i=1}^{N}\delta[\mathbf{r}-\mathbf{r}_i(t)+\mathbf{r}_i(0)]\Big\rangle \tag{2.22a}$$

$$G_d(\mathbf{r},t) = \frac{1}{N}\Big\langle \sum_{i=1}^{N}\sum_{j\neq i}^{N}\delta[\mathbf{r}-\mathbf{r}_j(t)+\mathbf{r}_i(0)]\Big\rangle \tag{2.22b}$$

We will appreciate better in the next sections and chapters the convenience of this separation. For now, we can observe that in the limit $t = 0$, $G_s(\mathbf{r},0) = \delta(\mathbf{r})$ and $G_d(\mathbf{r},0) = \rho g^{(2)}(\mathbf{r})$. This last equality can be simply obtained exploiting the properties of the $\delta$-function (as done in Eq.(2.20)) and using the definition of two particle density (Eq.(2.18)). With increasing time $t$, the peaks in the correlation functions broaden: the *self* part becomes a bell-shaped function and the peaks in the *distinct* part blur. In the end, for $t \to \infty$, both functions become $\mathbf{r}$-independent [44]

$$\begin{aligned} G_s(\mathbf{r},t\to\infty) &= \frac{1}{V} \\ G_d(\mathbf{r},t\to\infty) &= \rho \end{aligned} \tag{2.23}$$

While the van Hove correlation function provides a real space direct measurement of the degree of correlation of particles, it is useful to consider the Fourier space counterpart. This equivalent approach is justified since scattering experiments probe the Fourier components of that observable. We can then define the *intermediate scattering function* (ISF) as the correlation of the density Fourier components

$$F(\mathbf{q},t) = \frac{1}{N}\langle \rho_{\mathbf{q}}(t)\rho_{-\mathbf{q}}(0)\rangle \tag{2.24}$$

with $\mathbf{q}$ the wave-number of the density Fourier component. It is straightforward to show that the ISF is the Fourier transform of the van Hove correlation function

$$F(\mathbf{q},t) = \int G(\mathbf{r},t)e^{i\mathbf{q}\cdot\mathbf{r}}d\mathbf{r} \tag{2.25}$$

It is important to stress the fact that the frequency power spectrum of the intermediate scattering function is the *dynamic structure factor* [44]

$$S(\mathbf{q},\omega) = \frac{1}{2\pi}\int F(\mathbf{q},t)e^{i\omega t}d\omega \tag{2.26}$$

The dynamic structure factor can be probed with energy-resolved scattering techniques, such as inelastic neutron scattering, inelastic X-ray scattering and Brillouin spectroscopy. It is easy to show, exploiting the properties of the Fourier transform, that the energy integrated dynamic structure factor is equivalent to the zero-time intermediate scattering function

$$S(\mathbf{q}) = \int S(\mathbf{q},\omega)d\omega = F(\mathbf{q},0) \tag{2.27}$$

$S(\mathbf{q})$ is known as the *static structure factor*, and it is a measurement of the degree of correlation between the density components. In fact, it can be written in terms of the pair correlation function

$$S(\mathbf{q}) = \frac{1}{N}\Big\langle \sum_{i=1}^{N}\sum_{j=1}^{N} e^{i\mathbf{q}\cdot\mathbf{r}_i}e^{-i\mathbf{q}\cdot\mathbf{r}_j}\Big\rangle = 1 + \rho\int (g(\mathbf{r})-1)e^{i\mathbf{q}\cdot\mathbf{r}}d\mathbf{r} \tag{2.28}$$

If the system is isotropic, the integral can be further simplified using the real notation

$$S(q) = 1 + \rho\int dr 4\pi r^2 \frac{\sin qr}{qr}\left[g(r)-1\right] \tag{2.29}$$

An example of a static structure factor is shown in Fig.(2.4), right panel. Like its real counterpart, $g(r)$, $S(q)$ is an oscillating function, with the first peak (located at $q_m$) related to the inverse average distance ($r_m$) of nearest-neighbor particles. It is then clear, from the Fourier relation, that $r_m q_m \approx 2\pi$. Finally, we can remark that for liquids the structure factor is proportional to the isothermal compressibility $\chi_T$ for small $q$-values [44]

$$\lim_{q\to 0} S(q) = \rho k_B T \chi_T \tag{2.30}$$

### 2.2.2 The intermediate scattering function for free diffusing particles

We now show an example of intermediate scattering function for a simple system, i.e. an ensemble of Brownian particles. The diffusion process is described by the second Fick's law [46]

$$D\nabla^2\rho = \frac{\partial\rho}{\partial t} \tag{2.31}$$

where $D$ is the diffusion coefficient. We recall that the Van-Hove correlation function, defined in the previous section, is nothing but the probability of finding a particle at position $\mathbf{r}$ at time $t$ given another one at the origin at $t = 0$. The (self) van Hove function can be considered, for very diluted systems, solution of Eq.(2.31) [47]

$$D\nabla^2 G(\mathbf{r}, t) = \frac{\partial G(\mathbf{r}, t)}{\partial t} \tag{2.32}$$

To solve this partial differential equation, it is useful to move to Fourier space, rewriting it in terms of the intermediate scattering function

$$-Dq^2 F(\mathbf{q}, t) = \frac{\partial F(\mathbf{q}, t)}{\partial t} \tag{2.33}$$

Imposing the boundary condition obtained from Eq.(2.27), we finally get

$$F(\mathbf{q}, t) = S(\mathbf{q}) \cdot e^{-q^2 Dt} = S(\mathbf{q}) \cdot e^{-\frac{t}{\tau}} \tag{2.34}$$

where $\tau = 1/Dq^2$ is the $q$-dependent relaxation time. It is useful to note that the structural ($S(\mathbf{q})$) and dynamical ($e^{-\frac{t}{\tau}}$) properties of the system factorize. This is the reason why, when studying dynamical properties, one usually defines the normalized intermediate scattering function

$$\Psi(\mathbf{q}, t) = \frac{F(\mathbf{q}, t)}{S(\mathbf{q})} \tag{2.35}$$

In the following, we refer to the normalized intermediate scattering function simply as the ISF, reporting it with the nomenclature $F(\mathbf{q}, t)$. This decision is supported by the fact that with the photon correlation technique, extensively exploited in this work, we probe the normalized intermediate scattering function. Nevertheless, it will be clear from the context which function (normalized or not) we will be referring to.
Fig.(2.5) shows a sketch of the (normalized) intermediate scattering function for free diffusing particles at a given exchanged wave-vector $q$. The sketches above the curve represent the particles' configurations at different times (in dashed red line the original, $t = 0$, configuration). For $t \ll \tau$, particles move very little with respect to the lengthscale fixed by 1/q. At $t \sim \tau$, particles have moved on average $\langle \mathrm{d} \rangle \sim 1/\mathrm{q}$.

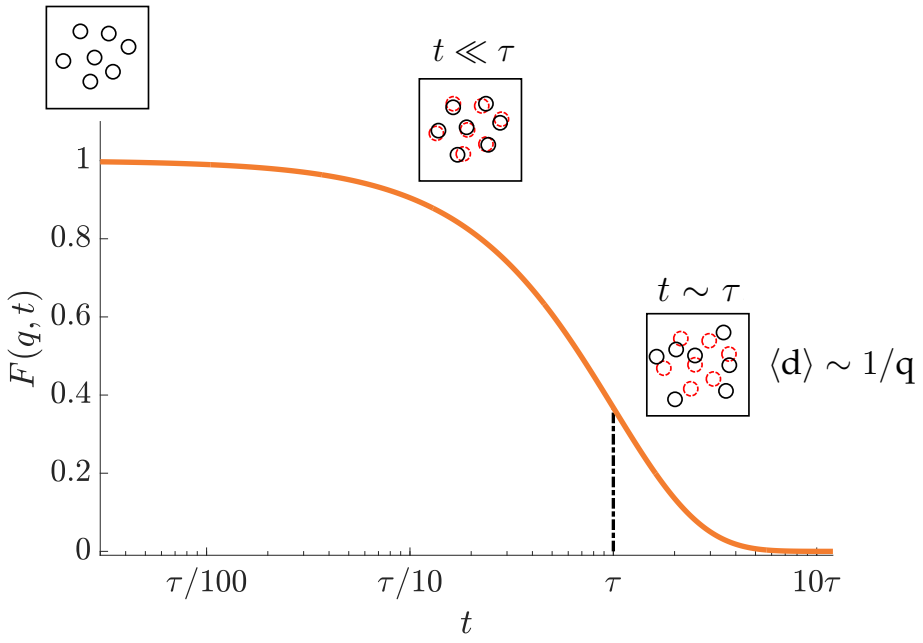


Figure 2.5: Schematic representation of an intermediate scattering function $F(q,t)$ for a given exchanged wave-vector $q$ as a function of time $t$ (here reported in units of the relaxation time $\tau$). The sketches above the curve represent the particles' configurations at different times.

### 2.2.3 Structural relaxation in glasses

We will explain in detail in the next chapter the experimental technique which gives the possibility to investigate the intermediate scattering function, however we introduce here what is observed in systems close to the glass transition. Experimentally, the decorrelation of the density fluctuations is characterized by the superposition of different relaxations [17–19], among which the slowest, the structural relaxation or $\alpha-$relaxation, is the one of interest in this thesis. This latter decay is well represented by the empirical Kohlrausch-Williams-Watts (KWW) function [48]

$$F(\mathbf{q},t) = f_q \exp\left[-\left(\frac{t}{\tau(q)}\right)^{\beta(q)}\right] \tag{2.36}$$

with $\beta(q)$, the so called stretching parameter, $< 1$ in undercooled liquids close to the glass transition.
Two pictures have been proposed in the past to explain this behavior. The first, called the *homogeneous* scenario, involves a real microscopic non-exponential relaxation for all particles. This picture originates from mean field studies on spin glasses, where this peculiar behavior can be attributed to the local disordered structure of the glass [49, 50]. However nowadays the accepted description is the *heterogeneous* one, where the system is seen as composed of

many (from this the term heterogeneous) different simple exponentially relaxing regions, each one with its own relaxation time. This picture is supported both by numerical simulation [51–55] and experimental [56–59] results. It is important to point out here that the complex dynamics of undercooled liquids is likely to be best described as being intermediate between these extreme scenarios, with the relaxation being indeed heterogeneous, with regions faster and slower than the average one [60]. Within this spirit, we can imagine the stretched exponential as a superposition of simple relaxing regions, thus writing

$$F(\mathbf{q},t) \sim \int G(\tau) e^{-\frac{t}{\tau}} d\tau \tag{2.37}$$

with $G(\tau)$ the distribution of relaxation times.
Recalling the concept of *cooperative rearranging regions* (CRR) introduced by Adam and Gibbs [28], we can now link it with the KWW. Upon cooling, the system starts to rearrange in a cooperative way, involving an increasing number of correlated particles. The growth of these regions is accompanied by an increase of heterogeneity, which is indeed reflected in the behavior of the stretching parameter: on lowering the temperature $\beta$ decreases, deviating more and more from the value $\beta = 1$ [61, 62]. A question naturally arises: how can we measure these cooperative rearranging regions?

### 2.2.4 Higher order correlation functions: the four-point susceptibility

The glass transition is challenging not only from a theoretical point of view, but experimentally too. Indeed, the almost indistinguishable structure of the glass with respect to the undercooled liquid makes two-body correlations weakly sensitive to the glass transition. Despite careful study of the van-Hove function (or the ISF), it remains difficult to catch whether the glass transition is accompanied by a growing length scale of correlations. It is then important to find a new observable to overcome this limitation.
The history of many-body correlations starts from the field of spin glasses. In such systems a long-range order is observed at the spin glass transition [63]. However, a simple correlation between two spins $\langle s_i s_j \rangle$ is useless, since the average over space will wash out any contribution. It was then proposed to square the correlation between the spins before averaging over the volume: this corresponds effectively to a four-point correlation function and it was shown that this correlation extends to the entire spin glass below the critical temperature $T_C$ [63, 64].
Starting from this idea, people asked if a 4-point correlator might be introduced for glasses that would capture the statistical space-temporal properties of the CRR. Soon, the heterogeneous, space-time correlation dynamics of CRR approaching the glass transition became known as *dynamical heterogeneities*.
While the observation of these dynamical heterogeneities dates back to the first years of 2000 (see for example [59, 65, 66]), we follow here the formalism developed by Berthier in [67] for of its direct connection to the intermediate

scattering function.
We have seen that in liquids approaching the glass transition the density remains homogeneous while the dynamics becomes heterogeneous; the natural quantity to consider is then the so called mobility field [67]

$$C(\mathbf{r},t) = \sum_{i}^{N} c_i(t)\delta(\mathbf{r}-\mathbf{r}_i) \tag{2.38}$$

Here $c_i(t)$ is the mobility of the particle $i$, namely a function that describes the particle displacement in a time interval given by $t$. The field correlation of two points separated by a distance $r$ (note here the modulus of $\mathbf{r}$, since the system considered is isotropic and homogeneous) can be defined as [67]

$$G_4(r,t) = \langle C(\mathbf{r},t)C(\mathbf{0},t)\rangle - \langle C(\mathbf{r},t)\rangle^2 \tag{2.39}$$

The function $G_4(r,t)$ is known as the *four-point dynamic correlation*, since it measures the degree of correlation in the motion (over a time $t$) of two points separated by a distance $r$. It is worth to highlight that the definition of mobility is kept obscure for a reason: it is not needed to define it specifically, since the four-point dynamic correlation can be build with any observable which probes the dynamics over a time-length scale, independently of the details. In the previous section we have defined the density Fourier components $\rho_{\mathbf{q}}(t)$; we can define a mobility field as $C(t) = \rho_{\mathbf{-q}}(t)\rho_{\mathbf{q}}(0)$, thus probing length-scales $\sim 1/q$. The four-point correlation function can then be rewritten as

$$G_4(r,t) = \langle \rho_{\mathbf{-q}}(\mathbf{0},0)\rho_{\mathbf{q}}(\mathbf{0},t)\rho_{\mathbf{-q}}(\mathbf{r},0)\rho_{\mathbf{q}}(\mathbf{r},t)\rangle - \langle \rho_{\mathbf{-q}}(\mathbf{r},0)\rho_{\mathbf{q}}(\mathbf{r},t)\rangle^2 \tag{2.40}$$

It is crucial to stress the fact that, with the choice of $\rho_{\mathbf{q}}(t)$ as observable, the spatial correlation is embedded both in $r$ and $q$. This will be of extreme importance, as we will see soon, since gives the possibility to probe the length-scale of spatial heterogeneities with scattering techniques. Nevertheless, going further in the development of the theory, we can define a susceptibility integrating over the volume

$$\chi_4(t) = \int_V G_4(r,t)d\mathbf{r} \tag{2.41}$$

The *four-point susceptibility* is by definition a measurement of the "volume" dynamically correlated. Manipulating Eq.(2.39), it is straightforward to show that $\chi_4(t)$ can be obtained as the variance of the total mobility $C(t) = \int C(\mathbf{r},t)d\mathbf{r}$, except for a volume-related factor [64, 67]

$$\chi_4(t) = N\left[\langle C(t)^2\rangle - \langle C(t)\rangle^2\right] \tag{2.42}$$

where we have assumed implicitly that the total mobility is a function normalized to unity [64]. If the chosen mobility field is then properly normalized, the four-point susceptibility is a direct measurements of the number of particles involved in a rearrangement (on average). An example of $\chi_4(t)$ for an undercooled liquid approaching the glass transition is shown in Fig.(2.6).

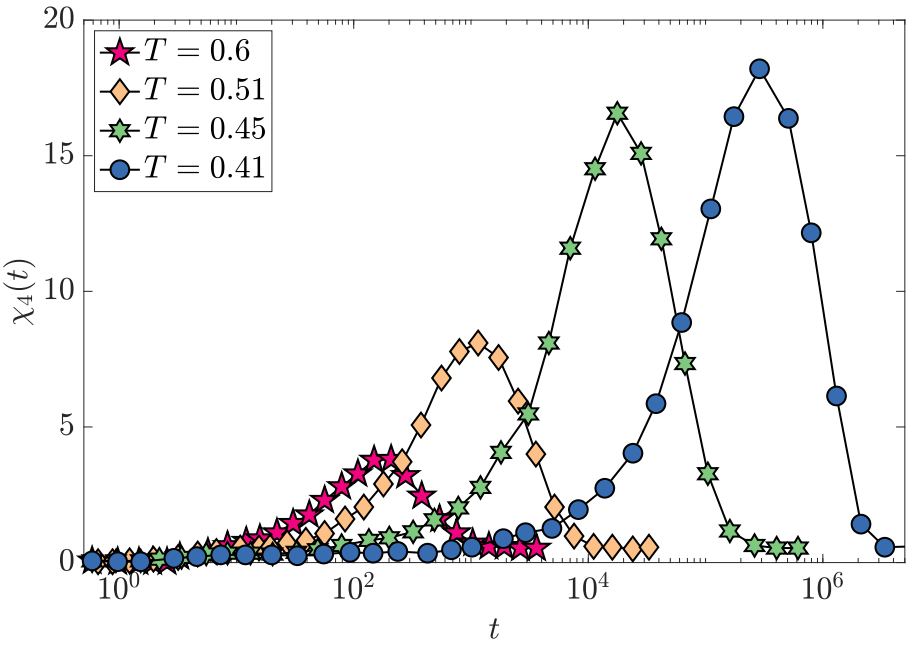


Figure 2.6: Example of four-point susceptibility $\chi_4(t)$ as a function of time obtained with molecular dynamics simulations for an undercooled Lennard-Jones liquid. *Data taken from [67].*

The bell-like shape of the $\chi_4(t)$ is readily explained if we think of its physical meaning. The dynamical susceptibility is a measurement of the degree of correlation of the motion as a function of time. At short times, we expect a vanishing value for the correlation, since particles are moving almost independently, rattling in the transient cage of neighbors particles. On the other hand, in the limit of long times, the trajectories of particles become completely uncorrelated for the many collisions they experience. The peak is found around a timescale typical of the structural relaxation time [64, 67] supporting, as already pointed out, that the $\alpha-$relaxation involves the cooperative motion of CRR. Furthermore, its maximum value is the average number of particles which participate in a rearrangement. This behavior can be well appreciated in Fig.(2.6): on lowering the temperature, the peak shifts towards longer times (symptom of the slowing down of the dynamics) and its value increases up to roughly 20 correlated particles in the average structural rearrangement.
It is important to stress a point in the theory developed up to now: the $\chi_4(t)$ gives the number of particles dynamically correlated, but we cannot directly link this to a correlated volume. This indeed requires the knowledge of the spatial dimension $d$ of the dynamical heterogeneities, from which $\max[\chi_4(t)] \sim \xi^d$ with $\xi$ the CRRs' length-scale. It was shown both in simulations and experiments that $d$ can be fractal too [52, 58, 59, 68], depending on the interaction potential [58] and becoming more compact on cooling [68]. Since in this thesis we are not employing direct space measurements (as the one reported in [59])

nor simulations, we will focus here on the number of particles dynamically correlated. However, sometimes we will try to estimate a correlated volume assuming for simplicity $d = 3$. This rough approximation cannot be considered as quantitative, but gives the possibility to grasp the length-scale we are talking about.

### 2.2.5 Experimental results on the $\chi_4$

In this last section of the chapter we want to spend a few words discussing the experimental challenges regarding measurements of the four-point susceptibility and recent advancements. In simulations one has direct access to all the ingredients required to compute the correlation functions (the mobility introduced in the previous section). However, experiments are usually performed in real-space (for example microscopy) or in Fourier-space (scattering).
In the former ones, the particle trajectories and the heterogeneous domains evolution are directly tracked. Colloidal systems are the main characters of these imaging techniques, since their relevant length-scale (µm) matches the space-resolution achievable with standard visible-light microscopes. For this reason, many experiments have been performed on colloidal glasses, exploring the influence and peculiarities of different interaction potentials [58, 59]. The results are in agreement with simulations and corroborate the idea that the glass transition is accompanied with a cooperative dynamics involving a number of particles in the order of $10^2$ [59, 67, 69]. Recently, electron correlation microscopy was successfully applied to the study of an undercooled liquid metal [70], demonstrating that the size of the dynamical heterogeneities approaching the glass transition temperature grows up to few nanometers, a result in agreement with previous studies based on different experimental techniques [56, 71].
As aforementioned the mobility field can be linked to any observable properly normalized: for our purposes is then convenient to consider the intermediate scattering function, $F(\mathbf{q}, t)$ and investigate the dynamics in Fourier space. The time-correlations will be probed on a length-scale dictated by the exchanged wave-vector with the relation $1/q$. We recall here that the visibility of the fluctuations due to the heterogeneous dynamics is proportional to the inverse number of particles, following the central limit theorem. It is clear that the intermediate scattering function, in order to carry information on the four point susceptibility, has to be probed on a "small" *scattering* volume, *i.e.* containing few dynamical heterogeneities. For structural glasses, this corresponds to consider nanometric-size volumes and only recent advancements in synchrotrons and free-electron lasers are enabling nano-focus beams, with important advancements in the field expected in the next years.
Finally we should highlight that the relevance of the four-point susceptibility is not restricted to the study of liquids approaching the glassy state. In fact, it is a powerful tool to investigate out-of equilibrium systems too, for example aging colloidal suspensions [72], foams [73] and gels [74, 75]. In the fifth chapter of

this thesis we will exploit the formalism of the $\chi_4(t)$ in order to investigate in details the stress-release mechanism in a colloidal glass, which determines long range cooperative structural rearrangements involving many thousands of particles [76].

# Chapter 3

# Photon correlation spectroscopy

This chapter is dedicated to the introduction of the experimental techniques exploited in this thesis. We will describe the general aspects of coherent scattering together with the theory of photon correlation spectroscopy. We will conclude this chapter discussing X-ray photon correlation spectroscopy (XPCS) and the fundamental elements regarding the experiments performed at synchrotron radiation centers.

## 3.1 Coherent scattering: theory

The scattering theory should be discussed using a quantum field theory approach in order to fully appreciate its different facets [77]. There are indeed scattering phenomena that can only be described using a quantum mechanics framework, as the well known example of Compton scattering which played historically an important role to emphasize the limitations of Classical Physics. For what regards coherent scattering from liquids and glasses at temperatures not too low, which is the main theme of this thesis, the results of the full quantum treatment differ little from those obtained using a classical approach, and is therefore customary in many textbooks to use a classical approach to introduce this topic, see e.g. the reference book by Berne and Pecora [47]. In this chapter, we will follow this approach as well since, despite being an approximation, it captures all the aspects needed for the discussion of the photon correlation spectroscopy experiments discussed in the following.
In a scattering experiment, the sample under investigation is illuminated with an incident beam (it can be any probe, for example neutrons, X-rays or visible light) and the diffused (scattered) radiation is collected at a given angle $\theta$, called scattering angle. In this section, to simplify the description, we decided to consider a monochromatic (visible light) plane-wave as incident radiation. The extension of the theory to other types of radiation is straightforward. Each probe couples to a different property of the sample, for example visible light is scattered by modulations of the refractive index, X-rays by electron density and neutrons by nuclei. However, despite the exact mechanism of scattering, the physical information that can be extracted, as we will see, is very much

the same.

### 3.1.1 Visible light scattering

An example of a scattering experiment is reported in the scheme in Fig.(3.1) *top-right*. In the sketch, all optical elements (slits, lenses, pinholes) used to shape the beam and collect the light have been omitted for the sake of clarity. The incident radiation is characterized by a polarization vector, $\hat{\mathbf{n}}_i$, an angular frequency, $\omega_i$, and a propagation vector $\mathbf{k}_i$ with magnitude $k_i = 2\pi/\lambda$, where $\lambda$ is the wavelength of the incident radiation (inside the sample)

$$\mathbf{E}_i(\mathbf{r}, t) = \hat{\mathbf{n}}_i E_0 e^{i(\mathbf{k}_i \cdot \mathbf{r} - \omega_i t)} \tag{3.1}$$

with $\mathbf{r}$ the position with respect to a given reference system. The field interacts with the sample and a portion of it ($\mathbf{E}_s$) is scattered with a propagation vector $\mathbf{k}_f$, with the direction given by the scattering angle $\theta$, see Fig.(3.1).

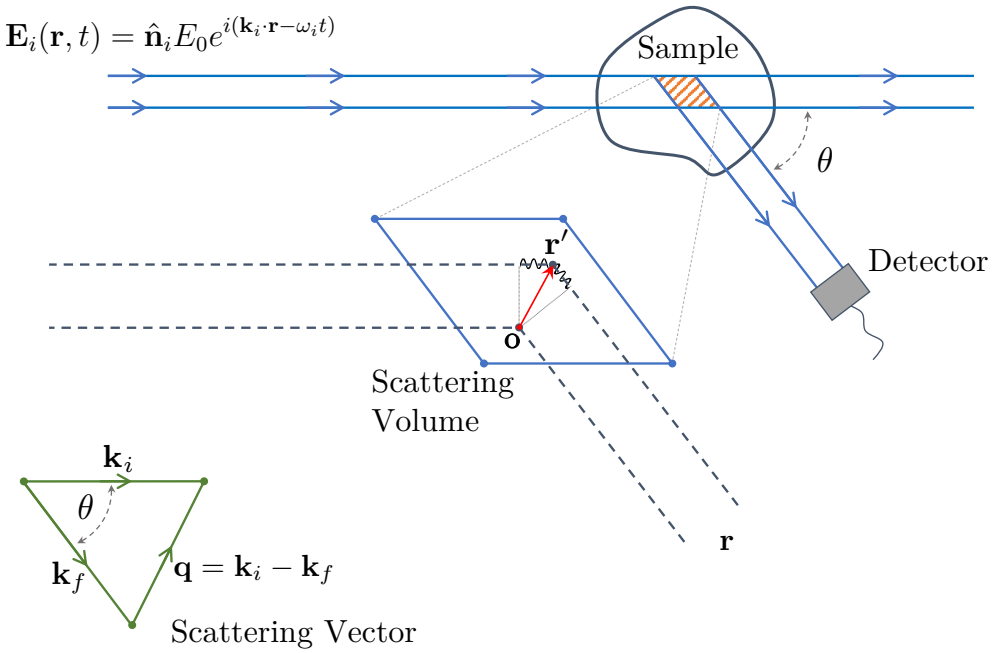


Figure 3.1: Sketch of a scattering experiment (*top-right*). An incident plane wave beam of monochromatic light is shined onto a sample. The scattered light is collected at a given angle $\theta$. The scattering volume (the intersection between the incident beam and the scattered one) is marked in orange. The optical path difference for two scattered spherical waves originating in $\mathbf{o}$ and $\mathbf{r}'$ respectively is reported in the zoom in the *center*. From geometrical considerations (*bottom-left*), the phase factor gain is given by $\exp[i\mathbf{q} \cdot \mathbf{r}']$. *Figure adapted and redrawn from [45].*

We now ask how much of the incident radiation is scattered as a function of the

outgoing propagation vector $\mathbf{k}_f$. To answer this question we start by defining the dielectric tensor [47, 78]

$$\boldsymbol{\epsilon}(\mathbf{r},t) = \epsilon_0\mathbf{1} + \delta\boldsymbol{\epsilon}(\mathbf{r},t) \tag{3.2}$$

where $\epsilon_0\mathbf{1}$ is the dielectric tensor for a linear, homogeneous and isotropic material while $\delta\boldsymbol{\epsilon}(\mathbf{r},t)$ is the local fluctuation. The displacement vector can be written multiplying the total electric field with the dielectric tensor (the $\mathbf{r}$ and t dependence is implied to lighten the notation)

$$\mathbf{D} = (\epsilon_0\mathbf{1} + \delta\boldsymbol{\epsilon})\cdot(\mathbf{E}_i + \mathbf{E}_s) \simeq \epsilon_0(\mathbf{E}_i + \ \mathbf{E}_s) + \delta\boldsymbol{\epsilon}\cdot\mathbf{E}_i \tag{3.3}$$

Here, in the last step, the second order term $\delta\boldsymbol{\epsilon}\cdot\mathbf{E}_s$ has been dropped since negligible with respect to the others. Using Maxwell's equations, we obtain an expression for the scattered displacement vector

$$-\frac{1}{c^2}\frac{\partial^2\mathbf{D}_s}{\partial t^2} = \nabla\times\nabla\times\mathbf{E}_s \tag{3.4}$$

which can be rewritten, together with Eq.(3.3), as

$$\nabla^2\mathbf{D}_s - \left(\frac{\epsilon_0}{c^2}\right)\frac{\partial^2\mathbf{D}_s}{\partial t^2} = -\nabla\times\nabla\times(\delta\boldsymbol{\epsilon}\cdot\mathbf{E}_i) \tag{3.5}$$

While this equation can be readily solved [78], it is simpler to introduce the so called Hertz vector $\boldsymbol{\pi}$ [47]

$$\mathbf{D}_s = \nabla\times\nabla\times\boldsymbol{\pi} \tag{3.6}$$

from which we end up with the wave-equation for the Hertz vector itself

$$\nabla^2\boldsymbol{\pi} - \left(\frac{\epsilon_0}{c^2}\right)\frac{\partial^2\boldsymbol{\pi}}{\partial t^2} = -\delta\boldsymbol{\epsilon}\cdot\mathbf{E}_i \tag{3.7}$$

The exercise of solving this last equation with the retarded Green's function can be found in any textbook of classical fields (see for example [79]). We report here just the final solution

$$\boldsymbol{\pi}(\mathbf{r},t) = \frac{1}{4\pi}\int d^3r'\frac{-\delta\boldsymbol{\epsilon}(\ \mathbf{r}', t-\frac{\sqrt{\epsilon_0}}{c}|\mathbf{r}-\mathbf{r}'|)\cdot\mathbf{E}_i(\mathbf{r}', t-\frac{\sqrt{\epsilon_0}}{c}|\mathbf{r}-\mathbf{r}'|)}{|\mathbf{r}-\mathbf{r}'|} \tag{3.8}$$

from which we readily obtain, substituting the incident plane wave defined in Eq.(3.1)

$$\mathbf{D}_s(\mathbf{r},t) = \nabla\times\nabla\times\left[\frac{E_0}{4\pi}\int d^3r'\frac{\delta\boldsymbol{\epsilon}(\mathbf{r}',t')\cdot\hat{\mathbf{n}}_i}{|\mathbf{r}-\mathbf{r}'|}e^{i(\mathbf{k}_i\cdot\mathbf{r}'-\omega_i t')}\right] \quad \text{with} \quad t' = t-\frac{\sqrt{\epsilon_0}}{c}|\mathbf{r}-\mathbf{r}'| \tag{3.9}$$

In order to conclude this calculation, we need to introduce few approximations. First of all, the detector is far away from the sample (in the so called far field)

and we can expand the term $|\mathbf{r}-\mathbf{r}'|$ as a function of the outgoing direction. Secondly, the modulation of the dielectric tensor evolves in time much slower than the incident frequency. This is readily satisfied for visible incident radiation. In the end, one gets a scattered field with propagation vector $\mathbf{k}_f$, polarization $\hat{\mathbf{n}}_f$, frequency $\omega_f = \omega_i$ and amplitude [47]

$$E_s(\mathbf{r},t) = \frac{E_0}{4\pi\epsilon_0 r} e^{i(k_f r - \omega_i t)} \int d^3r' e^{i\mathbf{q}\cdot\mathbf{r}'} \hat{\mathbf{n}}_f \cdot [\mathbf{k}_f \times \mathbf{k}_f \times [\delta\boldsymbol{\epsilon}(\mathbf{r}',t)\cdot\hat{\mathbf{n}}_i]] \tag{3.10}$$

with $\mathbf{q} = \mathbf{k}_i - \mathbf{k}_f$ and $|\mathbf{k}_i| = |\mathbf{k}_f| = k$. Here $\mathbf{q}$ is the already introduced scattering wave-vector which, for geometrical considerations, can be calculated starting from the scattering angle $\theta$, see Fig.(3.1)

$$q = \frac{4\pi}{\lambda}\sin\left(\frac{\theta}{2}\right) \tag{3.11}$$

where $\lambda = \lambda_{vacuum}/n$, with $n$ the refractive index of the material.
In order to grasp the physical meaning of Eq.(3.10), the triple vector cross product can be worked out defining $\delta\epsilon_{if}(\mathbf{r}',t) = \hat{\mathbf{n}}_f \cdot \delta\boldsymbol{\epsilon}(\mathbf{r}',t)\cdot\hat{\mathbf{n}}_i$. The total scattered amplitude can then be written as the sum of the amplitudes of the fields scattered by the infinitesimal volume elements $d^3r'$ [45]

$$E_s(\mathbf{r},t) = \int_V dE_s(\mathbf{r},\mathbf{r}',t) \tag{3.12}$$

with

$$dE_s(\mathbf{r},\mathbf{r}',t) = -\frac{k^2 E_0}{4\pi}\frac{\exp[i(kr-\omega_i t)]}{r}\left[\frac{\delta\epsilon_{if}(\mathbf{r}',t)}{\epsilon_0}\right] d^3r' \exp(i\mathbf{q}\cdot\mathbf{r}') \tag{3.13}$$

We can now discuss in detail the different contributions present in Eq.(3.13). First of all, the term $k^2$ is reminiscent of an emitting dipole. Indeed, the incident electric field induces in the volume element $d^3r'$ an oscillating dipole with frequency $\omega_i$, which radiates a spherical wave (second term in Eq.(3.13)). The coupling between the incident field and the sample is given by the third term, $\left[\frac{\delta\epsilon_{if}(\mathbf{r}',t)}{\epsilon_0}\right]$. It is clear that for a completely optically homogeneous sample (no modulation in the dielectric constant or equivalently in the refractive index) the radiation cannot be scattered. Finally, the last phase term arises from the spatial position of the volume element $d^3r'$: the light scattered at $\mathbf{r}'$ needs indeed to travel an overall extra distance given by $\mathbf{r}'\cdot(\mathbf{k}_i - \mathbf{k}_f)/k$, see Fig.(3.1) for more details.

### 3.1.2 Generalizing the scattering theory

With the considerations above, we are now ready to generalize the scattering theory to an ensemble of discrete scatterers. First, let us define the *density of scattering material* [45]

$$\Delta\check{\rho}(\mathbf{r},t) = \frac{k^2}{4\pi}\left[\frac{\delta\epsilon_{if}(\mathbf{r},t)}{\epsilon_0}\right] \tag{3.14}$$

This definition is extremely useful since it not only simplifies the notation, but will be crucial to extend the theory to different probes, as we will see.
We can now consider an group of $N$ particles of volume $V_j$ and centre of mass described by the time-dependent position $\mathbf{R}_j(t)$. The scattered field from this ensemble of particles will be

$$E_s(\mathbf{r},t) = -E_0\frac{e^{i(kr-\omega_i t)}}{r}\sum_{j=1}^{N}\left[\int_{V_j}\Delta\check{\rho}(\mathbf{r}_j,t)e^{i\mathbf{q}\cdot\mathbf{r}_j}d^3r_j\right]e^{i\mathbf{q}\cdot\mathbf{R}_j(t)} \tag{3.15}$$

where we have split the phase term for each particle $j$ calling $\mathbf{r}_j$ the position of the volume element $d^3r_j$ with respect to the center of mass $\mathbf{R}_j$.
As a last step, we can define the so called *scattering length* as [45]

$$b_j(\mathbf{q},t) = \int_{V_j}\Delta\check{\rho}(\mathbf{r}_j,t)e^{i\mathbf{q}\cdot\mathbf{r}_j}d^3r_j \tag{3.16}$$

which is nothing but the Fourier transform of the density of scattering material. It is worth to notice here that the name scattering length derives from the fact that the unit of measurement is [m]. The final result for the scattered field is

$$E_s(\mathbf{r},t) = -E_0\frac{e^{i(kr-\omega_i t)}}{r}\sum_{j=1}^{N}b_j(\mathbf{q},t)e^{i\mathbf{q}\cdot\mathbf{R}_j(t)} \tag{3.17}$$

With Eq.(3.17) we have founded a general theory of coherent scattering: indeed, any structural probe gives rise to one such contribution, the only difference being the scattering length which is specific instead to the probe. For example, in the case of X-rays, scattering is related to the electrons in the sample (Thompson scattering), with each electron contributing with a scattering length $r_e = 2.8\times10^{-5}$Å. For neutrons the scattering length is different for each isotope, and can be found in dedicated tables. We emphasize that the theory discussed above covers a particular channel of the scattering process. In fact, we assumed only single, non-resonant scattering and, although such kinematic approach accounts for all the phenomena discussed in this thesis, there are many situations where a more general theoretical treatment is required. Some examples are the scattering of low energy electrons from surfaces [80], X-ray resonant scattering [81] or neutron magnetic scattering [82].
In real world experiments, however, we are not able to measure the scattered field but the intensity, $I(\mathbf{q},t) = |E(\mathbf{q},t)|^2$. For clarity we keep proceeding from Eq.(3.17) and write the average scattered intensity at a given $\mathbf{q}$ as

$$\langle I_s(\mathbf{q})\rangle = \frac{E_0^2}{r^2}\Big\langle\sum_{j=1}^{N}\sum_{k=1}^{N}b_j(\mathbf{q})b_k^*(\mathbf{q})e^{i\mathbf{q}\cdot(\mathbf{R}_j-\mathbf{R}_k)}\Big\rangle \tag{3.18}$$

with $\langle ... \rangle$ an ensemble average (or time average for ergodic systems). We assume now that all scatterers are equal (this condition can be relaxed, see [83] for binary mixtures)

$$\langle I_s(\mathbf{q}) \rangle = \frac{E_0^2}{r^2} \langle |b(\mathbf{q})|^2 \rangle \sum_{j=1}^{N} \sum_{k=1}^{N} \langle e^{i\mathbf{q}\cdot(\mathbf{R}_j - \mathbf{R}_k)} \rangle \tag{3.19}$$

Recalling the definition of static structure factor, Eq.(2.28), and defining the *form factor* as $P(\mathbf{q}) = \langle |b(\mathbf{q})|^2 \rangle / \langle |b(\mathbf{0})|^2 \rangle$, we get a general equation to describe a scattering experiment

$$\langle I_s(\mathbf{q}) \rangle = \alpha \langle |b(\mathbf{0})|^2 \rangle N P(\mathbf{q}) S(\mathbf{q}) \tag{3.20}$$

### 3.1.3 More on the form factor

We want now to spend few words about the form factor and show few examples which will be important, especially for the study regarding the colloidal systems reported in chapter 5.
By definition, the form factor is the Fourier transform of the *density of scattering material* (squared and normalized to unity). Note here that, for particles dispersed in a solvent, it corresponds to the difference in dielectric constant (for visible light) or electron density (for X-rays) between the solvent and the particles themselves. The form factor as we have seen, is defined by (we have omitted the average brackets)

$$P(\mathbf{q}) = \frac{|b(\mathbf{q})|^2}{|b(\mathbf{0})|^2} \tag{3.21}$$

As a first example, we want to consider the case for a homogeneous sphere with radius $R$. We can write

$$b(q) = \Delta\check{\rho} \int_{V_{sphere}} \exp[i\mathbf{q}\cdot\mathbf{r}] dV = \Delta\check{\rho} \frac{4}{3}\pi \frac{3}{q^3} (\sin(qR) - qR\cos(qR)), \tag{3.22}$$

with the integral easily done switching to spherical coordinates. In the end, the form factor for a sphere can be expressed as

$$P(q) = \left[ \frac{3}{(qR)^3} (\sin(qR) - qR\cos(qR)) \right]^2 \tag{3.23}$$

A plot of Eq.(3.23) is reported in Fig.(3.2 *left*). The minima of the sphere form factor are located at $\tan(qR) = qR$.
As a last example, we want to introduce the atomic form factor for X-rays. This factor is generally evaluated from ab-initio calculations of the electron charge density [84]. In most cases, however, assuming a spherical symmetry is a good starting approximation [84]. In Fig.(3.2 *right*) the scattering lengths, normalized for the classical electron radius $r_e$ and the atomic number $Z$, have

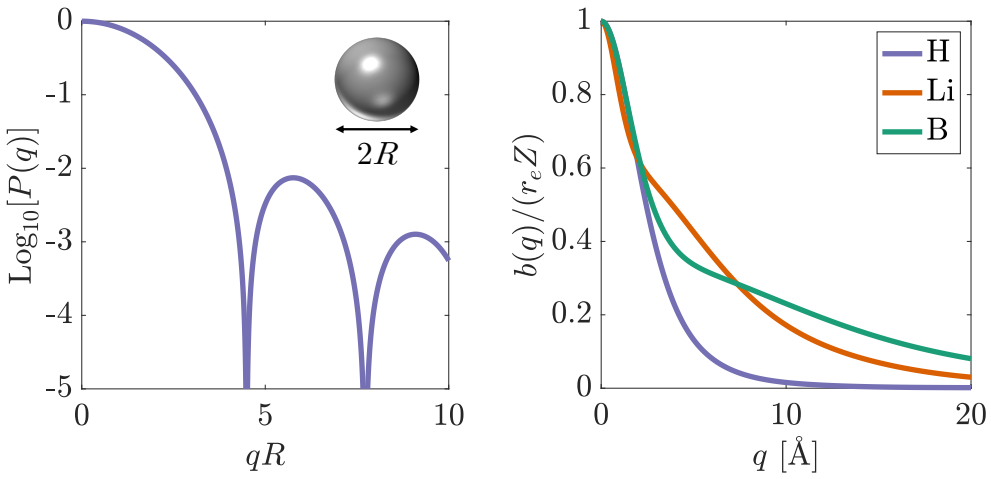


Figure 3.2: The form factor for an homogeneous sphere of radius $R$ is reported in a semi-logarithmic scale (*left*); the positions of the minima are located at $\tan(qR) = qR$, which correspond to $qR \simeq 4.5, 7.7, \ldots$ . On the *right* panel the atomic scattering length (normalized for $r_e$ and $Z$) is reported for hydrogen, lithium and boron.

been reported for 3 nuclei. As it can be clearly seen from the definition, the scattering length for a given atom is proportional to $Z$ for small exchanged momentum, since for X-rays it is the Fourier transform of the atomic electron density. The scattered intensity is then $I \propto Z^2$.

## 3.2 The speckle pattern and its properties

In the previous section we have seen what happens to a monochromatic plane-wave when it is shined onto a material. The scattered field, collected at a given $q$ (or scattering angle $\theta$), is usually averaged over many different configurations with an ensemble average, or a time-average for ergodic systems (see Eq.(3.18-3.20)). This procedure gives a smooth intensity profile, where the instantaneous local position of each scatterer is washed out. However, since the incident field is coherent, at any instant of time $t$ the scattered field at any position $\mathbf{r}$ must contribute coherently. By this consideration, for a disordered system a grainy intensity pattern is thus expected due to the field interference, where the size of each "grain" is determined by geometrical aspects.
Those grainy intensity patterns, first observed with the development of lasers, are called *speckle* patterns and are nothing but the many body equivalent of the Young's double slit experiment; see Fig.(3.3) for an example of a measured speckle pattern.
In the following sections we want to elucidate the speckles statistical properties, which will be crucial in developing the *photon correlation technique*.

### 3.2.1 The speckle statistics

A speckle pattern is generated whenever a coherent beam (we will relax this condition soon) is scattered by a randomly distributed medium. As an example, we consider here a rough surface illuminated by such beam. The term "rough" must be intended on the length-scale dictated by the incident wavelength $\lambda$, implying that the scattered field gains a position dependent random phase factor.
The scattered field at a given position $\mathbf{r}$ will be the sum of all the scattered fields from the surface elements $j$, see Fig.(3.3)

$$E_{tot}(\mathbf{r}) = \sum_{j=1}^{N} E_j(\mathbf{r}) = \sum_{j=1}^{N} |E_j(\mathbf{r})| e^{i\phi_j(\mathbf{r})} \tag{3.24}$$

with the phase $\phi_j(\mathbf{r})$ embedding the $j$-th scattering element position. Assuming that the field amplitude $E_j(\mathbf{r})$ and the phase $\phi_j(\mathbf{r})$ are statistical independent variables with $\phi_j(\mathbf{r})$ uniformly distributed on the space $[-\pi, \pi]$, one can demonstrate that the real and imaginary parts of $E_{tot}(\mathbf{r})$ are zero mean Gaussian variables, with $\sigma^2 = \langle \mathrm{Re}(E(\mathbf{r}))^2 \rangle = \langle \mathrm{Im}(E(\mathbf{r}))^2 \rangle$ [85]. Finally, the probability density of the scattered intensity is given by [85]

$$P(I) = \frac{1}{\langle I \rangle} e^{-\frac{I}{\langle I \rangle}} \quad \text{with} \quad I \geq 0 \tag{3.25}$$

Note here that the $n$-th moment of the distribution can be easily evaluated and is given by the following equation

$$\langle I^n \rangle = n! \langle I \rangle^n \tag{3.26}$$

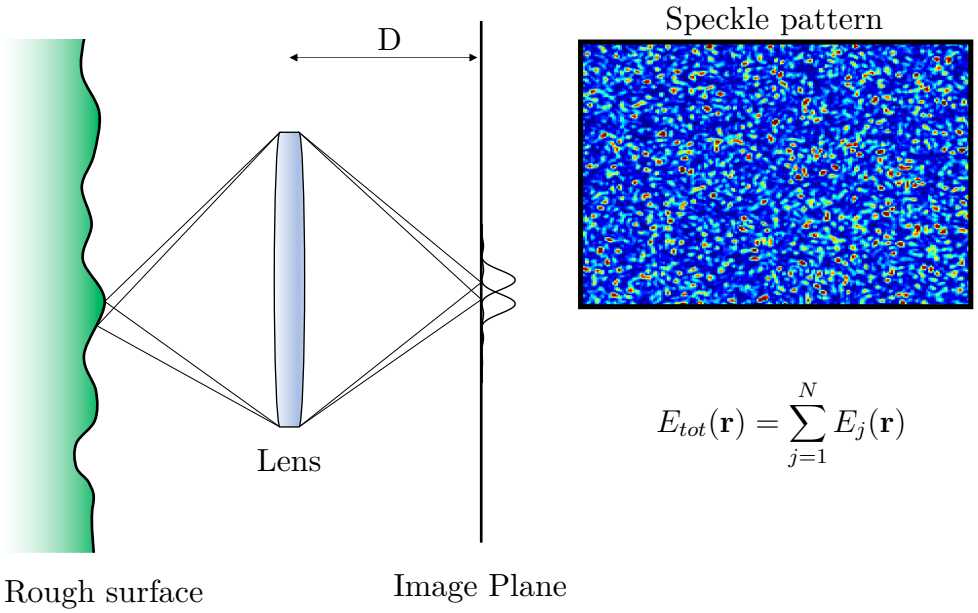


Figure 3.3: Sketch of a rough surface illuminated by a monochromatic light (*left*). The scattered radiation is collected through a lens and imaged on a screen. An example of measured speckle pattern for a colloidal sample is reported (*right*).

It is straightforward to see that the variance of the intensity, defined as $\sigma^2 = \langle I^2 \rangle - \langle I \rangle^2$, is equal to the squared average intensity: $\sigma^2 = \langle I \rangle^2$. The contrast of a speckle pattern is defined as

$$C = \frac{\sigma^2}{\langle I \rangle^2} \tag{3.27}$$

For the case reported above, we have $C = 1$: we say that the speckle pattern is fully developed.
We can now ask ourselves how the speckles are spatially distributed. To answer this question, let's have a look at the sketch reported in Fig.(3.3). Neglecting for the moment the diffraction of the optics, consider two near points on the screen, let us say $X$ and $X + \delta X$, close enough that the phase change of the scattered light is negligible. Given a lens of diameter $d$ and located at a distance $D$ far away from the screen, the condition $I(X) \sim I(X + \delta X)$ is fulfilled if [86]

$$d\frac{\delta X}{D} \ll \lambda \tag{3.28}$$

We can find the linear size of the speckle with Eq.(3.28) considering an optical path difference of $\lambda$. We end up with [86]

$$\Delta \simeq 2\lambda\frac{D}{d} \tag{3.29}$$

The very same considerations can be carried out in the case of a free diffusing speckle pattern, that is without the insertion of optical elements between the source and the screen. In this case [47], the linear size of a speckle is given by

$$\Delta \simeq \frac{\lambda}{\delta\alpha} \tag{3.30}$$

with $\delta\alpha$ the angle of the source subtended at the screen.

### 3.2.2 The dynamics of speckle patterns: intensity auto-correlation

It is clear from the aforementioned considerations that, if the system's density of scattering material changes with time, the speckle pattern will change accordingly. We can then consider again the sketch reported in Fig.(3.1). Assuming the linear size of the detector comparable or smaller than the linear size of a single speckle, let us collect the scattered intensity as a function of time. If the speckle pattern changes slowly with respect to the integration time of the detector, we will measure something like the signal reported in Fig.(3.4 *left*).

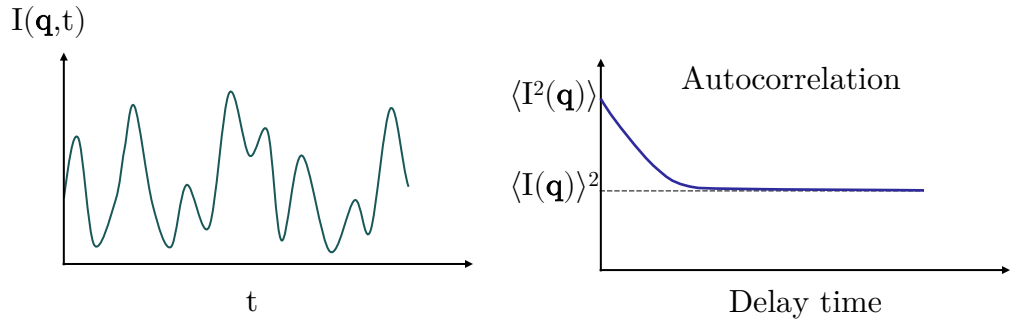


Figure 3.4: A sketch of the measured intensity at a point-like detector for an evolving speckle pattern (*left*). Each oscillation corresponds to a new speckle entering the detector. The typical time between two peaks (or valleys) can be measured and used to compute the intensity autocorrelation (*right*).

Not very much information can be extracted from a plot like the one reported in Fig.(3.4 *left*), but it should be noted that the average time between two peaks (or valleys) in the intensity is related to how fast the speckle pattern changes. It is then natural to measure such *time* computing an auto-correlation (or self-correlation) of the intensity

$$\langle I(0)I(t)\rangle = \lim_{T\to\infty} \frac{1}{T}\int_0^T I(t')I(t+t')dt' \tag{3.31}$$

with $t$ the so called *delay time*. Note here that the dynamics of the speckle pattern are considered stationary, meaning that there is no dependence on the chosen initial time; in other words, $\langle I(t)\rangle = \langle I\rangle \ \forall\ t$. Moreover, it is easy to demonstrate that $\langle I^2\rangle \geq \langle I(0)I(t)\rangle$, and that in the limit of large times $t$ the two series considered in Eq.(3.31) become uncorrelated, $\lim_{t\to\infty}\langle I(0)I(t)\rangle = \langle I\rangle^2$. The autocorrelation function will be a decaying function, starting from $\langle I^2\rangle$ and reaching a plateau equal to $\langle I\rangle^2$, see Fig.(3.4 *right*). It is useful now to normalize such correlator in order to separate the contribution of external parameters, for example the incident beam intensity or the efficiency of the detector. We define then the normalized intensity autocorrelation function [47]

$$g_2(t) = \frac{\langle I(0)I(t)\rangle}{\langle I\rangle^2} \tag{3.32}$$

Note that $g_2$ is a second-order degree of coherence, hence a 4-field correlation function, and it is also known as the homodyne autocorrelation function, since the correlation involves intensities rather than 2-fields as in heterodyne detection. Without entering in the details of this last technique (see [47] for a complete overview), we just report here the definition of first-order degree of coherence

$$g_1(t) = \frac{\langle E(0)E^*(t)\rangle}{\langle I\rangle} = \frac{\langle \Delta\check{\rho}(\mathbf{q},0)\Delta\check{\rho}^*(\mathbf{q},t)\rangle}{\langle \Delta\check{\rho}(\mathbf{q},0)\rangle^2} = F(\mathbf{q},t) \tag{3.33}$$

with the last two equalities following from the expression of the scattered field. We recall here that $F(\mathbf{q},t)$ is the intermediate scattering function, the Fourier transform of the van Hove density-density correlation function.
Eq.(3.32) and Eq.(3.33) can be linked together if the fields are Gaussian random variables (Gaussian approximation) [87]

$$g_2(t) = 1 + A|g_1(t)|^2 \tag{3.34}$$

with $A$ a parameter determined by the experimental conditions. Eq.(3.34) is the well-known Siegert relation, and paved the way of *photon correlation spectroscopy*. The first application of Eq.(3.34) is dated back to the '50s, when Hanbury Brown and Twiss performed the first astronomical homodyne *photon correlation* experiment, measuring the angular size of celestial radio sources. For this historical reason, the Siegert relation is also known as "Hanbury Brown and Twiss" effect.
Coming back to scattering experiments, performing heterodyne detection is challenging in many situations (for such experiments a local oscillator is needed) while the homodyne configuration is much simpler experimentally. In a homodyne photon correlation (also called *dynamic light scattering*) experiment, the scattered intensity is collected at a given $q$-value. The intensity autocorrelation (hardware or software) is then performed, and the intermediate scattering function calculated through the Siegert relation, Eq.(3.34).
It is important to conclude this section highlighting that the contrast $A$ is by definition 1 when the detector is point-like and decreases approximately

as $1/N$, where $N$ is the number of speckles that are collected by the detector [47]. Despite the exact value of the contrast in a real experiment depends on many factors [88], including the beam profile, as a rule of thumb the best configuration is achieved when the speckle size is roughly equal to the size of the detector (or of its pixels in case of a 2D detector).

## 3.3 The multi-speckle technique

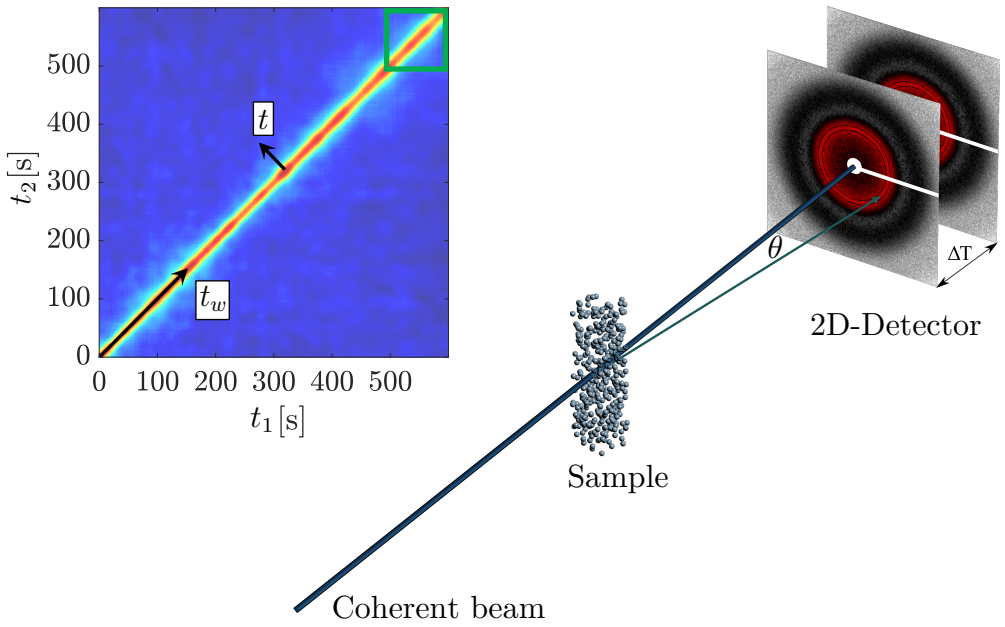


Figure 3.5: Sketch of a photon correlation experiment using a 2D detector (*right*). Here the detector is positioned in the so called small-angle configuration (downstream of the beam). A series of images separated by a time interval are collected for the subsequent software correlation. On the *left* an example of two time correlation function is reported. The green square represents a subset of the matrix from which a partial autocorrelation function can be extracted.

The Siegert relation, presented above, is a powerful method to probe density rearrangements in a system. However, its validity is restricted to the case where the (almost) full speckle pattern distribution is sampled and the dynamics are stationary.
For example, let us consider a dilute colloidal suspension of nanoparticles (100 nm in diameter) dispersed in water at ambient temperature ($\eta \simeq 1\text{mPa} \cdot \text{s}$). Considering a incident laser wavelength of 500 nm and $\theta = \pi/2$, the probed $q$ is roughly $\simeq 23\mu\text{m}^{-1}$. Using the Stokes–Einstein relation, the diffusion coefficient can be written as

$$D = \frac{k_B T}{6\pi\eta R} \tag{3.35}$$

with $k_B$ the Boltzmann constant, T the system's temperature and $R$ the particle radius. Substituting the experimental parameters and recalling that $\tau^{-1} = Dq^2$, we get $\tau \sim 450\,\mu s$. It is clear that in few minutes of experiment, one is able to probe millions of speckles, building up a strong estimate of the speckle pattern statistics and ending up with a reliable intermediate scattering function. However, this approach is not always feasible. In the case of slow relaxing systems (for example a glass close to $T_g$) the time required for obtaining a good enough statistics usually exceeds the available experimental time. Moreover, if the system ages, the temporal average in Eq.(3.31) will lead to a wrong result. To overcome these limitations, since the end of the '90s a new approach was developed involving the use of 2D detectors [89, 90]. The idea was to probe simultaneously many speckles (ideally, one per pixel) and perform both a time and ensemble average on the pixels of the detector. An example of such an experiment is reported as a sketch in Fig.(3.5). The pixels related to the same exchanged wave-vector interval $[q - \Delta q, q + \Delta q]$ are selected (note that in the sketch reported in Fig.(3.5) these pixels belong to rings) and a sequence of $N$ images is collected at even time-intervals $\Delta T$. Choosing two images collected at times $t_1$ and $t_2$ we can calculate the degree of correlation between them

$$C(t_1, t_2) = \frac{\langle I(t_1) I(t_2) \rangle_p}{\langle I(t_1) \rangle_p \langle I(t_2) \rangle_p} \tag{3.36}$$

with the average $\langle ... \rangle_p$ performed over the detector pixels. The procedure can be repeated for all pairs of images, building the so called *autocorrelation matrix* or *two time correlation function*. An example of such matrix is shown in Fig.(3.5 *left*). The main diagonal (in figure reported in red), corresponds to the term $C(j, j)$, thus the correlation of an image with itself. This leads to the correlation maximum decreasing with time $t$ between images. Note that Eq.(3.36) can be rewritten considering the lag time $t$ and defining the waiting time $t_w = t_1$: $C(t_1, t_2) = C(t_w, t_w + t)$ (see Fig.(3.5) for the graphical representation). It is clear from this last definition that the intensity autocorrelation function, defined with Eq.(3.32), can be obtained averaging the two times correlation function over the waiting time

$$g_2(t = k\Delta T) = \langle C(t_w, t_w + t) \rangle = \frac{1}{N - k} \sum_{j=1}^{N-k} C(j, j + k) \tag{3.37}$$

Despite the higher computational effort needed for the multispeckle technique with respect to the single speckle approach, the advantages are not only limited to the possibility to investigate slow relaxing systems. Indeed it is possible to probe the out of equilibrium dynamics on time-scales comparable to the relaxation time $\tau$. If the speckle statistics are good enough (here good depends not only on the number of the sampled speckles but on their signal to noise ratio too) one can obtain a reliable autocorrelation function correlating a series

of images collected over a time $\sim \tau$. This autocorrelation corresponds, for example, to cutting out a square from the two times matrix (the green square in Fig.(3.5)) and calculating a reduced $g_2(t)$. Note that the autocorrelation function obtained is reliable and a good estimate of the underlying relaxation if the evolution of the dynamics (for example, aging) is negligible in the chosen integration window. Considering a set of images starting at $t_w$ and ending at $t_w + \delta t$ this condition can be expressed as

$$\tau(t_w)/\tau(t_w + \delta t) \simeq 1. \tag{3.38}$$

### 3.3.1 The role of dark noise

Up to now, all the theoretical approaches assume a noise-free and homogeneous detection of the scattered signal. In a real experiment, however, these effects must be taken into account in order to extract correctly the dynamical information from the experimental data. First of all, let us assume a uniform illumination of our detector (for example a CCD camera). The measured signal for each pixel $p$ will be superimposed to an intrinsic electrical noise, also known as dark noise

$$S_p(t) = I_p(t) + D_p(t) \tag{3.39}$$

with $D_p(t)$ the dark counts of the $p$th pixel. Note that the dark noise is usually composed of a static baseline (pixel dependent) plus a random (zero mean) instantaneous fluctuation. This can be written as

$$D_p(t) = D_{0p} + \delta D_p(t) \tag{3.40}$$

To lighten the notation, we drop now the subscript $p$. The autocorrelation of the measured signal can be expressed taking into account Eq.(3.39)

$$\langle S(t_1)S(t_2)\rangle = \frac{\langle [I(t_1) + D(t_1)][I(t_2) + D(t_2)]\rangle}{\langle I(t_1) + D(t_1)\rangle\langle I(t_2) + D(t_2)\rangle} \tag{3.41}$$

To proceed in the simplification of Eq.(3.41), we assume that the average scattered intensity remains constant over time, that is $\langle I(t_1)\rangle = \langle I(t_2)\rangle = \langle I\rangle$. It must be pointed out that this assumption is not relevant for the following considerations, which are still valid in the case of fluctuating intensity; however, this choice increases the readability of the equations.
Following Eq.(3.40) the dark noise average is independent of time: $\langle D(t)\rangle = \langle D\rangle$. We assume here that the intensity and noise are mutually uncorrelated too; we can then write

$$\langle S(t_1)S(t_2)\rangle = 1 + \frac{\langle I(t_1)I(t_2)\rangle - \langle I\rangle^2}{\langle I\rangle^2 + \langle D\rangle^2 + 2\langle I\rangle\langle D\rangle} + \frac{\langle D(t_1)D(t_2)\rangle - \langle D\rangle^2}{\langle I\rangle^2 + \langle D\rangle^2 + 2\langle I\rangle\langle D\rangle} \tag{3.42}$$

This equation is extremely interesting for many reasons. First of all, if the noise is removed, we recover the simple form of the two time matrix, starting from

the value $A+1$ for $t_1 = t_2$ and decreasing to 1 when the two considered images are uncorrelated. Switching on a noise source has two consequences. On the one hand it decreases the measured contrast: indeed, the second term in Eq.(3.41) is somehow over-normalized. On the other hand, the noise itself introduces a correlation (third term of Eq.(3.41)), which is a constant term only if the fluctuating part of the noise $\delta D(t)$ in temporally uncorrelated (white noise). This is the most usual case, see for example [91]: the dark noise introduces a baseline which must be taken into account when applying the Siegert relation. One can measure directly $D_0$ (for example acquiring few dark images) and then subtract it from the measured $S(t)$ [92]. With this procedure, the effective noise on the images is just the instantaneous $\delta D(t)$, with $\langle \delta D(t) \rangle = 0$. We get then

$$\langle S(t_1)S(t_2)\rangle = 1 + \frac{\langle I(t_1)I(t_2)\rangle - \langle I\rangle^2}{\langle I\rangle^2} + \frac{\langle \delta D^2\rangle \delta(t_1 - t_2)}{\langle I\rangle^2} \tag{3.43}$$

with the last term being the autocorrelation of the noise. Note that its contribution can never be removed when correlating an image with itself and this is the reason why the zero-delay point of the intensity autocorrelation is never considered in the data analysis. We highlight that despite the equations derived here being obtained for dark noise arising from the detector electronics, the same approach can be followed for any other noise source.
For example, in an X-ray photon correlation experiment the scattered intensity is usually so low that single photons are counted and shot noise becomes relevant. The zero-delay point of the correlation function in this case is totally dominated by the last term in Eq.(3.43) and this is relevant for schemes relying on the single image photon statistics, such the X-ray speckle visibility (XSVS) [93]. Note that for shot noise the time correlation is exactly a Dirac-delta.
Another common source of noise encountered in visible-light based photon correlation spectroscopy is related to stray light coming from the sample, mostly in small angle geometry [91]. Although corrections to the Siegert relation are available [91] and the stray light can be included as for the dark noise, the best way to deal with it is to reduce as much as possible its contribution optimizing the optical elements in the setup (this also reduces the possibility of spurious heterodyne contamination to the measured speckle pattern and the need of further corrections [94]).

### 3.3.2 Non uniform detector illumination

Finally we want to discuss briefly the role of non uniform illumination of the detector. This effect is extremely common, and it is not only due to technical imperfections (collecting optics, dust on the camera chip and so on) but can be intrinsic to the scattered intensity, for example if we are measuring scattered radiation over a range corresponding to the peak of the static structure factor. The measured intensity on the $p$th pixel would then be

$$S_p(t) = I_p(t) \cdot M_p \tag{3.44}$$

with $M_p$ a spatially varying multiplicative factor. We assume that $M$ and $I$ are mutually uncorrelated again. It follows that

$$\langle S(t_1)S(t_2)\rangle = \frac{\langle I(t_1)I(t_2)\rangle}{\langle I(t_1)\rangle\langle I(t_2)\rangle} \cdot \frac{\langle M^2\rangle}{\langle M\rangle^2} \tag{3.45}$$

The contribution of a non uniform illumination is then a multiplicative factor proportional to the variance of the illumination profile. The impact of this effect can be drastically reduced applying the correction scheme as reported in [92]: each image is normalized for the "illumination" profile, measured averaging many uncorrelated images in order to wash out the speckle pattern. However there are situations where the illumination profile cannot be directly measured and each image properly corrected. An example of this case is an experiment with a not stationary intensity profile, as we will see in detail in Ch.(6). For these cases, one can rely on a modified Siegert relation introducing a multiplicative factor $\alpha$ or, more frequently, adding a baseline in order to capture eventual sources of noise too

$$g_2(t) = A'|F(q,t)|^2 + d \tag{3.46}$$

Finally note that the experimental contrast $A'$ obtained with the modified Siegert relation is in principle different from the setup's one.

### 3.3.3 The four-point susceptibility extrapolation

The two time correlation function gives the possibility to investigate the four-point susceptibility too. Indeed, knowing the number of particles $N$ in the scattering volume and the experimental contrast $A$ of Eq.(3.34), it is easy to show that the $\chi_4$ can be calculated recalling Eq.(2.42)

$$\chi_4(t) = \frac{N}{A^2}\left[\langle C(t', t+t')^2\rangle_{t'} - \langle C(t', t+t')\rangle_{t'}^2\right] = \frac{N}{A^2}\sigma_C^2(t) \tag{3.47}$$

Here particular care must be taken in case of non-uniform illumination of the detector. The factor reported in Eq.(3.45) can modify the measured contrast and thus lead to incorrect values of $\chi_4$. For this reason, in this thesis the "illumination profile" normalization is applied whenever we aim at extracting a four-point susceptibility.
We can then extract $\chi_4$ by calculating the variance of the diagonal of the two time correlation function. However, as noticed in [92], one needs to take into account the contribution of the limited number of speckles recorded. In the limiting case where the number of pixels $\to \infty$, the full speckle pattern is sampled and the variance of the diagonals in the two time correlation function is only due to the real dynamics. For a realistic number of pixels, a measurement noise $n(t_1, t_2)$ is introduced

$$C(t_1, t_2) = g_2(t_1, t_2) + n(t_1, t_2) \tag{3.48}$$

with $g_2(t_1, t_2)$ the value of the "instantaneous" real intensity correlation. With the additional noise term, the two time diagonals' variances are related both to the intrinsic heterogeneity of the sample and to the measurement noise. Duri *et al.* demonstrated in [92] that the variance of $C(t_1, t_2)$ can be written as the sum of a noise-related signal and the real dynamical signal

$$\sigma_C^2(t) = \frac{1}{N} \sum_k^3 \alpha_k \langle C(t', t + t') \rangle_{t'}^k + \sigma_{g_2}^2(t) \tag{3.49}$$

where $N$ is the number of sampled speckles (or pixels), $\alpha_k$ is a real coefficient and the third order polynomial term is calculated making use of the standard formula to propagate uncertainties for a function $f(x)$, $\sigma_{f(x)}^2 = J\sigma_x^2 J^T$, with $\sigma_x^2$ and $J$ the covariance and Jacobian matrices, respectively.
Note that, despite the exact functional form ($\alpha_k$) depending on the chosen normalization, the "measurement" noise term is multiplied by $1/N$, a feature coming from the central limit theorem. This ensures the possibility to remove it in a straightforward way as proposed in [92]: Eq.(3.49) is calculated for different values of $N$ and a linear fit is performed in order to extract the intercept $\sigma_{g_2}^2(t)$ for each time $t$. This procedure allows the extrapolation of the true value of the $\chi_4(t)$, and in this thesis such extrapolation has consistently been used to derive four-point susceptibilities.

## 3.4 Towards nanometric spatial resolution: X-ray photon correlation spectroscopy

We described in previous sections the properties of photon correlation spectroscopy (or dynamic light scattering), highlighting its applications to the study of slow relaxing systems such as liquids approaching the glass transition. However, little attention has been given to the role of the exchanged wave vector. We showed that the probed length-scale is somehow linked to the inverse of the scattering vector, which is defined as $q = \frac{4\pi n}{\lambda} \sin(\theta/2)$. Note that there is not theoretic limit to the smallest $q$-vector which can be probed in a scattering experiment (although experimental and geometrical constraints impose practical limits). However, the largest $q$ value accessible is bound by the incident wavelength $\lambda$ (the index of refraction $n$ introduces just a factor close to unity). With visible radiation, for example $\lambda \sim 500\,\text{nm}$, the maximum scattering value is $q \sim 25\mu\text{m}^{-1}$ ($n = 1$), which corresponds to length-scales in the order of few hundreds of nanometers.
It is clear that the only way to probe density rearrangements on smaller length-scales is to use smaller wavelengths, moving to ultraviolet and X-ray radiation.

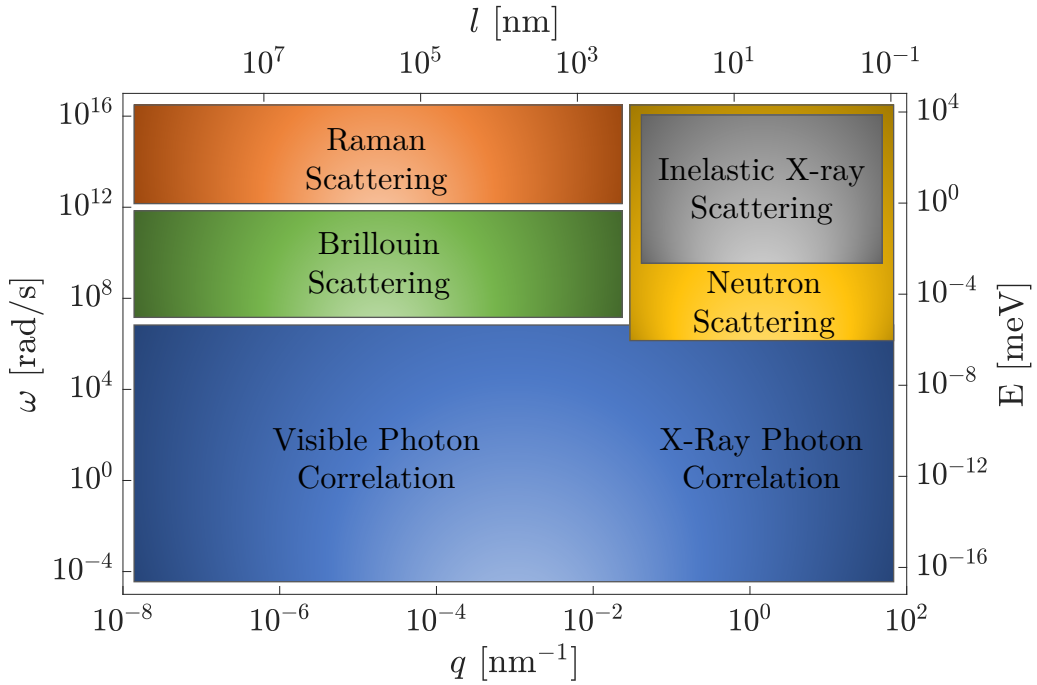


Figure 3.6: Energy-space range covered by different scattering techniques. *Figure adapted and redrawn from [2].*

X-ray photon correlation spectroscopy (XPCS) is overall a recent technique, despite being a natural extension of dynamic light scattering into the X-ray regime [2]. X-rays present many advantages: low interaction cross section (almost no multiple scattering), low refraction at the interfaces ($n \simeq 1$ for any material) and a wavelength comparable with inter-atomic distances are only few of them. In Fig.(3.6) the energy-scattering vector range accessible to different techniques has been highlighted. Note that the whole frequency (or, equivalently, energy) range is covered with visible probes at small exchanged wave-vector: Raman and Brillouin scattering are well established frequency-domain techniques for $\omega > 10^7$ rad/s, while for $\omega < 10^6$ rad/s we find visible photon correlation spectroscopy (PCS). At the nanometer length-scale, many techniques with different probes are nowadays available. Here we reported just few representative examples: at high energy transfer ($\omega > 10^8$ rad/s), both inelastic x-ray and neutron scattering (neutron spin-echo, inelastic and quasi-elastic) give the possibility to investigate the atomic dynamics. In the low frequency regime ($\omega < 10^6$ rad/s) dynamics can be probed with XPCS. Note that PCS and XPCS are represented in the same box: this is due to the fact that XPCS in small scattering angle configuration can cover almost the same range of PCS, but with all the advantages of using X-ray beams. Before proceeding, we should mention that the use of X-rays has sometimes severe drawbacks. When working with soft matter systems or biological samples particular attention must be posed to the radiation damage which can affect both structural and dynamical properties. The beam damage problem often

requires solutions where the sample is replaced frequently using, for example, flow cells and is of concern for new generation X-ray sources. A second drawback regards the relatively low coherent photon fluxes available in the X-ray range with respect to visible PCS. Experiments usually require a long beamtimes at synchrotron radiation centers, and only recently the atomic-scale study of liquids approaching the glass transition has became feasible, as reported in recent literature [95] and in this thesis.
In the next sections we will discuss briefly the requirements for beam coherence in order to perform XPCS measurements and we will show some experimental details regarding this scattering technique.

### 3.4.1 The coherence of chaotic sources

We started this chapter illustrating fundamental aspects of coherent scattering, but we have intentionally avoided talking about the coherence of real radiation sources. A monochromatic plane wave is by definition a coherent wave, but how is coherence exactly defined?
Coherence can be seen as the ability to create interference phenomena, and can be quantified by a field correlation at two positions $\mathbf{r}_1$ and $\mathbf{r}_2$ at times $t_1$ and $t_2$ [96, 97]

$$\Gamma(\mathbf{r}_1, \mathbf{r}_2, t_1, t_2) = \frac{\langle E^*(\mathbf{r}_1, t_1) E(\mathbf{r}_2, t_2) \rangle}{\sqrt{I(\mathbf{r}_1, t_1)} \sqrt{I(\mathbf{r}_2, t_2)}} \tag{3.50}$$

By definition, $|\Gamma(\mathbf{r}_1, \mathbf{r}_2, t_1, t_2)| \leq 1$ for every couple of positions and times. Moreover, if one performs a Young's double slit experiment, the contrast of the interference fringes is given by $|\Gamma|$. We say that the field is fully coherent if $|\Gamma| = 1$, while an incoherent field has $|\Gamma| = 0$. If $0 < |\Gamma| < 1$ the field is defined as partially coherent.
The coherence is then a measurements of how much a field is correlated in space and time. Equivalently, it is the time- and space-length over which one can predict the field phase knowing its value at the origin at time zero.
It is clear from this set of definitions that a laser is a coherent light source. The electromagnetic wave is built up inside the cavity as a standing wave, amplified by the stimulated emission of the active medium. When this monochromatic standing wave exits the cavity, it preserves the coherence: one can find indeed a well defined phase relationship between any two points in the beam path. However, interference patterns can be observed with thermal or chaotic light too (for example, the double slit experiment can be performed with a sodium lamp). In this case, tho source is partially coherent and it is characterized by two transverse and one longitudinal coherence lengths. In order to grasp the meaning of these lengths, two sketches are shown in Fig.(3.7). On the *top*, a source of diameter $w$ emits a monochromatic wave which impinges on a double slit (characterized by an aperture separation distance $d$) located at position $R$. The intensity is then measured on a screen far away from the slit, let say at $L$. Let us consider the wave emitted by an infinitesimal surface element of the

source, located at its center (blue-dashed lines in the sketch). On the screen we will measure an interference pattern with a spatial separation $\lambda L/d$, that is at diffraction angles integer multiples of $\lambda/d$. Consider now a point close to the edge of our source: the interference pattern on the screen will be shifted of a distance $wL/2R$, that is an angular deviation of $w/2R$ (yellow lines). It is clear from geometrical considerations that the two patterns interfere destructively if $d = \lambda R/w$. We define this distance as the transverse coherence [98]

$$\xi_t = \frac{\lambda R}{w} \tag{3.51}$$

For insertion devices at synchrotron radiation centers, such as undulators (see next section for details), the source intensity is usually well approximated by a Gaussian distribution; the transverse coherence is then defined as $\xi_t = \frac{\lambda R}{2\pi\sigma}$, with $\sigma^2$ the distribution's variance. Furthermore, the source size is usually smaller in the vertical direction ($\sigma_v \sim 10 - 50\mu$m) than in the horizontal one ($\sigma_h \sim 100 - 500\mu$m)[1]. This difference, which would cause $\xi_v \gg \xi_h$ at the sample, is compensated by an appropriate use of mirrors and slits (see Sect.(3.6) for details).

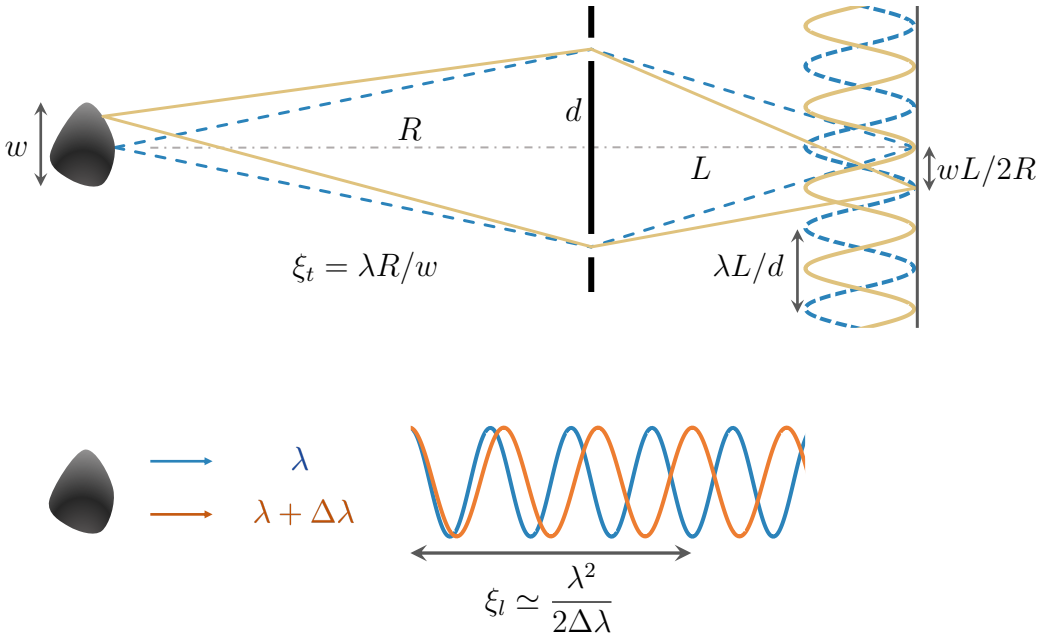


Figure 3.7: *Top*: Sketch of the double-slit diffraction pattern from a finite size source. *Bottom*: Sketch of the propagation of two plane waves of different color. *Figure adapted and redrawn from [98].*

Let us imagine now a source emitting plane waves with two different colors (or wavelengths) as reported in Fig.(3.7 *bottom*). Let us say that the first

[1]Note that for new generation of synchrotron sources, for example ESRF-EBS, the source is fairly symmetrical in the vertical and horizontal directions.

wave has a wavelength of $\lambda$ while the second $\lambda + \Delta\lambda$. Given the two waves in phase at position zero, by definition a length $N\lambda$ exists for which the waves are again in phase. This can be found imposing $N\lambda = (N-1)(\lambda + \Delta\lambda)$ from which we get $N = (\lambda + \Delta\lambda)/\Delta\lambda \simeq \lambda/\Delta\lambda$, with the last equality valid since we assume a small difference in wavelength. Similarly to what already done for the transverse coherence, we define the longitudinal coherence length as the distance over which the two waves become in antiphase, which is $N\lambda/2$ or [98]

$$\xi_l = \frac{\lambda^2}{2\Delta\lambda} \tag{3.52}$$

Note that an additional factor must be introduced depending on the spectrum of the source: for example, a Lorentzian spectrum has a factor $4/\pi$ [96]. For synchroton radiation one usually defines the coherence length as $\xi_l = \lambda^2/\Delta\lambda$ [2]. Typical values in XPCS experiments are in the order of $\sim 1\mu$m for Si(111) reflection monochromators ($\Delta\lambda/\lambda = 1.4 \times 10^{-4}$).
But what does exactly happen if we illuminate a sample volume much larger than the coherence volume? The measured intensity pattern would be the superposition of many (let us say $M$) independent speckle patterns. It can be demonstrated that the intensity distribution follows the function [85, 88]

$$P_I(M) = \left(\frac{M}{\langle I\rangle}\right)^M \frac{\exp[-MI/\langle I\rangle]I^{M-1}}{\Gamma(M)} \tag{3.53}$$

with $\Gamma(M)$ the gamma function. The first and second moments of the distribution are respectively $\langle I\rangle$ and $\sigma^2 = \langle I\rangle^2/M$. The contrast of the speckle pattern is then reduced to $C = 1/M$. A decrease is expected inversely proportional to the number of *modes* M, and in the limit $M \to \infty$ we completely wash out the speckle pattern. While Eq.(3.53) works well in describing speckle patterns for visible light, for X-rays the shot noise term must be included. Eq.(3.53) has then to be convoluted with the Poisson distribution $\langle k\rangle^k \exp[-\langle k\rangle]/k!$ with $k$ being the number of photons per pixel [93, 99]

$$P_I(k, M) = \frac{\Gamma(k+M)}{\Gamma(M)\Gamma(k+1)} \left(1 + \frac{M}{\langle k\rangle}\right)^{-k} \left(1 + \frac{\langle k\rangle}{M}\right)^{-M} \tag{3.54}$$

This represents a negative-binomial distribution function, and its second moment is given by $\sigma^2 = \langle I\rangle^2/M + \langle I\rangle^2/\langle k\rangle$. Note that the Poisson noise, as anticipated, plays a key role in determining the statistics at low count-rates.
In this thesis we will not talk about single image speckle contrast (see [93]), thus the term due to the shot noise can be discarded, as stated before. However, we point out that in a XPCS experiment usually $M \gg 1$ and particular attention must be paid to reduce its value (and thus increase the contrast). We will see in the next sections how this can be done, but before that we want to briefly discuss how partially coherent X-rays are produced at third generation synchrotron radiation centers.

### 3.4.2 Partially coherent X-rays

It is well known that when a charge is accelerated it emits radiation. Synchrotron radiation was first observed as a parasitic consequence of the acceleration of particles for high energy physics experiments. Nowadays, however, large facilities are completely dedicated to the production and use of this kind of radiation.
In synchrotron radiation centers, bunches of electrons are accelerated close to the light speed, $c$, and kept on a circular-like trajectory. When the very energetic electron beam (usually $E \sim$ GeV) is bent within a bending magnets, it emits synchrotron radiation in the range of hard X-rays. The emitted beam is characterized by the so called brilliance, $\mathcal{B}$, which is the number of photons per second emitted in a given solid angle and in a given bandwidth (BW) per source area. For a bending magnets, $\mathcal{B} \sim 10^{12} - 10^{14}$ ph/s/(mrad)$^2$/mm$^2$/0.1%BW.
In 1947 Ginzburg invented a new way to produce synchrotron radiation [100], that is forcing the relativistic electrons in an insertion device on a sinusoidal trajectory with period $\lambda_u$.

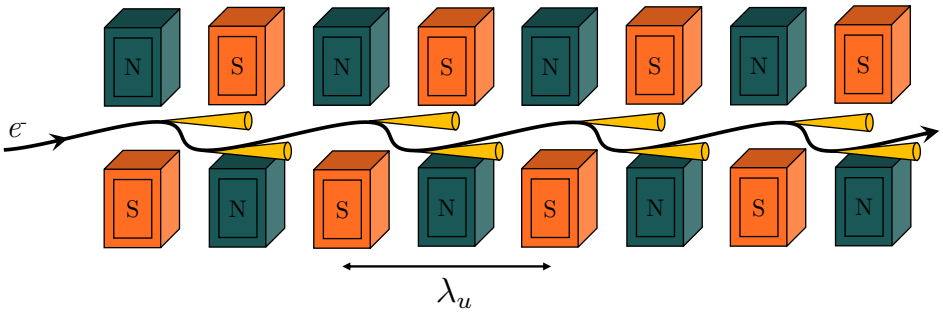


$$K = \frac{eB_0\lambda_u}{2\pi m_e c} \qquad \lambda_l = \frac{\lambda_u}{2\gamma^2}(1 + \frac{K^2}{2})$$

Figure 3.8: Schematic representation of an undulator. The electron trajectory is reported as a dark line, while the emitted light as a yellow cone.

Depending on the amplitude of the oscillation these insertion devices are called wigglers or undulators. In wigglers, the large amplitude of the electron trajectory causes the emission of a very broad spectrum; in undulators, instead, the oscillation of the particles has smaller amplitude, and the electrons oscillate within the cone of the emitted light. In this case the emitted spectrum is dominated by one, extremely bright, peak. A sketch of one of these devices is reported in Fig.(3.8). A sequence of magnets is positioned along the beam-path in order to create a sinusoidal-like magnetic field, $B = B_0 \sin(\lambda_u x)$ orthogonal to the direction of propagation of the beam [101]. In the electrons' reference system, the period of the undulator is reduced due to the relativistic contraction of lengths to $\lambda_u^* = \lambda_u/\gamma$, with $\gamma = 1/\sqrt{1-(v/c)^2}$ the Lorentz factor. They

emit then as a simple oscillating dipole, with a frequency given by $\nu_e = c/\lambda_u^*$. In the laboratory reference system, this emitted radiation is blue shifted due to the relativistic Doppler effect by a factor $\sim 2\gamma$, leading to $\lambda_l \simeq \lambda_u/(2\gamma^2)$. In Fig.(3.8) the exact solution of this electrodynamics problem is shown, where the sinusoidal trajectory of the electron-beam is taken into account. The final result is a slightly larger emitted wavelength (indeed the electrons forward velocity is slower if they are kept on a sinusoidal trajectory) [101]

$$\lambda_l = \frac{\lambda_u}{2\gamma^2}(1 + \frac{K^2}{2}) \tag{3.55}$$

where $K = \frac{eB_0\lambda_u}{2\pi m_e c}$ is the so called undulator strength parameter. When $K \ll 1$, the oscillation is well confined in the emitting cone ($\theta = 1/\gamma$); the emitted radiation consist of almost just one well defined peak at energy $E = \hbar\omega_l$ (the Fourier transform of the entire electron oscillation). If $K > 1$, the oscillation is not anymore contained in the angle $1/\gamma$ and, for symmetry reason, odd harmonics appear in the energy spectrum: $\lambda_h = \lambda_l/m$ with $m = 1, 3, ...$ the harmonics' order [101]. For $K \gg 1$ the oscillation is still more accentuated and the device is called a wiggler, as already introduced above.
It is crucial to stress the fact that the emission of an undulator is not coherent in a laser-like way. Actually, each electron emits coherently but independently of the other electrons in the bunch. Despite the emitted power is comparable to the one of a bending magnet with the same magnetic field [101], the radiation of an undulator is confined in a narrower angle and spectral band. For this reason, the brightness of such insertion device can exceed $\mathcal{B} \sim 10^{21}$ ph/s/(mrad)$^2$/mm$^2$/0.1%BW.

## 3.5 SAXS and WAXS: experimental considerations

Before proceeding, we should spend few words about the two main configurations used in X-ray scattering experiments. We have seen that the exchanged wave-vector determines the probed length-scale: while for hard condensed matter this length-scale is the atomic distance, the story is completely different for colloidal and biological materials. In the latter case, the relevant length-scale is few nanometers up to microns. It is then natural to optimize X-ray scattering experiments in two different configurations: the Wide Angle X-Ray Scattering (WAXS), devoted to the study of atomic length-scales, and the Small Angle X-Ray Scattering (SAXS), employed in the study of the mesoscopic length-scales. Despite technical details which will be touched in this thesis when required, the main difference is the scattering angle: for SAXS, one places the detector downstream of the incident beam, measuring scattering angles up to $\theta \sim 10^{-3}$, while in WAXS one covers a broad angle range that can sometimes reach back scattering ($\theta \sim \pi$). Next we discuss a few experimental parameters which are crucial in coherent SAXS and WAXS experiments. In particular,

since the number of impinging photons on the sample is much less than for typical visible scattering experiments and the elastic scattering cross section is small compared to photoelectric absorption, some attention must be taken to maximize the signal at the detector.

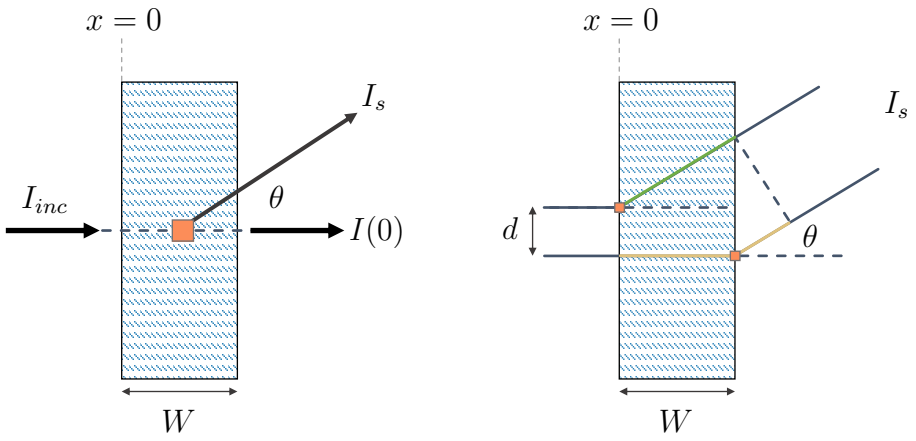


Figure 3.9: *Left*: Example of a sample of thickness $W$. *Right*: Optical path difference in a coherent scattering experiment with a beam of diameter $d$ and sample thickness $W$. The path length difference for the scattered waves from the two orange volumes can be calculated subtracting the green path from the yellow one.

Let us consider a piece of material of density $\rho$, thickness $W$ and linear attenuation coefficient $\mu$ as reported in Fig.(3.9 *left*) with a small scattering volume located at position $x$ (highlighted in orange in figure). The intensity measured at the detector will be dependent on the subtended solid angle, the polarisation, the material electron density, the detector efficiency and other contributions external to the scattering volume: we embed all this information in the term $\Sigma$, a sort of overall cross section (see [45] for the complete expression). The intensity at the detector scattered from the small orange volume element will then be [45]

$$dI_s = I_{inc} e^{-\mu x} \Sigma e^{-\mu \frac{W-x}{\cos(\theta)}} dx \tag{3.56}$$

where $I_{inc} e^{-\mu x}$ is the beam intensity reaching the volume element at $x$ and $e^{-\mu \frac{W-x}{\cos(\theta)}}$ is the further attenuation of the scattered radiation due to sample absorption. The integration over a length $W$ leads to

$$I_s = \Sigma I_{inc} \cos(\theta) \frac{e^{-\mu \frac{W}{\cos(\theta)}} - e^{-\mu W}}{\mu(\cos(\theta) - 1)} \tag{3.57}$$

The optimal thickness can be found maximizing Eq.(3.57)

$$W_{opt} = \cos(\theta)\frac{\ln[\cos(\theta)]}{\mu(\cos(\theta)-1)} \tag{3.58}$$

Furthermore, for small angles, we can expand the logarithm and obtain

$$W_{opt} \simeq \frac{\cos(\theta)}{\mu} \tag{3.59}$$

For small angle scattering $\cos(\theta)$=1 and thus the sample thickness should be chosen to match the absorption length. However, as we will see soon, this is not the most stringent condition to be considered in an XPCS experiment. In these experiments, it is usually preferable to increase the speckle contrast rather than to maximize the scattered intensity.
Consider now a partially coherent synchrotron beam of diameter $d$. The beam is designed to be coherent in the transverse direction, that is $d \leq \xi_t$ for both vertical and horizontal directions. However, the longitudinal coherence length $\xi_l$ is on the order of microns for standard monochromatic beams. In order to keep a high contrast, the waves scattered from the sample must lie in the same coherence volume. Let us then consider the scattered radiation from two points of the sample, as reported in Fig.(3.9 *right*). The difference in path length ($PLD$) can be calculated considering the two scattering paths reported in figure as green and yellow lines. It is easy to show from simple geometrical considerations that [2]

$$PLD \simeq 2W\sin^2(\theta/2) + d\sin(\theta) \tag{3.60}$$

To preserve the coherence between scattered waves inside the whole scattering volume, the condition $PLD \leq \xi_l$ must be satisfied. It is clear that for small angle scattering ($\theta \sim 10^{-3}$) this constraint is strongly relaxed and mm-thick samples can be used (then one can use Eq.(3.58) to maximize the scattered signal).
The situation for WAXS experiments is quite different since the thickness required to optimize the contrast is usually much less than the absorption length. A compromise sample thickness must then be chosen, in order to get a reliable signal with a sufficient contrast. For the experiments reported here on borate glasses, the thickness was chosen to be $\sim 100\,\mu m$, despite $\mu^{-1} \sim 600\,\mu m$. This guaranteed a contrast of a few percent at scattering angles $\theta \sim 0.35$.

## 3.6 Experimental setups: ID10 at the ESRF and P10 at PETRA III

In this last section we will discuss briefly the experimental setups for XPCS available at synchrotron radiation centers. In particular, the high flux and coherence required for XPCS experiments restricts the possible beamlines to a very few around the world. The experiments reported here have been performed at two different synchrotron radiation centers in Europe: the European

Synchrotron Radiation Facility, ESRF (Grenoble, France) and Petra III at DESY (Hamburg, Germany). The detailed description of these beamlines can be found in the respective websites [102, 103]; here a brief summary is reported to better explain how a XPCS experiment works.

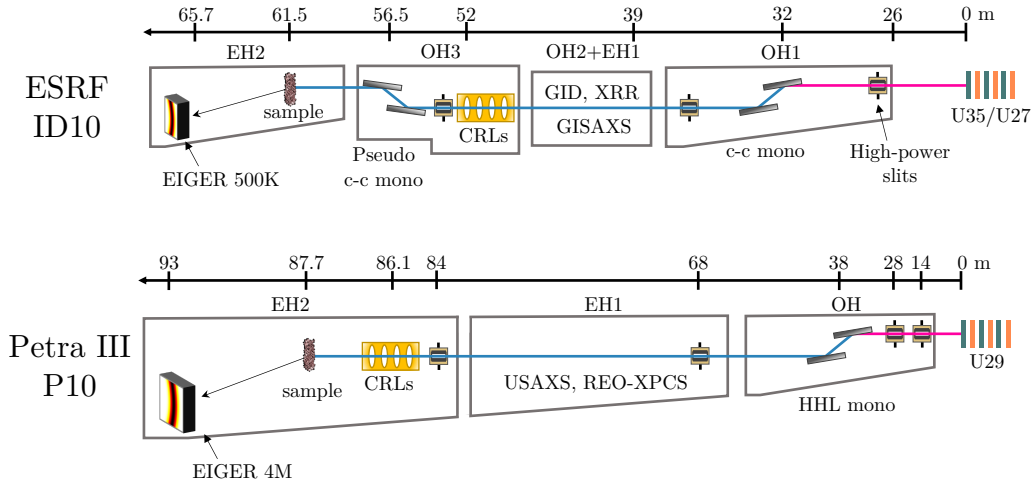


Figure 3.10: *Top*: Sketch of the ID10 beamline at the ESRF (Grenoble, France). A pink beam coming from the undulator is monochromatised and focused on the sample using a combination of slits and mirrors (not shown here). The scattered intensity is collected with a pixelated single photon counter detector. For the sake of clarity, just few beamline elements have been reported here. More details and the complete layout can be found in [102]. *Bottom*: Sketch of the P10 beamline at Petra III at DESY (Hamburg, Germany). The general layout is similar to ID10. Also in this case, only the beamline elements of interest here have been reported. More details and the complete layout can be found in [103].

In Fig.(3.10 *top*) a simplified layout of the ID10 beamline at the ESRF is reported. The "pink" beam from an undulator (U35 or U27) is shaped with high-power slits in order to reduce the angular divergence and then monochromatised with a silicon channel-cut monochromator in the Optics Hutch 1 (OH1). The beam then passes through additional optics (OH2) and enters the first experimental hutch (EH1). EH1 is devoted to grazing incident diffraction (GID), X-ray reflectivity (XRR) and grazing incident small angle x-ray scattering (GISAXS). Downstream of this hutch OH3 is located, where the beam is focused with compound refractive lenses (CRLs) and further monochromatised with a pseudo c-c monochromator (if the experiment requires it). Guard slits are used to select the coherent part of the beam. A beam spot of $8 \times 10\,\mu m^2$ (V×H) is thus obtained in the XPCS hutch, at roughly 60m from the source, with a typical flux of $10^{11}$ photons per second at 8keV. The sample is mounted in a vacuum environment and the scattered intensity is collected through vacuum pipes with a pixelated single photon counter detector (EIGER 500K, Dectris).

The sample-detector distance is chosen in order to match as close as possible the speckle size with the pixel size ($75 \times 75\,\mu m^2$ for the cited detector).
In Fig.(3.10 *bottom*) the layout of the P10 beamline at Petra III is shown. The overall setup is very similar to the one found at ID10: the pink beam is monochromatised with a high-heat load monochromator and then focused with CRLs placed close to the sample. At this beamline, the beam focus at the sample is usually in the range of $3 \times 3\,\mu m^2$ (V×H) with a flux close to $10^{11}$ photons per second at 8keV. The beamline is designed to perform rheology combined with XPCS (REO-XPCS) in the first experimental hutch, as well as ultra small angle scattering (USAXS), with the sample located in EH1 and the detector at the end of EH2 (see the figure for some details).

# Chapter 4

# The equilibrium dynamics in undercooled liquids

## 4.1 $LiBO_2$ undercooled liquid

This chapter describes the experiments exploring the undercooled liquid state of lithium metaborate. We will start by presenting the sample preparation procedure; the physical properties of the borate family will be discussed in detail in the next chapter. We will continue here describing some experiments performed on $LiBO_2$ and the relative results: firstly XPCS measurements in the undercooled liquid state, carried out at the beamline P10 of the Petra III (DESY) synchrotron radiation center. The experiment clarifies the peculiar $q$-dependence of the relaxation time, showing similarities with other systems and in agreement with simulations and theoretical models. Secondly, we will report visible photon correlation measurements, utilized to characterize in detail the sample. The obtained results are in agreement with literature data.

### 4.1.1 Sample preparation and characterization

The samples studied in this thesis have been produced following the procedure reported in [104], except for pure boron oxide; the preparation of this last glass will be discussed in Ch.(5). We describe here the process followed for the lithium based borates, $(Li_2O)_x(B_2O_3)_{1-x}$, with $x$ the alkali molar fraction. The procedure is essentially the same for sodium and potassium borates [104].
Alkali borates can be prepared with different starting compounds and techniques. With the instrumentation available in our laboratory, we opted for lithium carbonate ($Li_2CO_3$, 99.99% purity) and anhydrous boron oxide ($B_2O_3$, 99% purity) as starting chemicals, both purchased from Sigma-Aldrich. A few grams of the powders were placed in an electric furnace (temperature stability $\pm 1$°C) and heated to 125 °C for 24 hours. This baking is essential to remove water traces in order to correctly weigh the amount of $Li_2CO_3$ and $B_2O_3$ needed to reach the target alkali molar fraction $x$. The powders were then mixed and melted in an aluminium oxide crucible at 1000°C for 4.5 hours. Note that in

[104] the fusion procedure was performed in two steps, in order to get enough material for casting. Here we decided to produce a smaller amount of glass, and thus melting the powder once was sufficient. We kept the mixture at a temperature above melting for a total time similar to that in the original receipt [104] since it is known that at high temperature the gaseous monomer $LiBO_2$ is released from the samples [105]. While this does not alter the composition for lithium metaborate ($x = 0.5$), for other compositions it can introduce a systematic error in the molar fraction estimation. The melt was then quenched between stainless-steel plates preheated at 200°C. The obtained slabs of few mm in thickness were then placed in a tubular oven and heated at 3°C/min up to a temperature 20°C below the tabulated glass transition temperature [106]. The sample was annealed at that temperature for 6 hours, and then slowly cooled down to 150°C at 0.5°C/min. Subsequently, the slabs were sealed in vacuum and, only few weeks before the XPCS experiments, they were cut, and then polished with silicon carbide sandpaper and ethanol down to the desired thickness, usually $\sim 100\,\mu m$. The use of ethanol as lubricant was preferred since borate glasses are highly hygroscopic. During the beamtime, just before putting the samples in the experimental chamber, a final polishing with a very fine silicon carbide sandpaper was done to remove any trace of possible surface contamination. The final exact thickness has been estimated measuring the attenuation of the X-ray beam through the sample with the Lambert–Beer law

$$I = I_0 \exp(-\mu W) \tag{4.1}$$

with $I$ and $I_0$ the transmitted and the incident beam intensities, respectively, both measured with a photo-diode downstream of the sample, $\mu$ the linear attenuation coefficient and $W$ the sample thickness. Despite the measurement is extremely precise (with a standard deviation $\sigma$ of $\sim \mu m$), the total uncertainty must include the variations of the sample thickness due to scratches and non planar surfaces: these features are intrinsic of the polishing procedure here utilized to produce the samples. We observed that a reasonable uncertainty on the sample thickness is around 10%.

The sample preparation of $LiBO_2$ glasses for visible photon correlation measurements was essentially the same. To perform the experiment, however, a much larger amount of material is required. The furnace designated for visible PCS, described in details in [107], is optimized for samples of 10 mm in thickness and few cm in height. The right amount of $LiBO_2$ glass was then produced as described above. The obtained slabs were reduced to a powder with the use of a mortar and then inserted in silica ($SiO_2$) cuvettes. The powder was then melted at 1000°C for few minutes in order to remove air bubbles. $LiBO_2$ is known to be a solvent for silica-based materials: we observed that the surface of the silica cuvette became indeed opaque, symptom that the lithium-metaborate was dissolving it. For visible measurements the flatness and transparency of the container surfaces are essential since spurious scattering can easily affect the sample's signal. The $LiBO_2$ glassy sample was then removed from the opaque cuvette, polished with sand-paper and then inserted in a new cuvette.

The sample was heated at 500°C in order to let it take the form of the new container. PCS measurements were then performed, taking particular attention to avoid lowering the temperature too much since the difference in thermal expansion between lithium metaborate and silica would crack the cuvette.

### 4.1.2 High temperature XPCS measurements

The data reported in the following chapters of this thesis have been collected both at beamline ID10 at the ESRF and at beamline P10 at Petra III. For this reason, we decided to give the main experimental details (for example incident photon flux, beam spot size and detector configuration utilized) whenever a new set of data is presented. With this choice, we hope to provide a self-consistent description for each section, avoiding the need to look for the relevant information elsewhere. Anyway, in this section we want to discuss briefly few aspects which are common to all the experiments.

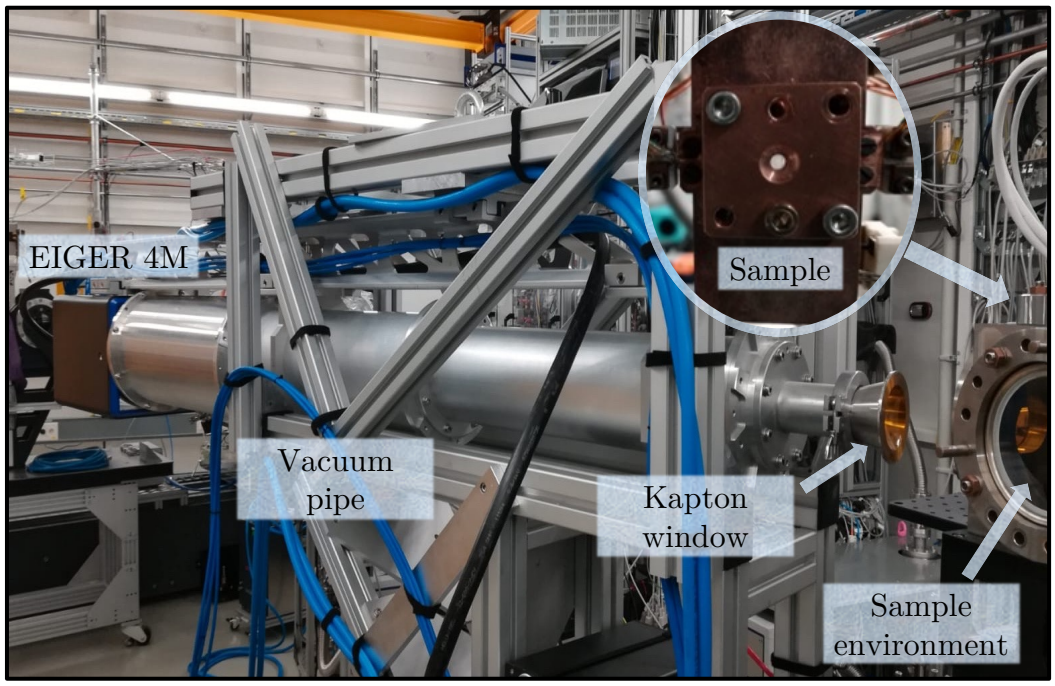


Figure 4.1: Photo of the XPCS end-station of the P10 beamline at the Petra III synchrotron radiation center (DESY, Hamburg). Starting from the left: EIGER 4M detector, 1.8 m long vacuum pipe, kapton window and sample environment. In the circle a frontal photo of the hot finger is reported, with the sample mounted on it (small whitish disk in the center). The diameter of the hole through which the X-ray beam goes through in transmission geometry is 2.5 mm for the present case.

In Fig.(4.1) we illustrated the experimental setup of the end-station at the P10 beamline at Petra III. The X-ray beam, focused with beryllium compound refractive lenses to a spot of few $\mu m^2$, impinges on the sample mounted on

a hot-finger in a vacuum environment (rightmost part in the image). The scattered photons exit the sample-chamber and are collected in a vacuum tube mounted on a motorized goniometer. At the end of the pipe, the detector is mounted in air, with kapton (polyimide) windows separating the different vacuum sections. While at first sight the vacuum pipe could seem not necessary, it is fundamental to perform wide-angle XPCS experiments. At the standard energies of XPCS beamlines ($\sim 8$ keV) the absorption length of air is roughly 1-1.5 meters. If the pipe reported in figure is omitted (being $\sim 2$ m in length), more than 70% of the scattered photons would be absorbed by air.
The sample of $\sim 100\,\mu$m in thickness is mounted between the two copper pieces screwed to the hot finger (insert in the figure). The thermal contact between sample and holder is improved by means of thin copper or aluminum sheets inserted in between. Measurements are performed in transmission geometry, with an available sample surface of about 6 mm$^2$. Note that a small hole without sample is usually kept to provide the opportunity of measuring the reference beam intensity $I_0$ (see Eq.(4.1)) before/after the transmission measurements carried out to estimate the sample thickness. This allows us to correctly normalize the data for possible time-dependent fluctuations in the incident photon flux.
In XPCS experiments, the scattered photons are collected with 2D detectors (multi-speckle technique, as described in Ch.(3)). Nowadays many types of detectors are available, among which hybrid photon counting detectors are the most suitable for XPCS measurements. These new-generation detectors, such the here utilized EIGERs of Dectris, allow for high repetition rates (above the kHz range) with few millions of pixels (depending on the model). Not only these detectors are much faster than standard X-ray CCDs, where the typical time in between frames is limited by the read-out time (in the order of seconds), but are noise-free: the photon discrimination is automatically performed in real time and produces images with zero dark counts, where the integer number of photons detected by each pixel is directly reported.
Fig.(4.2 *a*) shows an example of an image for a $LiBO_2$ glass collected with an EIGER 4M detector. The image is the average of 18000 frames exposed for 0.1 s each. The blue grid is due to the intrinsic hardware structure of the detector, composed of different modules, while the circular shape is the shadow of the vacuum pipe. The images were collected at $\theta = 23°$ corresponding to the maximum of the structure factor for the energy utilized in that experiment (8.4 keV). The profile of the structure factor (or, to be more precise, of the scattered intensity), as a function of the scattering angle $\theta$, is seen as a change in color between light-green (left of Fig.(4.2 *a*)) to light-red (center of Fig.(4.2 *a*)). The configuration here adopted, with the detector 1.8 m away from the sample to match speckle size and pixel size (75 µm), implies that the detector covers almost 5°. To improve the angular resolution, the images can be divided in regions of interest (ROI) as reported in Fig.(4.2 *b*). The regions are calculated according to geometrical considerations, mapping the position of each pixel in space and associating it to the relative scattering angle. The procedure is

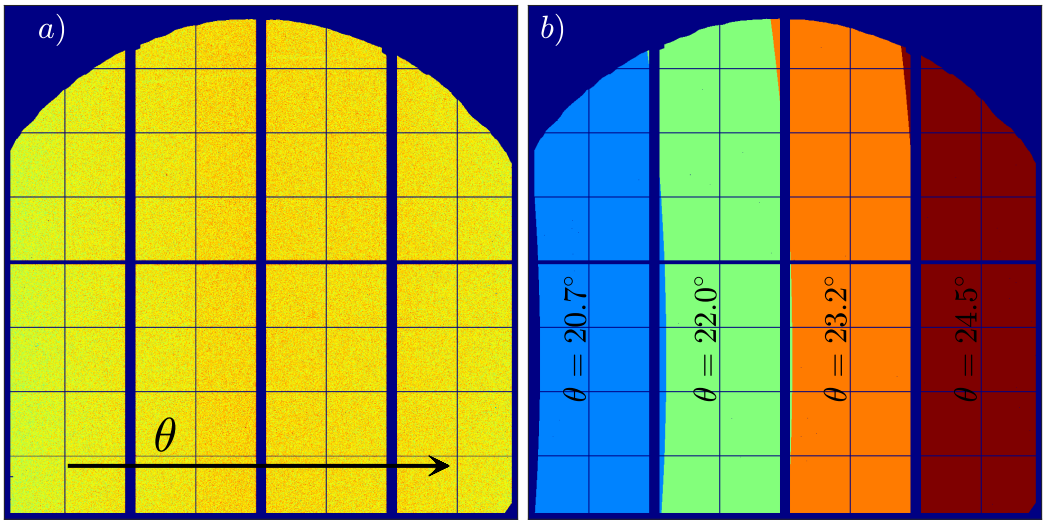


Figure 4.2: *a*) Example of an image recorded with an EIGER 4M detector, composed of $\sim 4\times10^6$ pixels. The reported image is the average of 18000 frames. The direction of increasing scattering angle is indicated by the arrow. The experimental scattering geometry involves the detector moving in the horizontal scattering plane. *b*) Example of the region of interest (ROIs) considered for the analysis of the XPCS data.

performed by dividing the detector in a variable number of "slices" depending on the scattered intensity: on the peak of the structure factor, for example, dividing the detector in 4 ROIs still results in reliable correlation functions, while at small angles ($\theta \sim 5°$) the best compromise is obtained reducing the ROIs to 3 (we recall here that the signal to noise ratio is proportional to the square root of the number of pixels [99]). Finally, note that the same "slicing" procedure is applied for the calculation of the scattered intensity as a function of $\theta$ (or $q$). In this specific case the detector was divided in a variable number of ROIs comprised between 20 and 30 and depending on the scattering angle. The calculated scattered intensity for liquid $LiBO_2$ is reported in Fig.(4.3).
In this thesis we discuss in some detail the properties (both structural and dynamical) of our sample glasses as a function of the X-ray irradiation. The quantity which characterizes the amount of energy absorbed by the sample is the dose, measured in Gray, $\mathrm{Gy} = \frac{\mathrm{J}}{\mathrm{kg}}$. The photon flux of the incident beam is estimated during each experiment, using both a measurement of the scattered radiation by a thin kapton foil intercepting the beam and directly with the use of a silicon diode [108]. The beam profile is measured by knife-edge scans, utilizing a thin tungsten wire as knife. However, what shall we define as the average absorbed dose by the sample? It is clear that the almost Gaussian beam

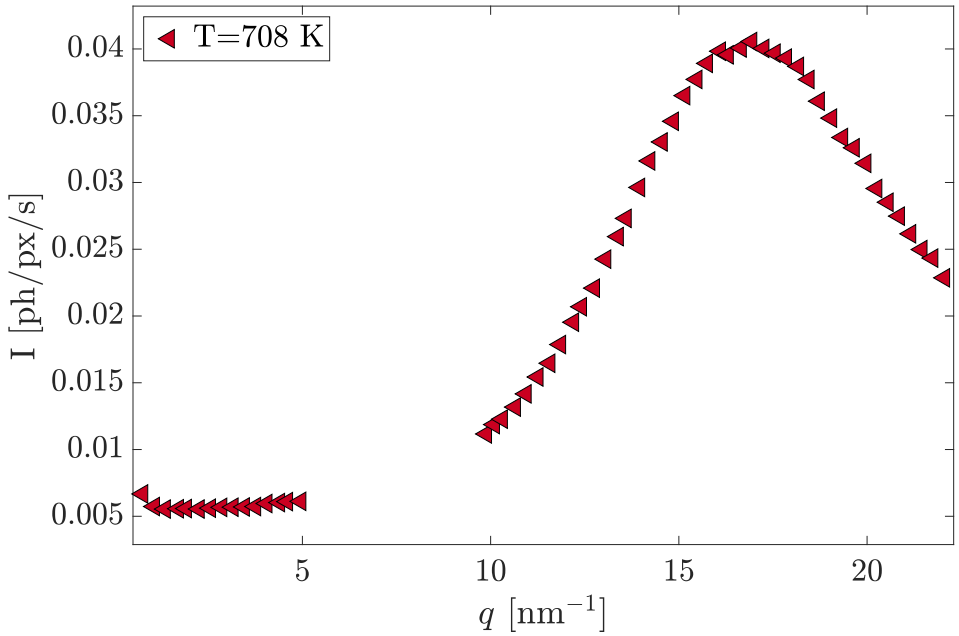


Figure 4.3: Scattered intensity for liquid $LiBO_2$ as a function of $q$. The missing points between 5 and 10 $nm^{-1}$ are caused by a flange present in this setup which blocks the scattered radiation at the corresponding angles.

profile is reflected in a distribution of dose across the scattering volume. In a similar way, the beam is attenuated as it penetrates the sample ($\exp[-\mu W]$). We decided, in agreement with the previous works [9, 109, 110], to assume that the whole energy is deposited in a volume whose surface is given by the beam full-width at half maximum ($FWHM_{h,v}$ for the horizontal and vertical directions respectively). Regarding the beam-attenuation, we utilized samples with $W \ll 1/\mu$, thus it is safe to assume that the absorbed dose is almost constant across the sample thickness. The volume of interest it then described by $V = FWHM_h \times FWHM_v \times W$. This definition will be utilized in all the calculations involving the dose hereafter.
The XPCS data reported in the following section have been collected during an experiment at P10 (Petra III) with a beam of 8.0 keV photons focused on $3.3 \times 3\,\mu m^2$ H × V (FWHM). The full flux of $F_0 = 9.7 \times 10^{10}$ ph/s was attenuated by a factor 4.84 with silicon foils (25 µm each) as absorbers. The sample, $W = (175 \pm 25)\,\mu m$, was mounted in the furnace (hot finger) described above and heated to different temperatures, with a maximum of T=773K. We observed that, despite the thermal contact between the sample and the hot finger being improved with copper foils, a temperature gradient was present between the real sample temperature and the one read by the thermocouples. We estimated a difference of 65 K at the maximum temperature probed (T=773 K), which is reflected in an effective temperature of T=708 K, as hereafter reported.

### 4.1.3 The *q*-dependence of the relaxation time

In the following chapters we will discuss in detail an unusual effect observed in oxide glasses probed with XPCS: the X-ray photons not only probe the dynamics but induce it themselves. This effect, known as beam-induced dynamics [8], can be mitigated in the liquid state, as we will show in detail in Ch.(6) and as originally demonstrated in [9]. For the sake of clarity, we will not enter in this discussion here. We only say that, despite some dynamics being induced by the photon beam, the use of an attenuated beam ($F_1 = 0.2067F_0$) together with the fact that the structural relaxation is on the order of few seconds, allows us to probe with XPCS the $q$-dependence of the spontaneous, structural relaxation in a reliable way. We anticipate that, on the peak of the structure factor, the equilibrium structural relaxation time is a factor two longer with respect to the values reported hereafter: this aspect, together with possible correction schemes, will be discussed in details in Ch.(6).
In order to perform measurements in the liquid state and avoid possible beam damage, the images' acquisition scheme was spread over smaller scan series on different sample's spots. In detail, between 20 and 30 scans with duration of 210 seconds each were performed for the different probed scattering angles. The sample was moved 5 µm after each acquisition, keeping the absorbed dose always below 0.4 GGy. The sample's homogeneity in thickness was checked before performing the scans: we aim in fact at collecting data with the same contrast in order not to deform their average (different thicknesses would imply different experimental contrasts, see Ch.(3) for more details). The images were not normalized for the average intensity profile [92], thus a baseline must be introduced to correctly model the intensity autocorrelation function, as discussed in Sect.(3.3). The stretched exponential function (KWW function [48]) was utilized for the fit

$$g_2(t) = c\exp[-2(t/\tau)^{\beta}] + d \tag{4.2}$$

where $c$ is the experimental contrast and $d$ the baseline.
Since the collected correlation functions are characterized by a stretched behavior with fast relaxation times, we decided to divide the fitting procedure in two steps in order to increase its reliability. First of all, a straightforward fit of Eq.(4.2) to the experimental data is performed. The most sensitive parameters are the stretching parameter and contrast: their values are dominated by the statistical fluctuations of the first few points in the autocorrelation function. For this reason, the average stretching parameter is calculated over the whole probed exchanged wave-vector range, leading to a value of $\beta = 0.5 \pm 0.1$. This average value is then fixed at all $q$s in a second fit run carried out to extract the relaxation time. An example of a measured autocorrelation function is reported in Fig.(4.4 *a*). Together with the experimental data (logarithmically binned to improve visibility) we reported 3 different fits using Eq.(4.2) and fixing the stretching parameter $\beta$ to 3 values, namely 0.3, 0.5 and 0.7. The relaxation is well captured by all curves with a small difference at short delays:

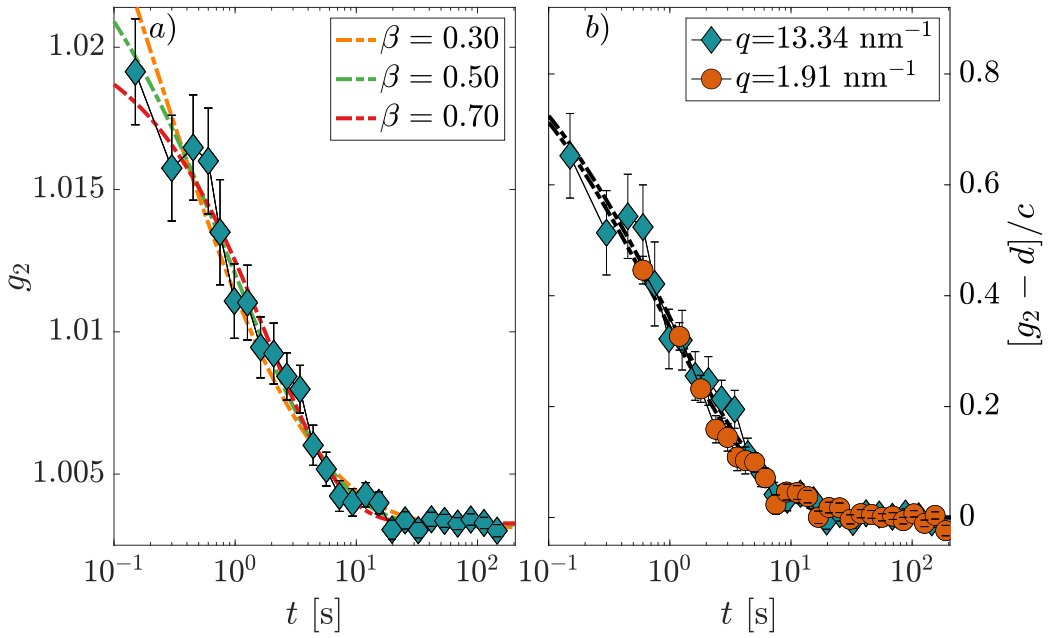


Figure 4.4: *a*) Intensity autocorrelation function for liquid $LiBO_2$ (T=708 K) at the exchanged wave-vector $q = (13.34 \pm 0.44)\,\mathrm{nm}^{-1}$ together with three KWW fits (colored-dashed lines) with different fixed stretching parameters (as reported in the legend). *b*) Normalized intensity autocorrelation functions for two representative exchanged wave-vectors. The black dashed lines are the best KWW fits with $\beta = 0.50$.

this gives a direct idea of the level of (in)sensitivity of the fit to the stretching parameter. Furthermore, literature data report that the stretching parameter for undercooled lithium metaborate is close to $\beta = 0.64$ [111], while our dynamic light scattering measurements, to be presented in the final part of this chapter, suggest $\beta = 0.57 \pm 0.04$. It is clear that the choice of fixing the stretching parameter to the average value of $\beta = 0.5$ in the whole exchanged wave-vector range is compatible with the equilibrium data within $\pm 0.1$.
In Fig.(4.4 *b*) the autocorrelation functions for two selected $q$ values have been reported. The $g_2$ functions have been normalized for the fitted experimental contrast $c$ after the subtraction of the baseline $d$. As it can be clearly seen, the two curves superpose almost perfectly, symptom that the relaxation time is the same at the two $q$ values. The KWW best fits, reported as black dashed lines, confirm this.
In Fig.(4.5) we show the relaxation time as a function of $q$ in the liquid $LiBO_2$ system (T=708 K). The relaxation time shows an almost flat $q$-dependence, with a small peak close to the maximum of the structure factor. We will discuss these data just after a small theoretical detour.

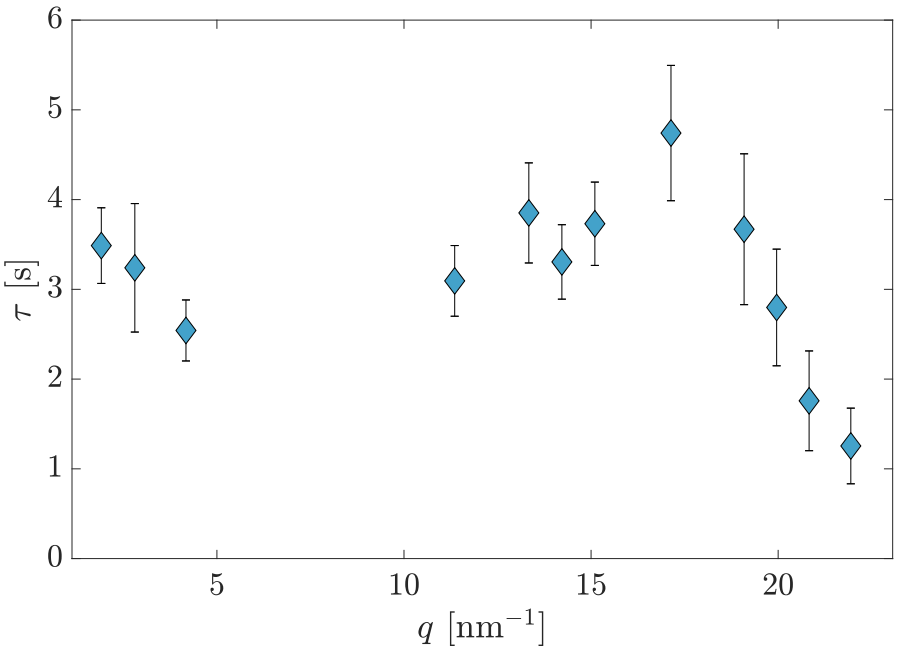


Figure 4.5: Relaxation time for the $LiBO_2$ undercooled liquid as a function of the exchanged wave vector $q$.

### 4.1.4 The density relaxation approaching the glassy state

In order to discuss the results reported in Fig.(4.5) and thereafter the ones regarding the photo-annealed glasses in Ch.(6), we need to spend few words on the theoretical models at the basis of the description of liquids approaching the glassy state. We intentionally avoided introducing this argument at the beginning of the thesis, since its relevance is better appreciated here.
Before tackling the discussion about density relaxation and its fundamental properties, we recall that in this work we always consider the collective density correlation function (namely the total van Hove function). While in simulations it is quite simple to split the density correlation in the total, distinct and self parts, (Eq.(2.20) and following), in XPCS experiments usually one has access only to the total (also known as coherent) density relaxation. We should note that the coherent correlation function reduces to the self part whenever the correlation between distinct particles is zero (for example in the case of Brownian diffusion of a dilute solution of macromolecules). In the following we will not discuss the properties of the self dynamics, but focus our attention only on the collective one.
It is well understood that approaching the glass transition the slowing down of the dynamics is accompanied by the decoupling of different relaxations [17–19]. The reference theory describing the behavior of the density relaxation in this regime is the Mode-Coupling-Theory (MCT) [112, 113]. The MCT is a first-principles theory which relies on the system's static properties (the static structure factor $S(\mathbf{q})$) and memory functions with the aim of describing the

temporal and exchanged wave-vector dependence of the intermediate scattering function $F(\mathbf{q},t)$ [114]. The theory developed in the 1984 [112], also known as "ideal" MCT, predicts for the density correlation a two-step behavior. $F(\mathbf{q},t)$ decays firstly to a plateau value (non-ergodicity parameter) and then a second slower decay, the structural ($\alpha$) relaxation, completely decorrelates the intermediate scattering function. From a physical point of view, the first, fast relaxation is due to the rattling of a particle in the transient "cage" of neighbor particles, while the slower structural one is due to the escape from these "cages". Note that the theory predicts a liquid-glass transition happening at a critical temperature $T_c$, with the relaxation time diverging in a critical fashion with a power law $\tau \sim (T - T_c)^{-|\gamma|}$. The theory analytically describes the short time and scaling behavior of the relaxation process and has been refined (for example considering the coupling between the momenta too [115]) in order to describe the main features observed in experiments and simulations; anyway, for the basic introduction we are giving here, we will stick to the ideal MCT. More details can be found in recent reviews [114] as well as in the original papers published on the topic [112, 113, 115].
The structural relaxation predicted by the ideal MCT displays a decay slower than exponential, which is well captured by the stretched ($\beta < 1$) KWW function commonly utilized to model it [116]. Note that the MCT equations cannot be solved analytically for what regards the $\alpha-$relaxation, whose details depend on the particular system considered since the interaction potential modifies the $q$-dependence of the dynamical parameters (the non-ergodicity factor, the relaxation time $\tau$ and the stretching parameter $\beta$). These aspects have been investigated numerically and experimentally in many different systems, examples being hard spheres [117, 118], Lennard-Jones liquids [119], water [116], ortho-terphenyl [120, 121], silica [122] and other liquids (polymers, patchy particles, Lennard-Jones binary-mixtures, metals [95, 123–126]). A common feature observed in almost all systems is that the relaxation parameters are weakly dependent on the exchanged wave-vector if not for an oscillation in phase with the static structure factor. This phenomenon gets its name from the first scientist who analyzed the relation between dynamics and structure, de Gennes [127]. The main signature of the de Gennes effect (or narrowing, since it was investigated with frequency-domain techniques) is a slowing down of the dynamics at $q$s corresponding to the first neighbor particle distance. It is associated with the cooperative nature of the dynamics approaching the glassy state: a particle (say $i$) is unlikely to move over a typical nearest neighbor distance $(i - j)$ since this has to involve the movement of particle $j$ too. The de Gennes approximation leads to a prediction of the relaxation time as $\tau \sim S(q)/q^2$. At intermediate exchanged wave-vectors, this equation captures the $q$-dependence of $\tau$ [116, 118, 120], but in the low-$q$ regime it fails. The de Gennes approximation is developed and valid for the dynamics at short times [118, 122], implying a long spatial-range diffusive-like behavior. It is then not surprising that it cannot describe correctly the collective slow structural relaxation for small $q$s, which from MCT predictions is found to be almost

$q$-independent. However, the de Gennes effect captures well the dependence of $\tau$ close to the peak of the structure factor and for this reason it is customary to refer to it whenever $\tau$ oscillates in phase with the structure factor.

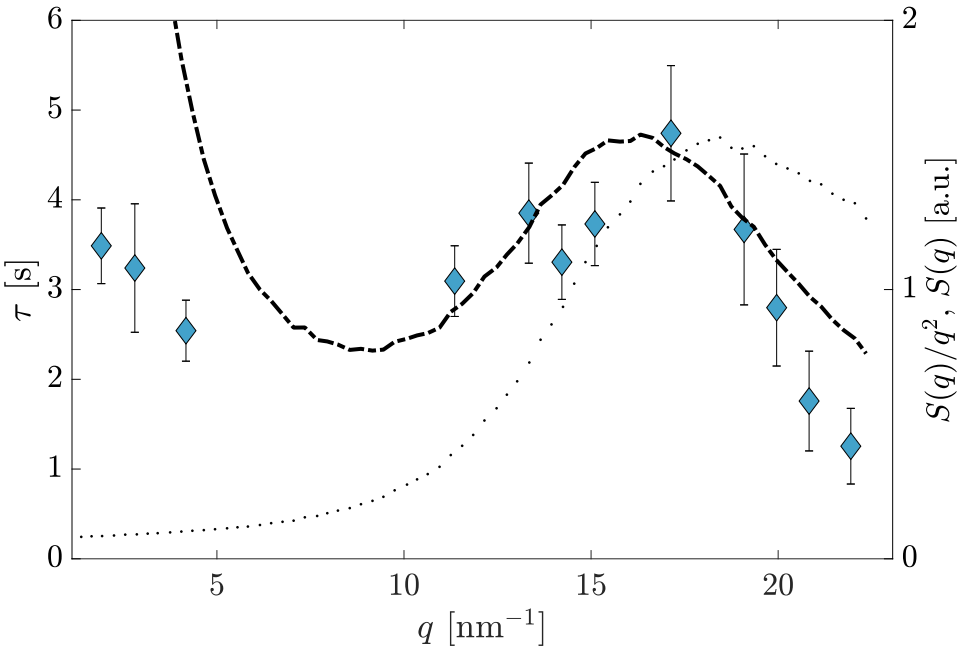


Figure 4.6: Relaxation time for the $LiBO_2$ undercooled liquid as a function of the exchanged wave vector $q$ together with the de Gennes narrowing approximation, $S(q)/q^2$ (black-dashed line), and the structure factor, $S(q)$ (black dots) properly normalized.

In Fig.(4.6) we show the same data as in Fig.(4.5), but plotted here together with the de Gennes narrowing approximation. The black dashed line reported here corresponds to $S(q)/q^2$, properly scaled in order to match the same scale of the relaxation time, while the black dots refer to the structure factor $S(q)$. Here the $S(q)$ is the total scattering structure factor, calculated normalizing the measured intensity to the square of the sum of the concentration-weighted atomic form factors

$$S(q) = I(q)/\sum_{i,j} c_i c_j f_i(q) f_j(q) \tag{4.3}$$

where $i, j$ runs over Li, B and O, $c_i$ is the fraction and $f_i(q)$ the atomic form factor of the $i$ atom, respectively. We recall that the atomic scattering factor is defined as the atomic scattering length normalized to the classical electron radius, $f(q) = b(q)/r_e$, see Sect.(3.1.3) for more details. The experimental total scattered intensity utilized here is additionally corrected for the contribution of the polarization (scaling as $\cos^2\theta$) and sample thickness, see Eq.(3.57).
The de Gennes effect captures the relaxation time oscillation observed close to maximum of the structure factor of the glass. However, it fails to describe the

low-$q$ limit ($q \leq 5\text{nm}^{-1}$), where the relaxation time becomes almost independent of $q$. To the best of our knowledge, this is the first XPCS measurement in oxide liquids that elucidates the $q$-dependence of the spontaneous dynamics at the atomic length-scale. Recent results on multi-component liquid metals [95] have shown that the dynamics of such systems are characterized by a marked de Gennes narrowing too.
To conclude this part, we highlight that the almost flat $q$-dependence of $\tau$ observed in liquids justifies the comparison in the following section of XPCS data with measurements performed with visible photon correlation: the $q$-value ratio between wide-angle XPCS and visible PCS is almost $10^3$, but the relaxation time does not change considerably.

## 4.2 Visible PCS measurements

The relaxation time dependence close to the glass transition temperature was characterized with visible dynamic light scattering (DLS) as anticipated at the beginning of this chapter. The experiments displayed here have been performed with the main goal of supporting the XPCS data reported in Ch.(6).
The utilized experimental apparatus is a custom setup, improved from the one described in [107]. In Fig.(4.7) we show a photo of it, in order to help discussing its main components.

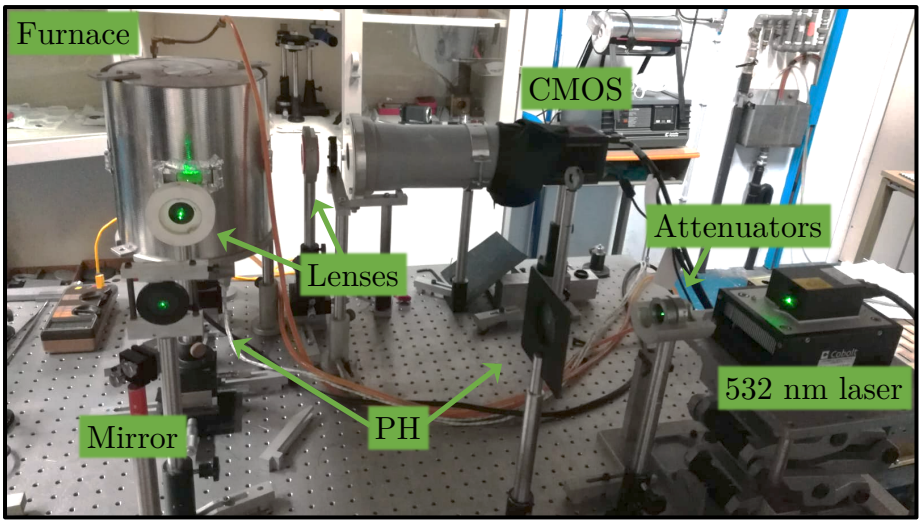


Figure 4.7: Experimental setup utilized for the DLS measurements.

A 532 nm continuous-wave diode-pumped laser (Cobolt Samba) was employed as light source; the output power (300 mW) was attenuated with the use of neutral filters to the desired power on the sample, which was on the order of 100 mW. The spurious scattering from the filters and the mirror was removed with pin-holes (PH) and the beam was then focused on the sample located inside a furnace. The geometry of the furnace allows us to collect the light scattered at 90°. A fixed lens to collect the light was then mounted in order to obtain the well-known photon correlation imaging configuration [128]. With this approach, the image of the scattering volume is projected on the camera chip, allowing easy selection of portions of the image where no parasitic light is present [129]. This setup was designed to achieve a magnification of about 3 on the camera chip. Finally, an iris positioned between the lens and the detector allowed the selection of the speckle size by controlling the solid angle, see Eqs.(3.29;3.30). Here, we decided to have one speckle each 2 pixels. The most significant difference with respect to the setup developed and reported in [107] is the detector. Here we used a Hamamatsu CMOS camera (Orca-FLASH 4.0, with $2048 \times 2048$ pixels of size $6.5 \times 6.5\,\mu m^2$) which permits very high frame rates ($> 25$ kHz on a reduced ROI). The sample environment was a

tubular furnace, specifically designed for visible scattering experiments that was controlled by a standard Eurotherm PID controller. In order to better control the temperature of the sample, a thermocouple was inserted in direct contact with the sample close to the scattering volume (temperature resolution: 0.5 K).

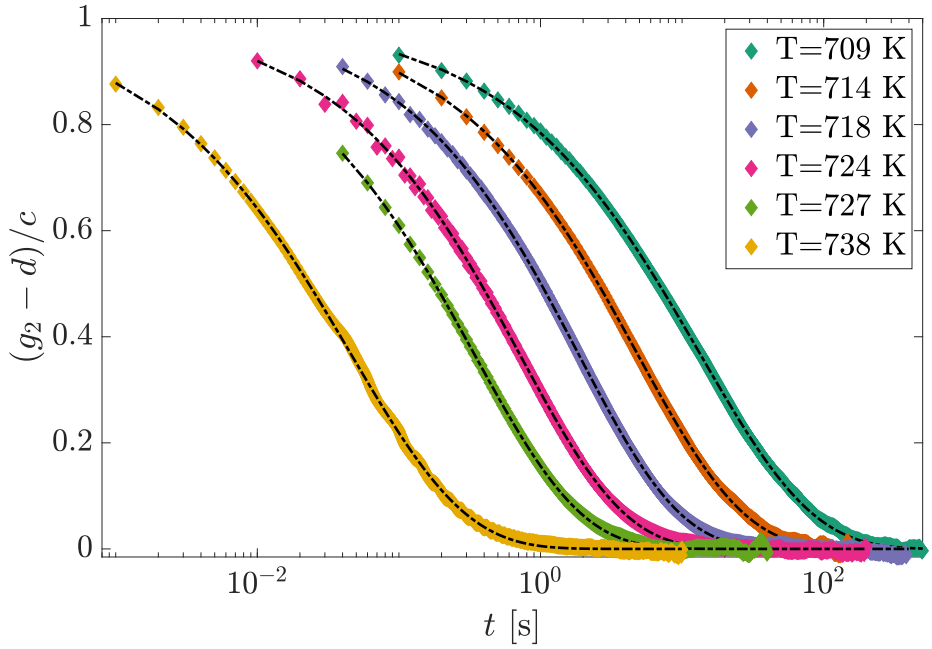


Figure 4.8: Normalized autocorrelation functions for liquid $LiBO_2$, measured at different temperatures as reported in the legend. Black dashed lines are the best KWW fits. The small oscillations in the yellow curve are an artifact due to the vibrations of the CMOS caused by the air cooling system.

In Fig.(4.8) we report a selection of normalized autocorrelation functions computed at different temperatures for the $LiBO_2$ undercooled liquid. The functions are fitted with a stretched KWW function, Eq.(4.2). The integration time has been varied from 1 ms (yellow diamonds) up to 1 second (not shown here), with sequences up to 20000 images and using $\sim$ 10000 pixels. The correlation functions have been computed with a custom MATLAB code, which first extract the two time correlation functions and then computes $g_2(t)$.
The autocorrelation functions display a stretched behavior, with $\beta \sim 0.6$. In these cases, enlarging the time window to cover both small lag-times ($t \ll \tau$) and large ones ($t \gg \tau$) helps correctly extract the shape of the autocorrelation function. Unfortunately, covering more than 5 decades with standard linear acquisition is almost prohibitive. The correlation of millions of images is nowadays the bottleneck of multi-speckle photon correlation and new schemes have been adopted, such the multi-tau correlation [91], which perform the correlation in a partially-logarithmic time spacing. However with that approach one loses information on the two time function and has to work with millions of images

anyway. Here we decided to tackle the problem from an hardware point of view. Instead of performing the multi-tau correlation, we adopted a pseudo multi-tau acquisition scheme (named here "Hardware Multi-$\tau$") proposed and developed very recently [130].

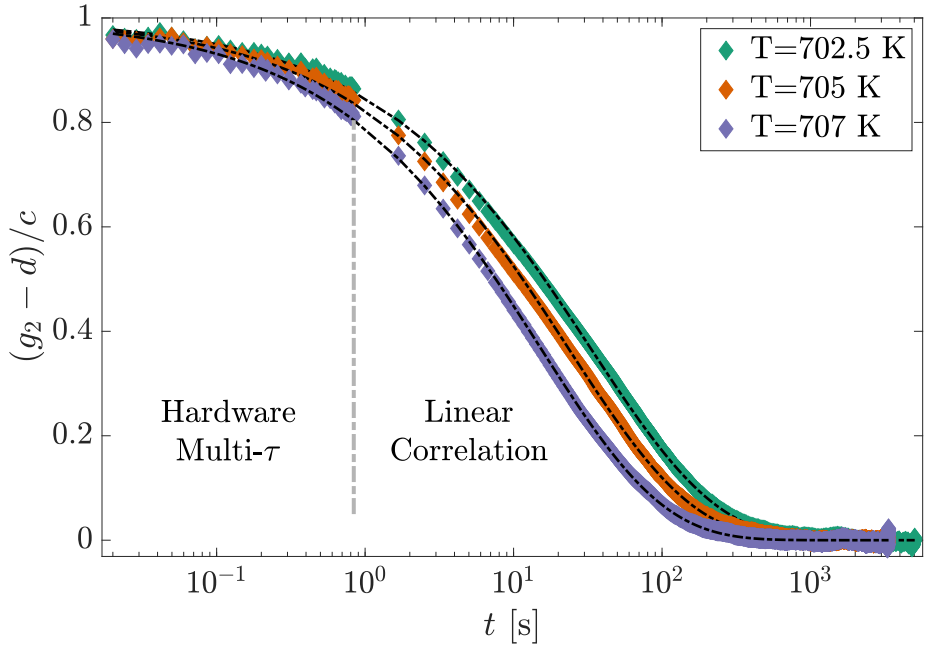


Figure 4.9: Correlation functions obtained with our custom code and acquisition scheme. Black-dashed lines are the best KWW fit.

In this scheme, a main linear acquisition is performed (let us say that images are acquired at times $t_{2i}$, with a given integration time $\Delta t$). An additional image is inserted between $t_{2i}$ and $t_{2(i+1)}$ at time $t_{2i+1}$. The lag between $t_{2i}$ and $t_{2i+1}$ is variable, and chosen to be spaced in time in a logarithmic fashion, between $\Delta t$ and $t_{2(i+1)} - t_{2i}$. This scheme is repeated many times (in the present case, between 100 and 400 cycles) and the final sequence of images saved on the computer. Post processing is the trickiest part of this approach: a simple two time correlation function can be calculated from the whole set of images, but the $g_2(t)$ cannot be extracted as reported in Ch.(3). Each point in the two-times matrix must be mapped with the correct lag, given by the difference of acquisition times $t_j$ and $t_k$. The same-lag image-correlations must then be averaged, which requires a high computational effort since one needs to cycle over all couples of acquisition times. To speed-up the process, we decided to utilize this approach only for lags smaller than the main time step $t_{2(i+1)} - t_{2i}$, keeping the standard linear correlation for larger lag-times.
The algorithm was implemented on a Field Programmable Gate Array (FPGA) board (Xilinx Spartan-3A) and the CMOS simply controlled with a low-TTL signal in edge-trigger mode. An example of the obtained autocorrelation functions is reported in Fig.(4.9). The curves have been calculated with a total

number of images up to 12000: a standard linear acquisition scheme, to cover the same timescale, would have required 250000 frames.

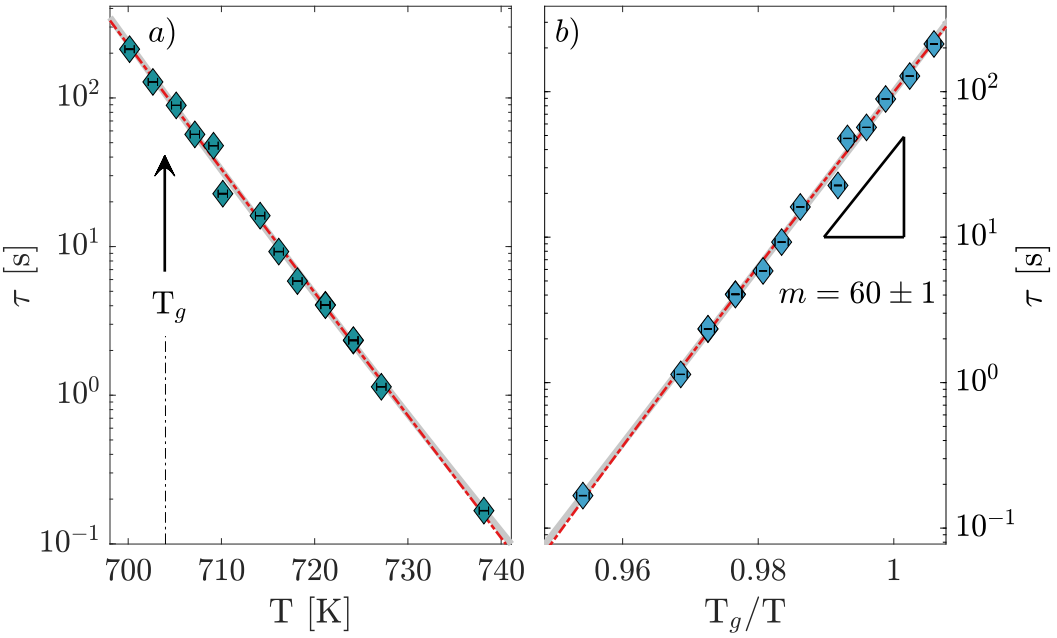


Figure 4.10: *a*) Relaxation time for $LiBO_2$ as a function of the temperature. *b*) The relaxation time is again reported as a function of the inverse temperature $T_g/T$. The fragility index $m$ can be calculated as graphically reported, $m = \lim_{T \to T_g} \frac{\partial \log_{10} \tau}{\partial \frac{T_g}{T}}$. Gray full lines are the best Arrhenius fit (Eq.(2.6)), while the red-dashed line are the best VFT one (Eq.(2.7)). In the small temperature range probed here, both functions well describe the experimental data.

Fig.(4.10 *a*) shows the relaxation time as a function of the temperature. The data can be modeled according to the equations reported in Ch.(2), which are a simple exponential behavior (Arrhenius-like, Eq.(2.6)) or faster than exponential (VFT, Eq.(2.7)). Both curves adequately describe the data (gray-full line and red-dashed line respectively) over the considered temperature range. The glass transition temperature, defined as the temperature where $\tau = 100$ s, is found to be $T_g = 704$ K. This $T_g$ is slightly higher but in substantial agreement with the $T_g = 694$ K reported in the literature [131]. Other authors report a much different glass transition temperature ($T_g = 663$ K) from calorimetric measurements [106]. This latter value has been utilized to anneal the samples, as anticipated at the beginning of the chapter. We recall that from the temperature dependence of the relaxation time (or, equivalently, of the viscosity) approaching the glass transition temperature one can extract the so called fragility $m$, Eq.(2.8). The meaning of this latter quantity is better grasped if the data are reported as a function of the inverse temperature, as displayed in Fig.(4.10 *b*). The graphical inset shows how to calculate the fragility, that is performing the derivative of the logarithm of $\tau$ with respect to the inverse

normalized temperature. The value obtained utilizing the Arrhenius fit is $m = 60 \pm 1$, quite different from the one extrapolated from literature data of $m \sim 75$ [132].

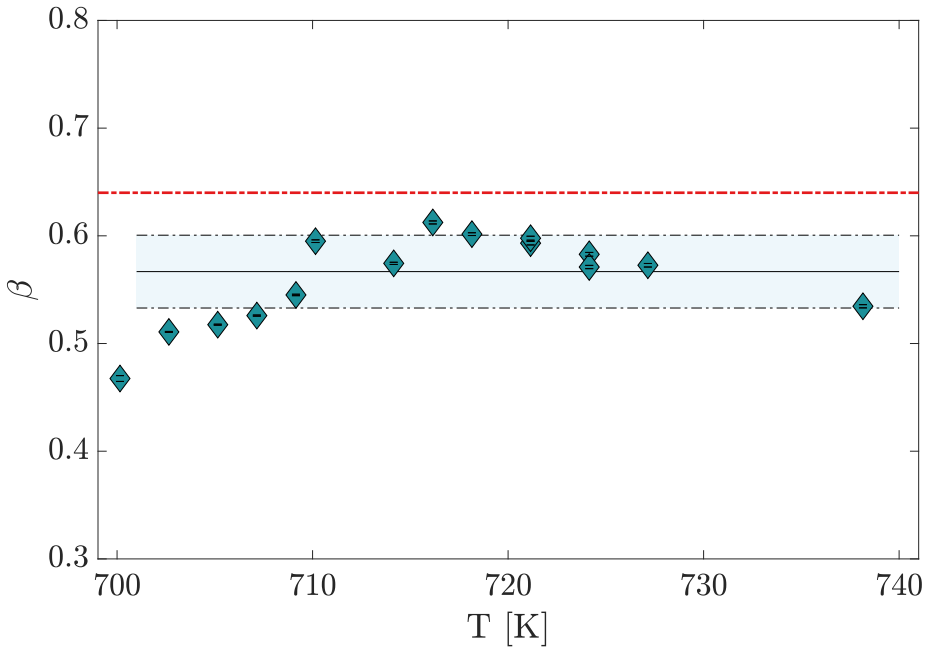


Figure 4.11: Stretching parameter $\beta$ obtained from the DLS measurements as a function of temperature. The red-dashed line is the value $\beta = 0.64$ reported in [111], while the continuous black line is the average of the green data (excluding the lowest temperature one). The shadowed region delimited by the black-dashed lines is the confidence's interval of the average value.

Finally, the stretching parameter as a function of the temperature is reported in Fig.(4.11). The non-monotonic behavior is quite surprising, and should be attributed to the quality of the data. The stretching parameter is expected to decrease when cooling the system [61, 62]: anyway, the probed temperature range is so small with respect to $T_g$ that we do not expect a substantial change in the shape parameter, at least not as large as the one reported in Fig.(4.11). We suspect that a few setup problems could affect our measurements. Above $T_g$, where the relaxation time is below 1 second, the minimum lag between images was chosen in the range of few ms. We noticed that vibrations originating from the air cooling system of the CMOS detector induce beatings in the autocorrelation function, see Fig.(4.8) leftmost curve. This spurious contribution could cause a small change in the shape of the stretching parameter. In addition, for low temperatures where the relaxation time is in the order of hundreds of seconds, we encountered a problem in the setup stability. Small fluctuations (in the order of 0.2 °C) of the laboratory temperature induce spurious correlations. For this reasons, we think that the temperature dependence of the stretching parameter deserves more attention from an experimental point of

view. However, the obtained average value, $\beta = 0.57 \pm 0.04$, is in reasonable agreement with the one reported in the literature of $\beta = 0.64$ [111].

# Chapter 5

# The stress driven dynamics in glasses

## 5.1 The arrested colloidal glass phase

In the first part of this chapter we will discuss the stress-driven dynamics in a colloidal glass. Although the main topic of the thesis regards oxide glasses, we have decided to include this part on colloidal systems since the observed peculiar dynamics has strong common points with the one of structural glasses below the glass transition temperature, as we will see. We will start discussing shortly the sample preparation of such systems and then concentrate on the main dynamical features observed: compressed correlation functions together with a ballistic like dynamics which proceed in a cooperative way, with the relaxation of regions of few µm in linear size.

### 5.1.1 The preparation of colloidal glasses and experimental details

Colloidal systems are mixtures of two phases, few examples of everyday life being toothpaste, mayonnaise, smoke or coffee. Their physical and mechanical properties depend on many factors: mayonnaise is liquid when the egg is added to the oil and vinegar, but once the two compounds are vigorously mixed oil droplets form a micro-emulsion in the water-based matrix, ending up in solid substance. Given the tunability of their properties and the range of possible applications, it is not surprising that colloidal systems are at the center of an huge effort in the scientific community.
Among the many different colloidal suspensions, we will concentrate on nanoparticles dispersed in a liquid solvent. In these systems the interaction between the particles can be precisely controlled, for example with the addition of salts, changing the temperature or with electric fields [133]. The success of colloidal suspensions lies in the possibility of mimic fundamental systems (such molecular liquids or glasses), but on a mesoscopic length-scale, thus much more easily accessible with standard experimental techniques (for example microscopy or

scattering). For these reasons such suspensions have been often utilized to explore the glass transition, for instance testing the mode-coupling theory introduced in Ch.(4) [134].
The fundamental quantity characterizing a suspension of nanoparticles is the volume fraction: it is defined as the ratio between the volume of the nanoparticles and the total volume of the system. At low volume fractions (or concentrations), particles are free to diffuse in the solvent, and their motion is governed by the Brownian dynamics (see Sect.(2.2.2)). When the volume fraction is increased, the particles start to interact and enter an undercooled-like liquid state. Further addition of particles in the solvent can induce a phase transition, with the crystallization of the system, or with the freezing of an amorphous configuration, namely a colloidal glass. The (inverse) volume fraction plays the same role of the temperature in structural glasses.
We discuss here the dynamical properties of a colloidal glass of silica ($SiO_2$) nanoparticles dispersed in a nearly critical binary mixture of water and 2,6-lutidine [135]. This system has been intensively investigated in the past due to the possibility of tuning the interaction potential between the silica nanoparticles. At low temperatures, the colloids interact with a repulsive Coulomb potential. Increasing the temperature, a preferential lutidine-wetting of the silica surface is observed, that is due to a partial separation of lutidine from water [135]. The layer which forms onto the nanoparticles screens the repulsive interaction and induces the aggregation with flocculation in the dilute solution [136] or a repulsive to attractive glass-glass transition in more concentrated systems [137]. This versatile toy-system was chosen to investigate the effect of the interaction potential on the dynamics and glass transition properties, for example the behavior of the four point susceptibility studied in the 2D version of this glass [58]. In this thesis we report the results obtained in the repulsive glass. Further investigations of the repulsive-attractive glass transition will be object of future studies.
The volume fraction of 2,6-lutidine ($C_7H_9N$, 99% purity purchased from Sigma Aldrich) with respect to the total solvent volume was chosen to be $C_L^v = 0.265 \pm 0.010$, well within the region where wetting of the silica surfaces occurs [135] on approaching the critical temperature of $T_C \sim 33\,^{\circ}\mathrm{C}$. All the measurements reported here have been performed at ambient temperature (T=298.15 K), far away from the critical temperature $T_C$ and deep in the repulsive region.
The plain surface silica nanoparticles (100 nm in diameter) were purchased from Micromod in a distilled water solution at mass concentration of 100 mg per 1 ml. The seller declares a density of particles of $2.0\,\mathrm{g/cm^3}$ and a polydispersivity index smaller than 0.2. Our colloidal samples have been prepared via a centrifugation procedure. First of all, the right amount of 2,6-lutidine is filtered with a 0.2-µm polytetrafluoroethylene (PTFE) filter and added to the solution of nanoparticles in order to achieve $C_L^v = 0.265 \pm 0.010$. The suspension is centrifuged at 15000g for 10 min to concentrate the nanoparticles on the bottom of the cuvette. The excess solvent is then removed mechanically

until the target volume fraction is obtained. The solid sample at the bottom of the cuvette is dispersed in the remaining solvent and vigorously mixed until it becomes again homogeneous. The obtained paste is transferred in borosilicate capillaries with wall thickness of 10 µm and inner diameter of $\sim$ 500 µm. A further centrifugation (100g for 60 s) is applied to the sample in order to remove any bubble and completely fill the capillary. Finally, the sample is sealed with a flame and stored for the experiment.
The experiments on these colloidal glasses have been performed at the beamline P10 of the Petra III synchrotron. The small-angle setup was employed, with a photon energy of 8.0 keV monochromatised with a Si(111) monochromator. The beam was focused on the capillaries with beryllium compound refractive lenses to a spot of $2 \times 3\mu m^2$ (V×H) full width at half maximum. The sample chamber described in Ch.(4) was directly connected to a 5 m vacuum pipe with a kapton window at the end. A beamstop was inserted at the end of the vacuum pipe, in order to block the direct beam from reaching the EIGER 4M detector mounted in air just after the kapton window (few cm away).
It is well known that organic materials are much more sensitive to radiation damage than oxide glasses. For this reason, we characterized the beam damage threshold very carefully at the beginning of the experiments. We found out that there is no signature of any radiation-induced effect in both the structure and the dynamics up to absorbed doses of 30 MGy. To be safe, we decided to set a limit to the total absorbed dose of 15 MGy. The full beam was attenuated with the use of silicon foils (25 µm of thickness) down to a value of $\sim 1.5 \times 10^8$ ph/s.

### 5.1.2 Characterization of the colloidal glasses

The aforementioned procedure to prepare the colloidal samples does not allow a precise estimate the final volume fraction of the glasses. In fact we do not know how many particles are lost during the adjustments of the solvent fraction, neither we can infer how much solvent evaporates during the preparation. For this reason, a more precise approach must be followed to estimate the volume fraction. To this end, we have used directly the Lambert-Beer equation, Eq.(4.1), taking into account the different components of the sample

$$I(y) = I_0 \exp\left[-(C(y)\mu_{capillary} + W(y)\varphi\mu_{SiO_2} + W(y)(1-\varphi)\mu_{WL})\right] \qquad (5.1)$$

Here $y$ is the horizontal direction orthogonal to the beam propagation vector, $I_0$ and $I(y)$ are the incident and transmitted intensity respectively, $C(y)$ is the thickness of the two capillary walls at position $y$ (to be geometrically calculated for each $y$-value), $W(y)$ is the thickness of the sample, $\varphi$ is the volume fraction, $\mu_{capillary}$, $\mu_{SiO_2}$ and $\mu_{WL}$ are the attenuation coefficients of the borosilicate capillary, silica nanoparticles and water-lutidine mixture, respectively. The water-lutidine attenuation coefficient is calculated summing up the attenuation coefficients of the two liquids, weighted for the relative volume fraction, that is $\mu_{WL} = C_L^v\mu_{lutidine} + (1 - C_L^v)\mu_{H_2O}$, with $C_L^v = 0.265 \pm 0.010$ the volume fraction

of lutidine with respect to the total binary solvent. The attenuation coefficients for each component have been obtained from the database of CXRO [138].

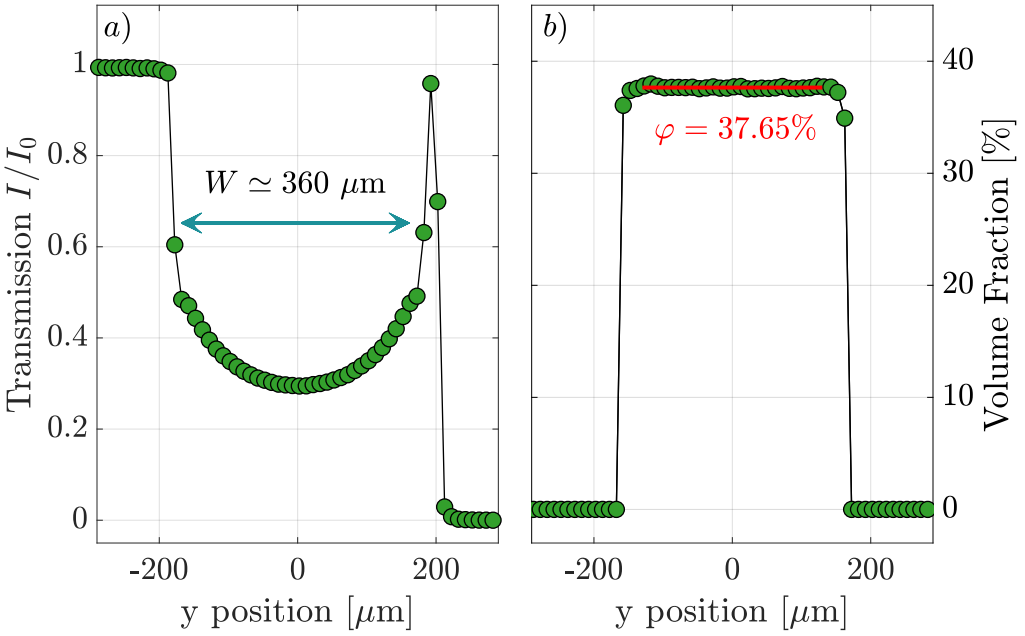


Figure 5.1: *a*) Transmission $I/I_0$ through the capillary containing the colloidal glass sample. *b*) The volume fraction is calculated as a function of the orthogonal beam direction $y$ inverting Eq.(5.1). The average value is indicated by the full-red line. *Figure adapted from [76].*

Fig.(5.1 *a*) shows an example of a transmission measurement, performed scanning the sample in the $y$ direction across the X-ray beam. The shape of the sample (a cylinder), determines the measured profile. Note that the diameter of the capillary is $W \sim 360\,\mu$m, notwithstanding the nominal value is 0.5 mm. Fig.(5.1 *b*) shows the obtained volume fraction, $\varphi$, utilizing Eq.(5.1) to model the transmitted intensity. Noticeably, $\varphi$ is constant along the whole capillary, indicating that the sample is homogeneous. The mean value can be calculated by averaging over the points inside the capillary, leading to $\varphi = (37.65 \pm 0.11)\%$. Considering the uncertainties on the the parameters of Eq.(5.1) we estimate an error of 0.2% on the absolute volume fraction. The major contribution comes from the uncertainty in the capillary wall thickness since the value declared by the producer (10 µm) was observed to fluctuate by a few microns for different capillaries. For this reason, the wall thickness is considered as a free parameter in the fitting of the absorption profile, see Fig.(5.1 *a*).
Before discussing the details of the dynamical properties of the colloidal glass, we will describe a little bit the structural aspects. In the small angle geometry, the detector is orthogonal to the direction of propagation of the beam. For this reason, each ring on the detector (centered at the transmitted beam position) corresponds to a given exchanged wave-vector $q$ (in modulus). We recall

Eq.(3.20), from which the scattered intensity can be written as $I(q) \propto S(q)P(q)$. The visibility of the particles with respect to the solvent is given by the difference in electron density between the two. The form factor can be measured directly if the structure factor contribution is negligible, that is $S(q) = 1$. This is achieved reducing the volume fraction of the sample, in the present case we have chosen $\varphi < 0.001$. The experimental data are reported in Fig.(5.2 *a*). Comparing the experimental results with the theoretical curve calculated in Fig.(3.2) we notice that, while we would expect sharp minima, a smoother dependence is observed experimentally. This effect has to be attributed to the polydispersivity of the particles: we can take this into account convolving Eq.(3.23) with the particle size distribution, which is well captured by the Schultz distribution [139]

$$f_z(r) = \frac{1}{z!}[z + 1/\bar{r}]^{z+1} r^z \exp\left[-(z+1)r/\bar{r}\right] \tag{5.2}$$

with $\bar{r}$ the average radius of the particles and $z$ a function of the second moment of the distribution, that is $\Delta r^2 = \bar{r}^2/(z+1)$.

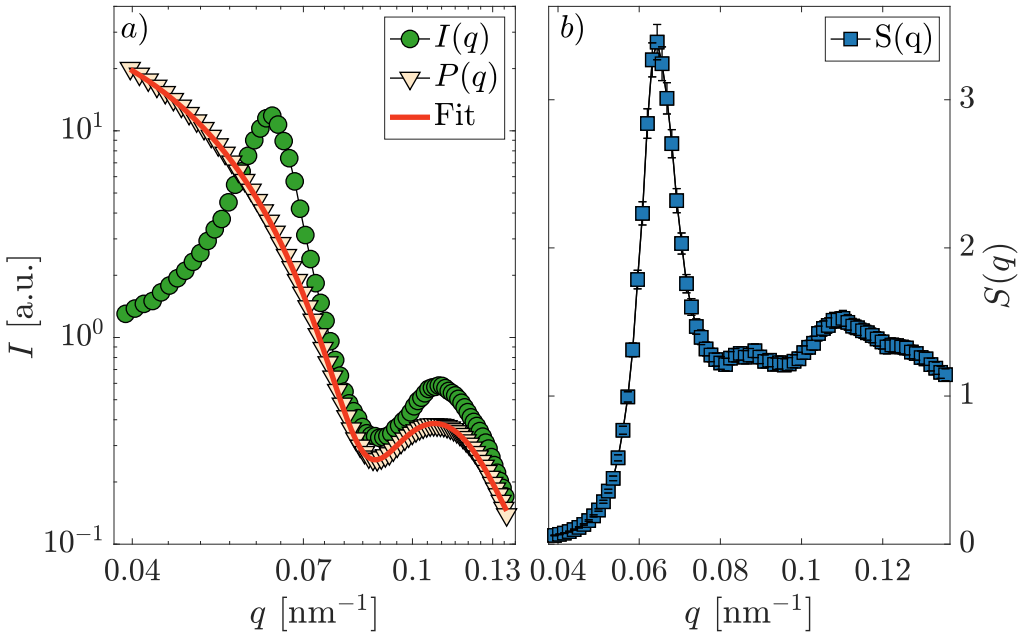


Figure 5.2: *a*) Scattered intensity for two relevant colloidal suspensions: white points correspond to a dilute sample ($\varphi < 0.001$) while green ones to the sample discussed in the main text, with $\varphi = (37.65 \pm 0.11)\%$. The red-continuous line is the best fit of Eq.(3.23) to the data taking into account the polydispersivity, Eq.(5.2). *b*) Static structure factor for the sample with $\varphi = (37.65 \pm 0.11)\%$, calculated as $I(q)/P(q)$. *Figure adapted from [76].*

The best fit to the experimental data with the polydispersed model is reported as a red continuous line in Fig.(5.2 *a*). The resulting parameters are an average radius of $\bar{r} = (50.8 \pm 0.3)\,\text{nm}$ and a polydispersivity of $\frac{\Delta r}{\bar{r}} = (9.4 \pm 0.6)\%$,

within the specifications reported by the producer.
Increasing the volume fraction of nanoparticles with respect to the solvent, the structure factor starts to play a role, an effect that is clearly visible for the solution at $\varphi \sim 37\%$, green dots in Fig.(5.2 *a*). The structure factor can be calculated experimentally as $I(q)/P(q)$, after background subtractions due to the solvent and capillary scattering [45] and is reported in Fig.(5.2 *b*).
The interaction between the particles could be modeled with a screened Coulomb potential plus a hard sphere contribution, which is known as Derjaguin-Landau-Verwey-Overbeek (DLVO) pair potential [140], and the structure factor could be calculated in the mean spherical approximation closure [141]. This approach has been followed in previous experiments, where the lower polydispersity of the particles lead to satisfactory results [129, 142]. The polydispersity should nonetheless be taken into account, for example as reported in [143]. Despite a simple DLVO interaction can be used to model the low temperature repulsive potential [129, 142], recent studies included a temperature-dependence interaction with a square well [137] and more complex long-range terms [144], finding good agreement with the experimental data in a wide temperature range. We avoid however to enter in this discussion here: the experimental structure factor will be used in the following only to show that the structural properties of our colloidal glass are isotropic.

### 5.1.3 Anisotropic compressed relaxations

The small angle scattering geometry offers the possibility to investigate the relevant properties of the system (both structural and dynamical) as a function of the vector **q**. As already mentioned, in SAXS a given $q$ value corresponds to a ring on the detector, see the inset of Fig.(5.3) for an experimental pattern. One can also select different sections of the detector, for example horizontal and vertical ones, and calculate the properties in that reduced regions of interest (ROIs). For instance, in Fig.(5.3) we report the structure factor calculated along the vertical (green) and horizontal (yellow) directions. The two curves perfectly overlap, a clear signature that the structure is isotropic, as expected for a glassy system.
The same considerations are valid for the dynamical properties. A ROI of pixels corresponding to the same $q$ can be selected and the intensity auto-correlation function fitted with a KWW function [48], Eq.(4.2). An example of such procedure is reported in Fig.(5.4 *a*), where the $g_2$ is calculated for $q = (11 \pm 1) \times 10^{-2}\,\mathrm{nm}^{-1}$ over the whole scattering ring (see insert). The KWW fit returns a stretching parameter of $\beta = 1.61 \pm 0.14$, but is not able to capture the long stretched tail of the correlation function. This effect has been sometimes reported in literature where the dynamics is strongly non-diffusive and dominated by stresses, see for example [145, 146], but its origin is still debated. Here, on the other hand, the stretched tail originates from geometrical aspects.

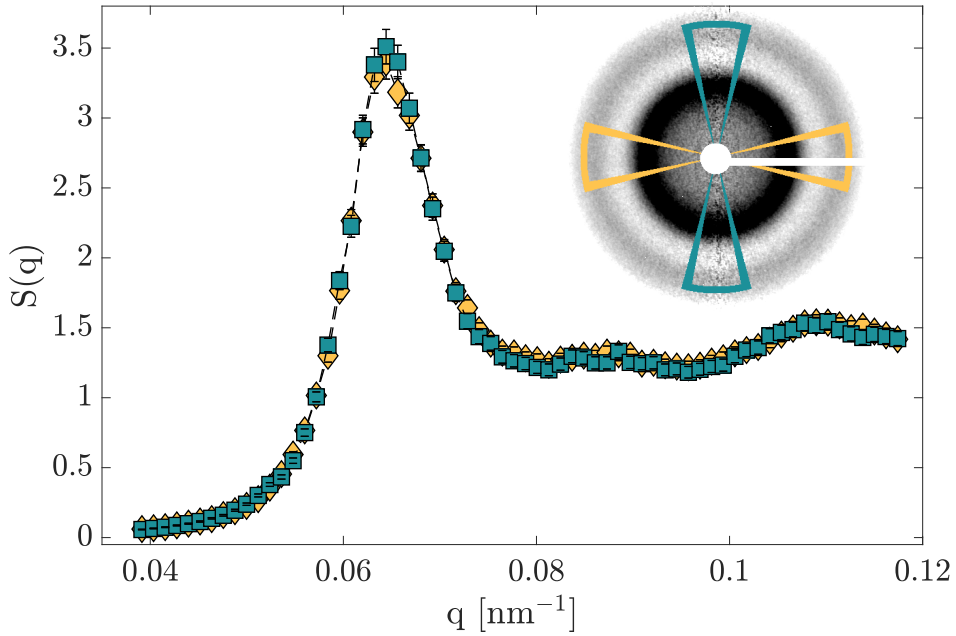


Figure 5.3: Structure factor calculated along the vertical (green squares) and horizontal (yellow diamonds) directions. The inset reports an experimental SAXS pattern, with the beam stopper clearly visible to mask the direct beam. The regions considered for the extraction of the $S(q)$ have been highlighted with the respective colors and correspond to an azimuthal angular range $\Delta\phi = \pi/6$. *Figure adapted from [76].*

In Fig.(5.4 *b*) the autocorrelation functions are calculated considering horizontal and vertical sectors, as already done for the structure factor $S(q)$. In this case the dynamics is strongly anisotropic, with relaxation times much faster in the horizontal direction. Averaging over the whole diffraction ring leads then to a convolution of the decay function with the distribution of relaxation times.

### 5.1.4 Stress dynamics and the stress-induced velocity field

In order to make a step further, we define the exchanged wave-vector utilizing the azimuthal angle $\phi$. Calling the horizontal direction $\hat{y}$ and the vertical one $\hat{z}$ (we keep here the convention adopted for the transmission measurements reported in the previous section), the exchanged wave-vector can be written as

$$\mathbf{q} = q[\hat{y}\cos\phi + \hat{z}\sin\phi] \tag{5.3}$$

For a graphical illustration of the azimuthal angle, see the inset in Fig.(5.4 *a*). The autocorrelation functions can then be calculated selecting an annular region within a given angular aperture, called $\Delta\phi$. Fig.(5.5) shows the normalized $g_2$

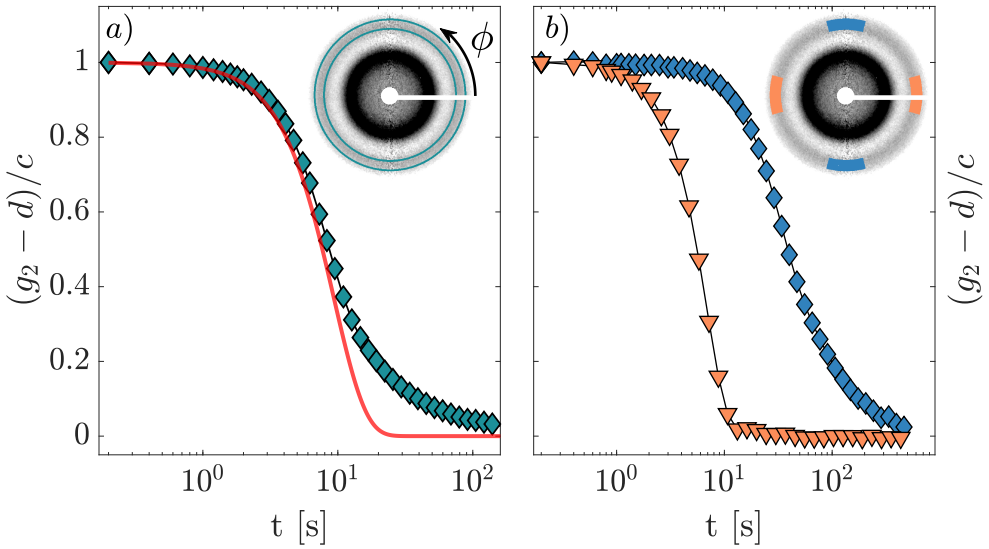


Figure 5.4: *a*) Autocorrelation function calculated for $q = (11 \pm 1) \times 10^{-2}\,\mathrm{nm}^{-1}$ over the whole scattering ring (insert). The azimuthal angle is reported, with the 0 fixed in the horizontal direction. *b*) The autocorrelation functions have been calculated for the horizontal (orange points) and vertical (blue points) ranges. A strong anisotropy is present, causing the stretching of the curve reported in *a*). *Figure adapted and redrawn from [76].*

for a selection of azimuthal angles (reported in the legend), computed within a range $\Delta\phi = \pi/16$. The relaxation time increases in a monotonic way starting from $\phi = 0$ up to the vertical direction, $\phi = \pi/2$.
The fits of the KWW function to the curves, as in the example shown in Fig.(5.5) as red-dashed line, now capture satisfactorily the whole relaxation. Note that the stretching parameter is now very close to the Gaussian value, $\beta = 2$. The set of inverse relaxation times as a function of the azimuthal angle is reported in Fig.(5.6 *a*).
The data correspond to a single exchanged wave-vector value, $q = (12.0 \pm 0.3) \times 10^{-2}\,\mathrm{nm}^{-1}$, and have been computed with $\Delta\phi = \pi/16$. The distribution of $1/\tau$ is almost a perfect cosine of the angle $\phi$. Going back to Eq.(5.3), it can easily be observed that this effect can be accounted by a scalar product between the $\mathbf{q}$ and a horizontal vector field, let us call it $\delta\mathbf{v} = \delta v\hat{y}$. Furthermore, the dimensions of the involved quantity clarify that the field $\delta\mathbf{v}$ is a velocity. The obtained modulus for the field is $\delta v = (0.97 \pm 0.03)\,\mathrm{nm/s}$ and is dictated by the release of stresses, as we will see soon, which in turn induce the particles' displacements.
The observed effect can be compared to the one investigated in shear flow studies, see for example [147]. The intermediate scattering function can be factorized as

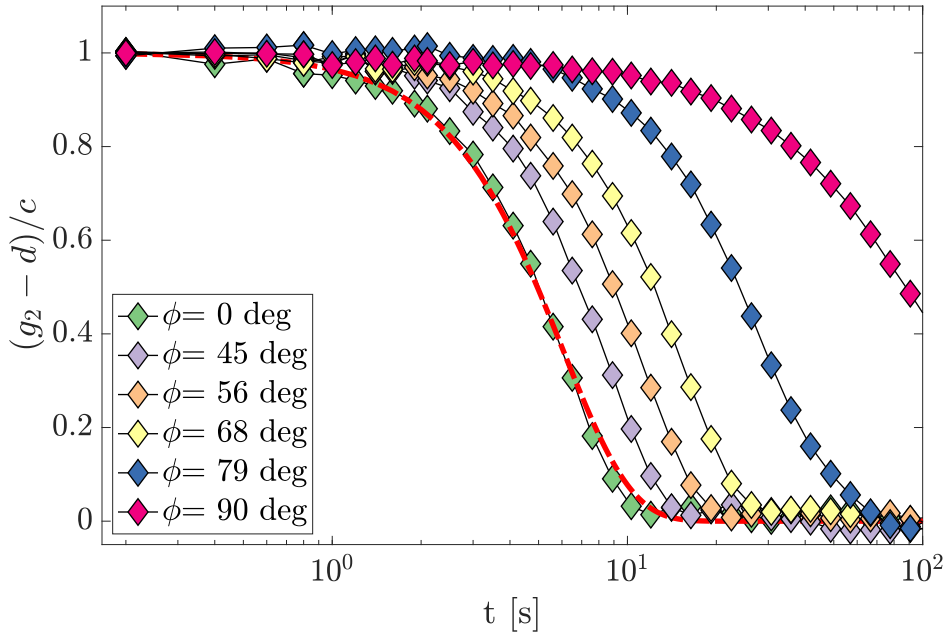


Figure 5.5: Autocorrelation functions calculated for different azimuthal angles with $\Delta\phi = \pi/16$ and at $q = 0.12\,\mathrm{nm}^{-1}$. The dynamics is faster in the horizontal direction (leftmost curve) with a monotonic slowing down with increasing angle. An example of KWW fit is reported as red-dashed line, leading a $\beta \sim 2$. *Figure adapted from [76].*

$$\begin{aligned} F(\mathbf{q},t) &\sim \exp[-i\mathbf{q}\cdot(\mathbf{r}_j(0) - \mathbf{r}_k(t))] \\ &\sim \exp[-i\mathbf{q}\cdot(\mathbf{r}^d_j(0) - \mathbf{r}^d_k(t))] \times \exp[i\mathbf{q}\cdot\langle\mathbf{v}\rangle t] \times \exp[i\mathbf{q}\cdot\delta\mathbf{v}t] \end{aligned} \tag{5.4}$$

Here we omitted for clarity the double sum over the particles $j, k$; the displacement of the two considered particles can be split if we assume the presence of a velocity field $\mathbf{v}$. Indeed, in the second row of the equation above the first term represents the intrinsic displacement of the particles (it could be, for example, diffusive-like), the second term is the displacement due to common flow of both particles, with $\langle\mathbf{v}\rangle$ being the average drift velocity. Finally, the third term accounts for the flow difference between the two particles, which we defined as $\delta\mathbf{v} = \delta\mathbf{v}_{j,k}$.

In a homodyne experiment the square modulus of $F(\mathbf{q},t)$ is measured. For this reason, the term due to the average velocity $\langle\mathbf{v}\rangle$ cancels out. We should note, however, that it can play a role as the scattering volume is "replaced" over time: the typical time of the process would be given by the ratio of the beam size ($h$) with the average velocity, $\tau_V \sim h/|\langle\mathbf{v}\rangle|$. For the simplest case of a Gaussian beam profile it introduces a contribution in the $g_2$ function of the type $\sim \exp[-(t/\tau_V)^2]$ [147]. If that would be the case for our sample, we should observe a variation of the volume fraction in the scattering volume (a

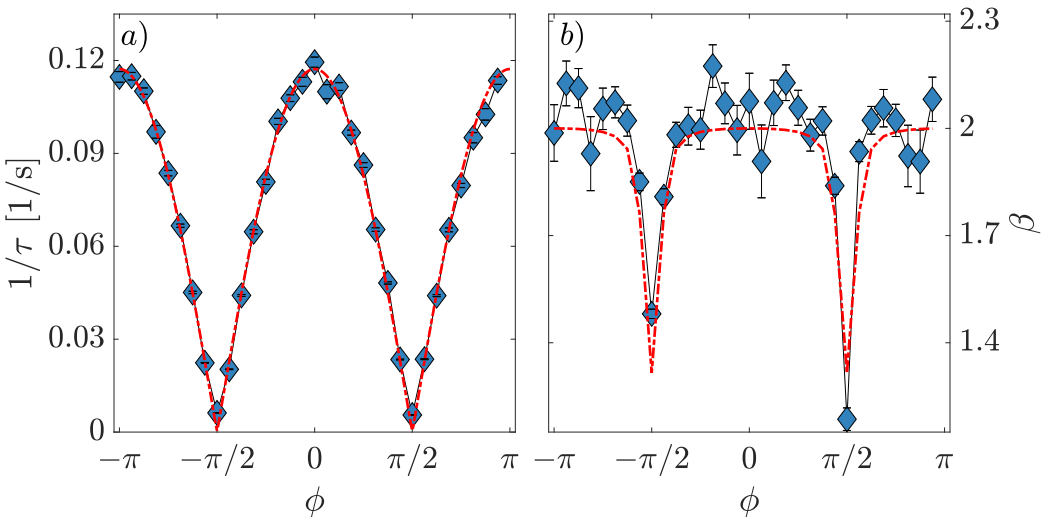


Figure 5.6: *a*) Relaxation time calculated at $q = (12.0 \pm 0.3) \times 10^{-2}\,\mathrm{nm}^{-1}$ for different azimuthal angles. The red line corresponds to a fit with $1/\tau = |q\delta v \cos(\phi)|$, leading to $\delta v = (0.97 \pm 0.03)\,\mathrm{nm/s}$. *b*) Shape parameter as a function of $\phi$ calculated at the same exchanged wave-vector reported in *a*). The drop in the value for $\phi \approx \pm\pi/2$ is an artifact due to the finite $q$-resolution. The red dashed line is obtained fitting with a KWW ansatz the function $\exp[-2(q\delta v t \cos(\phi))^2]$ convoluted with the experimental resolution in $\phi$. *Figure adapted from [76].*

net particle flow must be present pointing towards the center or the walls of the capillary). This, however, is not observed, see Fig.(5.1). Most importantly, this finite-volume contribution should be independent of the exchanged wave-vector as it is dictated only by the time needed to replace the scattering volume with new material. We can thus rule out that the glassy sample reported here experiences this effect.

The cause of the dynamics here observed must then be looked for in the third term of Eq.(5.4). The contribution of the relative velocity field can be calculated by summing over every pair of particles in the scattering volume. A classical configuration encountered in flow experiments is the Couette flow, for which the analytical integration leads to a term in the $g_2$ proportional to a sinc-like decay [147]. In general, the shape of the corresponding intensity autocorrelation function (neglecting diffusion), is dictated by the distribution of the relative velocity field [148]. In fact it is clear that the intermediate scattering function can be written as [148]

$$F(\mathbf{q}, t) = \int d[\delta\mathbf{v}] f(\delta\mathbf{v}) \exp[it\mathbf{q} \cdot \delta\mathbf{v}] \tag{5.5}$$

with $f(\delta\mathbf{v})$ the distribution of the relative velocity. Working out the equation in spherical coordinates and reducing the vector notation to a scalar one for isotropic systems, one can link the shape of the intermediate scattering function ($\sim \exp[-(t/\tau)^\beta]$) $\beta$ to a Levy distribution $\mathcal{L}_{\beta,0}(z)$ [148, 149]

$$\mathcal{L}_{\beta,0}(z) = \frac{1}{2\pi}\int_{-\infty}^{\infty} dk e^{ikz} e^{-C|k|^{\beta}} \tag{5.6}$$

where $C$ is a normalization parameter. Comparing Eq.(5.5) and Eq.(5.6) it is clear that the Levy distribution is related to the velocity distribution. In particular, the asymptotic behavior of $\mathcal{L}_{\beta,0}(z)$ is $\sim z^{-(\beta+1)}$ for $0 < \beta < 2$ [149], which is equal to the asymptotic behavior of the isotropic relative velocity distribution, $f_{iso}(v)$, given by [148]

$$f_{iso}(v) = -\frac{2v}{\langle v\rangle}\frac{d}{dv}\mathcal{L}_{\beta,0}\left(\frac{v}{\langle v\rangle}\right) \underset{v\to\infty}{\Longrightarrow} \sim v^{-(\beta+1)} \tag{5.7}$$

In consideration of the fact that the stretching (in this case *compressing*) parameter is dictated by the distribution of the relative particle velocities, regardless of the microscopic mechanism giving rise to this distribution, it is not surprising that different stretching exponents are reported in literature. For example, in gels and colloidal systems near the jamming transition a value of $\beta = 1.5$ is often observed (corresponding to a $v^{-2.5}$ asymptotic decay of the velocity distribution) [5, 148, 150, 151], with a physical interpretation, supported by numerical simulations, in terms of micro-collapses of the gel's network [5, 152]. On the other hand, a Gaussian distribution of particles' velocities would lead to $\beta = 2$. In Fig.(5.6 *b*) the stretching parameter calculated as a function of the azimuthal angle $\phi$ is shown. In the horizontal sectors $\beta = 2.05 \pm 0.05$, confirming that in our colloidal glass the distribution of relative particles velocity is almost Gaussian. Note that the drop of $\beta$ in the proximity of the vertical directions is an artifact due to the finite $q$-resolution. A simple numerical model, taking this into account, is shown as a red-dashed line, and confirms this conclusion. Finally, we note that the first term in Eq.(5.4), related to the intrinsic dynamics, cannot play a role here. The almost pure cosine behavior of the inverse relaxation time, Fig.(5.6 *a*), clearly indicates that the dynamics is governed by the velocity field distribution.

From the considerations made so far, it is clear that our glass exhibits a peculiar symmetry break which is usually not observed in similar systems. While in flow experiment the (anisotropic) velocity field is due to a macroscopic, externally induced, flow of the sample, here the field must originate from an internal mechanism. As proposed for colloidal gels [5], it must be related to the release of the stresses stored in the sample. In the present case, they are a leftover of the preparation procedure: the centrifugation performed in order to fill the sample inside the capillary induces stresses in the network. Those stored in the vertical direction have time to relax between the centrifugation phase and the measurements, while the stress field in the horizontal direction is not able to relax macroscopically as it is constrained by the capillary walls [76]. For this reason, the observed dynamics are confined to the horizontal plane.

Regardless of the exact details of the mechanism leading to the anisotropic stress (and, consequently, velocity) field, we want to investigate in more depth the dynamical properties of these compressed dynamics. In particular, the

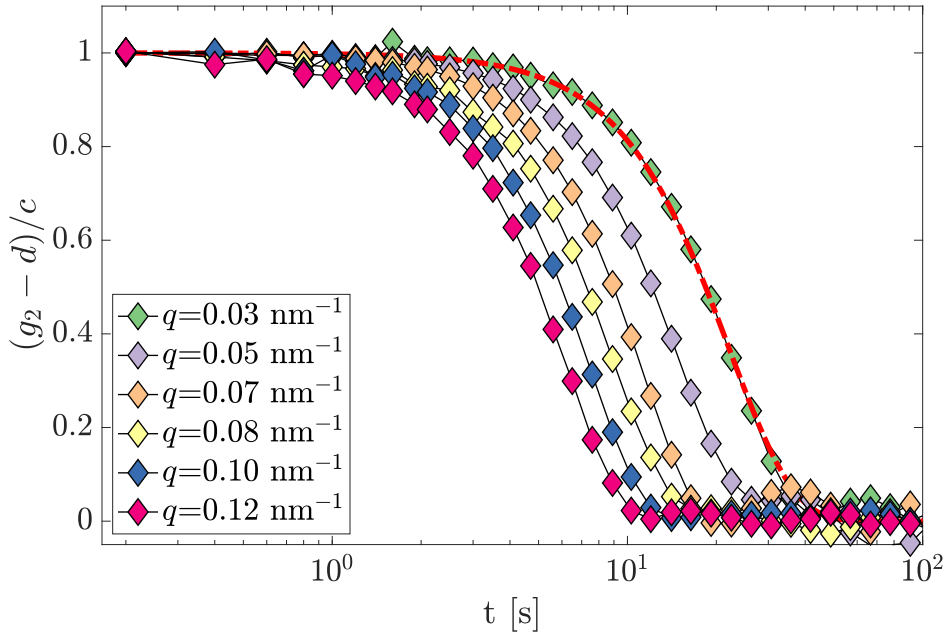


Figure 5.7: Autocorrelation functions calculated for different exchanged wave vectors for horizontal sectors, $\Delta\phi = \pi/16$. *Figure adapted from [76].*

$q$-dependence of the relaxation time and the stretching parameters give valuable information on the process. Fig.(5.7) shows a set of correlation functions corresponding to the horizontal sectors ($\Delta\phi = \pi/16$) as a function of the exchanged wave-vector.
The inverse relaxation time, reported in Fig.(5.8 *a*), scales as $1/\tau = |\mathbf{q} \cdot \delta\mathbf{v}|$, with $\delta v = (0.99 \pm 0.02)\,\mathrm{nm/s}$, consistent with the previously reported value. Furthermore, the stretching parameter is constant in the whole probed range, Fig.(5.8 *b*), leading to an average value of $\beta = 2.04 \pm 0.02$.
Note that compressed correlation functions are usually accompanied by a ballistic-like dynamics ($\sim 1/q$), in the spirit of the equations previously mentioned. This is observed in many soft system [5, 74, 75, 145, 148, 150, 151, 153] and the overall picture was recently enriched by simulation results [152, 154] and new studies on both gels and colloidal glasses [76, 155], as the one discussed here and recently published [76]. We will show in the last chapter of this thesis that ballistic dynamics together with compressed correlation functions are observed in structural glasses too, and are again attributed to the relaxation of stresses.
We conclude this discussion by bringing attention to the $q$-dependence of Fig.(5.8 *a*). The observed dynamics are dictated by a velocity field over the whole range of probed length-scales, up to at least few particle distances (the smallest $q$ reported is indeed $q \simeq 0.03\,\mathrm{nm}^{-1}$). We will tackle this aspect in the next section, where we will show that the dynamics proceeds with cooperative rearrangements of few-thousands of particles.

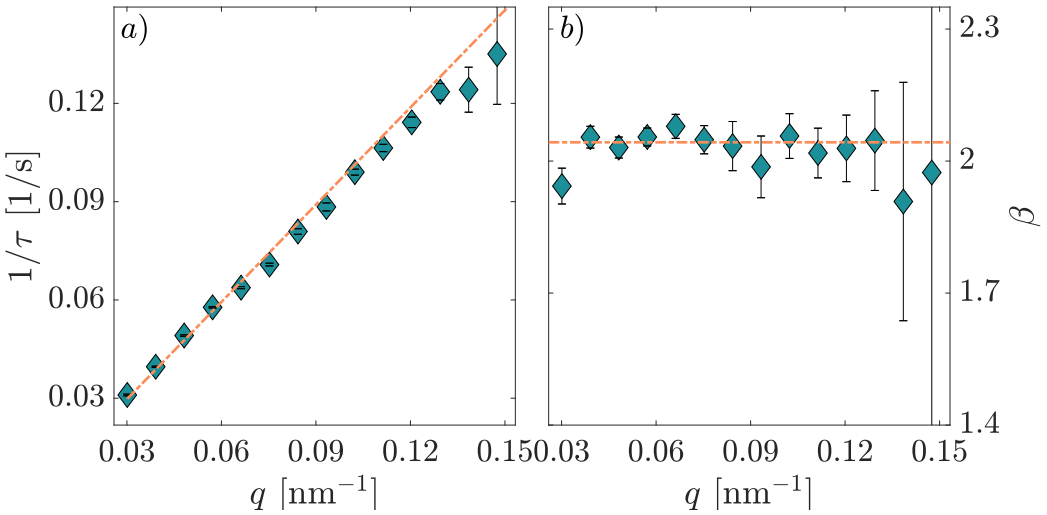


Figure 5.8: *a)* Inverse relaxation time as a function of the exchanged wave-vector $q$ for the horizontal sectors, $\Delta\phi = \pi/16$. The orange dashed line is a linear fit to the data: $1/\tau = |\mathbf{q} \cdot \delta\mathbf{v}|$. *b)* Stretching parameter as a function of $q$. The average value of $\beta = 2.04 \pm 0.02$ is reported as the orange dashed line. *Figure adapted from [76].*

### 5.1.5 Dynamical heterogeneities: the cooperative nature of the stress relaxation

In the last part of Ch.(2) we discussed the four-point susceptibility, $\chi_4(q,t)$, and its relation to the cooperativity of the dynamics. We introduced how the visibility of this observable is related to the dimension of the scattering volume, or to the number $N$ of elemental particles in it. In order to measure a $\chi_4(q,t)$ we require a limited number of correlated regions in the scattering volume, so that we can effectively probe the fluctuations of the dynamics. The visibility of $\chi_4(q,t)$ will be proportional to $1/N$, following the central limit theorem. In the present XPCS experiments the scattering volume is determined by the spot size (here $2 \times 3\,\mu m^2$ FWHM) and the thickness of the sample, $W \simeq 360\,\mu m$ and, with the considered volume fraction of $\varphi \sim 37\%$, we have $N = (1.6 \pm 0.3) \times 10^6$ [76]. Although the number of particles in the scattering volume is considerable, $\chi_4(q,t)$ is still observable. This can be visually appreciated directly from the two time correlation function, as the one reported in the inset of Fig.(5.9). The signatures of the dynamical heterogeneities are fluctuations in the typical relaxation time of the correlation function, which can be seen as "blobs" or "bubbles". Calculating the variance of each diagonal of the two-times matrix one can build the complete time evolution of the $\chi_4(q,t)$, see Fig.(5.9).
A reliable estimation of the value of the $\chi_4(q,t)$ requires the extrapolation scheme proposed in [92] and discussed in Ch.(3). The extrapolation works through different steps: first of all, the considered ROI (defined by the azimuthal angle $\phi$ and exchanged wave-vector $q$) is divided in subsets. For each of these subsets, the variance of the autocorrelation ($\sigma^2_{g_2}$) is calculated. An example of

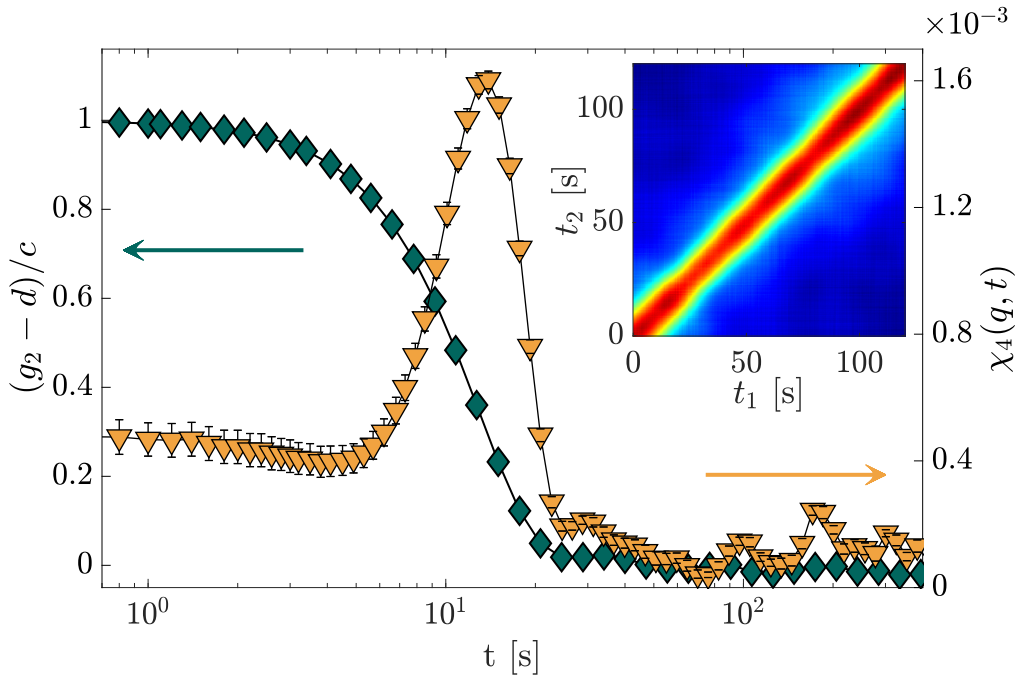


Figure 5.9: Autocorrelation function (green points) together with the $\chi_4(q,t)$ (yellow points), calculated at the peak of the structure factor, $q = q_{max} = (6.4 \pm 0.3) \times 10^{-2}\,\mathrm{nm}^{-1}$ and considering horizontal sectors with $\Delta\phi = \pm\pi/4$. The inset shows a portion of the corresponding two time correlation function from which the main curves are extracted. *Figure adapted from [76].*

the obtained curves is shown in Fig.(5.10) for a variable number of pixels $N_{px}$, from 215 up to 1615.
For each time $t_i$ the obtained points are reported as a function of $1/N_{px}$ and a linear fit is performed. The intercept of the curve is the value of the $\chi_4(q,t_i)$ in the limit of an infinite number of pixels, then it is the best estimator of the real value of the four-point susceptibility. The extrapolated curve shown in Fig.(5.10) as blue diamonds shows a much more defined peak with respect to the ones obtained with a finite-ensemble of pixels. The extrapolation scheme is therefore essential for capturing the real fluctuations in the dynamical properties.
As already discussed, the $\chi_4(q,t)$ is expected to exhibit a peak in the time domain. This is mainly due to the fact that the motion of a particle is correlated with the neighbors for a typical time in the order of the relaxation time: such peak is clearly visible in Fig.(5.9). On the other hand, a similar peak-shaped dependence is expected as a function of the exchanged wave-vector. At large distances (small $q$s), the particles are so far-away that they weakly interact and their motion is uncorrelated. At high $q$s the contribution of the collective dynamics starts to vanish, and one expects here too a weak correlation in the motion. At intermediate $q$ values the dynamics finds the maximum of its correlation, since a particle moves in "phase" with the neighbors.
In Fig.(5.11 *b*) the maximum values of the $\chi_4(q,t)$ have been reported as a

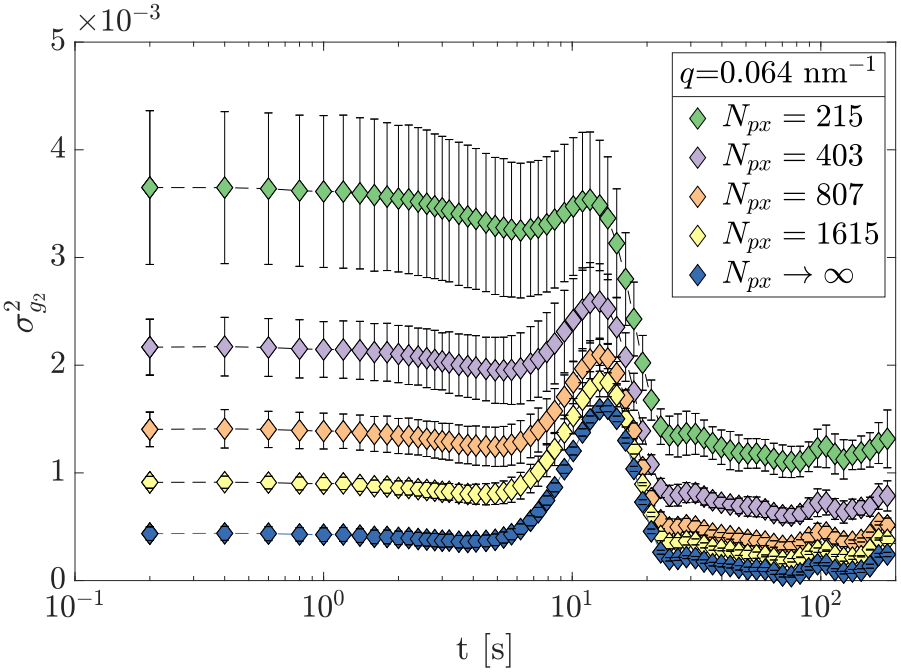


Figure 5.10: Sequence of the variance of the autocorrelation function $\sigma^2_{g_2}(N_{px}, t)$ calculated at $q_{max} = (6.4 \pm 0.3) \times 10^{-2}\,\mathrm{nm}^{-1}$ and for different $N_{px}$ values. The extrapolated $\chi_4(q_{max}, t)$ for $N_{px} \to \infty$ is reported as blue diamonds. *Figure adapted from [76].*

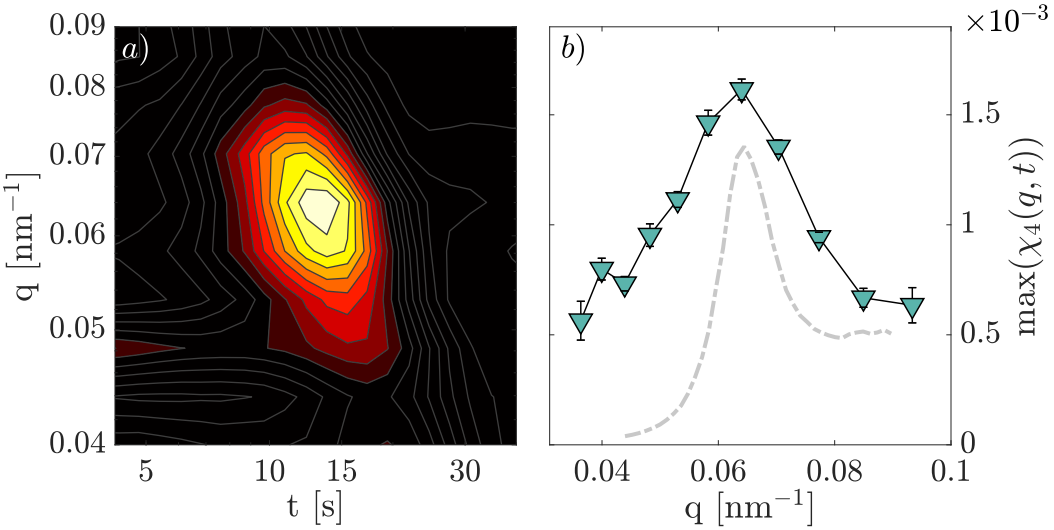


Figure 5.11: *a*) Map of the $\chi_4(q, t)$ as a function of the exchanged wave-vector $q$ and time $t$. *b*) Maximum value of the $\chi_4(q, t)$ as a function of $q$. Gray-dashed line is the structure factor (opportunely scaled). *Figure adapted from [76].*

function of $q$ together with the structure factor (opportunely scaled, gray-dashed line). The time-length scale of the dynamical heterogeneities is better appreciated in a map as the one reported in Fig.(5.11 *a*). The $\chi_4(q, t)$ is

characterized by a single, broad peak centered at $q \simeq q_{max}$ and time $t \sim \tau$. Note that the peak at $q_{max}$ is a symptom that the maximum of dynamical correlation is observed over distances corresponding to the nearest neighbor shell of particles. This is different with respect to the observations reported for the bi-dimensional version of this glass [58]: there the authors report that the maximum of the $\chi_4(q,t)$ is located at distances much smaller than the average neighbor distance. However, in that case they were investigating spontaneous, near equilibrium dynamics while we are focusing on stress-driven dynamics. Note that our results are in good agreement with the observations made on colloidal gels [75] where the dynamics is dominated by stress-related phenomena, but we also find an interesting similarity with the results of theoretical studies on super-cooled liquids [156].
The peak value of the four-point susceptibility can be normalized for the squared experimental contrast (measured with a xerogel) and multiplied for the total number of particles in the scattering volume: the procedure leads to an estimation of the number of particles dynamically correlated $N_{corr}$. Note that a $q$-dependent pre-factor should be introduced in order to correctly account for $N_{corr}$ [75]. Despite that, this rough estimate leads to $N_{corr} \approx 10^4$ particles, which correspond to regions of $\approx 2\,\mu m$ in size. In this last step we made the strong assumption that the fractal dimension of the dynamical correlated regions is 3. However, in the bi-dimensional version of our glass, string-like dynamical heterogeneities were observed [58]. Notwithstanding that, this coarse calculation captures the typical length-scale of the regions that relax upon the stress release, which is much larger than the inter-particle distance and is in the order of the µm.

## 5.2 Oxide glasses probed with XPCS

In the second part of this chapter we want to tackle the problem of the X-ray induced relaxation in oxide glasses. It is clear that, since a glass is intrinsically out of equilibrium, some stresses must be frozen in during the cooling process. We have already seen the extreme case of colloidal glasses where the dynamics can be completely driven by the stress release process. One can expect a similar behavior in structural glasses, where the faster the quench, the higher the quantity of stresses trapped in the network. These hypotheses have been recently confirmed for the case of metallic glasses studied with XPCS [3, 4], where well-below the glass transition temperature fast compressed ($\beta > 1$) relaxation functions are a clear symptom of stress-related dynamics.
A similar, but intrinsically different, phenomenon was soon observed in oxide glasses where deep in the glassy state fast relaxations were measured [7–9]. In these systems, however, the dynamics are characterized by a relaxation time which scales inversely to the incident flux: it is thus not an internal mechanism that triggers the density rearrangements but the incident X-ray beam, which induces a relaxation in the glass much faster than the one expected for the equilibrium system, simultaneously pumping and probing the atomic motion. Interestingly, this effect corresponds to the fact that X-rays locally "fluidize" the glass through probably radiolysis, as proposed in [8], and each absorbed photon gives rise, in average, to a "liquid-like spur" with a length-scale of few nanometers [9, 104]. Incidentally, this nm length-scale is the same over which the cooperative motions of the spontaneous glassy dynamics takes place but the interplay between these two processes is yet under investigation. This *beam-induced dynamics* has been observed in different systems, ranging from silicates [7, 8], germanates [8] and borates [9, 109, 110]. XPCS experiments have reported different stretching exponents for different glasses: silica shows compressed correlation functions while borates stretched ones. We will show in the next chapter of this thesis that in borates compressed correlation functions can be observed too, as long as the absorbed dose is kept below a given, sample dependent, threshold. We anticipate here that the relaxation time does not change considerably as a function of the absorbed dose (at least up to the doses considered in this chapter), thus the considerations carried out in the next sections are still valid despite the dose is such that $\beta \leq 1$.

### 5.2.1 The preparation of boron-oxide glass

We have already explained the sample preparation of borate glasses in Ch.(4), where we have discussed the near-equilibrium dynamics of liquid $LiBO_2$. While the preparation protocol is very very similar to that of alkali-based glasses [104, 157], a slightly different approach has been followed for pure boron oxide. The extremely high hygroscopicity of this sample requires particular attention in order to avoid any water contamination since a small amount of water trapped in the glassy network is known to change the glass transition temperature $T_g$

by many tens of degrees [158].
In order to prepare a boron oxide glass, the starting material was boron oxide powder (99%-purity) purchased from Sigma-Aldrich. A few grams of powder were dried in a furnace at 150°C in an aluminum oxide crucible for 24 hours. Then the temperature was raised to 1000°C for 4 days, in order to remove as much water contamination as possible. The glassy samples were produced as 1 mm thick slabs quenching the melt between steel plates previously heated at 200°C. The obtained samples were cut in small disks (5 mm in diameter) and polished with silicon-carbide sandpaper down to the desired thickness ($\sim 100\,\mu$m). In this last step, pure ethanol was used as a lubricant to avoid sample contamination caused by the ambient humidity.

### 5.2.2 The X-ray flux-dependent relaxation

As anticipated, in XPCS experiments on oxide glasses the measured dynamics in the glassy state is faster the higher the incident flux. To be precise, the relaxation time is related to the absorbed number of X-ray photons [9]

$$\tau \propto \frac{1}{F_0[1 - e^{-\mu W}]} \tag{5.8}$$

where $F_0$ is the incident flux, $W$ the sample thickness and $\mu$ the attenuation coefficient. Eq.(5.8) has been verified in many experiments [8, 9, 109, 159] on different families of glasses and it is an accepted signature of the beam-induced dynamics.
Recently, this flux-dependence of the relaxation time has been additionally verified in an experiment at beamline ID10 of the ESRF on a $B_2O_3$ glass [110]. XPCS measurements were performed on the peak of the scattered intensity (which corresponds to the peak of the structure factor) at a scattering vector $q = (15.2 \pm 0.2)\,\mathrm{nm}^{-1}$, as highlighted in green in Fig.(5.12 *a*). Sequences of up to $10^4$ images were collected with an EIGER 500K detector placed at a distance D=4.1 m from the sample in order to match the speckle size with the pixel size (see Sect.(3.6) for further experimental details). The sample was moved by 20 µm after each run in order to avoid beam damage [9]. The incident beam intensity modifies the relaxation time (see Eq.(5.8)) but not the shape parameter. This can be observed in Fig.(5.12 *b*), where the intensity autocorrelation functions are shown for two different incident fluxes: $F_0 = 11 \times 10^{10}$ ph/s and $F_1 = 3.5 \times 10^{10}$ ph/s at the energy of 8.1 keV [110]. The time has been rescaled using the relaxation time $\tau$ of the fitted KWW function [48], here reported again for clarity

$$g_2(t) = c\exp[-2(t/\tau)^{\beta}] + d \tag{5.9}$$

where we include the experimental contrast $c$ and an additional baseline $d$, as discussed in Sect.(3.3). The ratio between the relaxation times of the curves shown in Fig.(5.12 *b*) is $3.0 \pm 0.2$, compatible with the expected one of $F_0/F_1 = 3.1$ [110]. Furthermore, it should be pointed out that the stretching

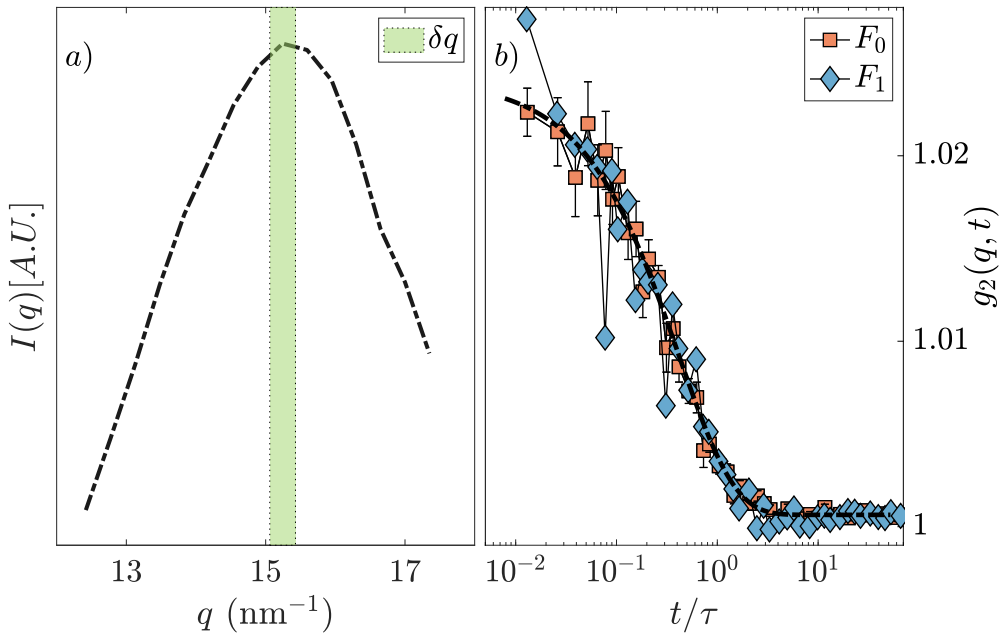


Figure 5.12: a) Scattered intensity in arbitrary units as a function of the exchanged wave-vector $q$ for the $B_2O_3$ glass. The green box indicates the $\delta q$ covered by the detector at the ID10 beamline of the ESRF. *b)* Autocorrelation functions measured at T=563 K for two different incident photon fluxes ($F_0 = 3.1F_1$).The curves are averages of 20 scans of $10^4$ images each with integration time of 50 ms. The time axes have been rescaled for the relaxation time and the KWW best fit is reported as a black dashed line. Error bars are calculated as the standard deviation of the different measurements and reported only for the $F_0$ data (orange squares) for the sake of clarity. *Figure adapted from [110].*

parameter $\beta$ does not change upon changing the incident flux: the two rescaled autocorrelation functions indeed overlap. This feature is crucial since it is related to the fact that the dynamics must be intrinsic to the absorption of a photon and not to the average power delivered by the beam. It is then natural to expect that each absorbed photon, on average, "fluidizes" a given number of atoms (or atomic units) on a length-scale $1/q$.
We can rationalize these ideas in a plot like the one shown in Fig.(5.13). There, the relaxation time has been displayed as a function of the average incident flux. The green points correspond to the autocorrelation functions shown in Fig.(5.12 *b*). The violet diamonds are the data reported in [9] and collected at different temperatures but with the same photon energy (8.1keV) and beam size ($10 \times 8\,\mu m^2$ H $\times$ V FWHM). The average beam flux coincides with the incident flux for the green data, while for the violet diamonds it is calculated correcting for the read-out time of the CCD detector, since the shutter was open only during acquisition and not during read-out [9].
It is clear from the data that the typical relaxation time is inversely proportional

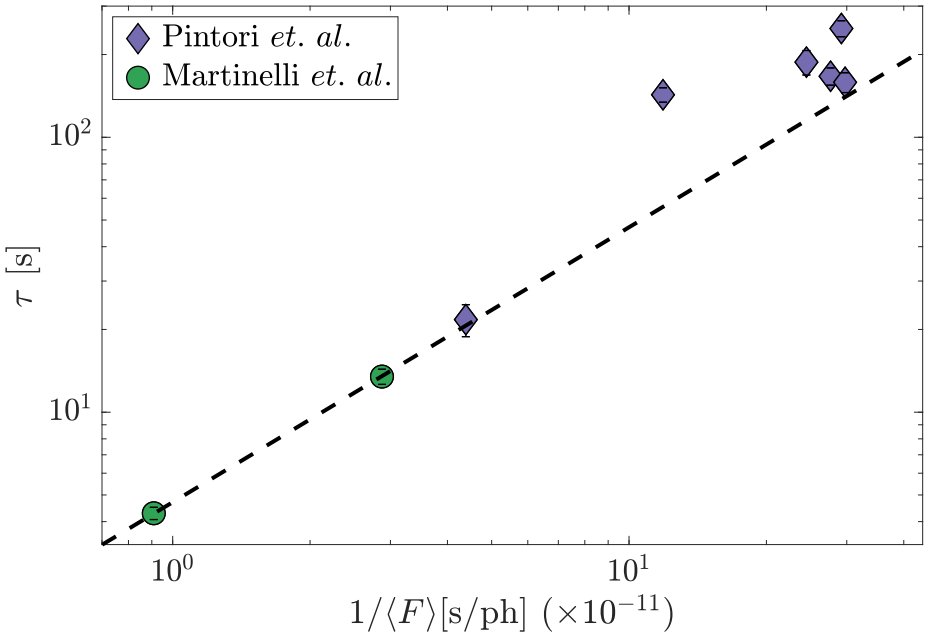


Figure 5.13: Relaxation time as a function of the inverse of the average incident beam. The black dashed line is the fit of Eq.(5.10) to the green points. The violet diamonds correspond to measurements collected at different temperatures, however for the $B_2O_3$ glass no temperature dependence of the relaxation time is observed [9, 110].

to the average absorbed flux, in agreement with Eq.(5.8). In detail, $\tau$ can be interpreted as the time after which the fraction $1 - 1/e$ of atoms (or particles) in the scattering volume has moved of $1/q$. The natural quantity to calculate is then the ratio between the total number of atoms that have moved of $1/q$ in the time $\tau$ and the number of photons absorbed in the same time yielding the number of units (or atoms) that have moved after the absorption of a single photon, $N_u$. We can thus write the relaxation time as a function of the number of $B_2O_3$ units $N_u$ (in this case 5 atoms) that move following a photon absorption event [9, 110]

$$\tau = \frac{e-1}{e} \frac{N_{tot}/N_u}{F_0[1 - e^{-\mu W}]} \tag{5.10}$$

with $N_{tot} = \frac{\rho V N_A}{M}$ the total number of chemical units in the scattering volume ($\rho = 1.83\,\mathrm{g/cm^3}$, $V$ is the scattering volume, $N_A$ is the Avogadro number, $M$=69.6 g/mol for $B_2O_3$) and $W = (73 \pm 10)\,\mu\mathrm{m}$. We note that the beam-induced relaxation time is independent on the thickness of the sample if $W\mu \ll 1$. Indeed, expanding the denominator of Eq.(5.10) in Taylor's series we get

$$\tau = \frac{e-1}{e} \frac{\rho S N_A}{M N_u F_0 \mu} \tag{5.11}$$

with $S$ the beam spot size. For the energy considered here, $1/\mu = 670\,\mu m$, thus much longer than the thickness of the samples measured both in [9] and [110]. This explains the coherence of Fig.(5.13), where the data collected in two different experiments have been reported without correction for the thickness. For the case of boron oxide, the number of units that move following an absorbed photon is $N_u = 1340 \pm 100$ [110], in agreement with the value found in [9]. Hereafter, however, we will try not to mix results coming from different experiments, in order to minimize the risk of propagating possible errors due to independent measurements of absolute X-ray fluxes.

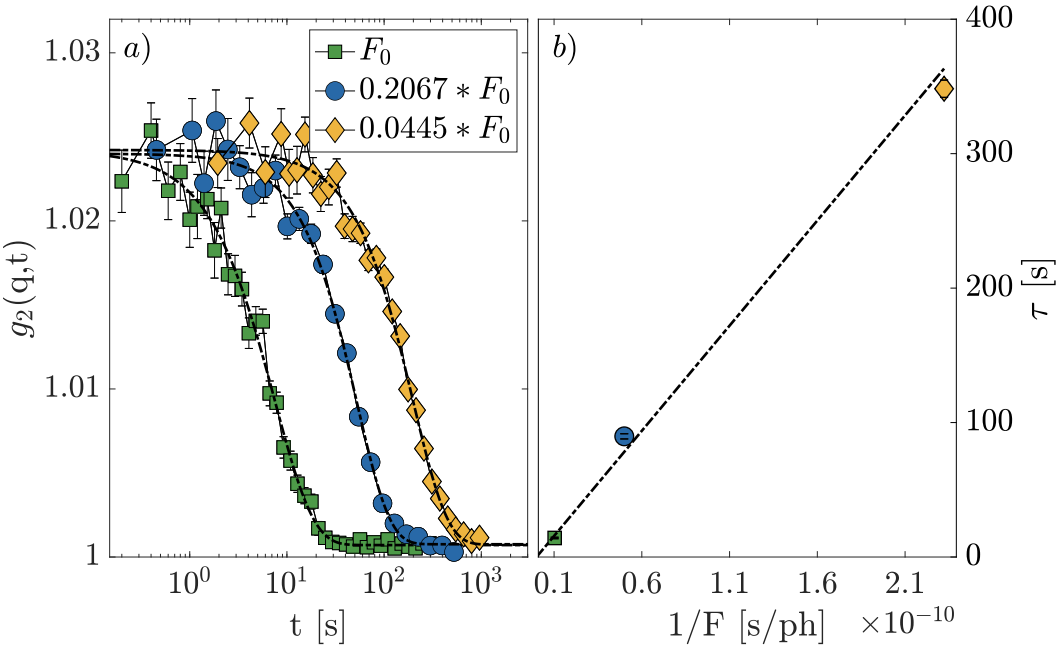


Figure 5.14: a) Autocorrelation functions at different incident fluxes (see legend) for a lithium metaborate glass at T=575 K measured at P10 (Petra III, DESY). The curves show a relaxation time inversely proportional to the flux. This behavior is confirmed in *b)*, where the relaxation time is reported as a function of the inverse incident flux. More details on this particular system and on the relaxation process as a function of the temperature will be given in the next chapter.

As introduced at the beginning of this section, the beam-induced effect has been observed on different borates and, in general, oxide glasses. However, it was quickly understood that different materials are characterized by a different number of atoms that move when an X-ray photon is absorbed. As an example, we now discuss lithium metaborate, $LiBO_2$, the main sample studied in this thesis (a complete description of the dynamical properties of $LiBO_2$ will be given in the next chapter). In Fig.(5.14 *a*) the intensity autocorrelation functions measured at the peak of the structure factor ($q \sim 17\,nm^{-1}$) are shown for three different incident fluxes. These data have been recorded at the temperature

T=575K, below the glass transition temperature, measured in Ch.(4). Despite a linear dependence of the relaxation time on the inverse incident flux, Fig.(5.14 *b*), $N_u$ for $LiBO_2$ is more than a decade smaller than for pure boron oxide. This suggests that the introduction of an alkali-modifier in the network must play a crucial, but unknown, role.
We will see in the following that $N_u$, for a given family of glasses, is controlled by the network's structural connectivity rather than the type of alkali modifiers introduced in the system [104, 157].

### 5.2.3 The structural units of borate glasses

Borate glasses are an interesting class of materials for many reasons. Their chemical durability and stability when mixed with silica and the relative low processing temperature of the resulting borosilicate glass make them ideal for applications in everyday life (windows, food containers). Also, they have peculiar optical properties when doped with rare-earth elements. Finally, their use as containers for radioactive wastes aroused interest in the scientific community [160].
Despite the effort in studying and engineering those systems, alkali-borates are still under active investigation. The difficulty of simulating the network and the lack of a uniquely accepted structural model leave many problems still open.
The simplest system is pure boron oxide $B_2O_3$. Its structure has been studied with different techniques, among which nuclear magnetic resonance (NMR) has been one of the most successful in providing detailed information [161–163]. The network is composed of almost planar $BO_3$ units of one boron atom coordinated to three oxygens. These triangular structures are found to assemble in *structural* rings called boroxol units, see Fig.(5.15). However, not all trigonal $BO_3$ units assemble in boroxol rings and, while still debated, experimental data suggest that on average the ratio of boroxol rings to non-ring $BO_3$ units is one to one, that is 75% of B atoms are located in boroxol units [164].
The network of borate glasses becomes more interesting upon addition of an alkali oxide $(M_2O)_x(B_2O_3)_{1-x}$, where $M$ is the alkali modifier and $x$ is the molar fraction of the alkali oxide. The alkali atoms distribute around the network, but do not disrupt it in an essential way (we will discuss their exact role in the next sections). For low alkali molar fractions, the major contribution is played by the increased number of oxygen atoms, which tend to convert the boron coordination from three to four [161, 163–165]. This change in coordination, clearly observed in NMR measurements, is reflected in the trend of the glass transition temperature as $T_g$ increases up to $x \sim 1/3$ (effect known as "boron anomaly"). Above this threshold, however, it is no longer possible to convert the boron coordination from three to four. As a result, the formation of non-bridging oxygens ($O^{NB}$) is observed. $O^{NB}s$ weaken the network, and the glass transition temperature $T_g$ decreases accordingly. As in the case of pure $B_2O_3$, the network can be seen as composed of intermediate range order structural

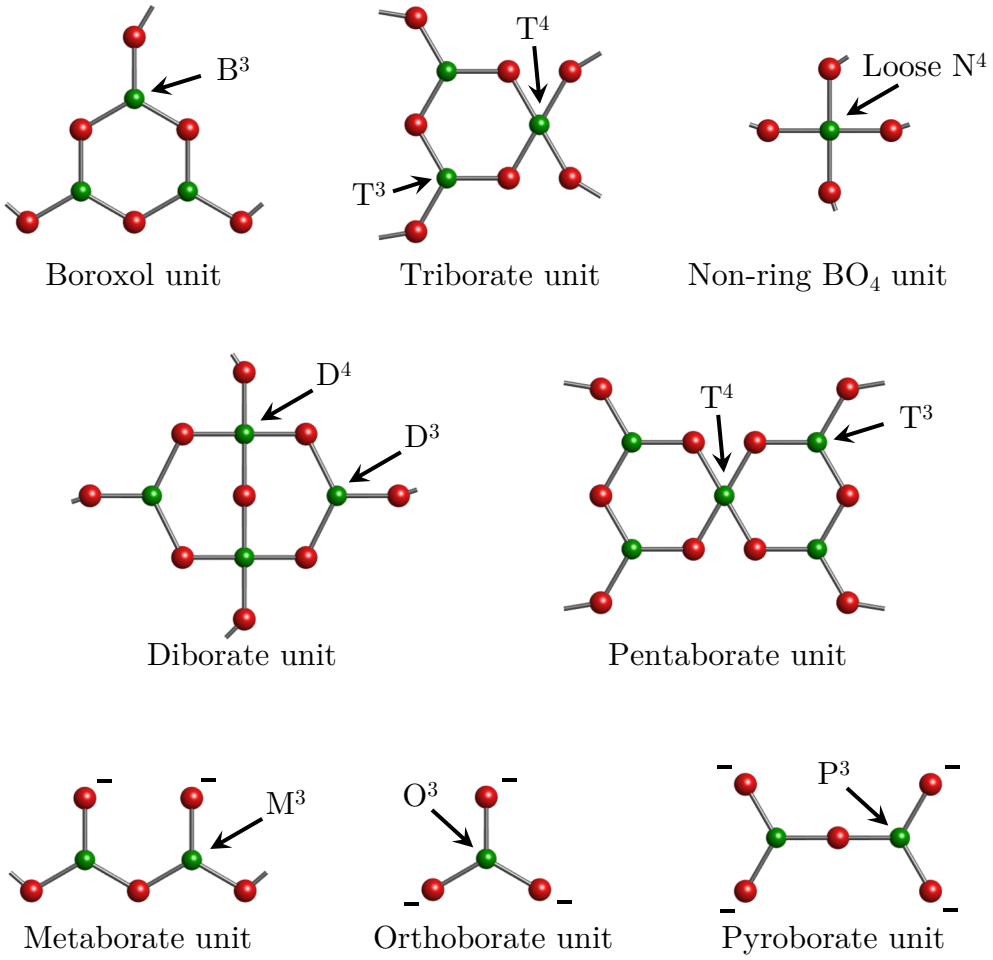


Figure 5.15: Structural groups for the alkali-borate glasses. Green spheres represent the boron atoms, while red ones are the oxygen atoms. For each structural unit representative boron structural configurations are reported. The negative charges - are located at non-bridging oxygens $O^{NB}$.

groups whose fraction depends on the alkali content. The pioneering work of Feller *et al.* [165] has quantified the fraction of these units in alkali-borate systems. In particular, they investigated the neighborhood network around each $^{10}B$ atom. The boron structural configurations are shown in Fig.(5.15) and their weight as a function of the alkali modifier (in the present case Li) in Fig.(5.16).

### 5.2.4 The topology of borate glasses

It is a matter of fact that not all materials can be vitrified with melt-quench techniques. For example, when cooling a $TiO_2$ melt, one always obtains one of the three crystalline structures: rutile, anatase or brookite. Zachariasen was one

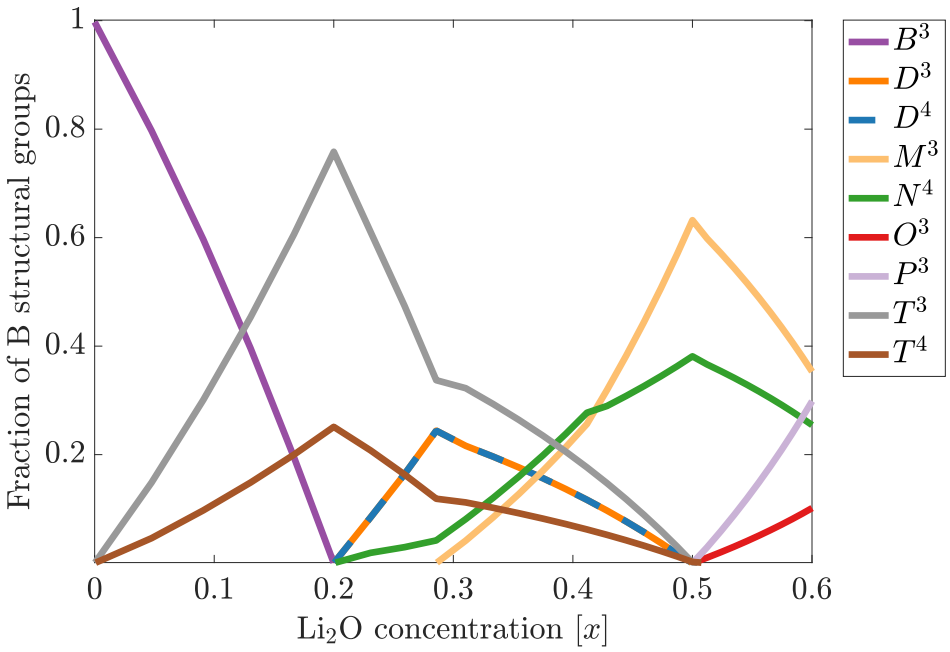


Figure 5.16: Fraction of boron structural configurations as reported by Feller *et al.* [165]. Note that for pure boron ($x = 0$) all the B atoms are considered in boroxol rings. This is in contrast with the more recent studies [164] which find a 1:1 ratio of boroxol rings to non-ring $BO_3$ units, as already said. Anyway, we can assume here that the non-ring units are included in the $B^3$, as suggested in [166]. *Data from [165].*

of the first scientists asking why some oxide melts tend to vitrify ($SiO_2, B_2O_3$) while other to crystallize ($TiO_2, Al_2O_3$) when cooled below the melting temperature [167]. In one famous paper, he reported the following about glass formers: "*the substance can form extended three-dimensional networks lacking periodicity with an energy content comparable with that of the corresponding crystal*" [167]. This statement can be quantified in the well known three Zachariasen's rules: "*(1) an oxygen atom is linked to not more than two atoms A; (2) the number of oxygen atoms surrounding atoms A must be small; (3) the oxygen polyhedra share corners with each other, not edges or faces.*" [167].
This work was the first attempt to describe the glassy network using a topological language, linking the macroscopic properties to the local ones. The ideas proposed there were extended few decades later when glasses started to be described in terms of an ensemble of constraints [168, 169]. All amorphous materials can be classified "topologically" in three major categories: flexible networks have a number of constraints per atom ($n_c$) which is less than the atomic degrees of freedom (in 3-dimensions it is equal to 3), stressed rigid have $n_c > 3$ and isostatic systems have $n_c = 3$ [170]. The number of atomic constraints is the link between the atomic-scale properties and the macroscopic ones: for example, glasses with $n_c > 3$ (stressed-rigid) exhibit brittle fracturing,

while flexible networks dissipate better the excess energy in an elastoplastic fashion; for a recent review on this topic see [170]. The topological models have been recently refined in order to describe the fragility index and the glass transition temperature too in $Ge_xSe_{1-x}$ and alkali-borates [171, 172], taking into account the temperature dependence of the constraints.
We will focus here on the case of alkali-borates systems, $(M_2O)_x(B_2O_3)_{1-x}$ , where 4 types of constraints are considered [166, 172, 173].

- $\alpha$ are the strongest constraints and are linear B-O bonds. There are 2 of this type of constraints at each bridging oxygen.
- $\beta$ are angular O-B-O constraints, and we have 5 of them at each $G^4$ and 3 at each $G^3$ structural configuration (G=T,D,...), see Fig.(5.15).
- $\gamma$ are angular B-O-B, B-O-M* constraints and we have one of them at every bridging oxygen.
- $\mu$ are additional constraints caused by the clustering effect of the alkali modifier [174]. We have two of them for each alkali ion which participates to the network.

Upon cooling the alkali-borate melt, constraints start to freeze in, leading to a stiffening of the glassy network. It is a good starting approximation to assume that the temperature dependence corresponding to this freezing of constraints is a step-like function [171]. The relative bond strength then orders the activation temperatures of the different constraints as follows [172, 173]

$$T_\gamma < T_g(0) < T_\beta < T_\mu < T_\alpha \tag{5.12}$$

with $T_g(0) = 526\,\mathrm{K}$ the glass transition temperature of pure boron oxide ($x = 0$).
We are now ready to build up the topological model for alkali-borates glasses. The number of constraints per atom can be calculated averaging the number of constraints (both linear and angular) for all the network forming atoms. To do that, the first step is to recognize the structures that contribute to the network and then, for each one, calculate the associated constraints.
In this thesis we have investigated borate systems in the range $0 \leq x \leq 0.5$. For the sake of clarity, we will limit our considerations up to $x = 0.5$. Observing Fig.(5.16), it is then clear that the boron structural configurations $O^3$ and $P^3$ can be discarded, since they start to contribute for $x > 0.5$. The B atoms are thus found in the following main groups: four-coordinated borons in tetraborate ($T^4$) and loose $N^4$ (not contributing to any superstructural group); four-coordinated borons in diborate units ($D^4$); three-coordinated borons in boroxol rings ($B^3$), triborates ($T^3$) and diborates ($D^3$); and finally three-coordinated borons in metaborate units ($M^3$). For more details about these structures see Fig.(5.15). The fractions of different boron configurations (Fig.(5.16)) can be used to calculate the fraction of the network forming species (appropriately normalized, as shown below). In addition to the groups just mentioned, oxygen atoms must

be taken into account whenever they are in a so-called bridging configuration $O^B$ (thus forming bonds). The alkali ions will also contribute to the formation of a network, although their exact contribution is not yet completely clear. We focus next on the case M=Li, since the majority of the reported measurements have been performed with lithium as a modifier. However, as we will see at the end of the chapter, the model developed here works independently of the chosen alkali ion. We consider here that the lithium cations play a role in the network only when they are compensating the negative charge of non-bridging oxygens ($Li^{NB}$). Finally, the fraction of network forming species, reported as $N(...)$, are

$$N(B^4) = \frac{T^4 + \text{Loose}\, N^4}{\Omega} \tag{5.13}$$

$$N(D^4) = \frac{D^4}{\Omega} \tag{5.14}$$

$$N(B^3) = \frac{B^3 + T^3 + D^3 + M^3}{\Omega} \tag{5.15}$$

$$N(O^B) = \frac{2[T^4 + \text{Loose}\, N^4 + D^4] + 1.5[B^3 + T^3 + D^3] + M^3}{\Omega} \tag{5.16}$$

$$N(Li^{NB}) = \frac{M^3}{\Omega} \tag{5.17}$$

where the normalisation factor $\Omega$ is given by

$$\Omega = 3[D^4 + \text{Loose}\, N^4 + T^4 + M^3] + 2.5[D^3 + B^3 + T^3] \tag{5.18}$$

The assignment of the constraints for each boron structural configuration is not an easy task due to the complex nature of alkali borates. However, the models, with the support of experimental data, are becoming more and more precise in accounting for them [172, 173, 175]. We assign here the constraints as reported above, with the exception of the $\beta$ constraints for the $B^4$ structures, which are counted as 4.5. In particular in the diborate unit one of the tetrahedron's angles is determined by the other constraints and, as suggested in [173], must not be included in the count of the constraints. At low temperature, where all the constraints are present (see Eq.(5.12)), the average number of constraints per atom, $n_c$, is then given by

$$n_c = 3N(O^B) + 5N(B^4) + 4.5N(D^4) + 3N(B^3) + 3N(Li^{NB}) \tag{5.19}$$

Eq.(5.19) is shown as a blue-solid line in Fig.(5.17).

Note that the model reported here is different from the one developed in [173], shown as the blue-dashed line in Fig.(5.17). The ionic bonds between lithium cations and Loose $N^4$ are here not included in the topology of the network and thus the relative $\mu$ constraints are discarded. Our choice is justified by two arguments. First of all, numerical simulations have shown that the

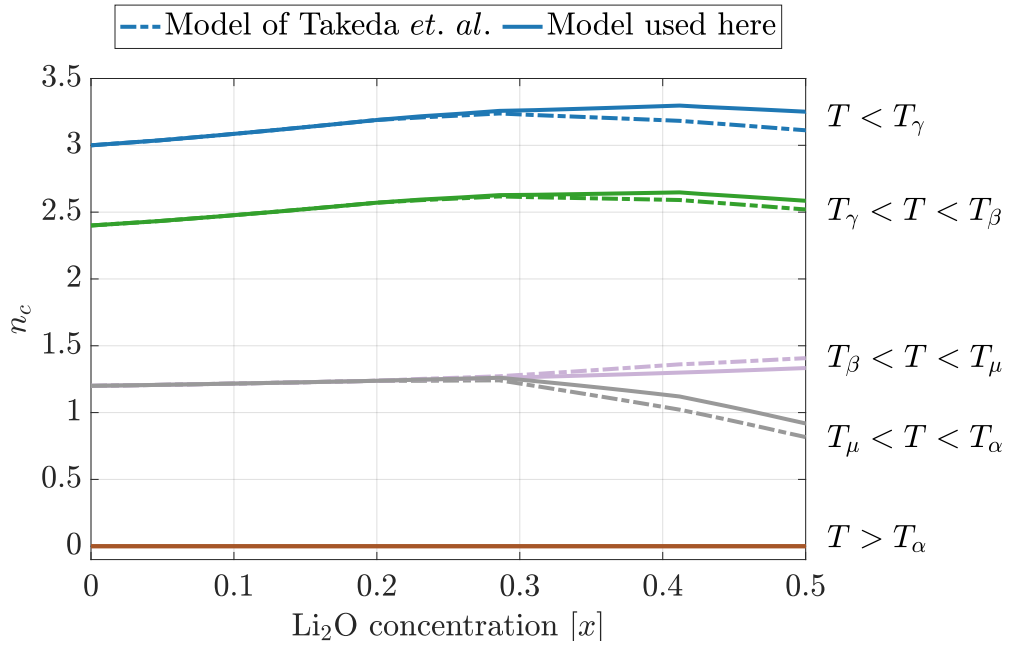


Figure 5.17: Number of constraints per atom, $n_c$, as a function of molar lithium oxide concentration. The values are calculated from Eq.(5.13-5.19) taking into account the temperature dependence given by Eq.(5.12) too (solid-lines). For comparison, the model developed by Takeda *et al.* is reported as dashed lines [173].

position of the lithium cations depends strongly on the structural group [176]. In fact, when the $Li^+$ cations compensate the negative charge of a $sp^3$-hybridised loose $N^4$ boron, their distance with respect to the B atoms is $\geq 3$Å. On the other hand, when lithium cations compensate negatively charged non-bridging oxygens, they are much closer to the O atom ($1.9 - 2.0$Å) [176]. This is also reflected in the lithium vibrational modes. Numerical simulations show that the frequencies of those modes are a factor 2 higher when the alkali is close to a non-bridging oxygen rather than to a loose $N^4$ boron [176]. Despite the possibility that lithium ions play a role when they are close to loose $N^4$ borons, we do not include those configurations in our version of the model.

### 5.2.5 The beam-induced dynamics as a probe of network connectivity

The investigation of the beam-induced dynamics in alkali-borates glasses has been carried out in detail by Pintori in her PhD thesis [104], and in successive papers where more properties have been elucidated [9, 109]. Here, we link the topological properties of the borate network to XPCS results, as reported in our last submitted work [157].
The $(M_2O)_x(B_2O_3)_{1-x}$ glasses have been studied in detail with M= Li, Na, K

and $x = 0.14$ while for the Li modifier the molar range has been extended to $x = 0.22, 0.3, 0.5$. The data reported next have been collected during XPCS experiments performed at the beamline P10 at PETRA III. The chosen X-ray beam energy was 8.4 keV with an energy resolution of $\sim 1$ eV. The beam was focused to $3 \times 3\,\mu m^2$ with compound refractive lenses, ending up in a photon flux of $6 \times 10^{10}$ ph/s. The scattered radiation was collected in transmission geometry using a Princeton CCD ($1340 \times 1300$ pixels, $20 \times 20\,\mu m^2$ pixel size) positioned $\sim 40$ cm downstream of the sample and mounted on a motorized goniometer. The measurements were performed at the peak of the scattered intensity, corresponding to the peak of the structure factor. The integration time was chosen between 0.2 s and 2 s and up to 6000 images per scan were collected. Particular attention was paid to avoid X-ray beam damage. As already observed for the pure boron oxide glass [9], beam damage is negligible up to absorbed doses of about 2.5 GGy. A more detailed discussion of the dynamics as a function of the absorbed dose will be given in the next chapter. The relevant parameters of the investigated samples are reported in Tab.(5.1), including the glass transition temperature, the density and the stretching parameter $\beta$ of the KWW fits. This last parameter has been used to calculate the mean relaxation time $\langle\tau\rangle = \tau\Gamma(1/\beta)/\beta$ [48] in order to get robust estimations and reduce the correlation between $\beta$ and $\tau$.

| Sample $(M_2O)_x(B_2O_3)_{1-x}$ | $\rho$ (g/cm$^3$) | $T_g$ (K) | $v_l$ (m/s) | $\beta$ | $\langle N_u \rangle$ |
|---|---|---|---|---|---|
| $B_2O_3$ | 1.83 | 526 | 3488 | $0.84 \pm 0.03$ | $990 \pm 50$ |
| Na, $x = 0.14$ | 2.10 | 660 | 4840 | $0.93 \pm 0.03$ | $260 \pm 10$ |
| K, $x = 0.14$ | 2.08 | 633 | 4439 | $0.84 \pm 0.04$ | $270 \pm 10$ |
| Li, $x = 0.14$ | 2.01 | 679 | 5246 | $0.99 \pm 0.06$ | $280 \pm 20$ |
| Li, $x = 0.22$ | 2.15 | 753 | 6106 | $0.9 \pm 0.2$ | $150 \pm 20$ |
| Li, $x = 0.30$ | 2.24 | 771 | 6687 | $0.91 \pm 0.07$ | $120 \pm 10$ |
| Li, $x = 0.50$ | 2.18 | 694 | 6780 | $0.75 \pm 0.05$ | $56 \pm 3$ |

Table 5.1: List of selected physical properties for the borates glasses. In the first column the borate glass $(M_2O)_x(B_2O_3)_{1-x}$ is reported indicating the alkali M and the molar fraction $x$. The mass density $\rho$ has been tabulated from [177, 178], the glass transition temperature for pure boron oxide and M=Na,K from [106], while for M=Li from [131]. The longitudinal sound velocity $v_l$ has been taken from [179–181]. The stretching parameter and average number of units (calculated from the mean relaxation time $\langle\tau\rangle$) that move following the absorption of an X-ray photon are also reported for the studied borate glasses. *Table adapted from [157].*

In Fig.(5.18 *a*) we show the different densities for the alkali borates as a function of the molar fraction $x$. Two main features can be appreciated from the plot. First, as expected, for a given molar fraction different alkalis lead to different densities. Second, the density of lithium-metaborate ($x = 0.5$)

is smaller than the one of $x = 0.3$ (non-monotonic behavior, related to the boron anomaly). A similar non-monotonic dependence is observed for the glass transition temperature, see Tab.(5.1).

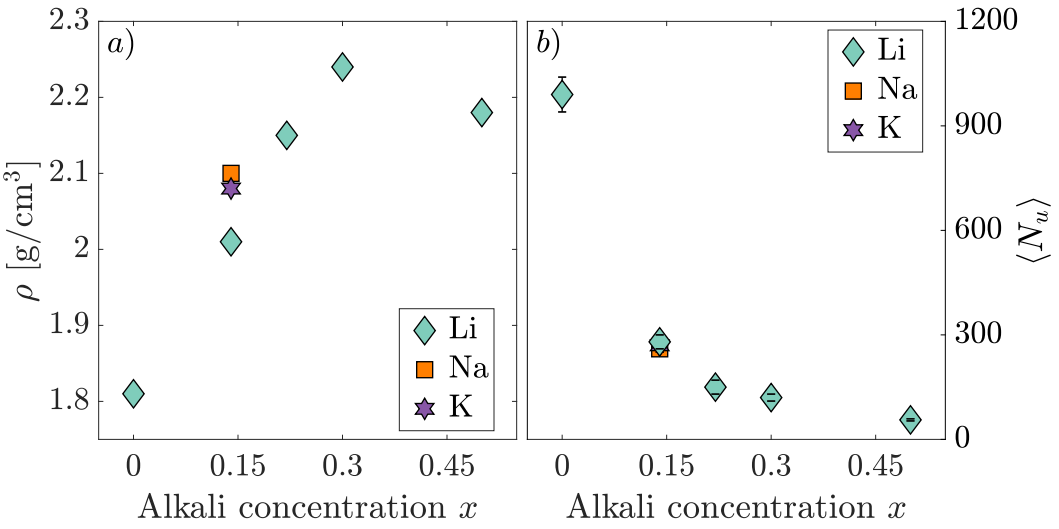


Figure 5.18: *a*) Density of alkali borate glasses as a function of the molar fraction $x$, as reported in Tab.(5.1). Data from [177, 178]. *b*) Average number of units $\langle N_u \rangle$ as a function of the molar fraction $x$ for the different borates investigated here. *Figure adapted from [157].*

These features are not present if we plot the average number of units $\langle N_u \rangle$ as a function of $x$, Fig.(5.18 *b*). $\langle N_u \rangle$ behaves indeed in a monotonic decreasing way as a function of the mole fraction $x$ and is insensitive to the different alkali modifier. This is in contrast with the interpretation proposed in [159], where it was claimed that the glass transition temperature fixes the timescale (and therefore $N_u$) for a given glass. However, if that were the case, we would expect a non-monotonic behavior of $\langle N_u \rangle$ vs $x$ in the same way as for $T_g$. Furthermore, the almost identical value of $N_u$ for alkalis with very different atomic numbers (Li, Na, K) in Fig.(5.18 *a*) shows that the crucial parameter accounting for the dependence of $N_u$ on $x$ must be the structure of the glass itself, namely the topology of the local and medium range structures.
We can then apply the topological model developed in the previous section. All the data reported in Tab.(5.1) have been collected at ambient temperature (T=300 K), thus we should refer to the blue-lines reported in Fig.(5.17) in order to calculate $n_c$. Moreover, the terminology related to $N_u$ can be made more self-explanatory if we convert it to an effective volume that relaxes upon the absorption of an X-ray photon. That is, if we imagine that the $N_u$ units belongs to a compact ($d = 3$) volume, i.e. spherical for simplicity, we can write [9, 104, 157]

$$\xi = \sqrt[3]{3\langle N_u \rangle V_u/(4\pi)} \tag{5.20}$$

where $V_u$ is the volume occupied by a chemical unit. $\xi$ is thus the average linear size of the region that is "fluidized" by one X-ray photon. In Fig.(5.19 *a*) the value of $\xi$ is reported as a function of the average number of constraints per atom calculated in Fig.(5.17).

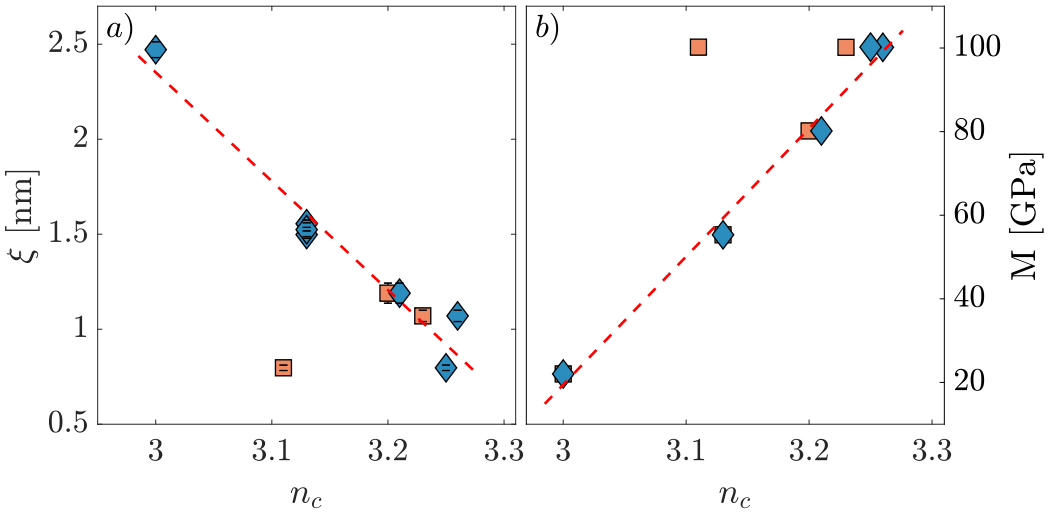


Figure 5.19: *a*) Average size of the relaxing regions $\xi$ following the absorption of an X-ray photon as a function of the atomic number of constraints $n_c$. Two different values of $n_c$ have been here reported: blue diamonds correspond to the model developed here, while orange squares to the one reported by Takeda *et al.* [173]. *b*) Longitudinal elastic moduli calculated from Brillouin measurements [179–181] with the equation $\mathrm{M} = \rho v_l^2$, with $\rho$ from [177, 178]. Also in this case, the blue diamonds correspond to the topological model reported here, while the orange squares to the one reported by Takeda *et al.* [173]. *Figure adapted from [157].*

We should highlight here that $n_c$ is related not only to the short range order of the glass, but on the medium range order too. Indeed, in calculating it, we took into account all the superstructural configurations typical of the alkali-borate systems. The linear behavior reported in Fig.(5.19 *a*) shows that a strong correlation exists between the average number of constraints (or the network rigidity) and the size of the regions that move when X-rays perturb the glass. Assuming a spherical compact volume, Eq.(5.20), we observed a dependence of $\xi$ inversely proportional to the number of constraints per atom. This behavior is readily understood since the rearrangement of those regions requires the rupture and formation of new bonds and thus has to be related to the local elasticity of the network. In this spirit, the average energy density is captured by the number of constraints per atom, $n_c$.
The observed dependence is furthermore reminiscent of the well known mechanisms for fracture of tempered glasses. What glasses do beyond the elastic limit is to dissipate stress via the development of free surfaces which ends up in cracking the glass with a consequent macroscopic breakage into fragments.

The more the glass is strengthened (thus more stressed), the smaller are the fragments upon cracking. Fig.(5.19 *a*) shows a similar behavior since values of $n_c$ beyond 3 correspond to a stressed-rigid glass. In the present case, however, the system cannot physically create new surfaces. Thus, the network excess energy is dissipated through nanometric rearrangements towards new configurations, where the size of these "rearranging fragments" is smaller the more stressed is the glass.
Finally, we can further validate the topological model developed here observing the behavior of the longitudinal elastic moduli (M) as a function of $n_c$. From simple qualitative considerations, we expect that the elastic modulus should be linearly related to the energy density stored in the glassy network, in turn quantified by $n_c$. Fig.(5.19 *b*) shows indeed this linear behavior (blue diamonds), confirming that the topological model developed here is coherent both with XPCS measurements and Brillouin studies.

# Chapter 6

# The photo-induced transition from stress driven to stress free dynamics

This last chapter is dedicated to a discussion of the photo-induced transition from a stress driven dynamics to a stress free one observed in oxide glasses probed with XPCS. In the first part, we will discuss the glass behavior approaching the glass transition temperature, highlighting the properties of the relaxation time and of the stretching parameter. In the second half, we will tackle the dependence of the dynamics on the absorbed dose. We will show that the X-rays "fluidize" the glass, as speculated in Ch.(5), inducing strong modifications in the dynamical properties and relaxing the system towards a fluid-like condition.

## 6.1 From the glass to the supercooled liquid: a temperature investigation

We start by reporting an XPCS study of the lithium metaborate ($LiBO_2$) glass as a function of the temperature. Different experiments have been performed both at the European Synchrotron Radiation Facility (ESRF), beamline ID10, and at the Petra III synchrotron (DESY), beamline P10.
We will focus on the beam-induced dynamics approaching the glass transition. In the spirit of Eq.(5.11), for a given material the beam-induced relaxation time does not depend on the thickness of the sample as long as it is much thinner than the absorption length. In the present case, we prepared samples of thickness $W \sim 150\,\mu m$ ($1/\mu \approx 600\,\mu m$ for the energies used), so absorption plays a negligible role in the beam-induced relaxation. In the following, we report the details of each sample, together with other experimental parameters, for all sets of data here presented.

### 6.1.1 The scaling of the beam-induced dynamics in $LiBO_2$

The data reported in this subsection have been collected at the Petra III synchrotron, during the same beamtime discussed in Ch.(4). Two samples of $LiBO_2$, of thickness $W = (150 \pm 10)\,\mu m$ and $W = (175 \pm 25)\,\mu m$, have been placed in a furnace in vacuum and heated at few selected temperatures across the glass transition. The detector (EIGER 4M) was placed at the peak of the scattered intensity, here located at $\theta = 23.9$ deg. The corresponding $q$-window covered by the detector was $q = (16.8 \pm 2.0) nm^{-1}$. We recall that the glass transition temperature for the lithium metaborate glass was measured independently with dynamic light scattering and found to be $T_g = 704$ K, compatible with the values reported, for example, in [131, 173].

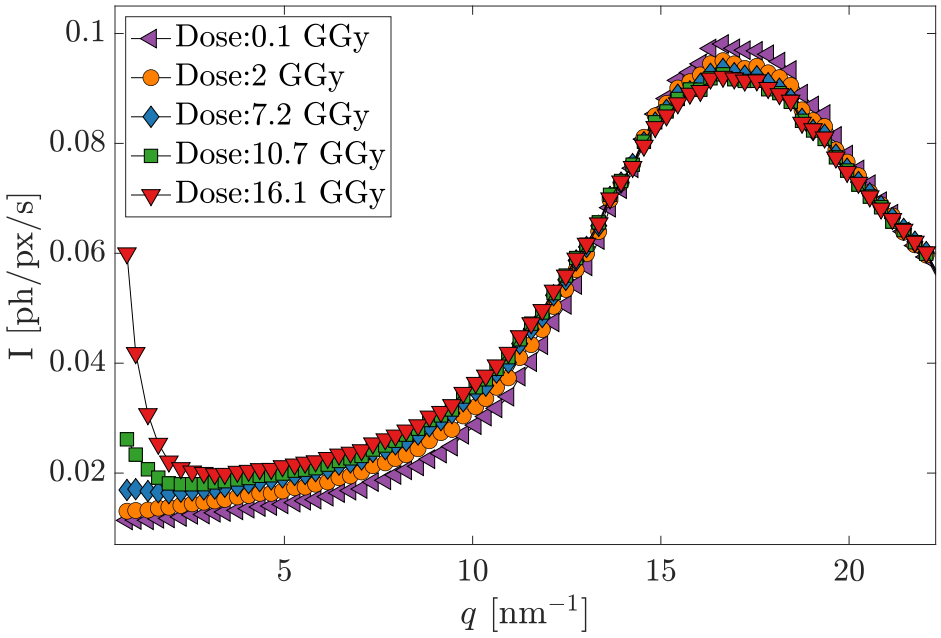


Figure 6.1: Scattered intensity for the $LiBO_2$ glass at T=300 K as a function of the exchanged wave-vector $q$ for different total absorbed doses. Note the strong intensity increase at small $q$s ($q \sim 1\,nm^{-1}$) for doses above about 10 GGy.

As noted in previous works on borate glasses studied with XPCS [9, 104, 109], the scattered intensity profile experiences a small change upon irradiation. For completeness, we remember here that the absorbed dose is calculated assuming that all the absorbed energy is deposited in the volume defined by the vertical and horizontal full-width half maximum and the thickness of the sample. This is a fair estimate when the thickness is much smaller than the linear attenuation length, which is the case for all the samples here considered.
Fig.(6.1) shows the scattered intensity for different irradiation doses as a function of the exchanged wave vector $q$. In agreement to what observed on the same sample by Dallari *et al.* [109], the peak intensity decreases with a

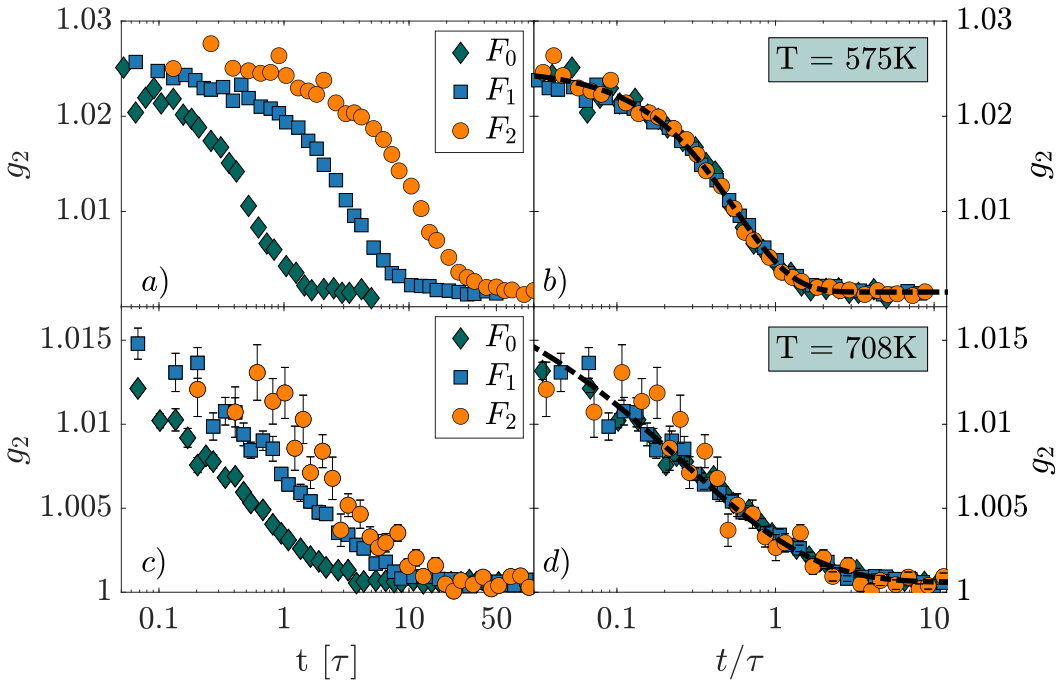


Figure 6.2: Set of $g_2$ data collected for the $LiBO_2$ glass at two different temperatures for different incident fluxes. On the left (panels $a, c$), the time scale has been normalized to the fitted relaxation time $\tau$ corresponding to the full beam data (green diamonds). On the right (panels $b, d$), the time scale has been normalized for the respective relaxation times of the curves: all the correlation functions collapse on a master curve. The black dashed lines corresponds to the best KWW fits.

simultaneous increase of full-width half maximum (FWHM). Simultaneously, the scattered intensity in the small $q$ region increases. At very small scattering angles, corresponding roughly to $q \sim 1\,\mathrm{nm}^{-1}$ a pronounced tail starts to appear for doses greater than about 10 GGy. This feature is likely a symptom of sample damage, with the increase of small angle scattering due to the formation of structures with typical size of $\sim$ nm. This could be due, for example, to nano-separation or to the formation of nanometric-size holes. The measurements reported in this section are performed while keeping the absorbed dose below 2 GGy, a dose which induces changes in the intensity at the peak of the structure factor of only a few percent. More details about the dose effect on the structure and, more importantly, on the dynamics will be given in the next section.
We discussed in the previous chapter that the beam-induced dynamics relaxation is triggered by the absorption of X-rays photons, with the decorrelation time inversely proportional to the incident flux, Eq.(5.8). Fig.(6.2) shows a set of representative correlation functions of the $LiBO_2$ glass. The fluxes employed for those measurements are $F_0 = 9.7 \times 10^{10}$ ph/s, $F_1 = 0.2067 F_0$ and $F_2 = 0.0445 F_0$. At low temperatures (below $T_g$) the relaxation time scales inversely to the incident flux, becoming faster the higher the flux, Fig.(6.2 $a - b$). All the curves

collapse on a master plot if the time-scale is normalized to the corresponding relaxation time, Fig.(6.2 *b*), showing that the dynamics are triggered by a single photon absorption event and does not depend upon the average power delivered to the sample (at least in the range considered here). The $g_2$ functions can be modeled by a KWW ansatz, and it is possible to describe simultaneously all the three curves by simply introducing a scaling factor between the respective relaxation times. We emphasize that the obtained stretching parameter is greater than one ($\beta > 1$), at variance to previous experiments on borate glasses [104, 109, 157, 159]; we will concentrate on this aspect soon.

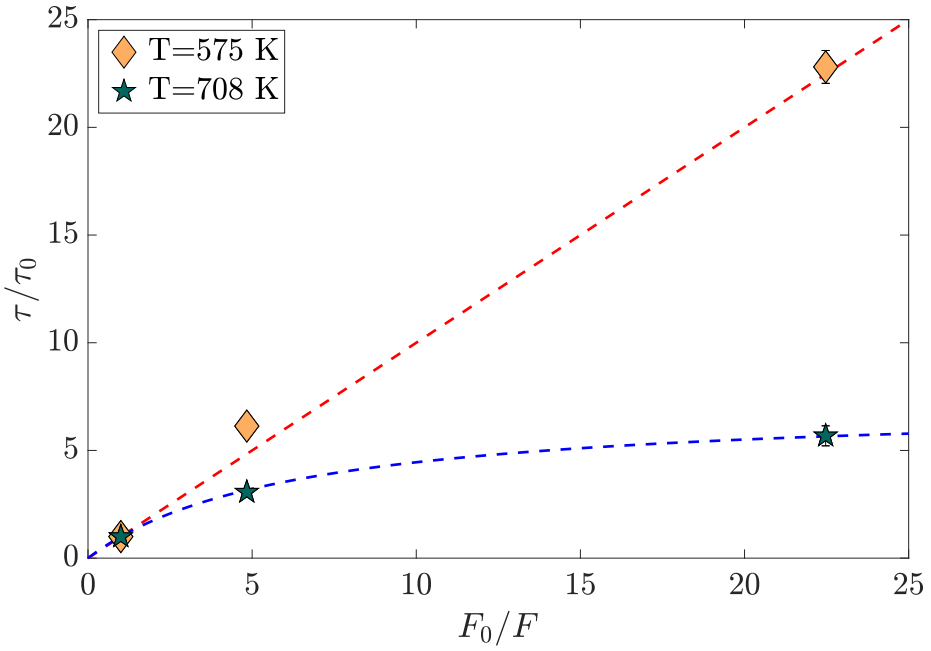


Figure 6.3: The flux dependence of the relaxation times corresponding to the data reported in Fig.(6.2). All data are rescaled to the relaxation time and flux corresponding to full beam conditions. The red dotted line shows the linear dependence of the relaxation time deep in the glassy state while, close to $T_g$, Eq.(6.2) leads to a saturation in the inverse flux dependence of the measured relaxation time (blue dotted line) which corresponds to the value of the structural relaxation time for $F \to 0$. At T=575 K, $\tau_0 = (15.4 \pm 0.5)$ s while at T=708 K, $\tau_0 = (1.47 \pm 0.08)$ s.

The situation is different for a temperature above the glass transition, Fig.(6.2 $c - d$). Here the relaxation time still has a clear correlation with the incident flux, Fig.(6.2 *c*), but the dependence is weakened with respect to the linear behavior observed at low temperatures. The curves can again be placed onto a master curve by scaling the time-axes to the corresponding relaxation times, but now the stretching parameter is less than one ($\beta < 1$), Fig.(6.2 *d*).
The scaling of the relaxation time close to the glass transition was studied in $B_2O_3$ by Pintori *et al.* in [9], where it was shown that, approaching the

glass transition, the beam-induced process and the structural relaxation start to compete. The same considerations reported there are valid for the $LiBO_2$ glass; the measured relaxation rate is the sum of the relaxation rates of the two processes [9]

$$\frac{1}{\tau} = \frac{1}{\tau_{ind}} + \frac{1}{\tau_\alpha} \tag{6.1}$$

where $\tau_{ind}$ and $\tau_\alpha$ are the beam-induced and structural relaxation times, respectively. We know that $1/\tau_{ind}$ is proportional to the flux $F$; we can then rewrite the above equation defining $1/\tau_{ind} = BF$, leading to

$$\tau = \frac{\tau_\alpha}{BF\tau_\alpha + 1} \tag{6.2}$$

with $B$ the correct normalization factor which can be simply calculated from Eq.(5.10).
Fig.(6.3) presents the relaxation times for the curves reported in Fig.(6.2) as a function of the inverse flux. Both the relaxation times and the flux have been normalized for the values corresponding to full beam conditions ($\tau_0, F_0$, respectively). At low temperatures (T=575 K), the relaxation time shows a linear dependence in agreement with Eq.(6.1-6.2), since $\tau_\alpha \gg \tau_{ind}$ and the induced dynamics are dominating the overall relaxation. Close to $T_g$, however $\tau_\alpha \approx \tau_{ind}$ and the sum in parallel of the two relaxation times (structural and beam-induced) smears the flux dependence of the measured relaxation time: in the end, the function of Eq.(6.2) saturates for small fluxes $F$, allowing the measurement of the structural relaxation time, Fig.(6.3). The extrapolated structural relaxation time (obtained fitting Eq.(6.2) to the experimental data) at the peak of the structure factor at T=708 K is found to be $\tau_\alpha = (10.6 \pm 0.6)$ s. Note that this value is comparable to that obtained from the dynamic light scattering measurements reported in Ch.(4), supporting the present analysis. Finally, we should spend few words regarding the value obtained for the number of $LiBO_2$ units that move after a photo-absorption event. In fact, from the estimation of the beam-induced relaxation time through Eq.(6.2) and using Eq.(5.10) discussed in the previous chapter, we estimate a number of units $N_u = 665 \pm 40$ at T=708 K, a value almost a factor 10 larger with respect to the one obtained at room temperature. The value might reflect a change of the number of topological constraints in the network above the glass transition temperature, but further studies are required to clarify this point.

### 6.1.2 The temperature dependence of the beam-induced dynamics

A more detailed temperature investigation of the beam-induced dynamics in the lithium metaborate glass has been performed during the experiment at the ESRF reported in Sect.(5.2.2). The setup used was optimized for high contrast and the measurement of fast correlation functions in the liquid (detector: EIGER 500K). This limited the accessible $q$-range to very few angles across the

peak of the structure factor. We decided then to perform the acquisitions at a fixed $q = (17.0 \pm 0.2)\,\mathrm{nm}^{-1}$ at the peak of the scattered intensity. A sample of glassy $LiBO_2$, $W = (120 \pm 10)\,\mu\mathrm{m}$, was mounted in a copper sample holder; care was taken to improve as much as possible the thermal contact between the sample and the holder by inserting thin aluminum sheets in between. The sample holder was then mounted in a dedicated vacuum furnace with kapton windows. The measurements were performed with full beam ($F = 11 \times 10^{10}$ ph/s) and the sample temperature scanned several times across the glass transition. Once again, we paid particular attention to avoiding beam damage, as reported above and in the literature [9, 104, 109, 157]. For this reason, the absorbed dose was kept below 1 GGy.

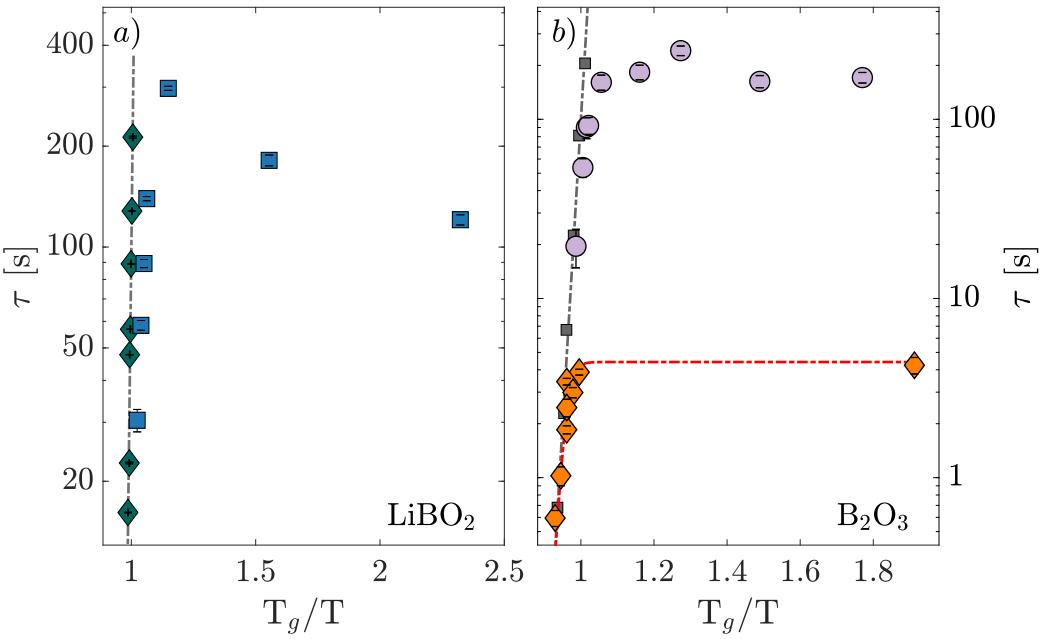


Figure 6.4: *a*) Relaxation times as a function of the normalized inverse temperature for a $LiBO_2$ glass measured with XPCS (blue squares) and with visible light scattering (green diamonds). The grey dashed line is a VFT fit (see Eq.(2.7)) to the DLS data. *b*) Relaxation times as a function of the normalized inverse temperature for a boron-oxide glass measured with XPCS at the ESRF (orange diamonds) during the here considered beamtime and compared with the data reported in [9] (light purple circles). The gray dashed line is an Arrhenius fit to the equilibrium data from [62]. The red dashed line is a fit with Eq.(6.1) to the XPCS relaxation times.

Fig.(6.4) shows the relaxation time as a function of the inverse temperature (normalized to the glass transition temperature $T_g$) for two samples, namely lithium metaborate ($LiBO_2$) and pure boron oxide ($B_2O_3$) glasses. For the boron oxide glass, Eq.(6.1) holds for the whole probed temperature range with a temperature-independent beam-induced relaxation time, i.e. from ambient

(T=300 K) to above the glass transition temperature, see Fig.(6.4 *b*) for details. The situation is very similar for the $LiBO_2$ glass. As shown in Fig.(6.3), Eq.(6.1) is still fully valid at a given temperature for different incident fluxes and close to $T_g$ too. However, here we have to hypothesize that the beam-induced relaxation time is temperature dependent in order to describe the experimental data below the glass transition where $\tau_\alpha \gg \tau_{ind}$. In Fig.(6.4 *a*) it is clear that the relaxation time decreases by a factor almost 3 while cooling the sample from T=613 K to ambient temperature (T=303 K). The relaxation time has an overall behavior very similar to the one observed in pure boron oxide where, well below the glass transition temperature, with the structural relaxation completely frozen, the beam-induced effect triggers density rearrangements with each absorbed photon moving a given number of atoms.
A similar behavior is observed in silicates [7] where, despite the beam dynamics were still unknown at the time of the experiment, the authors showed that the relaxation time tends to decrease upon heating, meaning that the beam-induced dynamics are somehow activated by the temperature of the sample. On the other hand, in the lithium-borate glass studied here, the photo-induced relaxation becomes less efficient approaching the glass transition: we will show in the following that this behavior can be associated with stresses frozen in during the sample preparation.

### 6.1.3 The glass transition in $LiBO_2$

We conclude here the investigation of the beam-induced dynamics as a function of the temperature in the lithium-metaborate glass, discussing our findings in more detail.
The measurements have been performed while cycling the sample temperature from ambient condition to just above the glass transition temperature and back. In Fig.(6.5 *a*) the relaxation time has been reported for three subsequent temperature runs: starting from room temperature the glass was heated up to T=703 K (orange squares); the sample was then kept in the under-cooled liquid for 24 hours and cooled to room temperature (blue circles); measurements have been collected at selected temperatures on the way back. The sample was then heated once again to $T$=633 K (light-purple diamond). All the reported changes in temperature have been performed with temperature ramps of 3 K/min.
The temperature paths followed are shown as colored arrows in Fig.(6.5 *a*). As can be clearly seen, the relaxation time deep in the glassy state, where the dynamics are completely dominated by the beam-induced effect, shows an effect of annealing, with the relaxation time increasing after the first cooling (the temperature was decreased at 3 K/min). We recall that the pristine glass was produced quenching the liquid between preheated steel-plates and the obtained glass kept for 6 hours at 643 K and then cooled down to room temperature at 0.5 K/min. We initially chose 643 K aiming at annealing the glass 20 K below the calorimetric glass transition temperature reported in literature [106]. We

discovered afterwards, thanks to light scattering measurements, that $T_g$=704 K was much higher, in agreement with other references [131]. Therefore, we conclude that the cooling protocol followed during run 2 has effectively annealed the as-prepared glass. This is reflected in the fact that, close to room temperature, the relaxation time increases by a factor 2 after the thermal protocol (right-most blue and orange points), and that heating up again the sample (run 3) the dynamics slows down even more. Summarizing, a more equilibrated structure shows a slower beam-induced relaxation time.

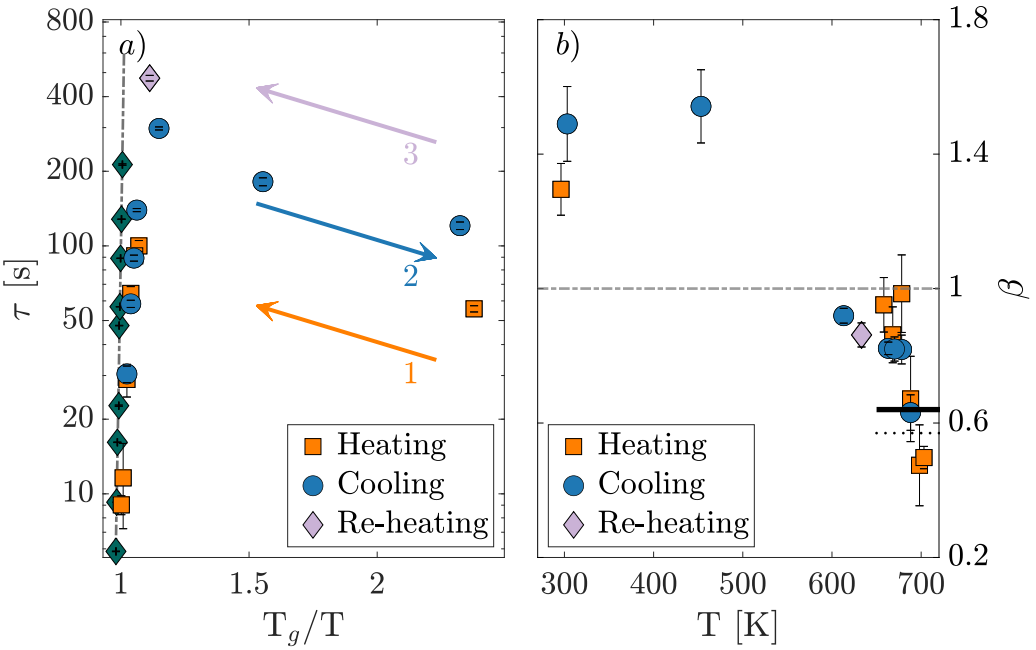


Figure 6.5: *a*) The relaxation time for a $LiBO_2$ glass is reported as a function of the normalized inverse temperature for three successive thermal runs: heating (orange squares), cooling (blue circles) and heating again (light-purple diamond). The measured DLS data are reported as green diamonds, together with the VFT fit (gray dashed line). *b*) The stretching parameter $\beta$ as a function of temperature is reported for the three thermal runs indicated in *a*). The gray-dashed line corresponds to $\beta = 1$. The equilibrium values measured here with DLS and taken from the literature [111] are shown as a black-dotted line and black-continuous line, respectively.

These aspects suggest that, despite the overall behavior being described as a sum of spontaneous fluctuations and beam-induced relaxation rates, the details are related to the stress frozen in the network. We recall that the inverse relaxation time ($1/\tau$) is proportional to the number of atoms that rearrange after a photon-absorption event, $N_u$, as indicated by Eq.(5.10) [9]. Cooling the liquid down slowly across the glass transition, as done here, gives rise to a more equilibrated glass (lower in enthalpy) than the as prepared glass. The experimental observation is that the more equilibrated is the glass, the smaller

is the number of atoms that move when the X-ray beam perturbs the local structure. The relaxation time of the beam-induced dynamics would then be, in the end, related to the stresses frozen in the glass.
Note that the result can also be rationalized using a purely structural point of view. In fact, as reported in Ch.(5), the $LiBO_2$ glass is composed of two superstructural units, namely the metaborate ($M^3$) and (loose) $N^4$. Their ratio is well known in the glassy state from NMR measurements [165] and is roughly 60% and 40%, respectively (see Fig.(5.16)). Recently, it was demonstrated that upon heating the system above the glass transition temperature, the $sp^3$ hybridized $N^4$ are converted in three coordinated $sp^2$ [182–184]. From charge conservation arguments [165], it is clear that the $N^4$ units can only be converted into $M^3$ ones, leading to an effective change in the topology of the network as the temperature is increased. In the liquid state, the fraction of four-coordinated borons decreases down to $\sim 12\%$ [183, 184]. When the liquid is quenched below $T_g$ to produce a glass, the ratio between three- and four-coordinated borons will depend on the cooling rate, as observed in borosilicate glasses [185]. In fact, a fast quench of the liquid will end up in a higher fictive temperature (that is the temperature at which the liquid has the same structure as the glass), with a structural configuration more similar to that of the high temperature liquid. Recalling Fig.(5.19), we can calculate that an increase by a factor two in the number of atoms that move following the absorption of an X-ray photon would correspond to a $\sim$5% larger fraction of $M^3$ units. Note that changes on the order of a few percent between the fraction of different structural groups have been observed for borosilicate glasses [185] when the cooling rate is changed by three decades.
The picture that emerged in this section could seem, at first sight, in contradiction with the discussion carried out in Sect.(5.2.2). There we showed that the more the network is stressed-rigid, the smaller the number of atoms that move following the absorption of a photon. Following the topological model of Mauro *et al.* [172], we would expect that increasing the temperature of the system and approaching the glass transition would decrease the number of constraints per atom (see Fig.(5.12) for details). In particular, the temperature at which the angular constraints B-O-B and B-O-M* soften is claimed to be close to the VFT temperature for pure boron oxide ($T_0$=328 K) [172]. Above that temperature, the number of constraints per atom starts to decrease. Taking pure boron as the prototypical example, we would expect that at the glass transition temperature all the $\gamma$ constraints are relaxed and the number of constraints per atom drops to $n_c \sim 2.4$. In the spirit of this model, we would then predict a strong temperature dependence of the dynamics, with shorter relaxation times upon heating. This is clearly not the case for both samples studied here. What is the reason of that? We believe the answer must be sought in the relevant time-scale of the involved processes. We can expect that the softening of the angular constraints (that is in fact the breaking and modification of the angular coordination) has a time-scale comparable to the one of the structural relaxation (at least close to $T_g$). On the other hand, the beam-induced relaxation must be much faster:

the radiolysis process triggers a structural rearrangement which likely takes place in the pico- to nano-second time range. The picture is confirmed by the fact that the beam-induced dynamics appears as "instantaneous" in our experiments, just defined by the photon beam flux: the underlying process is surely faster than all the time-scales involved in the experiment. Despite not having precise values for the physical timescale over which the photo-induced relaxation takes place, we can safely assume that it is much faster than that related to the relaxation of the angular constraints close to $T_g$. In other words, when the X-ray photon beam induces a density rearrangement, the glass appears frozen on the timescale of the process. The temperature does not then play any relevant role here, neither at low temperature nor close to $T_g$. This further explains why Eq.(5.10) works so well in the undercooled liquid. If our interpretation is correct, we could observe an interplay between spontaneous and beam-induced dynamics at high temperatures, i.e. at a temperature where the timescale of the spontaneous density relaxations in the liquid matches that of the beam-induced effect. However, this timescale is for the moment out of range for XPCS experiments at synchrotron radiation sources.

The role of stresses in the beam-induced relaxation was quickly recognized in the first works on the $SiO_2$ silica glass [8]. There the authors found out that this relaxation is characterized by compressed correlation functions ($\beta > 1$), a phenomenon nowadays observed in many systems and considered an accepted symptom of stress-related dynamics [3–5, 145, 152, 186], as discussed in detail in Ch.(5). Until now, however, borate glasses have always shown stretched or near simple exponential relaxations [9, 104, 109, 159]. Here we report that this class of glasses show compressed correlation functions, in agreement with observations of pure silica glass [8]. The stark contrast of our findings with respect to the previous studies [9, 104] is attributed to two reasons. First of all, the use of new generation, single photon counter detectors in place of CCD cameras has greatly improved the quality of wide angle XPCS data. The high frame rate of the EIGER detector utilized here does not limit the lowest reachable integration time, which is actually fixed by the intensity scattered by the sample. A second reason regards the peculiar dose-dependence of the dynamics in borate glasses. In the second part of this chapter we will discuss in detail that these systems exhibit a stretching of the correlation functions that takes place after a few GGy of absorbed dose. This could be the reason why compressed correlation functions were not observed in [159], where the steady-state, high-dose regime was studied.

Finally, a few comments should be made regarding the experimental setup. We have observed that compressed correlation functions can arise from artifacts in the setup, in particular from a rigid macroscopic movement of the sample, see Ch.(5) for the theoretical aspects and [187] for a work dedicated to the nature of these spurious compressed correlation functions. The results reported in this thesis have been obtained on different beamtimes at both the ESRF and PETRA III. In order to cause a spurious decorrelation, the beam position should move a considerable fraction of its linear size to cause a drop to $1/e$ of

the contrast. If we consider the ID10 beamline at the ESRF, the beam pointing stability is of the order of a micron, and the sample is mounted on a motorized stage with comparable or better stability. Being the beam of $10 \times 8\,\mu m^2$ (H × V FWHM), the observed decorrelation is incompatible with a macroscopic relative movement of the sample with respect to the beam. Furthermore, if that was the reason behind our observations, one would expect pure Gaussian-like correlation functions ($\beta = 2$). The very same considerations hold for the setup at P10 of PETRA III. We definitely exclude the possibility of artifacts of this kind for our results: these setups have been employed for measurements of extremely slow dynamics and their overall stability is in the range of several hours [4, 6, 7].
Fig.(6.5 *b*) shows the stretching parameter for the three thermal cycles discussed above as a function of the temperature. As clearly seen, deep in the glassy state ($T \ll T_g$) compressed correlation functions are measured for the beam-induced dynamics, with $\beta \sim 1.5$, incidentally close to the value measured in the silica glass by Ruta and co-authors [8]. This behavior validates our hypothesis that the relaxation proceeds through the stress-release mechanism upon radiolysis. Heating the sample close to $T_g$ we observe a stretching of the density correlation functions, with $\beta$ eventually falling below one and reaching the equilibrium value of the undercooled liquid. The value reported as a black-continuous line is the one reported in the literature [111], $\beta = 0.64$, and is compatible with the one measured here using DLS, $\beta = 0.57 \pm 0.04$ (black-dotted line). A similar temperature behavior was previously reported in metallic glasses [6] and in the pure boron oxide glass [110], despite not observing compressed correlation functions in the latter case.
The compressed nature of the correlation functions reported here does not depend on the annealing procedure: $\beta$ is always larger than one in the glassy state. This suggests that, as discussed above, the relaxation process is always stress-induced, and that only the effective size of the regions that rearrange after a photon absorption event is modified by annealing. We can observe in Fig.(6.5 *b*) that the stretching parameter $\beta$ decreases below 1 before reaching the glass transition temperature $T_g$. This last conclusion, however, is supported by just a few experimental data points and it is difficult to claim at this stage that it is a real signature of a physical process. If this result were confirmed by further experiments, it would highlight that the stretching parameter is extremely sensitive to the approach to the glass transition in a temperature range where the spontaneous relaxation time is still orders of magnitude longer than any accessible experimental timescale.

## 6.2 X-ray induced non-thermal annealing

In the second part of this chapter we tackle the problem of the dose dependence of the beam-induced dynamics. In the first paper on this effect, Ruta *et al.* showed that in $SiO_2$ and $GeO_2$ glasses the dynamics are stationary and completely reversible, at least up to given absorbed doses [8]. Beyond that threshold, structural modifications are clearly visible in the scattered intensity. We demonstrate here that, together with the structure, the dynamics of the glass change as well. This modification is permanent, suggesting that the beam-induced changes the glass to a new, more relaxed state.

### 6.2.1 The stretching of the correlation functions

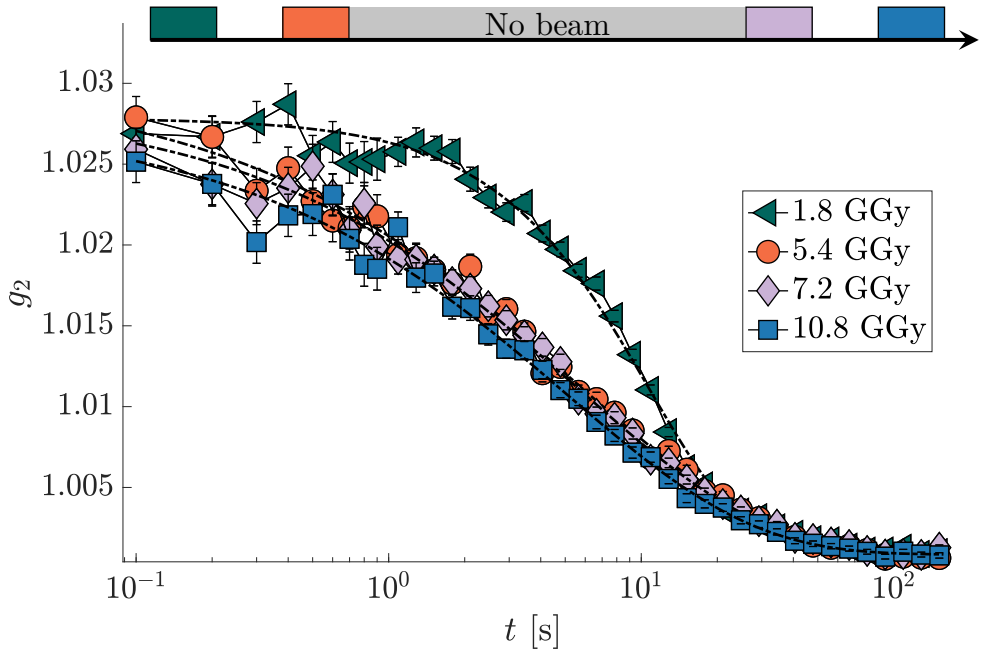


Figure 6.6: Correlation functions collected at the peak of the scattered intensity, $q = (17.0 \pm 1.8)\,\mathrm{nm}^{-1}$, for a $LiBO_2$ glass. The curves correspond to different total absorbed doses. On top of the figure, a sketch of the analysis procedure is reported, highlighting the 20 minutes of waiting time between the different parts of the measurement.

The data reported in this section have been collected in an experiment performed at beamline P10 at Petra III. A beam of 8.4 keV photons was focused with beryllium compound refractive lenses onto a spot of $1.9 \times 2.7\,\mu\mathrm{m}^2$ V×H full width half maximum (FWHM) on samples of lithium borate glasses, $(Li_2O)_x(B_2O_3)_{1-x}$, with two different compositions: x=0.22 and 0.5. The thickness was chosen to be well below the attenuation length for both compositions, and was in the

range W $\sim$ 100-150 µm. XPCS measurements have been performed at ambient temperature (T=295 K) and the scattered photons were collected using an EIGER 4M detector mounted on a goniometer arm in order to cover different scattering angles ($\theta \sim 2^\circ - 30^\circ$).
Fig.(6.6) shows the correlation functions measured for a $LiBO_2$ glass and for different absorbed doses. With the experimental parameters described above, the absorbed dose is 9 MGy per second. The green diamonds correspond to the first 200 seconds (thus 1.8 GGy) of exposure to the X-ray beam and the intensity correlation function $g_2$ is characterized by a compressed shape ($\beta > 1$). However, if the images starting from 400 to 600 seconds of exposure are correlated (corresponding to a total absorbed dose of 5.4 GGy), the $g_2$ clearly changes shape, becoming stretched ($\beta < 1$, orange circles) but with the same relaxation time as before. In order to check whether this stretching effect is due to a thermal effect in the sample, the beam was switched off for 20 minutes (see the sketch reported on the top of the figure) and then an additional measurement performed on the same spot. As can be seen, the function has not regained the compressed shape displayed at the very beginning of the measurement and we conclude that the effect is not a transient feature caused by a temperature-induced change. Finally, we note that the curves essentially do not change with further increases of the absorbed dose (7.2 GGy and 10.8 GGy). We now focus on the low-dose regime first, in order to highlight similarities and differences with the well studied case of the silica ($SiO_2$) glass.

### 6.2.2 The low-dose regime: ballistic like-dynamics

To begin with, let us consider the already discussed $LiBO_2$ glass. For each scattering angle, the detector has been divided in 3 or 4 regions of interest (ROIs), see Ch.(4) for details, depending on the scattered intensity at that given angle. In order to keep the absorbed dose as low as possible and catch the first transient behavior of the beam-induced dynamics in our borate glasses, we repeated measurements on a grid of points in the sample: each point is irradiated for few tens/hundreds of seconds, and then the sample is moved 10 µm away (in horizontal or vertical directions). We composed in this way grids up to 500 points covering few hundreds of microns of sample. During the post-processing, the right number of images is selected and the correlation function $g_2$ calculated for each point and averaged over the mesh. We carefully checked the homogeneity of the sample before performing the meshes (as already discussed in Ch.(4)) which is essential since, in order to average, we require the contrast to be the same for each scan. The obtained correlation functions then have extremely good statistics, comparable to those of a long-exposure scan, but with a relatively low dose, much less than 1 GGy. In order to understand the effect of the dose and to choose the best compromise between the duration of the measurement and the quality of the data, we calculated the KWW fit parameters for different subsets of images. An example for the $LiBO_2$ glass at small angles is shown in Fig.(6.7). The low-$q$ range is the most critical, since

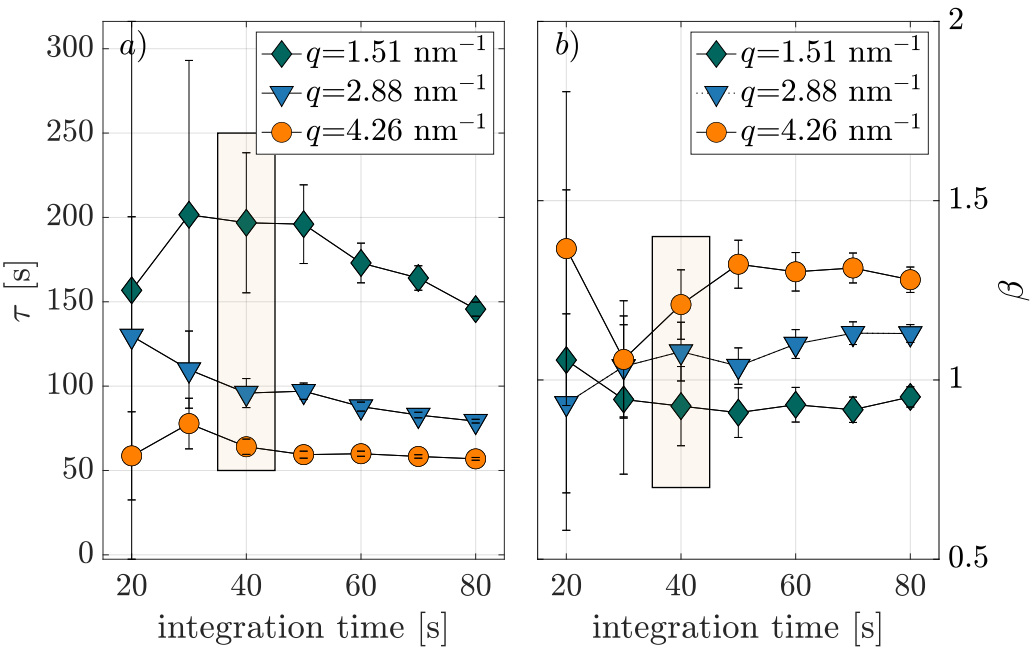


Figure 6.7: KWW fitting parameters for different lengths of the images' sequences at few selected $q$s. While for large $q$-values the relaxation time is shorter compared to the duration of the measurement, at the smaller $q$s only the first part of the decay is measurable: it is therefore necessary to accurately define a minimum duration to obtain good quality curves keeping the absorbed dose as low as possible. We decided to select 40 seconds of integration (highlighted rectangles) as a compromise.

there the correlation functions are longer and barely decay in the available time-window. We decided to utilize the lowest $q$-data to find the upper limit of the acceptable number of images for each point of the grid. The compromise between the duration of the measurement and a dose as low as possible is crucial, and in the end we opted for a maximum of 40 seconds of integration time, as shown in Fig.(6.7), corresponding to a total absorbed dose of 0.36 GGy. In that time window the relaxation time does not change considerably. The relaxation times of the derived correlation functions, in particular at the smallest scattering angles, are comparable with the duration of the measurement itself, as we anticipated. In order to better fit a KWW function to the data, we have fixed the baseline to the value obtained correlating images corresponding to different points of the mesh. Since those belong to different structural configurations, we obtain a reliable estimate of the baseline, which is essentially due to the non-uniform detector illumination (see Ch.(3) for details). This procedure allows us to correctly fit the data even if only the first part of the decay is present. A few representative experimental curves are shown in Fig.(6.8). The autocorrelation functions have been normalized to the experimental contrast $c$ after subtraction of the baseline ($d$) calculated as

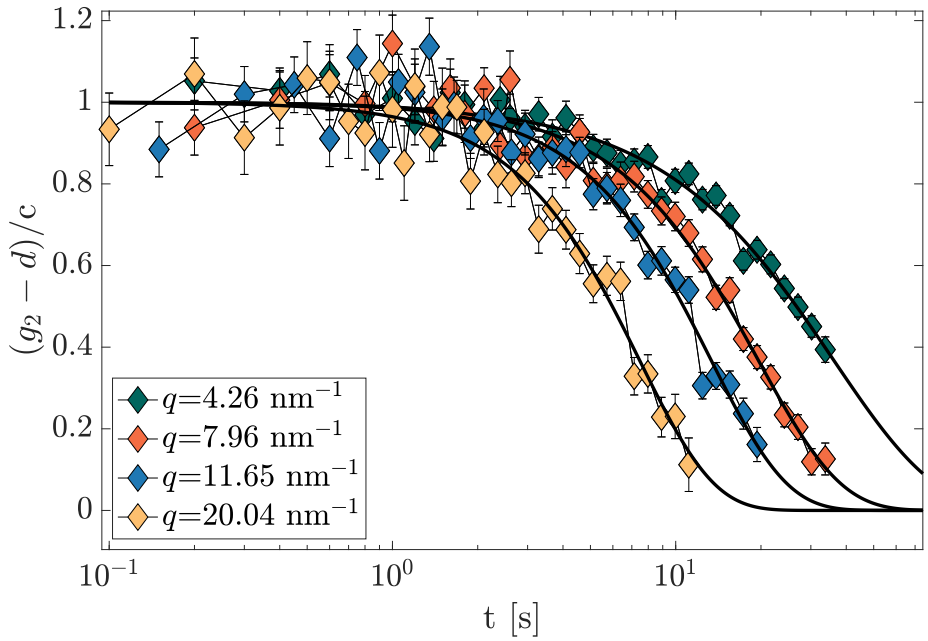


Figure 6.8: Correlation functions, with the baseline ($d$) subtracted and normalized to the experimental contrast ($c$), for different exchanged wave-vectors and with a total integration times of 40 seconds (green and orange diamonds), 23 seconds (blue points) and 13 seconds (yellow points). The black-continuous lines are the best KWW fits to the experimental curves.

described above. Note that the length of the scans is not fixed to 40 seconds for all momentum transfers but, instead, a variable dose is selected for different $q$-points. We in fact expect that, if the dynamics is characterized by a non stationary behavior, its dose dependence scales as that of the relaxation time (at that specific exchanged wave-vector value). The number of images used to calculate the correlation function has then been fixed to correspond to one relaxation time, $\tau$, up to an upper bound of 40 seconds.
In Fig.(6.9 $a$) the relaxation times obtained from fitting the KWW model to the $g_2$ functions are reported. The dynamics are characterized by a ballistic-like dependence, with $1/\tau \sim q$: the red dashed line corresponds to a fit with a power law, leading to $\tau \propto q^{-\gamma}$ with $\gamma = 1.09 \pm 0.04$. In order to verify whether our choice of the integration windows (fixed to one relaxation time) is critical to grasp the peculiarity of the observed dynamics, we also calculated the correlation functions fixing the integration time to 40 s for all exchanged wave-vectors. The obtained relaxation times as a function of $q$ are displayed in Fig.(6.9 $b$). As can be clearly seen, the ballistic like dynamics is still preserved at low momentum transfer, where the relaxation time is comparable to the integration time (here the integration time is 40 seconds for both analyses). However, at higher exchanged wave-vectors we observe a different $q$-dependence, which ends up in a sub-linear dependence with $1/\tau \sim \sqrt{q}$.

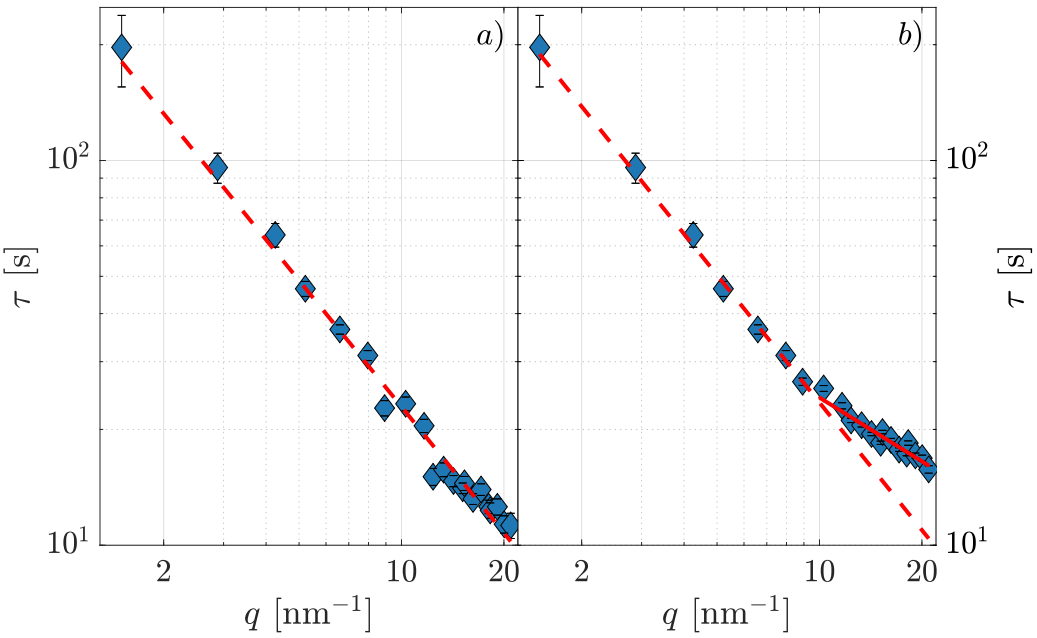


Figure 6.9: *a*) Relaxation time as a function of the exchanged wave-vector for the $LiBO_2$ glass. The doses absorbed by the sample were selected integrating for a time $T \sim \tau$, but with an upper limit of 40 seconds. The first 6 points have been exposed for this duration, corresponding to 0.36 GGy, while the others refer then to lower doses. The non-linear power law fit gives $\tau \propto q^{-\gamma}$, with $\gamma = 1.09 \pm 0.04$, compatible with the ballistic picture (red dashed line). *b*) Relaxation time as a function of the exchanged wave-vector fixing the integration time to 40 seconds for all points. For $q > 10\,\mathrm{nm}^{-1}$ the resulting dependence is $\tau \propto q^{-\gamma}$, with $\gamma = 0.55 \pm 0.06$ (red-full line).

This direct comparison confirms that the change in the $q$-dependence of the relaxation time from ballistic-like to sub-linear is clearly an effect introduced by the chosen integration window.
Fig.(6.10 *b*) shows the stretching parameter as a function of the scattering vector. At intermediate and high $q$s ($q \geq 8\,\mathrm{nm}^{-1}$) the value is almost $q$-independent and $\beta = 1.67 \pm 0.03$. A reduction is observed for $q < 8\,\mathrm{nm}^{-1}$, where $\beta$ tends to fall even below 1. However, note that this behavior does not change the picture discussed before. We still observe a ballistic-like dependence for the the average relaxation time $\langle\tau\rangle$, Fig.(6.10 *a*), which takes into account the $q$-dependence of $\beta$. We recall here that $\langle\tau\rangle = \tau/\beta\Gamma[1/\beta]$, where $\Gamma$ is the Euler function.
The drop in the stretching parameter at small angles is not observed, as we will show soon, for the $(Li_2O)_{0.22}(B_2O_3)_{0.78}$ glass and is probably an effect due to the fast changing dynamics. Fig.(6.11) shows the two time correlation functions for the lithium metaborate glass at $q = 1.5\,\mathrm{nm}^{-1}$ and $q = 15.3\,\mathrm{nm}^{-1}$ that exhibit non-stationary dynamics. However, at $q = 1.5\,\mathrm{nm}^{-1}$, a strong speed-up after few tens of seconds is observed together with an anomalous beating in

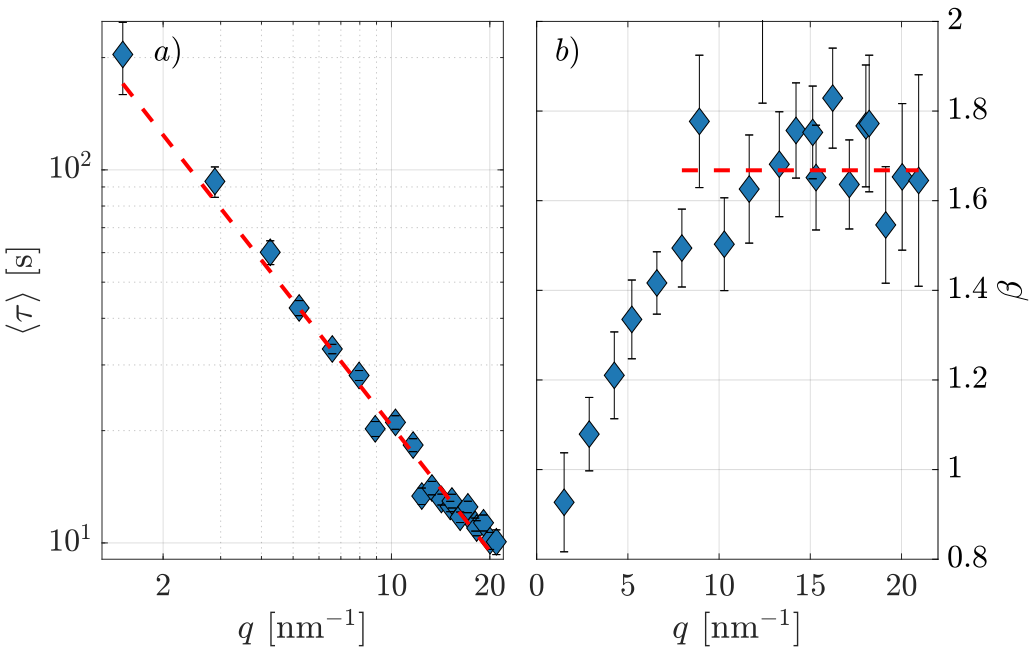


Figure 6.10: *a*) Wave-vector dependence of the average relaxation time for the $LiBO_2$ glass. The ballistic dynamics is well captured by the power-law fit, which leads to $\tau \propto q^{-\gamma}$, with $\gamma = 1.11 \pm 0.04$ (red dashed line). *b*) The stretching coefficient is reported as a function of the wave-vector. The average value for $q \geq 8\,\mathrm{nm}^{-1}$ is $\beta = 1.67 \pm 0.03$ (red dashed line).

the correlations. The window of 40 seconds for our "low-dose" investigation, despite being shorter than the first decay of correlation, could still be affected by the non-stationary dynamics. However, as reported in Fig.(6.10 *a*), the stretching of the correlation functions at low momentum transfer does not change the dependence of the average relaxation time that remains ballistic. The "beatings" in the two time correlation function are not observed after the sample has been irradiated. They may be due to the scattering from the surface changing upon X-ray irradiation but we do not have other evidence supporting this speculation.

The same measurements were performed on the $(Li_2O)_{0.22}(B_2O_3)_{0.78}$ glass. Here we applied the procedure reported for the $LiBO_2$ glass, keeping an integration time of up to 40 seconds per point (corresponding to an absorbed dose of 0.39 GGy) or equal to one relaxation time, when this is smaller than 40 s. Note that the small difference in the absorbed dose for 40 seconds of exposure for the two samples is due to small differences in thickness and attenuation length.

Fig.(6.12 *a*) shows the $q$-dependence of the relaxation time. As for the previous glass, $\tau$ obeys a ballistic-like $q$-dependence, namely $\tau \propto q^{-\gamma}$ with $\gamma = 1.10 \pm 0.02$. Furthermore, we observe that the stretching parameter is almost constant and compressed over the whole probed $q$-range ($\beta = 1.88 \pm 0.02$, Fig.(6.12 *b*)), confirming that the reduction observed in $LiBO_2$ at low $q$ is likely due to the

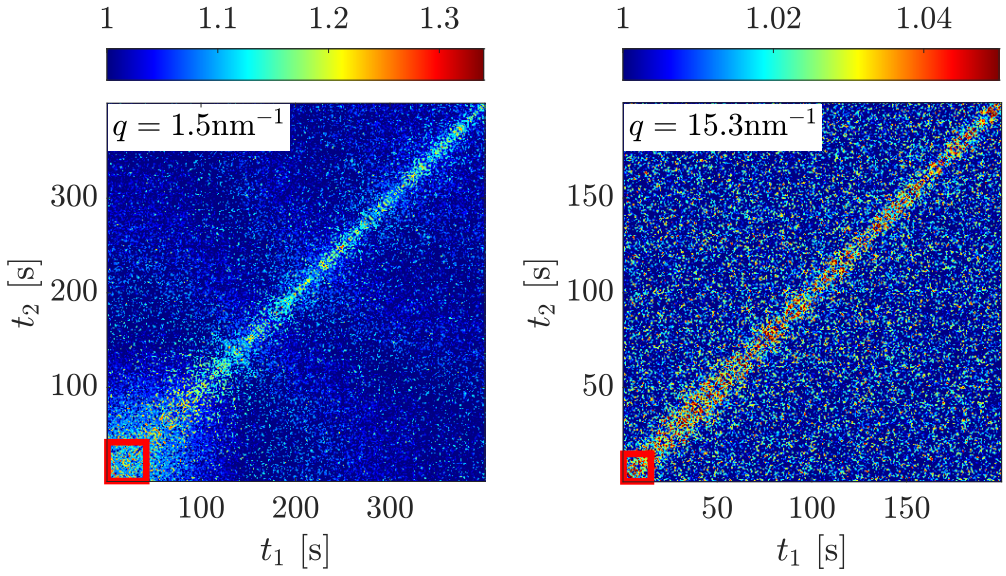


Figure 6.11: Two times correlation functions calculated for $q = 1.5\,\text{nm}^{-1}$ (*left*) and $q = 15.3\,\text{nm}^{-1}$ (*right*) for the $LiBO_2$ glass. The red squares at the bottom-left indicate the sub-matrix utilized to extract the correlation functions (40 and 14 seconds, respectively). An anomalous beating effect is observed only at small angles, and not at high $q$s. Note the different colorbars' scale for the two matrices, reflecting the higher contrast at low angles due to the reduced path length difference in the scattering volume, Eq.(3.60).

fast speed-up of the dynamics.

The dynamical properties reported in this section shine some light on the nature of the beam-induced relaxation. For very low doses, the emergence of a $\tau \propto q^{-1}$ for compressed correlation functions is a clear signature of a stress-induced process, as discussed in detail in Ch.(5). The role of stresses in the beam-induced dynamics was suggested in the first work on silica glasses, where compressed correlation functions were observed [8]. Here we captured an additional distinguishing feature of stress relaxation, which is the ballistic $q$-dependence. Recalling the considerations carried out in the chapter dedicated to the colloidal glasses, the dynamics here can be described in terms of stress-induced velocity fields. The values of the $\beta$ parameter obtained for the lithium borate glasses, close to 2 for the $(Li_2O)_{0.22}(B_2O_3)_{0.78}$, suggest that the dynamics proceed with the ballistic displacement of atoms over a distance $1/q$ with a relative particle velocity distribution close to a Gaussian (see Ch.(5)). Note that for $LiBO_2$, it is difficult to discriminate whether the observed $\beta = 1.67 \pm 0.03$ is due to an effectively different microscopic velocity field distribution or an artifact caused by non-stationary dynamics.

We highlight as well that the linear $q$-dependence of the relaxation time is ob-

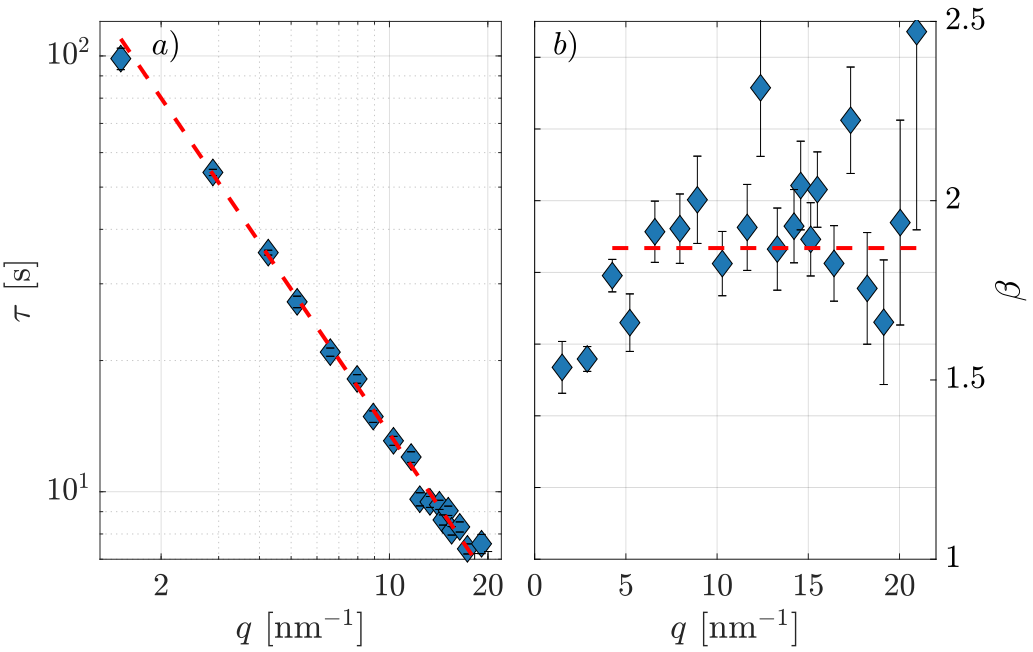


Figure 6.12: *a*) Wave-vector dependence of the relaxation time for the $(Li_2O)_{0.22}(B_2O_3)_{0.78}$ glass. The non-linear power law fit to the data gives a relaxation time $\tau \propto q^{-\gamma}$, with $\gamma = 1.10 \pm 0.02$ (red-dashed line). *b*) Stretching parameter as a function of $q$. The weighted average (red-dashed line) of the values obtained for $q > 4\,\mathrm{nm}^{-1}$ gives $\beta = 1.88 \pm 0.02$.

served over the whole exchanged wave-vector range investigated here, implying that the dynamics are effectively ballistic from inter-atomic distances up to few nanometers. Incidentally, this is the typical size of the regions "fluidized" by a photon absorption event, as demonstrated in Ch.(5). Furthermore, the data show that the relaxation is not affected by the local environment (de Gennes effect), but is fully dictated by the release of stresses at all probed length-scales. To conclude, we comment on the different results obtained previously for $LiBO_2$ [104, 109]. There, the inverse relaxation time was observed to scale as a square root, $1/\tau \propto \sqrt{q}$. From Fig.(6.9), it is clear that, as soon as the absorbed dose is increased above a given threshold (here few relaxation times), the power law describing $\tau(q)$ weakens, leading to a sub-linear $q$-dependence. At the doses utilized in [104, 109] the sample is being effectively irradiated to a level where the ballistic dynamics is no longer observable and further analysis in this direction will be reported later in this chapter. Regarding the first experiment on $SiO_2$ glasses [8], a $1/\tau \propto \sqrt{q}$ dependence was also reported. It would be interesting to further investigate that sample at even lower doses in order to discriminate whether the ballistic dynamics is present there too.

### 6.2.3 The dose dependence of X-ray annealed samples

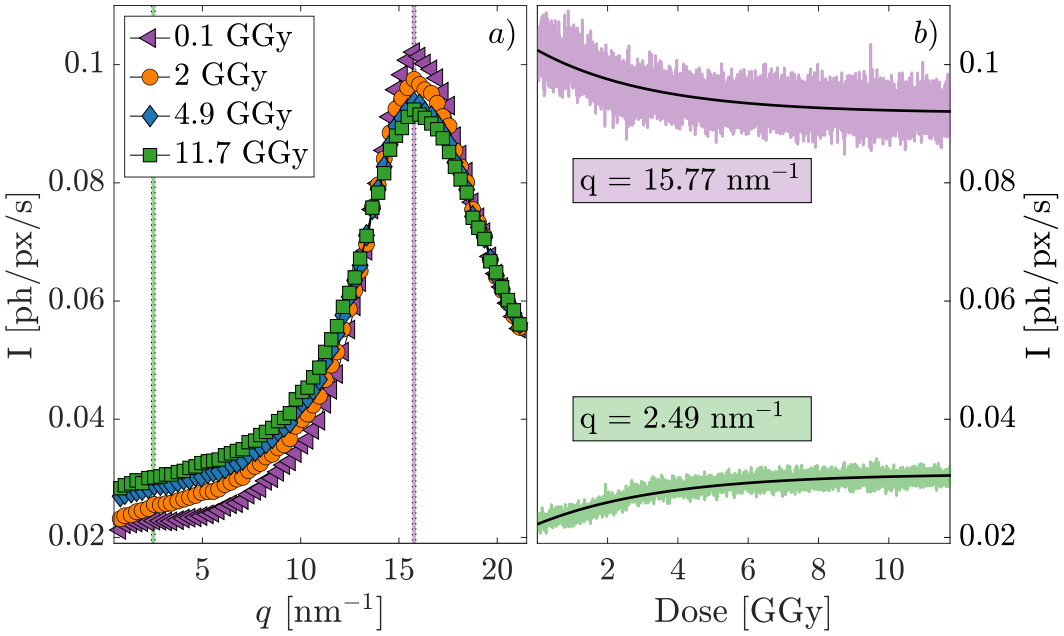


Figure 6.13: *a*) Scattered intensity for the $(Li_2O)_{0.22}(B_2O_3)_{0.78}$ glass as a function of the exchanged wave-vector, $q$, for different total absorbed doses. *b*) Two $q$-values have been selected and the dose-dependence of the scattered intensity modeled using $I(dose) = a + b\exp[-dose/\tau_d]$. The obtained values of the decay dose are $\tau_d = (3.53 \pm 0.05)$ GGy and $\tau_d = (3.24 \pm 0.07)$ GGy for $q = 2.49\,\text{nm}^{-1}$ and $q = 15.77\,\text{nm}^{-1}$, respectively.

As we have seen in the previous section, the dynamics of borate glasses are extremely sensitive to the absorbed dose. Thus, it is natural to investigate the relaxation properties as a function of the irradiation.
We start by discussing the structural modifications upon X-ray irradiation [8, 9, 104, 109] for the two different samples of interest here. Fig.(6.13 *a*) shows the scattered intensity for the $(Li_2O)_{0.22}(B_2O_3)_{0.78}$ glass. Two representative momentum transfer values have been selected ($q = 2.49\,\text{nm}^{-1}$ and $q = 15.77\,\text{nm}^{-1}$) and the intensity there is reported as a function of the dose, Fig.(6.13 *b*). We modeled the experimental dose-dependence as an exponential function, $I(dose) = a + b\exp[-dose/\tau_d]$, where $b > 0$ for $q > 14\,\text{nm}^{-1}$ and $b < 0$ for $q < 14\,\text{nm}^{-1}$ (following the intensity decrease/increase). The fit of this model to the dose-dependence of the intensity suggests a decay dose of $\tau_d \sim 3.3$ GGy at the considered exchanged wave-vector which is the typical time needed for the structure to change upon irradiation.
A similar analysis can be carried out over the investigated exchanged wave-vector range, as shown in Fig.(6.14). The dose-dependence of the scattered intensity is modeled at each $q$ and the obtained decay dose $\tau_d$ reported (red

squares). Two regimes are clearly observable. At small exchanged wave-vectors ($q < 3\,\mathrm{nm}^{-1}$) the typical decay dose seems to increase up to 5 GGy at the lowest probed $q$. For $q > 3\,\mathrm{nm}^{-1}$ the decay dose is almost independent of the exchanged wave-vector with a value close to 3 GGy. Note that the singular behavior at $q \sim 14\,\mathrm{nm}^{-1}$ and $q > 18\,\mathrm{nm}^{-1}$ is due to the fact that the scattered intensity does not change considerably in those ranges (see the scattered intensities shown in Fig.(6.14) for different doses). We conclude that the average dose which leads to a decay in the scattered intensity is $\sim 3$ GGy (value close to the one obtained from the two selected momentum transfer values in Fig.(6.13)). Note that this value is much larger than the total absorbed dose considered for the low-dose analysis reported in the previous section, where the maximum exposure was fixed to 0.39 GGy because the dynamics are more sensitive to the dose than the average structure. Finally, we observe that the intensity changes by about 15% at the peak of the structure factor while, at small angle, the change is much more marked, reaching 40% at $q \sim 2\,\mathrm{nm}^{-1}$.

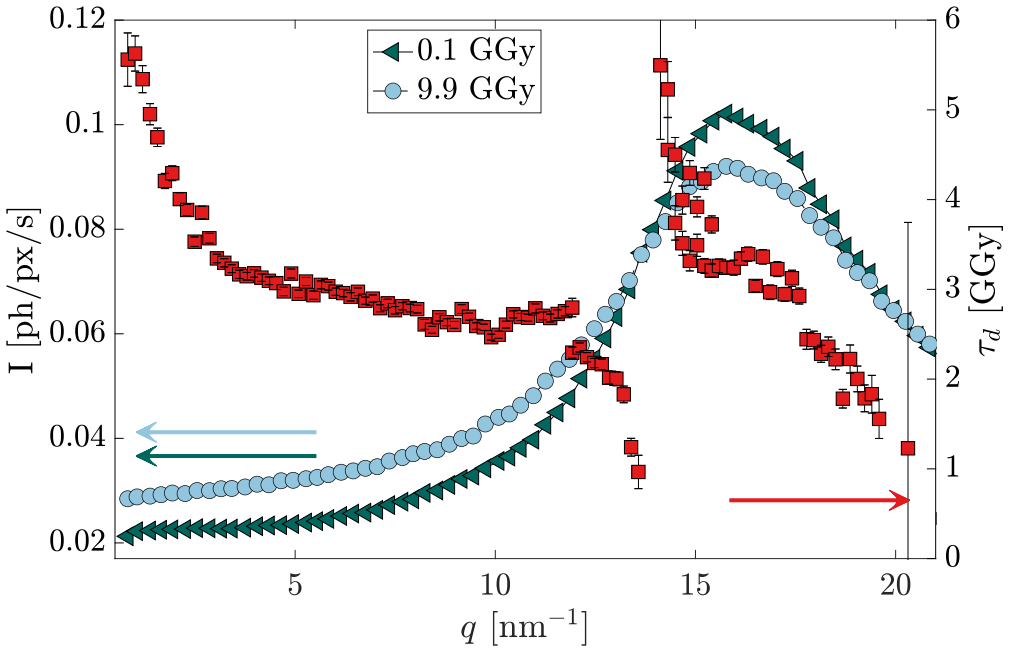


Figure 6.14: Scattered intensity of the $(Li_2O)_{0.22}(B_2O_3)_{0.78}$ glass as a function of the exchanged wave-vector for two representative doses. The red squares are the decay dose of the intensity as a function of $q$, according to the phenomenological equation reported in the main text.

The same procedure has been followed for the other sample of interest here, namely $LiBO_2$. Fig.(6.15 *a*) shows the scattered intensity for different doses at two representative exchanged wave-vectors (dashed regions) and the relative intensity as a function of the calculated dose (Fig.(6.15 *b*)). The fit to the model $I(dose) = a + b\exp[-dose/\tau_d]$ has been performed up to a total absorbed dose of 6 GGy (black-full lines). For $q \sim 1\,\mathrm{nm}^{-1}$, the formation of the low-$q$

tail discussed in Fig.(6.1) has been described adding an additional stretched exponential term (red line). The intensity starts to deviate from the simple exponential dependence after 5 GGy and a considerable difference is observed by 10 GGy. For this reason, 10 GGy could be indicated as a dose above which the glass suffers significant beam damage. However, we decided to use a more conservative threshold of 7 GGy for the discussions carried out in the following.

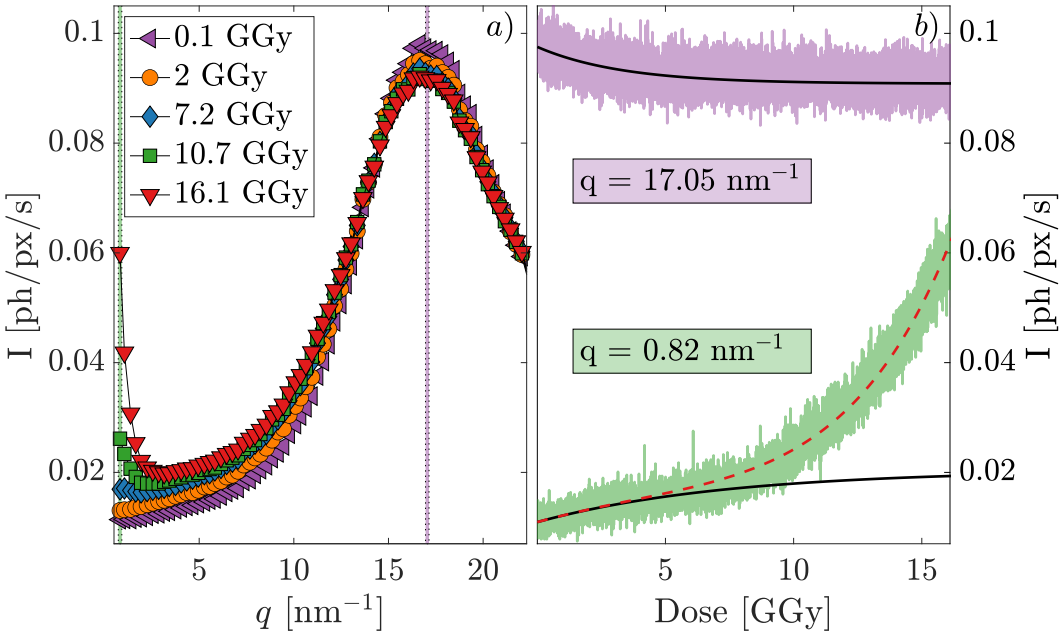


Figure 6.15: *a*) Intensity as a function of $q$ for different absorbed doses for the $LiBO_2$ glass. *b*) The dose-dependence of the scattered intensity at two exchanged-wave-vectors is reported, together with the best exponential fits (black-full lines) and the additional stretched exponential term related due to the small angle intensity increase (red dashed line). The obtained values of the decay dose (black lines) are $\tau_d = (7.4 \pm 1.3)$ GGy and $\tau_d = (3.3 \pm 0.3)$ GGy for $q = 0.82\,\mathrm{nm}^{-1}$ and $q = 17.05\,\mathrm{nm}^{-1}$, respectively.

Fig.(6.16) shows the fitted decay doses for the intensity as a function of $q$, as already done for the other glass of $(Li_2O)_{0.22}(B_2O_3)_{0.78}$. In this case, the decay is again almost constant for $q > 3\,\mathrm{nm}^{-1}$. A singular behavior in the fit results appears at points where the intensity does not change as a function of the dose. We can conclude that for $LiBO_2$ the scattered intensity also decays at $\sim 3$ GGy. A peculiar difference in the relative change in intensity is observed: while at small angles this change reaches 40 %, on the peak of the structure factor the intensity decay corresponds to a reduction of intensity of only about 6%, much less than for the $(Li_2O)_{0.22}(B_2O_3)_{0.78}$ glass.
At the beginning of this section we introduced the fact that in borate glasses, but possibly in other systems as well, the beam-induced dynamics is far from

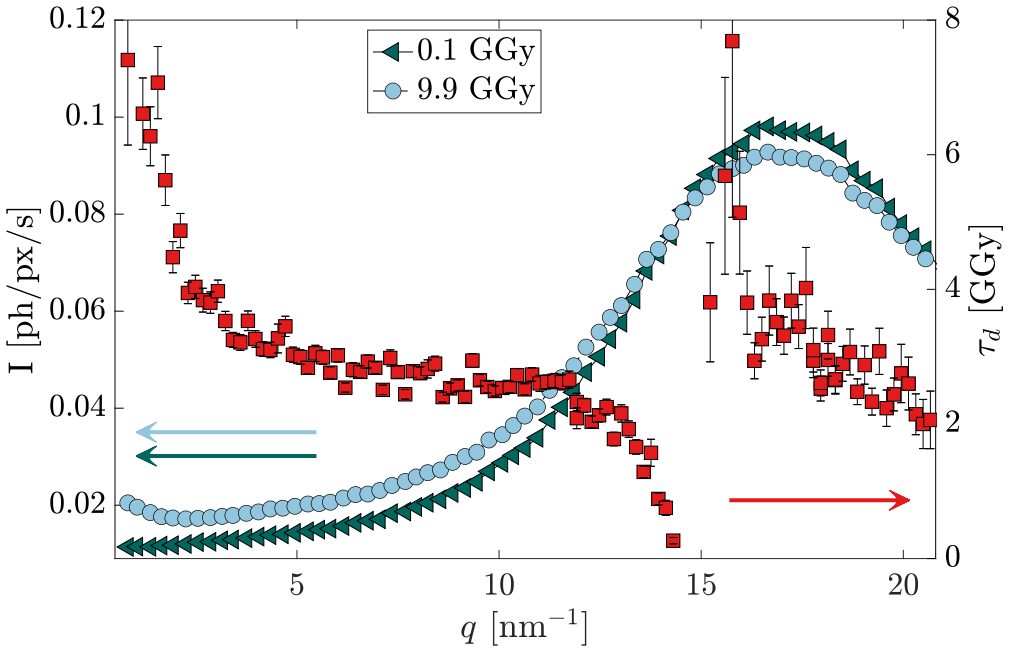


Figure 6.16: Scattered intensity for the $LiBO_2$ glass as a function of the exchanged wave-vector for two representative doses. Note that at 9.9 GGy the small angle peak starts to be visible. The red squares are the decay doses of the scattered intensity as a function of $q$, according to the phenomenological exponential equation reported in the main text. The fitting procedure has been performed up to 6 GGy for all $q$-points.

being a stationary process. Upon irradiation, the shape of the intensity correlation function changes strongly, passing from being compressed to stretched, see Fig.(6.6). For the sake of clarity, we now restrict our attention to the peak of the scattered intensity. The full $q$-dependence will be discussed in the next part of this section.
Fig.(6.17) shows the relaxation time and the stretching parameter for $LiBO_2$ as a function of the irradiation dose for $q = (17.14 \pm 0.45)\,\mathrm{nm}^{-1}$. For this analysis, we first computed a full two time correlation matrix for all the available images and then extracted small subsets lasting 300 seconds each. This "extraction" window has been moved in steps of 100 seconds in order to build up the dose dependence of the KWW parameters. Note that this procedure introduces some smoothing of the parameters, since we are considering partially overlapped intervals of images. However, the procedure allows the estimation of both the stretching parameter and the relaxation time. The lowest dose point reported in Fig.(6.17) has been extracted from the low-dose analysis discussed previously. Regarding the relaxation time, we observe that the reported values are constant for all absorbed doses, up to 15 GGy (see Fig.(6.6)). As we will show later, this result is not universal. However, the peculiarity of the beam-induced dynamics is captured by the stretching parameter, Fig.(6.17 *b*).

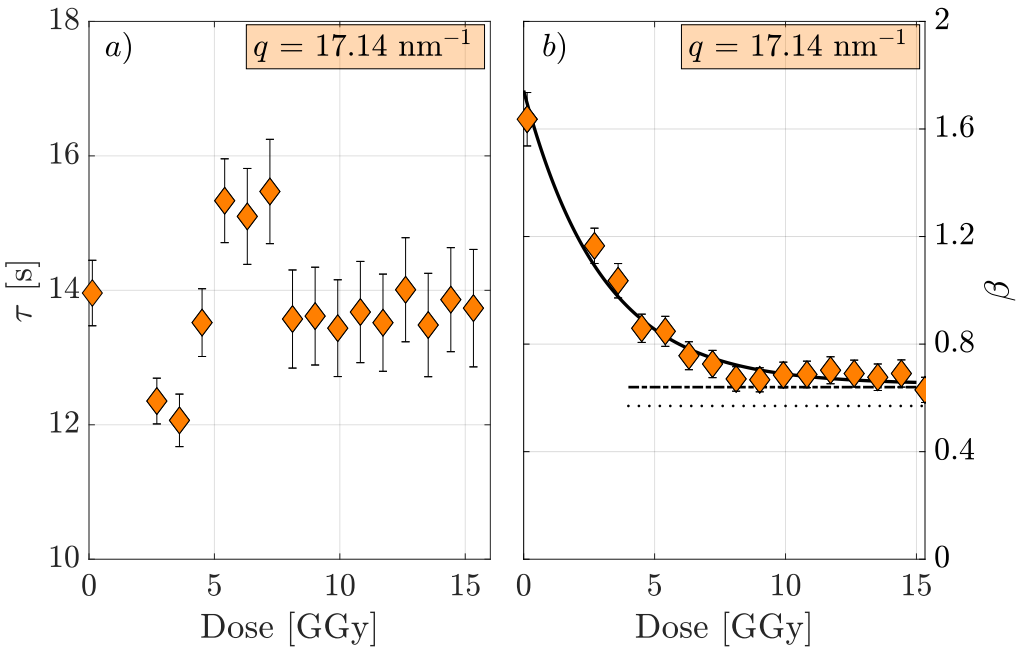


Figure 6.17: Relaxation time ($a$) and stretching parameter ($b$) as a function of the total absorbed dose for $q = (17.14 \pm 0.45)\,\mathrm{nm}^{-1}$ for the $LiBO_2$ glass. The intensity correlation functions used to extract these parameters have been calculated over 300 seconds of integration. The black-continuous line on the *right* is a fit of the experimental data with a simple exponential. The zero dose stretching parameter is $\beta(0) = 1.74 \pm 0.08$ while the infinite dose value is $\beta = 0.65 \pm 0.02$, compatible with the undercooled liquid values measured with visible dynamic light scattering (dotted points, $\beta = 0.57$) and reported in the literature (black-dashed line, $\beta = 0.64$) [111].

The decay of the stretching parameter, from the strongly compressed initial value down to a stretched plateau, is well described by a simple exponential law (black-continuous line). The model has no special physical basis, but gives the possibility to extract important information in a systematic way. In particular, the stretching coefficient is characterized by a decay dose of $\tau_d = (3.0 \pm 0.3)$ GGy, incidentally the same dose-scale reported for the intensity drop. Furthermore, the plateau value reached asymptotically is $\beta = 0.65 \pm 0.02$, a value in good agreement with that reported in the literature for the undercooled liquid [111] and measured here using dynamic light scattering. This is a quite surprising finding since, at room temperature, the glass of $LiBO_2$ is more than 400 K below the glass transition temperature and the dynamics that we are probing is purely dictated by X-ray photo-absorption. The fact that for the pristine glass compressed relaxation functions are observed is instead more expected. As discussed during the temperature investigation, the frozen-in stresses relax in a similar way as reported for metallic glasses [3, 4, 6], with the stresses being released by the beam-induced dynamics as for silica [8]. However, a drop

in the $\beta$ parameter was not observed before. In previous works on borates, the stretching parameter was always found smaller than one and even close to the equilibrium value [9, 104, 109, 159]. Here we observe the full story of the process. In the very beginning, the dynamics are governed by the stress relaxation while, after they have been fully released, the relaxation is very similar to the equilibrium typical, e.g., of the undercooled liquid (despite being our samples hundreds of degrees below the glass transition temperature). The process which is observed here is a sort of "X-ray annealing", where the photons effectively fluidize the network, restoring the ergodicity of the system. The main (relevant) difference with respect to what observed in a liquid is that the relaxation time is beam-induced, dictated by the incident X-ray flux.

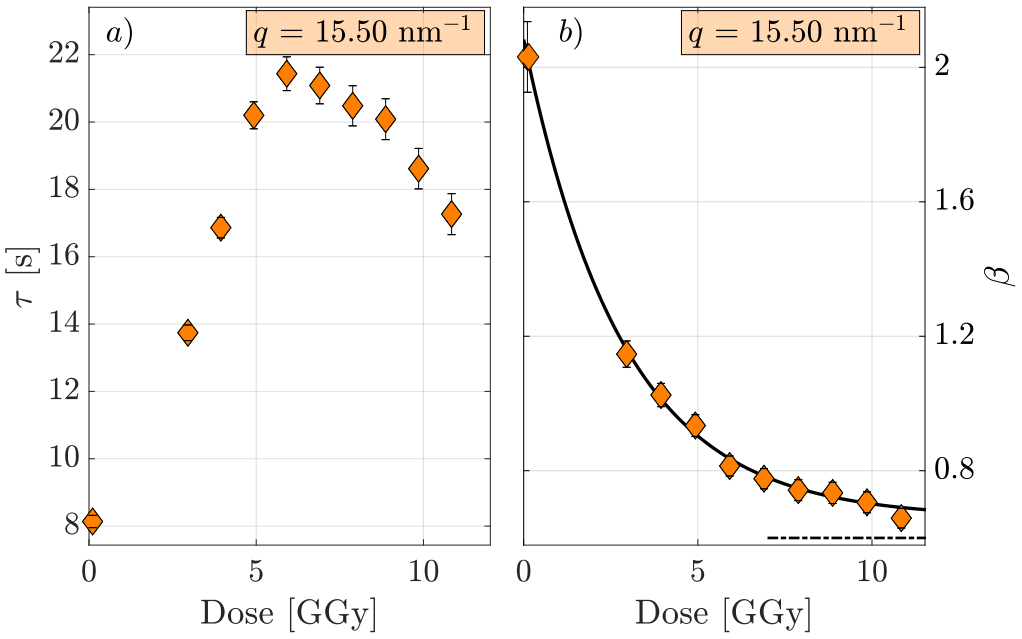


Figure 6.18: Relaxation time ($a$) and stretching parameter ($b$) as a function of the total absorbed dose for $q = (15.50 \pm 0.45)\,\mathrm{nm}^{-1}$ for the $(Li_2O)_{0.22}(B_2O_3)_{0.78}$ glass. The correlation functions have been calculated over a 300 seconds range. The black-continuous line on the *right* is a simple exponential decay fitted to the experimental data. The zero dose stretching parameter is $\beta(0) = 2.08 \pm 0.06$, compatible with a Gaussian shape, while the infinite dose limit is $\beta(\infty) = 0.66 \pm 0.02$, close to the undercooled liquid value reported in the literature [111] of $\beta = 0.60$ and shown in the figure as a black-dashed line.

A very similar dose dependence for the KWW fit parameters is observed for the $(Li_2O)_{0.22}(B_2O_3)_{0.78}$ glass. Fig.(6.18) shows the relaxation time and the stretching parameter for $q = (15.50 \pm 0.45)\,\mathrm{nm}^{-1}$. The relaxation time in this case is dose dependent, changing by almost a factor 3 between very low doses (0.11 GGy) and 6 GGy. The stretching parameter, reported in Fig.(6.18 $b$), shows a decreasing behavior once again well approximated by an exponential

decay. In this case, the plateau value reached for high doses is $\beta = 0.66 \pm 0.02$, still very close to the equilibrium value measured in the undercooled liquid [111].
For this glassy sample, the zero-dose correlation functions are almost Gaussians, with $\beta = 2.08 \pm 0.06$. The decay dose for the transition from the compressed to stretched behavior is $\tau_d = (2.8 \pm 0.2)$ GGy, a value again very similar to that corresponding to the decay of the scattered intensity (or to its increase, depending on the considered $q$). The similarity of the two dose-scales is intriguing since it suggests that a strong correlation exists between the change in the structural properties and in the dynamical ones. In particular, from the data reported here, we can conclude that the release of the stresses upon X-ray annealing drives the system to a new structural configuration, characterized by a different $S(q)$. Note that this corresponds to the evolution towards a new glassy state with reduced trapped-in stresses. While in $LiBO_2$ the increase of the scattered intensity in the range of $q \sim 1\,\mathrm{nm}^{-1}$ could suggest that some sort of damage is taking place (note the similar dose-scale for X-ray annealing and the growth of intensity at small angles), we can exclude that this plays a major role here. Indeed, the same photo-annealing process is observed for the $(Li_2O)_{0.22}(B_2O_3)_{0.78}$ glass, where no signature of small-angle scattering increase is visible up to $\sim 12$ GGy. We exclude then that the observed transition is due to beam damage. However, a dedicated small angle study of the irradiated $LiBO_2$ glass could clarify the nature of the small-angle scattering. In order to grasp more details about this X-ray annealing process and possible connections to the undercooled liquid state, we will discuss the exchanged wave vector dependence of the relaxation process in the next subsection.

### 6.2.4 The $q$-dependence of X-ray annealed samples: towards the liquid state

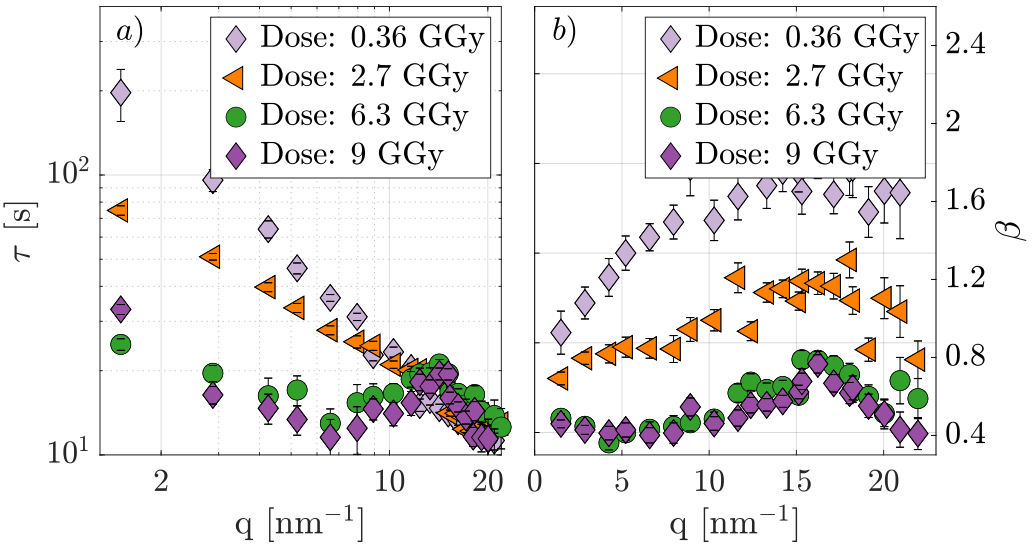


Figure 6.19: *a*) Relaxation time as a function of $q$ for different absorbed doses for the $LiBO_2$ glass. *b*) Stretching parameter as a function of $q$ for different absorbed doses. A clear de Gennes narrowing is observable in the $q$-dependence of $\tau$ and a related oscillation appears also in that for $\beta$ once the stresses have been annealed-out.

We now want to understand how similar the undercooled liquid and the X-ray annealed glass are. The analysis reported here has been performed in the same way as described above with the two time correlation matrix computed for each $q$ value and for all the available images. Subsequently, an appropriate sub-matrix is extracted (the time-length was chosen to be 300 seconds). Finally, the $g_2$ function is calculated from the (sub) two time matrix and described using a KWW model. The absorbed dose has been fixed in the whole exchanged wave-vector range by selecting the same integration window for all the different momentum transfer. Note that the low dose data, exhibiting ballistic dynamics, were previously discussed in Sect.(6.2.1).
First, let us start to consider the $LiBO_2$ glass. Fig(6.19 *a*) shows the relaxation time for different total absorbed doses. An unusual dose dependence is observed as a function of $q$. On the peak of the structure factor ($q \sim 17\,\mathrm{nm}^{-1}$) $\tau$ is almost dose-independent while, a strong dependence is observed at smaller exchanged wave-vectors, in the range $q \sim 1 - 10\,\mathrm{nm}^{-1}$. The relaxation time decreases abruptly by almost one decade at the smallest probed $q$. The net effect is a weakening of the $q$-dependence of the relaxation time and the formation of a "peak" of slower relaxation close to the maximum of $S(q)$: this is the de Gennes effect discussed in Ch.(4). A similar oscillation in phase with $S(q)$ is observed in the stretching parameter, Fig(6.19 *b*).
Fig.(6.20 *a*) shows the same relaxation times as before, but with a power law

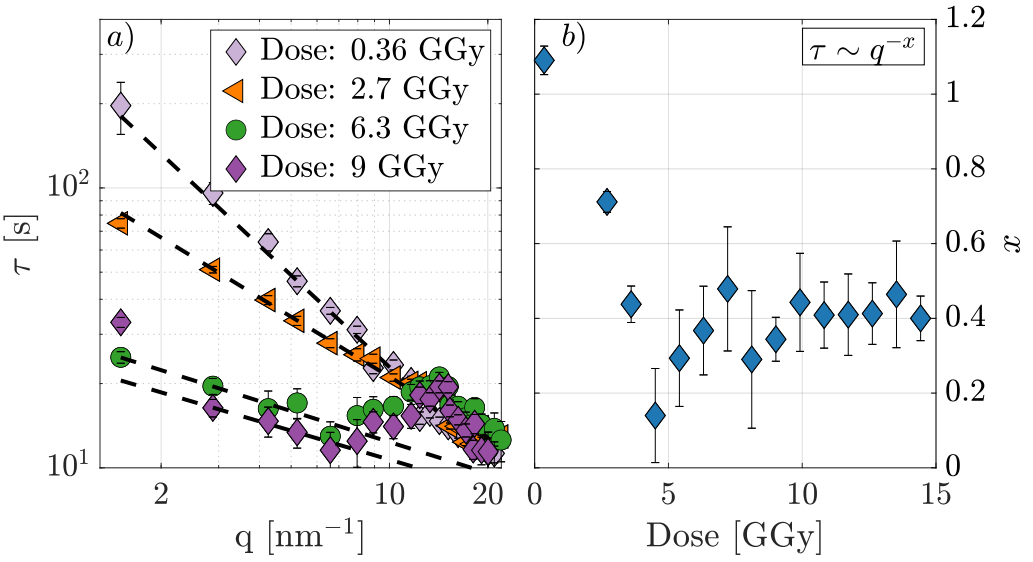


Figure 6.20: *a*) Relaxation time as a function of $q$ for different absorbed doses for the $LiBO_2$ glass, as already reported in Fig.(6.19). The black-dashed lines are power law ($\tau = \alpha \cdot q^{-x}$) fits to $\tau$ for $2 \leq q \leq 8\,\mathrm{nm}^{-1}$ (for the lowest dose, the fit has been performed over the whole available $q$-range). *b*) The fitted power law exponent $x$ is reported as a function of the absorbed dose.

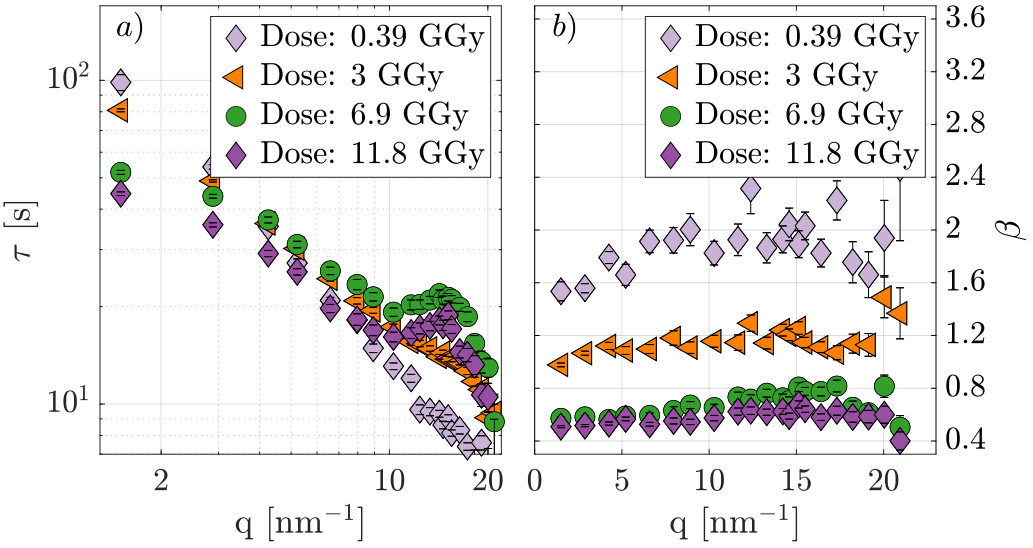


Figure 6.21: *a*) Relaxation time as a function of $q$ for different absorbed doses for the $(Li_2O)_{0.22}(B_2O_3)_{0.78}$ glass. *b*) Stretching parameter as a function of $q$ for different absorbed doses. The de Gennes effect is very pronounced in the $q$-dependence of the relaxation time, but the corresponding oscillation in the stretching parameter $\beta$ is very weak.

fitted over the low $q$ range (black-dashed lines). The power law weakens with increasing dose, as reported in Fig.(6.20 *b*), passing from a ballistic regime

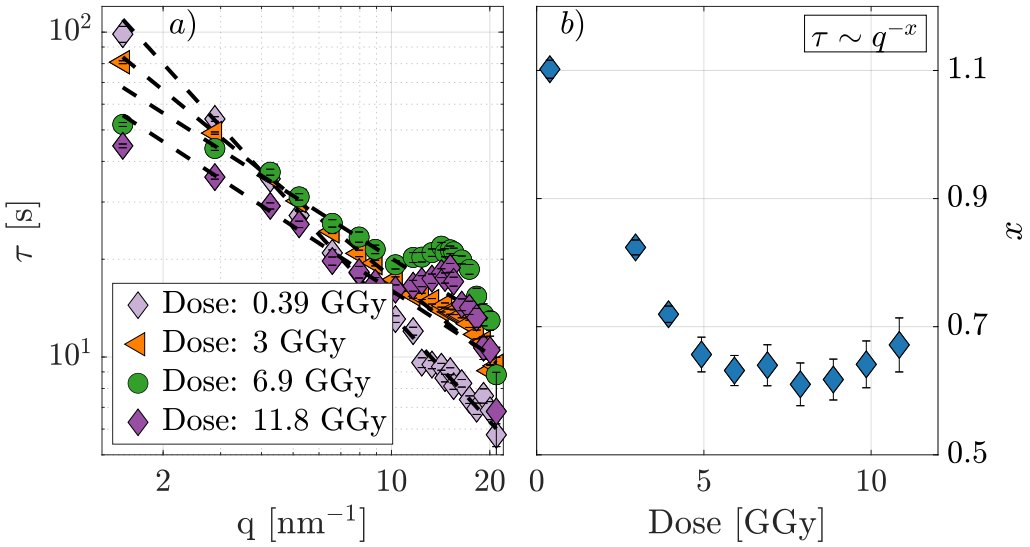


Figure 6.22: *a*) Relaxation time as a function of $q$ for different absorbed doses for the $(Li_2O)_{0.22}(B_2O_3)_{0.78}$ glass, as already reported in Fig.(6.19). The black-dashed lines are power law ($\tau = \alpha \cdot q^{-x}$) fits to $\tau$ for $1 \leq q \leq 8\,\mathrm{nm}^{-1}$ (for the lowest dose, the fit has been performed over the whole available $q$-range). *b*) The fitted power law exponent $x$ is reported as a function of the absorbed dose.

($1/\tau \sim q$) to $1/\tau \sim \sqrt{q}$. Observing the exponent $x$ as a function of $q$, it is clear that after a few GGy the ballistic dynamics are already washed out, reaching practically a $1/\tau \sim \sqrt{q}$ dependence as reported in [104, 109].
Very similar considerations are also valid for the $(Li_2O)_{0.22}(B_2O_3)_{0.78}$ glass. Fig.(6.21) shows both the relaxation time and the stretching parameter as a function of $q$ for a few relevant absorbed doses. Here we observe that the relaxation time is not constant at the peak of the structure factor ($q \sim 15\,\mathrm{nm}^{-1}$) but increases with the dose, as reported previously in Fig.(6.18 *a*). We still observe the development of a clear de Gennes narrowing, with a weakening of the overall $q$-dependence of $\tau$. The stretching parameter decreases accordingly with the absorbed dose, while in this specific case the oscillation in phase with the $S(q)$ is almost absent, in contrast to what observed in $LiBO_2$. In Fig.(6.22 *a*) the relaxation time is again shown together with the power law fit, $\tau = \alpha \cdot q^{-x}$. In this case too, the disappearance of the ballistic dynamics is evident after an absorbed dose comparable with the intensity decay dose (or stretching coefficient decay dose) of few GGy.

### 6.2.5 Direct comparison with the liquid

To better account for the similarities between X-ray annealed glasses and undercooled liquids, we can compare the XPCS results shown in Fig.(6.23) with the structural relaxation time of the undercooled liquid $LiBO_2$, investigated in Ch.(4) (plotted as light-blue circles appropriately normalized for its peak value $\tau_{max}$). Note the close similarity with the X-ray annealed glass: both display the de Gennes narrowing on top of an almost flat $q$-dependence, as expected from simulations of different systems [116, 120, 125, 126] and as reported in undercooled metallic liquids [95]. As discussed in Ch.(4), the stretching parameter for the correlation functions for the liquid has been fixed to the value $\beta = 0.50$ in the whole exchanged wave vector range, again very similar to what observed for the X-ray annealed glass. In Fig.(6.23) we reported the de Gennes approximation, $S(q)/q^2$, utilizing the structure factor of the pristine glass (black-dashed line) and the photo-annealed one (red-dashed line). It is clear that the curves, regardless of failing to capture the low-$q$ regime for the relaxation time as anticipated, well approximate the behavior around the peak. Moreover, the photo-annealed glass displays the peak of the relaxation slightly shifted towards lower $q$s, a behavior reproduced by the de Gennes narrowing approximation too.

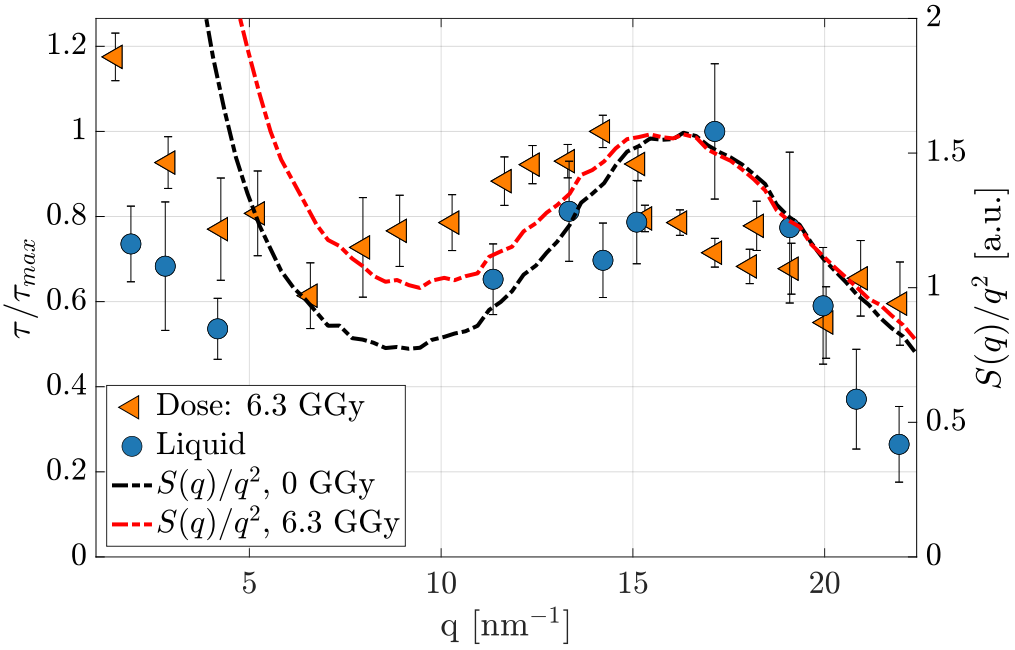


Figure 6.23: Relaxation time as a function of the the exchanged wave-vector $q$ for the undercooled liquid at T=708 K (light-blue dots) and the X-ray annealed glass (orange points). The data have been normalized to the value at the peak of the oscillation at finite $q$, $\tau_{max}$. The de Gennes approximation for $\tau(q)$ is reported as a black-dashed line and a red-dashed line for the pristine and photo-annealed glasses, respectively.

Fig.(6.24) shows the very same data as in the previous figure, but now compared to the structure factor, $S(q)$. As it can be seen, the flat $q$-dependence observed at small exchanged wave-vector is well captured by the $S(q)$, together with the increasing relaxation time before the peak value ($q \sim 17\,\mathrm{nm}^{-1}$). At high exchanged wave-vectors, instead, the relaxation time displays an important reduction which is not captured by the structure factor. However, overall the relaxation time for both the liquid and the photo-annealed glass oscillates in phase with the structure factor, as observed for example in [95], a clear sign that the observed dynamics involves a collective density relaxation.

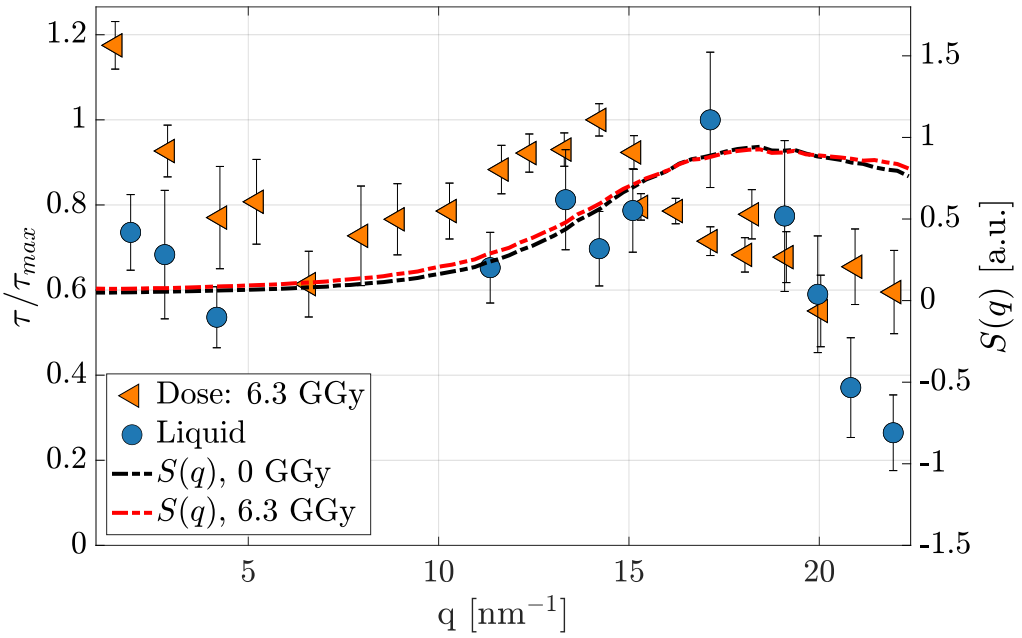


Figure 6.24: Relaxation time (normalized) as a function of the the exchanged wave-vector $q$ for the undercooled liquid at T=708 K (light-blue dots) and the X-ray annealed glass (orange points). The structure factor $S(q)$ has been reported for the pristine glass (black-dashed line) and the photo-annealed one (red-dashed line).

Note that an oscillation in $q$ in phase with the $S(q)$ is also observed in the stretching parameter for the X-ray annealed glass of $LiBO_2$, Fig.(6.19), while it is almost missing for the $(Li_2O)_{0.22}(B_2O_3)_{0.78}$ glass.
Despite our experimental data showing a fascinating agreement with most simulations [116, 120–122] (but not all, see [126]), we should spend few words here discussing the role of the beam-induced dynamics. In fact, recalling Fig.(6.3), we note that the true value of the structural relaxation is almost a factor 2 slower than the characteristic time measured experimentally. Utilizing the formalism discussed above, in particular Eq.(6.1-6.2), we can extrapolate a value of $\tau_\alpha = (10.6 \pm 0.6)\,\mathrm{s}$ at the peak of the structure factor ($q \sim 17\,\mathrm{nm}^{-1}$). All the data shown in Ch.(4) have been collected with an attenuated beam

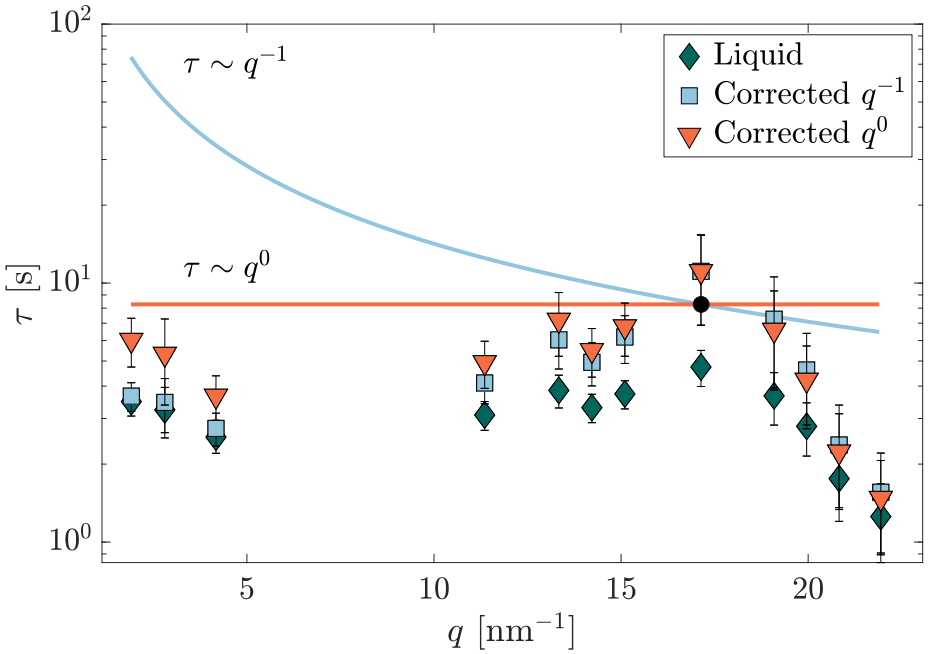


Figure 6.25: Relaxation time for undercooled $LIBO_2$ liquid at the temperature T=708 K (green points) together with the same data corrected for the beam-induced effect (light-blue and orange points). Two possible $q$-dependencies have been guessed for the $q$-dependence of the beam-induced characteristic time: $\tau_{ind} \sim q^{-1}$ (light-blue line) and $\tau_{ind} \sim q^0$ (orange line).

$F = 0.2067 F_0$. Following Eq.(6.1-6.2) we can estimate the contribution of the beam-induced dynamics, which is equal to $\tau_{ind} = (8.3 \pm 0.5)$ s. A possible correction scheme for the experimental data is thus the deconvolution of the beam-induced effect utilizing Eq.(6.1). While this is straightforward at the $q$-value corresponding to the maximum of the structure factor (where $\tau_{ind} = (8.3 \pm 0.5)$ s), we need to guess a possible $q$-dependence for the beam-induced dynamics in order to correct the data in the whole $q$-range. We have demonstrated that for very low doses the dynamics are almost ballistic and that $\tau$ tends to depend on $q$ as a square root on increasing the dose. However, this process is in competition with the structural relaxation and we do not have direct access to it. A step ahead can be made considering the findings on photo-annealing discussed in this chapter, where we have shown that the beam-induced relaxation becomes almost $q$-independent as soon as the sample is annealed towards the equilibrium state. In this spirit, in the undercooled liquid we could expect an almost flat $q$-dependence of the beam-induced dynamics. For these reasons, we show in Fig.(6.25) the experimental data for the $LiBO_2$ liquid (green points) together with the ones deconvoluted assuming a beam-induced dynamics with two different power laws: $\tau_{ind} \sim q^{-1}$ (light-blue points) and $\tau_{ind} \sim q^0$ (orange points). The black dot is the beam-induced relaxation time extrapolated from Fig.(6.3) and is a fixed point for both possible $q$-dependences.

The difference between the two correction schemes is small. The structural relaxation time remains basically $q$-independent, and shows the characteristic slow down of the dynamics in the proximity of the peak of the structure factor (de Gennes narrowing effect).

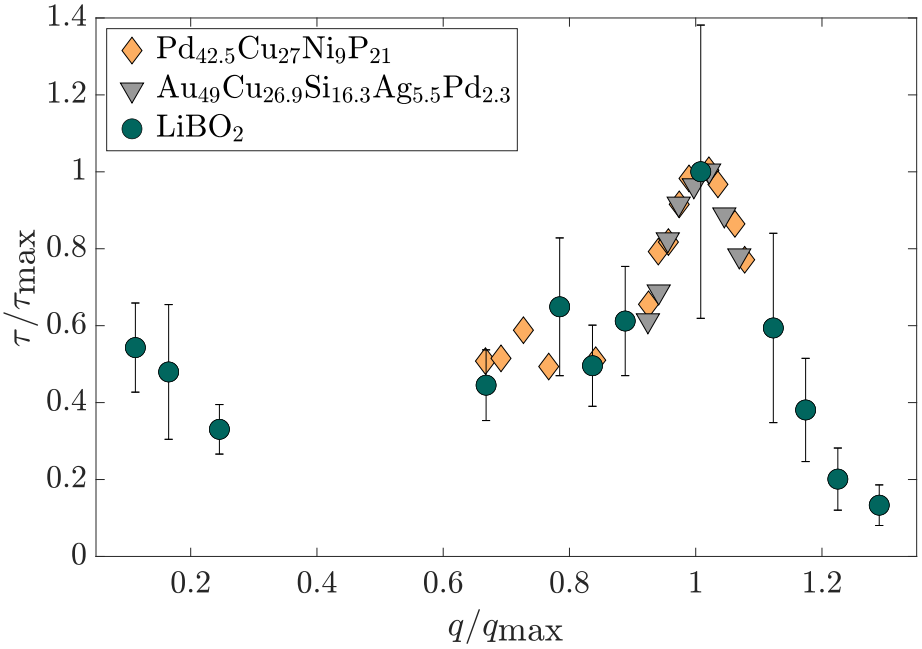


Figure 6.26: Relaxation time as a function of the exchanged wave-vector for three different systems. The exchanged wave-vectors have been normalized for the value, $q_{max}$, corresponding to the peak of the structure factor. The relaxation time has been normalized accordingly for $\tau_{max} = \tau(q_{max})$. The $LiBO_2$ data (T=708 K) have been corrected for the beam-induced dynamics effect, assuming for it a $\tau_{ind} \sim q^0$ dependence. *The data for the liquid metals are taken from [95].*

Recently, a very similar result was reported for liquid metals where the probed dynamics is purely spontaneous [95]. In Fig.(6.26) we show our data for the $q$-dependence of the structural relaxation time for liquid $LiBO_2$ together with the ones of [95]. For the purpose of comparing such different data, both in magnitude of the relaxation time and structure factor peak position ($q_{max}$), we normalized the exchanged wave-vector for $q_{max}$ and the relaxation time for the corresponding $\tau_{max} = \tau(q_{max})$. The data reported for the $LiBO_2$ have been corrected for beam-induced dynamics assuming a $\tau_{ind} \sim q^0$ dependence, which in our opinion is the most plausible one. In any case, as discussed above, the influence of this choice is very small. The strong similarity between the two considered systems is clear. The relaxation time peaks in phase with the structure factor, gaining almost a factor 2 with respect to the low-$q$ regime. This behavior confirms that the de Gennes narrowing effect is an "universal" feature of the structural relaxation close to the glass transition [116, 120–122].

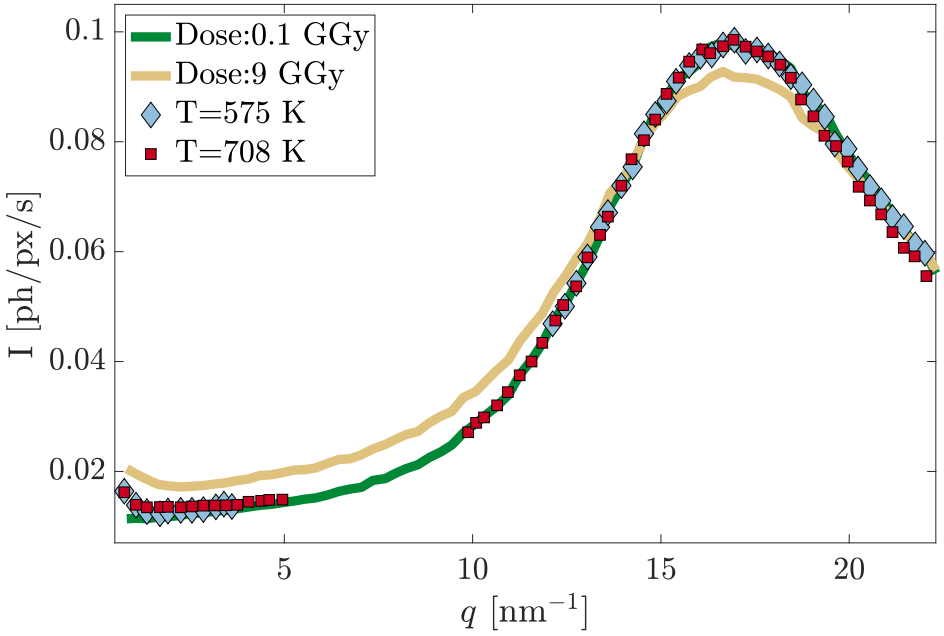


Figure 6.27: Scattered intensity as a function of the exchanged wave-vector for $LiBO_2$. The continuous lines are the data reported in Fig.(6.15) for two selected doses. The light-blue diamonds and red squares are the data (rescaled) collected during a different beamtime at P10 (Petra III, DESY). Note the presence of small angle intensity also for a negligible dose: this might be due to roughness of the sample surface.

To conclude this chapter, in Fig.(6.27) we compare the scattered intensity for different samples of $LiBO_2$. The continuous lines are the data already reported in this section for the glass at two relevant doses. The points (light-blue diamonds and red squares) have been collected during the beamtime discussed in Ch.(4,6) where the temperature dependence was investigated. They have been normalized in order to match the intensity on the peak at $q \sim 17\,\mathrm{nm}^{-1}$ which is necessary since in each beamtime we used samples with different thickness and different sample-detector distances, corresponding to different solid angles subtended by the detector pixels. After the normalization, we observe a perfect agreement with the pristine samples measured in the two different beamtimes (green-continuous line and light-blue diamonds). Heating the sample up to just above $T_g$ does not modify the structure of the system in any relevant way.
The main feature we note observing Fig.(6.27) is the strong difference between the scattered intensities of the pristine glass and the undercooled liquid with respect to the X-ray annealed one. This implies that the glass is X-ray annealed to a new, almost stress-free configuration, as suggested by the observation that the stretching parameter has basically reached its equilibrium value. We could

tentatively also say that this novel structure is more disordered, given the lower scattered intensity at the peak of the structure factor. These conjectures are, however, just speculations for the time being and will require additional investigations to be accepted or discarded.
In any case, strong similarities in the XPCS data have been here reported between X-ray annealed glasses and undercooled liquids. More studies have then to be carried out, employing different techniques in order to measure other properties (for example elastic moduli, density, effective temperature and enthalpy) of the X-ray annealed glasses and clarify the nature of these systems.

# Chapter 7

# Conclusions

In this thesis we have reported a detailed study of the relaxation processes happening in glasses close to the glass transition temperature $T_g$. Our attention was focused on two very different classes of materials, namely colloidal and structural glasses, in which stress-induced rearrangements are in competition with the spontaneous structural relaxation.

## Stressed colloidal glasses: the induced-velocity field

Stresses are well known companions of amorphous materials, among which colloidal systems exhibit the most extreme stress-driven processes. An example is provided by the micro-collapsing gels [5], which paved the way to an intense research on stress-induced dynamics. In this thesis, we investigated in detail a suspension of silica nanoparticles dispersed in a binary mixture of water-2,6 lutidine. The peculiarity of the samples discussed here is the strong directionality of the dynamics. Our preparation procedure introduces stresses in the network which do not relax before the experiment and trigger rearrangements at the particle-size length-scale, characterized by the same symmetry of the container, a cylindrical capillary. The dynamics can be modelled using a formalism describing a net relative velocity field between different particles, whose signature is a ballistic dynamics ($\tau \sim 1/q$) with compressed correlation functions. The stretching parameter $\beta = 2$ is a symptom of a Gaussian distribution of relative particle velocities. In addition, we investigated in detail other aspects of this peculiar stress-induced relaxation. Using the formalism of the four point susceptibility, $\chi_4$, we demonstrated that the rearrangements proceed in a cooperative way, involving the joint displacement of almost $10^4$ particles. While the exact number is difficult to estimate [75], the length-scale of these dynamical heterogeneities is an astonishing few micrometers. An accurate analysis of $\chi_4$ with respect to $q$ and $t$ has shown that the dynamics have a maximum of correlation at times corresponding to the relaxation time $\tau$ and length-scales corresponding to the first neighbor distance. This result is in agreement with existing simulations for undercooled liquids [156], despite the relaxation in our case being completely dominated by stresses.

## The role of the network connectivity

A large part of the work presented here regards oxide glasses probed with X-Ray Photon Correlation Spectroscopy (XPCS) with focus, in particular, on the beam-induced dynamics [8]. While in the first studies [7–9], as well as in the analysis of the XPCS measurements for the undercooled liquids reported here, the photo-induced relaxation is treated as a detrimental effect which masks or distorts the spontaneous rearrangements, we have shown in this thesis that one can actually exploit this non-perturbative mechanism to efficiently investigate fundamental properties of glasses. In Ch.(5) we utilized this mechanism to study the medium-range order of lithium borate glasses. The structure of this class of systems has been recently discussed in terms of network topology, mostly due to the complex structures involving super-structural units in the medium range. The development of new models to account for the network rigidity [172, 173] is based on the available experimental results (mainly nuclear magnetic resonance measurements [165]) and on the calculation of the average number of constraints per atom, here called $n_c$. Note that many details of the network topology for alkali borate glasses are still unknown, and models are becoming more and more precise only in recent years [173]. We have demonstrated that the number of atoms (or equivalently the size of the regions) that move upon the absorption of a hard X-ray photon (the beam-induced dynamics) depends on the topology of the glass. In particular, this average size is in the range of few nm and becomes smaller the more the glass is stressed. The exact value ranges between 2.5 nm for pure boron oxide (an isostatic glass, $n_c = 3$) down to 1 nm for $LiBO_2$ (a stressed-rigid glass, $n_c = 3.25$). The reported approach to probe the network topology is one of the first attempts to directly measure it at the local atomic length-scale with scattering techniques, despite it is known to play a role on macroscopic properties [170]. Furthermore, our experiments shine new light on the role of alkali ions in the network: our data suggest that the model proposed in [173] could be refined in the spirit of numerical simulations [176]. The modified model developed here is further supported by the fact that it captures the network topology dependence of other physical quantities, for example the elastic moduli in the lithium-borate glasses. The results that we have reported show the potential of exploiting beam-induced dynamics as a pump and probe technique, and could pave the way to a deeper understanding of medium-range order in glasses, a length-scale difficult to access experimentally.

## The undercooled $LiBO_2$ liquid

We have further exploited the versatility of XPCS in order to explore the wave-vector dependence of the density-density fluctuations in the liquid in the range $2 \lesssim q \lesssim 22\,\mathrm{nm}^{-1}$, a $q$ (across the maximum of the structure factor) and time (order of seconds) range inaccessible to other experimental techniques. We demonstrated that the relaxation time of the density fluctuation is almost

constant at all probed length-scales, with a signature of de Gennes narrowing close to the peak of the structure factor, as reported in simulations for many [116, 120–122] but not all [126] systems. In fact we directly compared our results with recent experimental data obtained in undercooled liquid metals, systems well known not to display the beam-induced dynamics. The similarities we observed support the thesis that the de Gennes effect is an universal feature of undercooled liquids.
Despite the beam-induced dynamics contribution can be deconvoluted convincingly from the undercooled liquid data, as shown in Fig.(6.25), it is clear that further investigations of the $q$-dependence of the beam-induced relaxation time, $\tau_{ind}$, could give important information about the nature of the process. In particular, it would be interesting to compare it with the photo-annealed data obtained in Ch.(6). The most straightforward approach would be to perform the same experiment for different $q$-values using different X-ray beam fluxes, as done at the peak of the structure factor. This approach would allow us to disentangle the beam-induced characteristic time $q$-dependence from that of the structural relaxation. Finally, in order to get rid of the beam-induced effect from the beginning and measure directly the structural relaxation, a possible approach would be the low-dose scheme of speckle visibility [93, 188]. In all cases, new experiments are required in order to get access to the missing information.

## Beam-induced dynamics and photo annealing

In the last chapter of this thesis we explored the effect of the beam-induced dynamics on the properties of the glassy state. In particular, we demonstrated that in alkali-modified glasses compressed correlation functions, a symptom of a stress-relaxation mechanism, are observed as long as the absorbed dose is kept below a given threshold. This finding, similar to what has been observed in silica and germanate glasses [8], has been further investigated in the $LiBO_2$ glass showing that, on approaching the glass transition, the stresses trapped in the network are released, which gives rise to stretched correlation functions.
This picture is confirmed by the investigation of the $q$-dependence of the beam-induced dynamics, carried out on two particular glasses of the family $(Li_2O)_x(B_2O_3)_{1-x}$, with $x$=0.22 and 0.5. Our findings show that the dynamics proceeds ballistically, with a relaxation time inversely proportional to the exchanged wave-vector, $\tau \sim 1/q$ in the whole probed $q$-range. The property, very similar to the results obtained in the colloidal glass, clearly shows that this dynamics can be related to a relative velocity field between the atoms. The observed correlation functions are strongly compressed, with a value of $\beta$ approaching 2 for the $(Li_2O)_{22}(B_2O_3)_{78}$, indication of an almost Gaussian relative velocity distribution. The characteristic $\tau \sim q^{-1}$ dependence is observed over the whole probed exchanged wave-vector range and suggests that the dynamics is effectively stresses-related at least up to ∼nm.
It was quickly recognized that the X-ray beam absorbed by oxide glasses tends to

modify the structure of the glass [8, 9, 104]. In previous studies, it was imagined that the structure remains basically unaffected until a threshold dose is reached, and beyond that dose the beam damages the material. In this thesis, we aimed at investigating in more detail the effect of these structural modifications on the dynamical properties. We observed that the dynamics are much more sensitive than the structure to the X-ray beam with the stress-induced ballistic dynamics starting to disappear and being replaced by a dynamics characterized by a weaker $q$-dependence very quickly and at very small doses. At the same time, the $\beta$ shape parameter decreases from a strongly compressed value ($\beta \sim 2$) down to the near-equilibrium one reported in literature [111]. The typical dose needed for the dynamics to reach this limit is almost equal to the one observed for the change of the structural properties and is about 3 GGy for both glasses here investigated. A straightforward comparison of the data collected for the liquid state and those collected for these irradiated samples has shown fascinating similarities. Considering the $LiBO_2$ glass, after $\sim$ 6 GGy of absorbed dose the beam-induced dynamics is characterized by an almost flat $q$-dependence with a marked de Gennes narrowing close to the peak of the structure factor. This fact, together with the observation that the stretching parameter has decreased to the equilibrium value, suggests that the beam-induced dynamics effectively anneals out the residual stresses in the glass. In other terms, the non-thermal rearrangements triggered by the photon absorption, whatever is their exact mechanism, locally "fluidize" the network restoring the ergodicity. The system can then relax towards a more equilibrated configuration, releasing the trapped-in stresses.

## 7.1 Future perspectives and applications

In this thesis we explored the relaxation of the density across the glass transition, highlighting the different aspects of near-equilibrium dynamics, for example in the undercooled liquid state, and non-equilibrium dynamics, dominated here by the internal stresses. In order to investigate fundamental aspects related to this latter process, namely the stress release mechanism, we decided to study both colloidal glasses and the prototypical family of oxide ones. If in colloidal systems the out-of-equilibrium relaxations are a well-established feature [5, 148, 150, 151], in structural glasses the picture is still incomplete, in part due to the difficulties of probing the slow timescales (seconds) on the atomic distances. The studies of Ruta *et al.* on metallic glasses have elucidated the role of stresses [3, 4, 6], but the peculiar beam-induced dynamics observed in oxide glasses [8] complicates measurement and interpretation for the interesting case of oxide systems.

We have studied in some detail beam-induced dynamics in the borate oxide glasses. Among the topics touched here, one of the most intriguing is the dose-dependence of the dynamical and structural properties. In particular, we have observed that compressed correlation functions come together with the signature of ballistic dynamics. A detailed characterization of the $q$-dependence

of the beam-induced dynamics was reported previously in $SiO_2$ [8], where a $1/\tau \sim \sqrt{q}$ was observed instead. Here, on the other hand, we demonstrated that at very low doses the dynamics are characterized by ballistic displacements. It is clear that a complete description of the mechanism behind this effect is still missing and more experiments are required in the light of the results here reported.

As a second interesting point, we have discussed the effect named *photo-annealing*. We observed that the signatures of a stress-induced dynamics can be erased if the samples are exposed long enough to hard X-rays. After a few GGy (the value is likely sample dependent) the structure changes a bit, but with no clear symptoms of beam-damage. The dynamics, however, become very similar to the those measured in the corresponding undercooled liquid state. These results suggest that the beam-induced dynamics is effective in producing a new configuration of the glass via a non-thermal route. However, it still has to be clarified how much the X-ray annealed glasses are different from the pristine ones in terms of structure but also in terms of thermodynamic properties, e.g., enthalpy. One interesting possibility would be that, under X-ray irradiation, the glass is annealed and therefore reaches states lower in the potential energy landscape. This would imply that X-ray irradiation would be effective in producing stable glasses. This, however, is just a speculation for the time being, and will require new studies and additional experiments to be confirmed or discarded.

# Bibliography


[1] Angell, C. A. Formation of glasses from liquids and biopolymers. *Science* **267**, 1924–1935 (1995).

[2] Grübel, G. & Zontone, F. Correlation spectroscopy with coherent x-rays. *Journal of alloys and compounds* **362**, 3–11 (2004).

[3] Ruta, B. *et al.* Atomic-scale relaxation dynamics and aging in a metallic glass probed by x-ray photon correlation spectroscopy. *Physical Review Letters* **109**, 165701 (2012).

[4] Ruta, B., Baldi, G., Monaco, G. & Chushkin, Y. Compressed correlation functions and fast aging dynamics in metallic glasses. *The Journal of chemical physics* **138**, 054508 (2013).

[5] Cipelletti, L., Manley, S., Ball, R. & Weitz, D. Universal aging features in the restructuring of fractal colloidal gels. *Physical Review Letters* **84**, 2275 (2000).

[6] Ruta, B. *et al.* Relaxation dynamics and aging in structural glasses. In *AIP Conference Proceedings*, vol. 1518, 181–188 (American Institute of Physics, 2013).

[7] Ruta, B. *et al.* Revealing the fast atomic motion of network glasses. *Nature communications* **5**, 1–8 (2014).

[8] Ruta, B. *et al.* Hard x-rays as pump and probe of atomic motion in oxide glasses. *Scientific reports* **7**, 1–8 (2017).

[9] Pintori, G., Baldi, G., Ruta, B. & Monaco, G. Relaxation dynamics induced in glasses by absorption of hard x-ray photons. *Physical Review B* **99**, 224206 (2019).

[10] Barron, A. R. CVD of $SiO_2$ and related materials: An overview. *Advanced Materials for Optics and Electronics* **6**, 101–114 (1996).

[11] Kearns, K. L., Still, T., Fytas, G. & Ediger, M. D. High-modulus organic glasses prepared by physical vapor deposition. *Advanced Materials* **22**, 39–42 (2010).

[12] Swallen, S. F. *et al.* Organic glasses with exceptional thermodynamic and kinetic stability. *Science* **315**, 353–356 (2007).

[13] Masciovecchio, C. *et al.* Structural relaxation in liquid water by inelastic UV scattering. *Physical Review Letters* **92**, 255507 (2004).

[14] Creus, G. J. *Viscoelasticity—basic theory and applications to concrete structures*, vol. 16 (Springer Science & Business Media, 2012).

[15] Landau, L. *et al. Theory of Elasticity: Volume 7*. Course of theoretical physics (Elsevier Science, 1986).

[16] Williams, M. L., Landel, R. F. & Ferry, J. D. The temperature dependence of relaxation mechanisms in amorphous polymers and other glass-forming liquids. *Journal of the American Chemical Society* **77**, 3701–3707 (1955).

[17] Stillinger, F. H. A topographic view of supercooled liquids and glass formation. *Science* **267**, 1935–1939 (1995).

[18] Ediger, M. D., Angell, C. A. & Nagel, S. R. Supercooled liquids and glasses. *The journal of physical chemistry* **100**, 13200–13212 (1996).

[19] Debenedetti, P. G. & Stillinger, F. H. Supercooled liquids and the glass transition. *Nature* **410**, 259–267 (2001).

[20] Angell, C. A. Relaxation in liquids, polymers and plastic crystals — strong/fragile patterns and problems. *Journal of Non-Crystalline Solids* **131-133**, 13 – 31 (1991).

[21] Vogel, D. H. Das temperaturabhaengigkeitsgesetz der viskositaet von fluessigkeiten. *Physikalische Zeitschrift* **22**, 645 (1921).

[22] Fulcher, G. S. Analysis of recent measurements of the viscosity of glasses. *Journal of the American Ceramic Society* **8**, 339–355 (1925).

[23] Tammann, G. & Hesse, W. Die abhängigkeit der viscosität von der temperatur bie unterkühlten flüssigkeiten. *Zeitschrift für anorganische und allgemeine Chemie* **156**, 245–257 (1926).

[24] Scherer, G. W. Editorial comments on a paper by Gordon S. Fulcher. *Journal of the American Ceramic Society* **75**, 1060–1062 (1992).

[25] Stillinger, F. H. & Debenedetti, P. G. Glass transition thermodynamics and kinetics. *Annual Review of Condensed Matter Physics* **4**, 263–285 (2013).

[26] Richert, R. & Angell, C. Dynamics of glass-forming liquids. V. On the link between molecular dynamics and configurational entropy. *The Journal of chemical physics* **108**, 9016–9026 (1998).

[27] Kauzmann, W. The nature of the glassy state and the behavior of liquids at low temperatures. *Chemical reviews* **43**, 219–256 (1948).

[28] Adam, G. & Gibbs, J. H. On the temperature dependence of cooperative relaxation properties in glass-forming liquids. *The journal of chemical physics* **43**, 139–146 (1965).

[29] Angell, C. Landscapes with megabasins: polyamorphism in liquids and biopolymers and the role of nucleation in folding and folding diseases. *Physica D: Nonlinear Phenomena* **107**, 122–142 (1997).

[30] Ito, K., Moynihan, C. T. & Angell, C. A. Thermodynamic determination of fragility in liquids and a fragile-to-strong liquid transition in water. *Nature* **398**, 492–495 (1999).

[31] Goldstein, M. Viscous liquids and the glass transition: a potential energy barrier picture. *The Journal of Chemical Physics* **51**, 3728–3739 (1969).

[32] Stillinger, F. H. Exponential multiplicity of inherent structures. *Physical Review E* **59**, 48 (1999).

[33] Heuer, A. Exploring the potential energy landscape of glass-forming systems: from inherent structures via metabasins to macroscopic transport. *Journal of Physics: Condensed Matter* **20**, 373101 (2008).

[34] Stillinger, F. H. & Weber, T. A. Packing structures and transitions in liquids and solids. *Science* **225**, 983–989 (1984).

[35] Stillinger, F. H. & Weber, T. A. Hidden structure in liquids. *Physical Review A* **25**, 978 (1982).

[36] Stillinger, F. H., Debenedetti, P. G. & Sastry, S. Resolving vibrational and structural contributions to isothermal compressibility. *The Journal of chemical physics* **109**, 3983–3988 (1998).

[37] Stillinger, F. H. & Debenedetti, P. G. Distinguishing vibrational and structural equilibration contributions to thermal expansion. *The Journal of Physical Chemistry B* **103**, 4052–4059 (1999).

[38] Sastry, S. The relationship between fragility, configurational entropy and the potential energy landscape of glass-forming liquids. *Nature* **409**, 164–167 (2001).

[39] La Nave, E., Mossa, S. & Sciortino, F. Potential energy landscape equation of state. *Physical Review Letters* **88**, 225701 (2002).

[40] Sciortino, F. & Tartaglia, P. Extension of the fluctuation-dissipation theorem to the physical aging of a model glass-forming liquid. *Physical Review Letters* **86**, 107 (2001).

[41] Sciortino, F. Potential energy landscape description of supercooled liquids and glasses. *Journal of Statistical Mechanics: Theory and Experiment* **2005**, P05015 (2005).

[42] Saika-Voivod, I. & Sciortino, F. Distributions of inherent structure energies during aging. *Physical Review E* **70**, 041202 (2004).

[43] Rehwald, C. *et al.* Aging effects manifested in the potential-energy landscape of a model glass former. *Physical Review E* **82**, 021503 (2010).

[44] Hansen, J.-P. & McDonald, I. R. *Theory of simple liquids* (Elsevier, 1990).

[45] Zemb, T. & Lindner, P. *Neutrons, X-rays and light: scattering methods applied to soft condensed matter* (North-Holland, 2002).

[46] Fick, A. Ueber diffusion. *Annalen der Physik* **170**, 59–86 (1855).

[47] Berne, B. J. & Pecora, R. *Dynamic light scattering: with applications to chemistry, biology, and physics* (Dover Publications, 1976).

[48] Williams, G. & Watts, D. C. Non-symmetrical dielectric relaxation behaviour arising from a simple empirical decay function. *Transactions of the Faraday society* **66**, 80–85 (1970).

[49] Young, A. P. *Spin glasses and random fields*, vol. 12 (World Scientific, 1998).

[50] Cavagna, A. Supercooled liquids for pedestrians. *Physics Reports* **476**, 51–124 (2009).

[51] Donati, C. *et al.* Stringlike cooperative motion in a supercooled liquid. *Physical Review Letters* **80**, 2338 (1998).

[52] Donati, C., Glotzer, S. C., Poole, P. H., Kob, W. & Plimpton, S. J. Spatial correlations of mobility and immobility in a glass-forming Lennard-Jones liquid. *Physical Review E* **60**, 3107 (1999).

[53] Perera, D. N. & Harrowell, P. Consequences of kinetic inhomogeneities in glasses. *Physical Review E* **54**, 1652 (1996).

[54] Kob, W., Donati, C., Plimpton, S. J., Poole, P. H. & Glotzer, S. C. Dynamical heterogeneities in a supercooled lennard-jones liquid. *Physical Review Letters* **79**, 2827 (1997).

[55] Berthier, L. Time and length scales in supercooled liquids. *Physical Review E* **69**, 020201 (2004).

[56] Russell, E. V. & Israeloff, N. Direct observation of molecular cooperativity near the glass transition. *Nature* **408**, 695–698 (2000).

[57] Kegel, W. K. & van Blaaderen, A. Direct observation of dynamical heterogeneities in colloidal hard-sphere suspensions. *Science* **287**, 290–293 (2000).

[58] Zhang, Z., Yunker, P. J., Habdas, P. & Yodh, A. Cooperative rearrangement regions and dynamical heterogeneities in colloidal glasses with attractive versus repulsive interactions. *Physical Review Letters* **107**, 208303 (2011).

[59] Weeks, E. R., Crocker, J. C., Levitt, A. C., Schofield, A. & Weitz, D. A. Three-dimensional direct imaging of structural relaxation near the colloidal glass transition. *Science* **287**, 627–631 (2000).

[60] Ediger, M. D. Spatially heterogeneous dynamics in supercooled liquids. *Annual review of physical chemistry* **51**, 99–128 (2000).

[61] Bucaro, J., Dardy, H. & Corsaro, R. Strain relaxation in glass by optical correlation and pressure jump relaxation. *Journal of Applied Physics* **46**, 741–746 (1975).

[62] Sidebottom, D., Bergman, R., Börjesson, L. & Torell, L. Two-step relaxation decay in a strong glass former. *Physical Review Letters* **71**, 2260 (1993).

[63] Binder, K. & Young, A. P. Spin glasses: Experimental facts, theoretical concepts, and open questions. *Reviews of Modern physics* **58**, 801 (1986).

[64] Berthier, L. & Biroli, G. Theoretical perspective on the glass transition and amorphous materials. *Reviews of Modern Physics* **83**, 587 (2011).

[65] Parisi, G. An increasing correlation length in off-equilibrium glasses. *The Journal of Physical Chemistry B* **103**, 4128–4131 (1999).

[66] Donati, C., Franz, S., Glotzer, S. C. & Parisi, G. Theory of non-linear susceptibility and correlation length in glasses and liquids. *Journal of non-crystalline solids* **307**, 215–224 (2002).

[67] Berthier, L. Dynamic heterogeneity in amorphous materials. *Physics* **4**, 42 (2011).

[68] Stevenson, J. D., Schmalian, J. & Wolynes, P. G. The shapes of cooperatively rearranging regions in glass-forming liquids. *Nature Physics* **2**, 268–274 (2006).

[69] Berthier, L. *et al.* Direct experimental evidence of a growing length scale accompanying the glass transition. *Science* **310**, 1797–1800 (2005).

[70] Zhang, P., Maldonis, J. J., Liu, Z., Schroers, J. & Voyles, P. M. Spatially heterogeneous dynamics in a metallic glass forming liquid imaged by electron correlation microscopy. *Nature communications* **9**, 1–7 (2018).

[71] Tracht, U. *et al.* Length scale of dynamic heterogeneities at the glass transition determined by multidimensional nuclear magnetic resonance. *Physical Review Letters* **81**, 2727 (1998).

[72] Maggi, C., Di Leonardo, R., Dyre, J. C. & Ruocco, G. Generalized fluctuation-dissipation relation and effective temperature in off-equilibrium colloids. *Physical Review B* **81**, 104201 (2010).

[73] Mayer, P. *et al.* Heterogeneous dynamics of coarsening systems. *Physical Review Letters* **93**, 115701 (2004).

[74] Duri, A. & Cipelletti, L. Length scale dependence of dynamical heterogeneity in a colloidal fractal gel. *EPL (Europhysics Letters)* **76**, 972 (2006).

[75] Trappe, V. *et al.* Investigation of q-dependent dynamical heterogeneity in a colloidal gel by x-ray photon correlation spectroscopy. *Physical Review E* **76**, 051404 (2007).

[76] Dallari, F. *et al.* Microscopic pathways for stress relaxation in repulsive colloidal glasses. *Science advances* **6**, eaaz2982 (2020).

[77] Kaku, M. *Quantum field theory: a modern introduction* (Oxford Univ. Press, 1993).

[78] Landau, L. D. & Lifshitz, E. M. *Electrodynamics of continuous media*, vol. 8 (Pergamon Press, New York, 1984).

[79] Landau, L. D. & Lifshitz, E. M. *The classical theory of fields*, vol. 2 (Pergamon Press, New York, 1975).

[80] VanHove, M. A., Weinberg, W. H. & Chan, C.-M. *Low-energy electron diffraction: experiment, theory and surface structure determination*, vol. 6 (Springer Science & Business Media, 2012).

[81] Altarelli, M. Resonant x-ray scattering: a theoretical introduction. In *Magnetism: A Synchrotron Radiation Approach*, 201–242 (Springer, 2006).

[82] Lovesey, S. W. Theory of neutron scattering from condensed matter (1984).

[83] Bhatia, A. & Thornton, D. Structural aspects of the electrical resistivity of binary alloys. *Physical Review B* **2**, 3004 (1970).

[84] Hubbell, J. H. *et al.* Atomic form factors, incoherent scattering functions, and photon scattering cross sections. *Journal of physical and chemical reference data* **4**, 471–538 (1975).

[85] Goodman, J. W. Statistical properties of laser speckle patterns. In *Laser speckle and related phenomena*, 9–75 (Springer, 1975).

[86] Rabal, H. J. & Braga Jr, R. A. *Dynamic laser speckle and applications* (CRC press, 2008).

[87] Siegert, A. *On the fluctuations in signals returned by many independently moving scatterers* (Radiation Laboratory, Massachusetts Institute of Technology, 1943).

[88] Dainty, J. C. *et al. Laser speckle and related phenomena*, vol. 9 (Springer, 1975).

[89] Kirsch, S., Frenz, V., Schärtl, W., Bartsch, E. & Sillescu, H. Multispeckle autocorrelation spectroscopy and its application to the investigation of ultraslow dynamical processes. *The Journal of chemical physics* **104**, 1758–1761 (1996).

[90] Wong, A. P. & Wiltzius, P. Dynamic light scattering with a CCD camera. *Review of Scientific Instruments* **64**, 2547–2549 (1993).

[91] Cipelletti, L. & Weitz, D. Ultralow-angle dynamic light scattering with a charge coupled device camera based multispeckle, multitau correlator. *Review of scientific instruments* **70**, 3214–3221 (1999).

[92] Duri, A., Bissig, H., Trappe, V. & Cipelletti, L. Time-resolved-correlation measurements of temporally heterogeneous dynamics. *Physical Review E* **72**, 051401 (2005).

[93] Li, L. *et al.* Photon statistics and speckle visibility spectroscopy with partially coherent x-rays. *Journal of synchrotron radiation* **21**, 1288–1295 (2014).

[94] Bremer, L. G., Deriemaeker, L., Finsy, R., Gelade, E. & Joosten, J. G. Fiber optic dynamic light scattering, neither homodyne nor heterodyne. *Langmuir* **9**, 2008–2014 (1993).

[95] Ruta, B. *et al.* Wave vector dependence of the dynamics in supercooled metallic liquids. *Physical Review Letters* **125**, 055701 (2020).

[96] Goodman, J. W. *Statistical optics* (John Wiley & Sons, New York, 1985).

[97] Vartanyants, I. A. & Singer, A. Coherence properties of third-generation synchrotron sources and free-electron lasers. In *Synchrotron Light Sources and Free-Electron Lasers: Accelerator Physics, Instrumentation and Science Applications*, 987–1029 (Springer, 2016).

[98] Van der Veen, F. & Pfeiffer, F. Coherent x-ray scattering. *Journal of Physics: Condensed Matter* **16**, 5003 (2004).

[99] Madsen, A., Fluerasu, A. & Ruta, B. Structural dynamics of materials probed by x-ray photon correlation spectroscopy. In *Synchrotron Light Sources and Free-Electron Lasers: Accelerator Physics, Instrumentation and Science Applications*, 1617–1641 (Springer, 2016).

[100] Ginzburg, V. *Izv. Akad. Nauk SSSR, Ser. Fiz.* **11**, 165 (1947).

[101] Schmüser, P., Dohlus, M. & Rossbach, J. *Ultraviolet and soft X-ray free-electron lasers: introduction to physical principles, experimental results, technological challenges*, vol. 229 (Springer Science & Business Media, 2008).

[102] `www.esrf.eu`.

[103] `www.desy.de`.

[104] Pintori, G. *Relaxation dynamics in borate glass formers probed by photon correlation at the microscopic and macroscopic length scale*. Ph.D. thesis, University of Trento (2017).

[105] Chryssikos, G. D., Kamitsos, E., Patsis, A., Bitsis, M. & Karakassides, M. The devitrification of lithium metaborate: polymorphism and glass formation. *Journal of Non-Crystalline Solids* **126**, 42–51 (1990).

[106] Shelby, J. Thermal expansion of alkali borate glasses. *Journal of the American Ceramic Society* **66**, 225–227 (1983).

[107] Dallari, F. *et al.* The structural relaxation dynamics in the glass-former $B_2O_3$: a multi-speckle dynamic light scattering study. *Philosophical Magazine* **96**, 800–808 (2016).

[108] Owen, R. L., Holton, J. M., Schulze-Briese, C. & Garman, E. F. Determination of x-ray flux using silicon pin diodes. *Journal of synchrotron radiation* **16**, 143–151 (2009).

[109] Dallari, F. *et al.* X-rays induced atomic dynamics in a lithium-borate glass. *Condensed Matter Physics* **22**, 43606 (2019).

[110] Martinelli, A. *et al.* Probing the dynamics of $B_2O_3$ across the glass transition: an x-ray photon correlation spectroscopy study. *Philosophical Magazine* **100**, 2636–2645 (2020).

[111] Matsuda, Y. *et al.* Calorimetric study of the glass transition dynamics in lithium borate glasses over a wide composition range by modulated DSC. *Fluid phase equilibria* **256**, 127–131 (2007).

[112] Bengtzelius, U., Gotze, W. & Sjolander, A. Dynamics of supercooled liquids and the glass transition. *Journal of Physics C: solid state Physics* **17**, 5915 (1984).

[113] Gotze, W. & Sjogren, L. Relaxation processes in supercooled liquids. *Reports on progress in Physics* **55**, 241 (1992).

[114] Janssen, L. Mode-coupling theory of the glass transition: A primer. *Frontiers in Physics* **6**, 97 (2018).

[115] Götze, W. & Sjögren, L. The mode coupling theory of structural relaxations. *Transport theory and statistical physics* **24**, 801–853 (1995).

[116] Sciortino, F., Fabbian, L., Chen, S.-H. & Tartaglia, P. Supercooled water and the kinetic glass transition. II. collective dynamics. *Physical Review E* **56**, 5397 (1997).

[117] Fuchs, M., Hofacker, I. & Latz, A. Primary relaxation in a hard-sphere system. *Physical Review A* **45**, 898 (1992).

[118] Fuchs, M. & Mayr, M. R. Aspects of the dynamics of colloidal suspensions: Further results of the mode-coupling theory of structural relaxation. *Physical Review E* **60**, 5742 (1999).

[119] Nauroth, M. & Kob, W. Quantitative test of the mode-coupling theory of the ideal glass transition for a binary Lennard-Jones system. *Physical Review E* **55**, 657 (1997).

[120] Rinaldi, A., Sciortino, F. & Tartaglia, P. Dynamics in a supercooled molecular liquid: Theory and simulations. *Physical Review E* **63**, 061210 (2001).

[121] Tölle, A. Neutron scattering studies of the model glass former orthoterphenyl. *Reports on Progress in Physics* **64**, 1473 (2001).

[122] Horbach, J. & Kob, W. Relaxation dynamics of a viscous silica melt: The intermediate scattering functions. *Physical Review E* **64**, 041503 (2001).

[123] Demmel, F., Diepold, A., Aschauer, H. & Morkel, C. Temperature dependence of the de Gennes narrowing in liquid rubidium. *Physical Review B* **73**, 104207 (2006).

[124] Rovigatti, L., Nava, G., Bellini, T. & Sciortino, F. Self-dynamics and collective swap-driven dynamics in a particle model for vitrimers. *Macromolecules* **51**, 1232–1241 (2018).

[125] Roldán-Vargas, S., Rovigatti, L. & Sciortino, F. Connectivity, dynamics, and structure in a tetrahedral network liquid. *Soft Matter* **13**, 514–530 (2017).

[126] Handle, P. H., Rovigatti, L. & Sciortino, F. q-independent slow dynamics in atomic and molecular systems. *Physical Review Letters* **122**, 175501 (2019).

[127] De Gennes, P. G. Liquid dynamics and inelastic scattering of neutrons. *Physica* **25**, 825–839 (1959).

[128] Duri, A., Sessoms, D. A., Trappe, V. & Cipelletti, L. Resolving long-range spatial correlations in jammed colloidal systems using photon correlation imaging. *Physical Review Letters* **102**, 085702 (2009).

[129] Dallari, F. *Slow dynamics in colloids and network glasses close to the structural arrest: the Stress-relaxation as a root to equilibrium.* Ph.D. thesis, University of Trento (2018).

[130] Philippe, A. *et al.* An efficient scheme for sampling fast dynamics at a low average data acquisition rate. *Journal of Physics: Condensed Matter* **28**, 075201 (2016).

[131] Feller, S. A. *et al.* Physical properties of alkali borosilicate glasses. In *Proceedings of the Second International Conference on Borate Glasses, Crystals, and Melts, Abingdon, United Kingdom*, 246–253 (Sheffield, United Kingdom: The Society of Glass Technology, 1997).

[132] Matsuda, Y., Fukawa, Y., Kawashima, M., Mamiya, S. & Kojima, S. Dynamic glass transition and fragility of lithium borate binary glass. *Solid State Ionics* **179**, 2424–2427 (2008).

[133] Israelachvili, J. N. *Intermolecular and surface forces* (Academic press, 2011).

[134] Götze, W. Recent tests of the mode-coupling theory for glassy dynamics. *Journal of Physics: condensed matter* **11**, A1 (1999).

[135] Beysens, D. & Esteve, D. Adsorption phenomena at the surface of silica spheres in a binary liquid mixture. *Physical Review Letters* **54**, 2123 (1985).

[136] Pontoni, D., Narayanan, T., Petit, J.-M., Grübel, G. & Beysens, D. Microstructure and dynamics near an attractive colloidal glass transition. *Physical Review Letters* **90**, 188301 (2003).

[137] Lu, X., Mochrie, S., Narayanan, S., Sandy, A. & Sprung, M. How a liquid becomes a glass both on cooling and on heating. *Physical Review Letters* **100**, 045701 (2008).

[138] `http://www.cxro.lbl.gov/`.

[139] Aragon, S. & Pecora, R. Theory of dynamic light scattering from polydisperse systems. *The Journal of Chemical Physics* **64**, 2395–2404 (1976).

[140] Verwey, E. J. W., Overbeek, J. T. G. & Van Nes, K. *Theory of the stability of lyophobic colloids: the interaction of sol particles having an electric double layer* (Elsevier Publishing Company, 1948).

[141] Lebowitz, J. & Percus, J. Mean spherical model for lattice gases with extended hard cores and continuum fluids. *Physical Review* **144**, 251 (1966).

[142] Martinelli, A., Dallari, F., Grübel, G., Zontone, F. & Monaco, G. The glass transition in colloidal suspensions of silica nanoparticles in a water-lutidine mixture: A photon correlation study. *Il nuovo cimento C* **41**, 1–10 (2018).

[143] Westermeier, F. *et al.* Structure and short-time dynamics in concentrated suspensions of charged colloids. *The Journal of chemical physics* **137**, 114504 (2012).

[144] Wang, Z., Guo, H., Liu, Y. & Wang, X. Investigating the effective interaction between silica colloidal particles near the critical point of a binary solvent by small angle neutron scattering. *The Journal of chemical physics* **149**, 084905 (2018).

[145] Madsen, A., Leheny, R. L., Guo, H., Sprung, M. & Czakkel, O. Beyond simple exponential correlation functions and equilibrium dynamics in x-ray photon correlation spectroscopy. *New Journal of Physics* **12**, 055001 (2010).

[146] Guo, H. *et al.* Slow, nondiffusive dynamics in concentrated nanoemulsions. *Physical Review E* **75**, 041401 (2007).

[147] Busch, S., Jensen, T. H., Chushkin, Y. & Fluerasu, A. Dynamics in shear flow studied by x-ray photon correlation spectroscopy. *The European Physical Journal E* **26**, 55–62 (2008).

[148] Cipelletti, L. *et al.* Universal non-diffusive slow dynamics in aging soft matter. *Faraday discussions* **123**, 237–251 (2003).

[149] Bouchaud, J.-P. & Georges, A. Anomalous diffusion in disordered media: statistical mechanisms, models and physical applications. *Physics reports* **195**, 127–293 (1990).

[150] Angelini, R. *et al.* Dichotomic aging behaviour in a colloidal glass. *Soft Matter* **9**, 10955–10959 (2013).

[151] Angelini, R. & Ruzicka, B. Non-diffusive dynamics in a colloidal glass: Aging versus rejuvenation. *Colloids and Surfaces A: Physicochemical and Engineering Aspects* **483**, 316–320 (2015).

[152] Bouzid, M., Colombo, J., Barbosa, L. V. & Del Gado, E. Elastically driven intermittent microscopic dynamics in soft solids. *Nature communications* **8**, 1–8 (2017).

[153] Falus, P., Borthwick, M., Narayanan, S., Sandy, A. & Mochrie, S. Crossover from stretched to compressed exponential relaxations in a polymer-based sponge phase. *Physical Review Letters* **97**, 066102 (2006).

[154] Gnan, N. & Zaccarelli, E. The microscopic role of deformation in the dynamics of soft colloids. *Nature Physics* **15**, 683–688 (2019).

[155] Jain, A. *et al.* Anisotropic and heterogeneous dynamics in an aging colloidal gel. *Soft Matter* **16**, 2864–2872 (2020).

[156] Charbonneau, P. & Reichman, D. Dynamical heterogeneity and nonlinear susceptibility in supercooled liquids with short-range attraction. *Physical Review Letters* **99**, 135701 (2007).

[157] Pintori, G. *et al.* X-ray induced dynamics in oxide glasses as a probe of network connectivity. *Submitted* (2020).

[158] Ramos, M., Moreno, J., Vieira, S., Prieto, C. & Fernandez, J. Correlation of elastic, acoustic and thermodynamic properties in $B_2O_3$ glasses. *Journal of non-crystalline solids* **221**, 170–180 (1997).

[159] Holzweber, K., Tietz, C., Fritz, T. M., Sepiol, B. & Leitner, M. Beam-induced atomic motion in alkali borate glasses. *Physical Review B* **100**, 214305 (2019).

[160] Pye, L. D., Fréchette, V. D. & Kreidl, N. J. *Borate glasses: structure, properties, applications*, vol. 12 (Springer Science & Business Media, 2012).

[161] Silver, A. & Bray, P. Nuclear magnetic resonance absorption in glass. I. Nuclear quadrupole effects in boron oxide, soda-boric oxide, and borosilicate glasses. *The Journal of Chemical Physics* **29**, 984–990 (1958).

[162] Jellison Jr, G., Panek, L., Bray, P. & Rouse Jr, G. Determinations of structure and bonding in vitreous $B_2O_3$ by means of $B^{10}$, $B^{11}$, and $O^{17}$ NMR. *The Journal of Chemical Physics* **66**, 802–812 (1977).

[163] Jellison Jr, G. & Bray, P. A structural interpretation of $B^{10}$ and $B^{11}$ NMR spectra in sodium borate glasses. *Journal of Non-Crystalline Solids* **29**, 187–206 (1978).

[164] Youngman, R. E. & Zwanziger, J. W. Network modification in potassium borate glasses: structural studies with NMR and Raman spectroscopies. *The Journal of Physical Chemistry* **100**, 16720–16728 (1996).

[165] Feller, S., Dell, W. & Bray, P. $^{10}$B NMR studies of lithium borate glasses. *Journal of Non-Crystalline Solids* **51**, 21–30 (1982).

[166] Bødker, M. S., Mauro, J. C., Youngman, R. E. & Smedskjaer, M. M. Statistical mechanical modeling of borate glass structure and topology: prediction of superstructural units and glass transition temperature. *The Journal of Physical Chemistry B* **123**, 1206–1213 (2019).

[167] Zachariasen, W. H. The atomic arrangement in glass. *Journal of the American Chemical Society* **54**, 3841–3851 (1932).

[168] Phillips, J. C. Topology of covalent non-crystalline solids I: Short-range order in chalcogenide alloys. *Journal of non-crystalline solids* **34**, 153–181 (1979).

[169] Gupta, P. & Cooper, A. Topologically disordered networks of rigid polytopes. *Journal of Non-Crystalline Solids* **123**, 14–21 (1990).

[170] Bauchy, M. Deciphering the atomic genome of glasses by topological constraint theory and molecular dynamics: a review. *Computational Materials Science* **159**, 95–102 (2019).

[171] Gupta, P. K. & Mauro, J. C. Composition dependence of glass transition temperature and fragility. I. A topological model incorporating temperature-dependent constraints. *The Journal of chemical physics* **130**, 094503 (2009).

[172] Mauro, J. C., Gupta, P. K. & Loucks, R. J. Composition dependence of glass transition temperature and fragility. II. A topological model of alkali borate liquids. *The Journal of chemical physics* **130**, 234503 (2009).

[173] Takeda, W., Wilkinson, C. J., Feller, S. A. & Mauro, J. C. Topological constraint model of high lithium content borate glasses. *Journal of Non-Crystalline Solids: X* **3**, 100028 (2019).

[174] Vegiri, A. & Varsamis, C.-P. E. Clustering and percolation in lithium borate glasses. *The Journal of chemical physics* **120**, 7689–7695 (2004).

[175] Smedskjaer, M. M., Mauro, J. C. & Yue, Y. Prediction of glass hardness using temperature-dependent constraint theory. *Physical Review Letters* **105**, 115503 (2010).

[176] Varsamis, C.-P. E., Vegiri, A. & Kamitsos, E. I. Molecular dynamics investigation of lithium borate glasses: Local structure and ion dynamics. *Physical Review B* **65**, 104203 (2002).

[177] Shartsis, L., Capps, W. & Spinner, S. Density and expansivity of alkali borates and density characteristics of some other binary glasses. *Journal of the American Ceramic Society* **36**, 35–43 (1953).

[178] Ohta, Y., Shimada, M. & Koizumi, M. Properties and structure of lithium borate and strontium borate glasses. *Journal of the American Ceramic Society* **65**, 572–574 (1982).

[179] Matsuda, Y. *et al.* Elastic properties and fragility of lithium borate glasses. *Physics and Chemistry of Glasses-European Journal of Glass Science and Technology Part B* **50**, 367–371 (2009).

[180] Fukawa, Y., Matsuda, Y., Kawashima, M., Kodama, M. & Kojima, S. Brillouin scattering study of elastic properties of sodium borate binary

glasses. *Physics and Chemistry of Glasses-European Journal of Glass Science and Technology Part B* **50**, 149–152 (2009).

[181] Kawashima, M. *et al.* Elastic properties of potassium borate glass in a wide composition range studied by Brillouin scattering. *Japanese Journal of Applied Physics* **48**, 07GA03 (2009).

[182] Cormier, L., Majérus, O., Neuville, D. & Calas, G. Temperature-induced structural modifications between alkali borate glasses and melts. *Journal of the American Ceramic Society* **89**, 13–19 (2006).

[183] Alderman, O., Benmore, C. & Weber, J. Consequences of $sp^2$-$sp^3$ boron isomerization in supercooled liquid borates. *Applied Physics Letters* **117**, 131901 (2020).

[184] Lelong, G. *et al.* Lithium borates from the glass to the melt: a temperature-induced structural transformation viewed from the boron and oxygen atoms. *Inorganic Chemistry* **60**, 798–806 (2021).

[185] Angeli, F. *et al.* Effect of temperature and thermal history on borosilicate glass structure. *Physical Review B* **85**, 054110 (2012).

[186] Guo, H. *et al.* Nanoparticle motion within glassy polymer melts. *Physical Review Letters* **102**, 075702 (2009).

[187] Gabriel, J., Blochowicz, T. & Stühn, B. Compressed exponential decays in correlation experiments: The influence of temperature gradients and convection. *The Journal of Chemical Physics* **142**, 104902 (2015).

[188] Verwohlt, J. *et al.* Low dose x-ray speckle visibility spectroscopy reveals nanoscale dynamics in radiation sensitive ionic liquids. *Physical Review Letters* **120**, 168001 (2018).